PROBING THE EARLY UNIVERSE USING DARK MATTER MINIHALOS

M. Sten Delos

A dissertation submitted to the faculty at the University of North Carolina at Chapel Hill in partial fulfillment of the requirements for the degree of Doctor of Philosophy in the Department of Physics and Astronomy.

Chapel Hill
2020

Approved by:

Adrienne L. Erickcek

Joaquín E. Drut

Charles R. Evans

Fabian Heitsch

Sheila J. Kannappan

ABSTRACT

M. Sten Delos: Probing the Early Universe Using Dark Matter Minihalos
(Under the direction of Adrienne L. Erickcek)

Through their observable properties, the first and smallest dark matter halos represent a rare probe of subkiloparsec-scale variations in the density of the early Universe. These density variations could hold clues to the nature of inflation, the postinflationary cosmic history, and the identity of dark matter. However, the dynamical complexity of these minihalos hinders their usage as cosmological probes. A theoretical understanding of the minihalo-cosmology connection demands numerical simulation, but minihalos are too small and dense to simulate up to the present day in full cosmological context. This dissertation meets this challenge by using controlled numerical simulations to develop (semi)analytic models of dark matter structure. These models describe the formation of the first halos and their subsequent evolution as they accrete onto larger systems, both through tidal forces and encounters with other objects. I also explore two observational applications of the minihalo-cosmology connection: breaking a degeneracy between the properties of thermal-relic dark matter and the postinflationary history, and probing inflation's late stages via the small-scale primordial power spectrum.

For Maeve and Anora.

ACKNOWLEDGEMENTS

TABLE OF CONTENTS

LIST OF FIGURES

LIST OF TABLES

LIST OF ABBREVIATIONS AND SYMBOLS

a Scale factor

A Asymptotic coefficient of the inner density profile

a_c Scale factor of collapse

a_eq Scale factor at matter-radiation equality

a_RH Scale factor at reheating

$\mathcal{A}_s$ Primordial spectral amplitude

BBN   Big Bang nucleosynthesis

c Halo concentration

CDM   Cold dark matter

CMB   Cosmic microwave background

d Distance

$D(a)$ Linear growth function

dSph   Dwarf spheroidal galaxy

e   Euler's number

e Ellipticity

E Energy

EMDE   Early matter-dominated era

erf   Error function

F Force

$\mathcal{F}$ Flux

G	Newton's gravitational constant
g_*	Effective number of relativistic degrees of freedom
GeV	Gigaelectronvolt
H	Hubble rate
H_0	Hubble rate today
h	Hubble parameter
IGRB	Isotropic gamma-ray background
J	Geometric factor in the dark matter annihilation rate
k	Comoving wavenumber
k_{cut}	Wavenumber associated with the free-streaming cutoff
k_{dom}	Wavenumber entering the horizon at the onset of early matter domination
k_{RH}	Wavenumber entering the horizon at reheating
keV	Kiloelectronvolt
kpc	Kiloparsec
L	Luminosity
m	Mass
M_{max}	Mass enclosed within the radius of maximum circular velocity
M_{vir}	Virial mass
m_χ	Mass of the dark matter particle
M_*	Mass of a star
$M_\odot$	Solar mass

MD	Matter domination
MeV	Megaelectronvolt
Mpc	Megaparsec
LAT	Large Area Telescope (of the Fermi satellite)
n	Number density or number of orbits
N	Number of simulation particles
n_s	Primordial spectral index
NFW	Navarro-Frenk-White
p	Prolateness
P	Probability
$\mathcal{P}(k)$	Dimensionless power spectrum
$\mathcal{P}_\zeta(k)$	Dimensionless primordial curvature power spectrum
PBH	Primordial black hole
pc	Parsec
q	Comoving radius or distance
QCD	Quantum chromodynamics
r	Radius
r_c	Circular orbit radius
r_{max}	Radius of maximum circular velocity
r_s	Scale radius
r_{vir}	Virial radius

RD	Radiation domination
sr	Steradian
t	Time
T	Temperature or orbital period
T_{RH}	Temperature at reheating
T_{dom}	Temperature at the onset of early matter domination
UCMH	Ultracompact minihalo
v	Velocity
V	Volume or velocity
v_{max}	Maximum circular velocity
WDM	Warm dark matter
WIMP	Weakly interacting massive particle
z	Redshift
Z'	Hidden-sector mediator particle
δ	Fractional density contrast or Dirac delta function
δ_c	Critical linear density contrast for collapse
δ_{ec}	Critical linear density contrast, in ellipsoidal collapse theory
δ_{sc}	Critical linear density contrast, in spherical collapse theory
δ_v	Critical linear density contrast for virialization
δ_t	Critical linear density contrast for turnaround
Δ	Fractional mass excess enclosed or the change in a quantity

ϵ	Force-softening length or the power-law index of Δ with respect to enclosed mass
η	Orbital circularity
θ	Angle
ρ	Mass density
$\bar{\rho}$	Spatially averaged density
$\bar{\rho}_0$	Cosmologically averaged dark matter density today
ρ_{crit}	Critical density today
ρ_s	Scale density
σ	Standard deviation
$\langle \sigma v \rangle$	Velocity-averaged velocity-weighted dark matter annihilation cross section
χ	Dark matter particle
Ω	Solid angle
Ω_m	Matter density today in units of the critical density
Ω_r	Radiation density today in units of the critical density

CHAPTER 1:
INTRODUCTION

1.1 Cosmic history

The Universe as we know it is believed to have begun with a period of accelerated expansion called *inflation* [1–3]. During inflation, tiny quantum fluctuations in the energy density rapidly expanded beyond the cosmological horizon, becoming frozen due to lack of causal contact. Through this process, initially minor variations in the density of the Universe were seeded [4]. After inflation, the Universe became dominated by relativistic particles—radiation—which gradually cooled as the Universe continued to expand. After about $52\,000$ years [5], the radiation cooled enough that its energy density fell below that of nonrelativistic particles, and the Universe entered a period of matter domination. Subsequently, the density variations that inflation seeded grew through gravitational attraction, as regions with excess density attracted surrounding matter to grow still denser; this process eventually produced the vast network of galaxies that characterize the Universe today. Figures 1.1 and 1.2 plot, respectively, the cosmic expansion history and the evolution of the energy density of the Universe. Figure 1.3 shows a timeline of major cosmic events.

While this broad picture is consistent with observations, its details remain uncertain. The Universe was opaque during the first $380\,000$ years [5], concealing this period from direct view. Our earliest definitive constraints on cosmic evolution come from the decoupling of neutrinos from the thermal plasma, a process that occurred at a time of about 1 second. The details of neutrino decoupling influence Big Bang nucleosynthesis (BBN)—the process that created the first nuclei heavier than hydrogen—and the evolution of cosmic density variations. Consequently, observationally inferred light-element abundances [6–9] and density variations [10, 11] demand that the Universe was radiation dominated as early as a time of about 0.1 seconds (corresponding to a temperature of 3 MeV).

The preceding inflationary epoch is invoked to solve the horizon and flatness problems [1–3] and to explain the presence of primordial density variations (see Ref. [4] for a review). However, we have
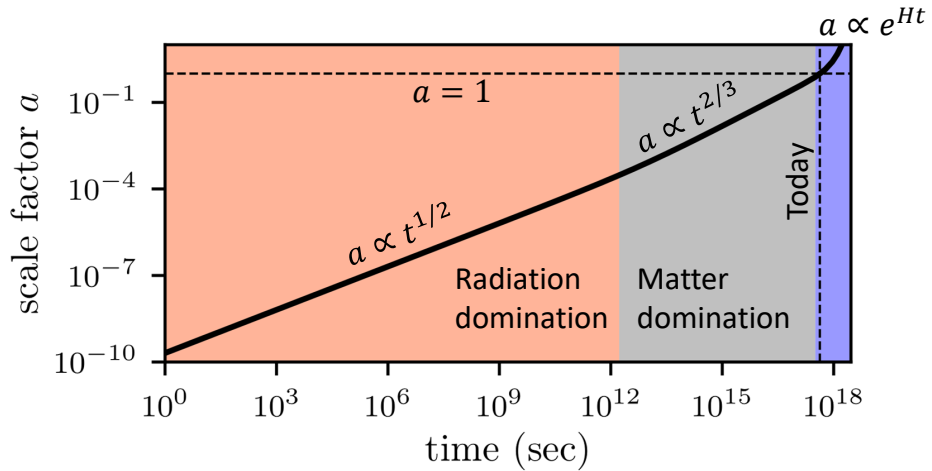
Figure 1.1: The known cosmic expansion history. The scale factor a—the size of the Universe relative to its size today—is plotted against time, starting at 1 second. When radiation dominates (red), the Universe grows with time t as $a \propto t^{1/2}$, while when matter dominates (gray), $a \propto t^{2/3}$. Dark energy is just beginning to dominate (blue) today; during both dark energy domination and inflation (not pictured), the scale factor grows exponentially in time.
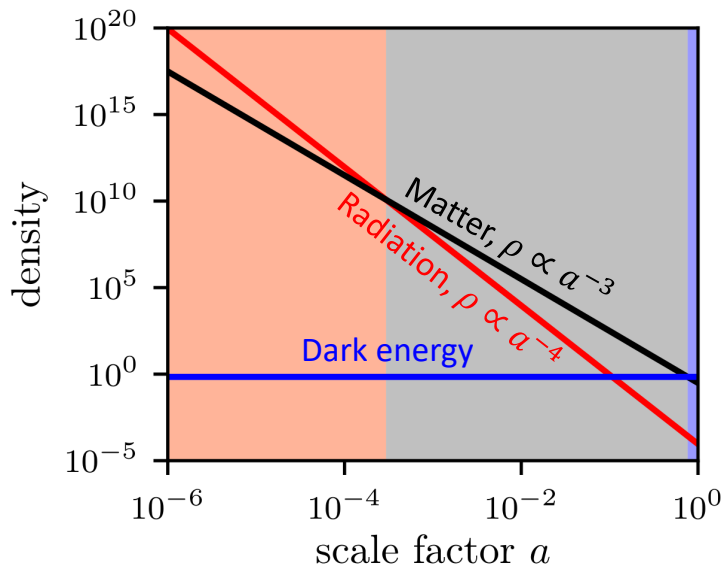
Figure 1.2: Evolution of the energy density ρ of the Universe, relative to the density today, as a function of the scale factor a (see Fig. 1.1). The density of (nonrelativistic) matter drops as $\rho \propto a^{-3}$ due to the expansion of the volume it occupies. Radiation additionally redshifts, so its energy density drops more quickly as $\rho \propto a^{-4}$. Consequently, radiation domination (red shading) eventually gives way to matter domination (gray). Dark energy's density is constant, and it is just beginning to dominate (blue shading) today ($a = 1$).
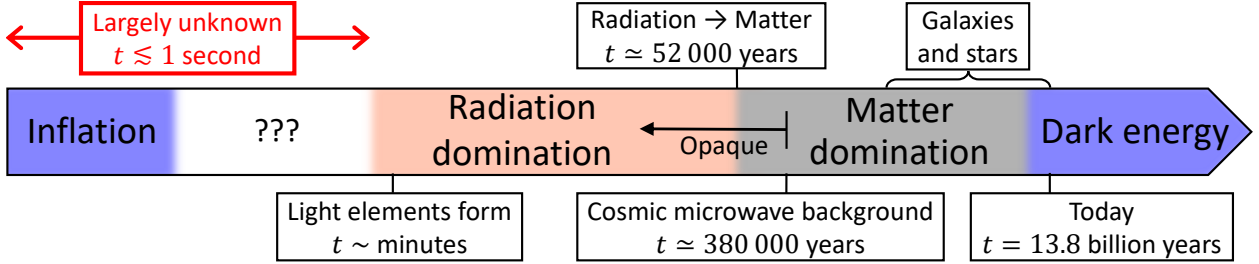
Figure 1.3: A schematic cosmic history. The Universe was opaque during the first 380 000 years, concealing this period from direct view, but indirect evidence, such as the observed abundances of the light elements deuterium, helium, and lithium, still constrains cosmic evolution during this time. However, the first second is largely unprobed (red arrows).

little observational guidance as to inflation's physical details, and the primordial density variations represent one of its few lasting imprints. Primordial fluctuations are observed to obey Gaussian statistics [12], allowing them to be solely described by a power spectrum $\mathcal{P}(k)$ quantifying the power contained in these fluctuations as a function of scale wavenumber[1] k. Fluctuations manifest themselves in the cosmic microwave background (CMB), light that last scattered the moment the Universe became transparent, so CMB has been employed to precisely measure the primordial power spectrum at scales above about 10 Mpc (e.g., Ref. [13]). Galaxy surveys largely confirm these measurements (e.g., Ref. [14]). $\mathcal{P}(k)$ has also been measured down to Mpc-scale wavelengths using the Lyman-α forest (e.g., Ref. [15]), the absorption lines in light from distant sources that, due to cosmological redshifting, mark the locations of hydrogen clouds. All of these observations are consistent with a weak power law $\mathcal{P}(k) \propto k^{n_s - 1}$ with $n_s = 0.9667 \pm 0.0040$ [16]; see Fig. 1.4. This nearly scale-invariant spectrum is consistent with the predictions of the simplest models of inflation.

However, the scales 10^{-4} Mpc^{-1} $\lesssim k \lesssim 3$ Mpc^{-1} that current observations measure correspond to only a small fraction of inflation's full dynamical trajectory. At smaller scales, which correspond to the later stages of inflation, Fig. 1.4 shows that only upper bounds on $\mathcal{P}(k)$ are accessible. Many inflationary models yield primordial curvature spectra that depart from scale invariance at small scales. Spectral features can arise through features in the potential of the inflaton field [27–37]—the field driving inflation—or through multiple episodes of inflation [38–40]. Features can also arise through interactions between the inflaton and other fields [41–48], such as energy transfer [49–52]

---

[1]$k \equiv 2\pi/\lambda$, where λ denotes wavelength.

3
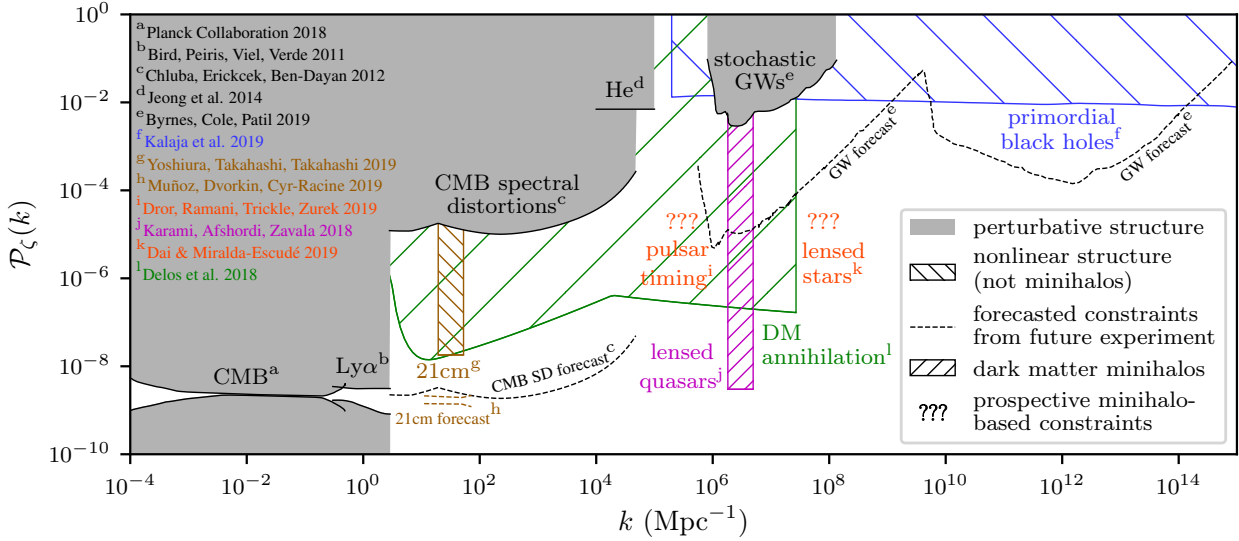
Figure 1.4: Observational constraints on primordial density variations, quantified by the power spectrum $\mathcal{P}_\zeta(k)$ of curvature fluctuations. Shaded and hatched ("//" or "\\") regions are ruled out by various observational tests, while dashed lines represent prospective constraints from future experiments. The CMB and the Lyman-α forest precisely measure $\mathcal{P}(k)$ at large scales [13, 15], and future measurements of the 21cm signal from neutral hydrogen promise to extend these constraints down to scales of order 10 kpc [17, 18]. At yet smaller scales, upper bounds on $\mathcal{P}(k)$ are derived from observational limits on distortions to the CMB spectrum [19], stochastic gravitational waves [20], and primordial black holes (PBHs) [21], and from the observed abundance of primordial helium [22]. Stronger bounds can be obtained by searching for dark matter microstructure using transient distortions within strongly lensed systems [23, 24], pulsar timing arrays [25], and dark matter annihilation [26]. Whereas shaded constraints are based on analytic perturbation theory, hatched constraints are based on uncertain models of nonlinear cosmic structure. Forward-hatched ("//") constraints, in particular, use models of small-scale dark matter structure, and question marks ("???") indicate prospective minihalo-based probes the forecasts for which have not yet been derived. To bolster the precision and robustness of these minihalo-based bounds, the research described in this dissertation aims to develop a precise understanding of the connection between primordial power and the smallest dark matter halos.

and nontrivial inflaton field trajectories [53–68], and from particular inflationary models such as axion-driven inflation [69, 70], running-mass inflation [71, 72], waterfall inflation [73–76], and others [77–83]. Additionally, alternatives to the inflationary picture have been widely considered [84–112], including cyclic-Universe models [113–135], and these theories leave their own imprints on the power spectrum of primordial fluctuations.

After inflation, relativistic Standard Model particles eventually come to dominate the energy density of the Universe. However, the energy scale associated with inflation could be as high as 10^{16} GeV [136, 137], and the absence of evidence from the Large Hadron Collider for physics beyond the Standard Model of particle physics (e.g., Refs. [138–144]) suggests that inflation's energy scale at least lies well beyond the 13-TeV energy scale that this particle collider probes. These energies are far higher than the highest temperature—3 MeV—at which radiation dominance has been observationally confirmed [6–11], and the Universe's evolution as it cooled through the vast temperature range between inflation and MeV scales remains completely unprobed. There is little reason to assume the Universe was radiation dominated during this full period (see Ref. [145] for a review of proposed dynamics). Since the energy density of radiation decreases more rapidly than that of nonrelativistic particles, any heavy field left over from the inflationary epoch would naturally come to dominate the energy density of the Universe, leading to an early matter-dominated era (EMDE). The early matter field is only observationally required to decay into radiation before the onset of neutrino decoupling at a time of about 0.1 seconds. Figure 1.5 depicts the density evolution in this scenario. Well motivated examples of such heavy fields include hidden-sector particles [146–158], moduli fields in string theory [159–166], and certain spectator fields invoked to generate primordial curvature variations during inflation [167–170]. After inflation ends, the inflaton itself can also behave as a pressureless fluid before its decay [171–180].

Like many of the aforementioned inflationary models, early matter domination also leaves a characteristic imprint on small-scale density variations. During an EMDE, the gravitational clustering of the dominant heavy particles boosts the growth rate of density perturbations that are inside the cosmological horizon, as shown in Fig. 1.6. Consequently, an EMDE can greatly amplify small-scale density variations [181–183]. Aside from early matter domination, another possibility—domination by a fast-rolling scalar field (e.g., Refs. [184–190])—also boosts small-scale density variations [191].
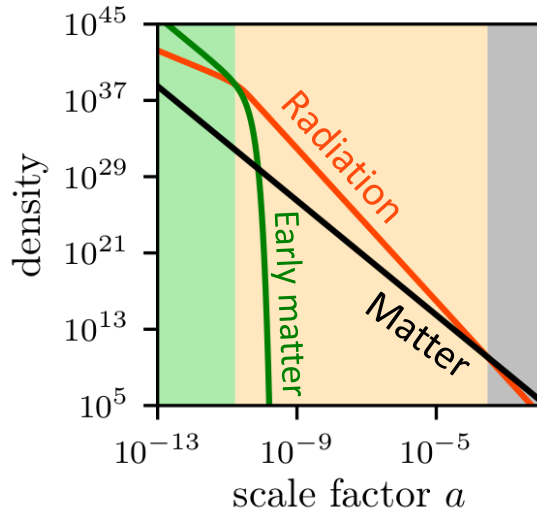
Figure 1.5: Density evolution that gives rise to an early matter-dominated era. An early matter species (green curve) dominates at early times (green shading), but it is unstable and decays into radiation (orange line). Radiation quickly comes to dominate (orange shading) and is eventually supplanted by stable matter (black; c.f. Fig. 1.2).
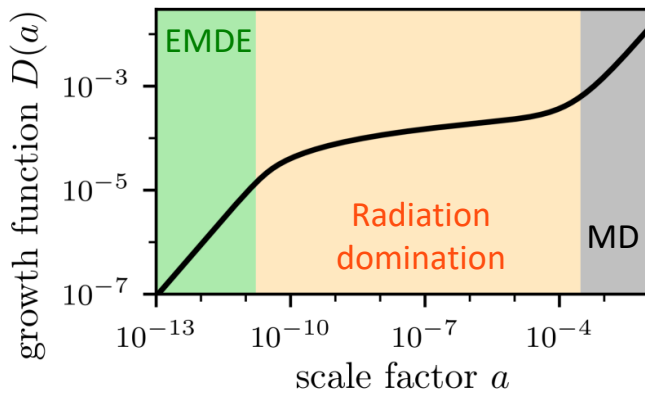
Figure 1.6: Growth of subhorizon density perturbations during and after early matter domination. Fractional density contrasts $\delta \equiv \delta\rho/\bar{\rho}$ grow proportionally to the growth function $D(a)$, plotted, as long as $\delta \ll 1$. During the EMDE (green), as during the last matter-dominated epoch (gray), density perturbations grow rapidly because the dominant species clusters. Since radiation does not cluster, perturbations grow much more slowly when radiation dominates (orange). Consequently, a early matter-dominated cosmology features greatly boosted small-scale density variations relative to if radiation dominated during the same period.

1.2 Dark matter minihalos as cosmological probes

In these ways, small-scale density variations could hold the answers to key questions about the early Universe and represent a promising probe of physics beyond the Standard Model of particle physics. In order to exploit this probe, we must extend our view of the primordial mass distribution to subgalactic scales. Variations in the density of ordinary ("baryonic") matter were washed out at these scales by complex processes, such as the diffusion of photons while the Universe was opaque and energetic feedback from stars during structure formation. However, it has been well established that ordinary matter accounts for only a small fraction of the Universe's matter content (e.g., Refs. [16, 192, 193]). The rest of the matter is "dark": it does not interact with light, so it is exposed to fewer physical processes. Fluctuations that were erased in the ordinary matter are expected to persist in this *dark matter*. While dark matter is difficult to directly observe, dark matter density variations still manifest in detectable ways. Regions with excess density collapse to form highly dense, gravitationally bound clouds of dark matter, or *halos* (see Ref. [194] for a review). Galaxies lie at the centers of the largest halos, but sufficiently extreme small-scale density excesses could form *minihalos*[2] long before galaxies appear. Since they form during a much denser epoch, these minihalos could be extraordinarily dense.

Despite dark matter's invisibility, the high density within minihalos leads to observational prospects. Dark matter is widely expected to have some interaction with ordinary (Standard Model) particles in order for it to be produced in the first place (see Refs. [195–199] for reviews of dark matter models). One of the best motivated explanations for dark matter's observed abundance is that it originated in matter-antimatter pairs within the early-Universe radiation bath. This pair production would have originally been in equilibrium with dark matter annihilation—the reverse process—but as the Universe expanded and cooled, both processes would have come to a halt and left a relic abundance of dark matter. Figure 1.7 describes this *freeze-out* process in detail, but the key consequence is that under this scenario, the dark matter would annihilate into detectable radiation today at a rate that is drastically boosted by the high density inside minihalos. Independently of the dark matter model, dense halos can also be detected through their gravitational signatures. For

---

[2]In this work, the terms "minihalo" and "microhalo" are interchangeable.

example, while minihalos are too small to be detectable as gravitational lenses on their own, they can produce detectable distortions within systems—distant quasars [23] or stars [24]—that are already strongly lensed. Minihalos can also be detected by their transient gravitational influence on the observed periods of pulsars [25], whether by passing near either the pulsar or the Earth (producing a Doppler shift) or by crossing the line of sight to the pulsar (producing a Shapiro time delay). Minihalos may also be detectable by their dynamical influence on cold astrophysical systems, such as stellar streams [200, 201].

Through detection efforts, minihalos can therefore serve as messengers from the early Universe. However, to employ them thus, we must establish the connection between minihalos' observable characteristics and properties of the small-scale density variations that preceded them, which are set by the early-Universe cosmology. This doctoral dissertation represents a study of this minihalo-cosmology connection and is organized as follows.

1.2.1 Ultracompact minihalos and probing inflation

Many previous works have used minihalos to place observational constraints on primordial curvature variations, but my research described in Chapter 2 challenges prior results. It has been commonly assumed, beginning with Ref. [202], that halos that form by the redshift[3] $z = 1000$—when the Universe was $430\,000$ years old and $1/1000$ its present size—develop the unusually steep density profile predicted by the analytic theory of Ref. [203]. This profile's density ρ scales with radius r as $\rho \propto r^{-9/4}$, and its compactness greatly boosts observational signals and has led to considerable interest in these objects. Observational limits on the abundance of these so-called *ultracompact minihalos* yielded the most stringent bounds on small-scale primordial density variations, which in turn led to powerful and unrivaled constraints on inflationary models [204]. However, using numerical simulations, Chapter 2 demonstrates exhaustively that the $\rho \propto r^{-9/4}$ profile does not arise from a realistic formation scenario. Instead, the first halos universally develop shallower $\rho \propto r^{-3/2}$ density profiles at small radii. This profile is still steeper than the $\rho \propto r^{-1}$ profile that arises within later-forming halos, such as those that surround galaxies [205].

This discovery significantly reduces the expected detectability of each minihalo, potentially

---

[3]$z \equiv 1/a - 1$, where a is the scale factor.
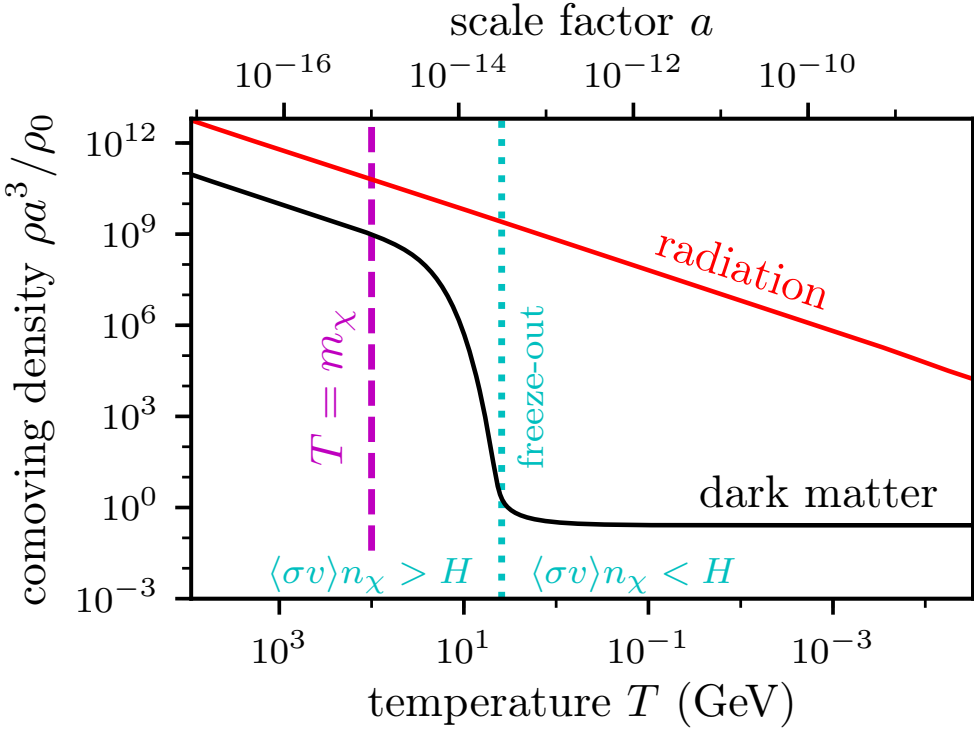
Figure 1.7: A depiction of dark matter freeze-out for a dark matter particle with mass $m_\chi = 100$ GeV. I plot the comoving energy density—that is, ρa^3, the density per expanding volume of space—of radiation (red) and dark matter (black) as a function of "time". Here, time is parametrized by the decreasing temperature of the radiation bath (bottom axis) or the increasing scale factor (top axis; $a = 1$ today). The radiation density gradually decreases due to redshifting caused by cosmological expansion. At early times (left), the dark matter particle is in equilibrium with the radiation bath; pair production and annihilation balance so that the dark matter density tracks the radiation density. Once the temperature T drops below the mass $m_\chi = 100$ GeV of the dark matter particle, pair production becomes disfavored because the radiation particles (e.g., photons) do not carry sufficient energy. At this point, the density of dark matter drops exponentially because annihilation is still efficient. Eventually, however, the annihilation rate per dark matter particle, $\langle\sigma v\rangle n_\chi$, drops below the expansion rate H; put differently, the expected time for a given particle to find a partner with which to annihilate becomes longer than the age of the Universe. Here, $\langle\sigma v\rangle$ is the velocity-averaged velocity-scaled cross section for dark matter annihilation, while n_χ is the number density of dark matter particles. At this point, the dark matter is said to *freeze out*: annihilation ceases and dark matter's comoving density stabilizes at the observed value of about 26% of the present-day energy density ρ_0.

impairing the capacity of these objects to constrain primordial density variations. On the other hand, it becomes no longer necessary to restrict an analysis to halos forming within the first 430 000 years, so the pool of halos that can contribute to constraints grows dramatically. By using simulation-tuned scaling arguments to relate minihalos to their precursor density excesses, Chapter 2 derives new bounds on primordial density variations that account for all minihalos. I find that, rather than being relaxed, constraints on density variations are tightened. The inclusion of all minihalos compensates for the reduction in signal from each one. This unexpected finding represents a new set of observational constraints that theories of inflation must satisfy.

1.2.2   Halo formation prior to matter domination, and probing hidden sectors

Sufficiently extreme density variations could collapse to form dark matter halos during the first 52 000 years, during which time the Universe was dominated by radiation instead of matter (see Figure 1.3). For instance, in hidden-sector dark matter theories—where a heavy mediator particle links dark matter to the Standard Model—the heavy mediator could drive an EMDE that amplifies density variations in the dark matter dramatically [181–183]. Using numerical simulations that account for the early presence of this short-lived heavy species, Chapter 3 studies halo formation during the radiation-dominated epoch. Since radiation does not cluster like matter, radiation dominance allows particles to drift freely without any net gravitational acceleration. Gravitationally bound structures cannot form where radiation dominates. Nevertheless, Chapter 3 demonstrates that localized regions can become matter dominated where freely drifting streams of dark matter converge. Bound halos form within these regions long before radiation globally gives way to matter. Their early formation would make these halos so dense—and hence so readily detectable—that observational limits on their abundance severely constrain the hidden-sector theories that my collaborators and I considered in Ref. [206].

1.2.3   Predicting the structures of dark matter halos

The observational constraints derived in Chapter 2 are based on simplifying approximations regarding the relationship between a primordial mass distribution and the demographics of the halo population that it forms. Motivated by the goal of precisely predicting minihalos' observational signals, Chapters 4–6 refine our understanding of this relationship. The small size and high internal density of the smallest halos make it infeasible to simulate their full populations and lifetimes on foreseeable hardware; in particular, the scale disparity between minihalos and the largest structures—

potentially 20 orders of magnitude in mass—is far too great to represent within a simulation's resolution.[4] Consequently, these chapters are devoted to the development of simulation-tuned mathematical models. In order to connect minihalo properties today to primordial density variations, these models characterize both the formation of minihalos and their subsequent evolution through cosmic time.

Formation of the first halos   Chapter 4 builds a framework that relates the internal structures of the first halos to properties of the initial density variations that formed them. Compared to other predictive models of halo populations, this framework is formulated more directly in terms of physical principles (as opposed to simply fitting simulation results). Consequently, it is unique in that its predictions are accurate across wildly disparate cosmological scenarios, so it spares the need to simulate every possible cosmology. By exploiting the statistical properties of the primordial mass distribution, this framework can rapidly characterize entire ensembles of minihalos, making it a powerful tool for predicting their observational signals.

Evolution due to tidal forces   After formation, the first generation of halos merge to create successively larger structures, and Chapter 5 develops a model that predicts the evolution of small subhalos inside much larger host halos. It is impractical to simulate a galactic-scale host halo together with a minihalo due to the vast difference in scales, so this chapter employs idealized simulations of N-body minihalos orbiting analytic hosts. Based on the results of these simulations, I develop a novel way to parametrize how a subhalo evolves due to a host halo's tidal forces; this parametrization reduces the entire complicated host-subhalo system to only three relevant physical parameters. Using this parametrization, Chapter 5 presents a model that predicts a subhalo's evolution with unparalleled accuracy.

Evolution due to stellar encounters   Minihalos inside galactic systems are also affected by encounters with individual stars. Chapter 6 uses numerical simulations to study how a halo responds to such an encounter and finds that, under most circumstances, only a single physical parameter—the energy that the encounter injects into halo particles—is relevant to the outcome. Using these simulation results, I develop a model that can predict the structural evolution of a halo passing

---

[4]Except when objects of different scales are spatially segregated. That is, the smallest halos can be resolved only where larger halos are absent (e.g., Ref. [207]).

through a stellar field with remarkable precision. Models of this sort are particularly valuable in treating the impact of stellar encounters because of their random nature. A simulation of this scenario would need to be repeated with different random stellar samples, at enormous computational expense. In contrast, the model described in Chapter 6 can characterize with minimal cost how stellar encounters affect whole ensembles of minihalos.

1.2.4 Breaking a degeneracy between dark matter and the early Universe

Finally, Chapter 7 applies these models to a problem that involves both the early Universe and the nature of dark matter. If dark matter originated in matter-antimatter pairs, then its microphysical properties are constrained by the requirement that it achieve its observed abundance. Under the standard assumption that radiation dominated the Universe when dark matter's production concluded, dark matter's (velocity-scaled, velocity-averaged) annihilation cross section $\langle \sigma v \rangle$ must be close to the particular value 3×10^{-26} cm^3/s [208]. This cross section presents an attainable target for indirect-detection experiments that search for annihilation products, such as gamma rays, sourced by nearby dark matter-rich dwarf galaxies [209–212]. However, a wide variety of dark matter candidates would have been produced entirely during the first second, when there is no reason to assume radiation was dominant. The possibility of an EMDE during this epoch vastly broadens the range of viable dark matter candidates; almost any annihilation cross section smaller than 3×10^{-26} cm^3/s is allowed [213–223]. Consequently, there is a degeneracy between dark matter properties and the history of the early Universe; the former cannot be determined without knowledge of the latter.

Fortunately, since early matter domination also amplifies small-scale density variations [181–183], it leads to a population of highly dense dark matter minihalos, and the density within these objects boosts the dark matter annihilation rate dramatically [206, 224, 225]. Chapter 7 uses the models developed in Chapters 4–6 (with some new refinements) to characterize the gamma-ray signals expected from the minihalo populations arising from this scenario. These minihalos are far too small to resolve as individual gamma-ray sources and would instead register as a diffuse signal, and I consider two complementary examples thereof:

(1) a background gamma-ray signal sourced by minihalos both within the Milky Way's dark halo and in the vast expanse outside our Galaxy;

(2) a directed gamma-ray signal sourced by minihalos within a particular dwarf galaxy; I pick the

Draco dwarf for its optimal combination of proximity and high mass. Chapter 7 compares the predicted gamma-ray signals with observational data from the Fermi Gamma-ray Space Telescope.

The signal from Draco (or any galactic system) is valuable because it can discriminate between different cosmological scenarios. Minihalos inside Draco suffer gradual disruption due to tidal forces and stellar encounters, and these effects suppress the annihilation signal near the system's center. The magnitude of this suppressive effect is sensitive to the detailed demographics of the minihalos, so measurements of the shape of a gamma-ray flux from Draco could be employed to probe these demographics. Through my models, this procedure would in turn probe primordial density variations and hence the Universe's first second. It would also distinguish minihalo-dominated dark matter annihilation from the decay of dark matter particles; the two unrelated processes produce almost identical signals that are differentiated only by minihalos' aforementioned central suppression.

However, absent a positive detection of dark matter-sourced gamma rays, the background signal offers significantly more constraining power than the signal from Draco due to the sheer volume sourcing the background. The precise strength of the dark matter constraints that Chapter 7 derives using the background signal depend on further details of dark matter's interactions with ordinary matter. Nevertheless, for plausible sets of parameters, its analysis rules out a broad range of dark matter candidates that early matter domination could otherwise make viable. Chapter 7 represents an important step toward constraints on dark matter that account for our ignorance of the Universe's early history.

CHAPTER 2:
DENSITY PROFILES OF ULTRACOMPACT MINIHALOS: IMPLICATIONS FOR CONSTRAINING THE PRIMORDIAL POWER SPECTRUM[1]

2.1 Introduction

Ultracompact dark matter minihalos have emerged as a powerful probe of early-Universe physics. Overdense regions with $\delta \equiv \delta\rho/\rho \gtrsim 10^{-3}$ at horizon entry seed the formation of dark matter minihalos near the time of recombination ($z \simeq 1000$) [202], and such early formation yields highly compact structures potentially visible through dark matter annihilation [227–243] or by their gravitational signatures [202, 244–246]. The nondetection of these structures thus constrains the amplitude of primordial density fluctuations, making it a probe of the primordial power spectrum [232–236, 246–249] and hence of inflationary models [204] and the thermal history of the Universe [250].

These ultracompact minihalos (UCMHs) provide access to perturbations on scales too small to be directly observed. Cosmic microwave background (CMB) observations indicate that the primordial power spectrum of curvature fluctuations $\mathcal{P}_\zeta(k)$ is consistent with a slightly red-tilted but otherwise featureless power law [251] with amplitude $\mathcal{A}_s = (2.142 \pm 0.049) \times 10^{-9}$ [16], and the Lyman-α forest tells a similar story [15]. However, these observations are only able to probe wavelengths longer than 2 Mpc, and numerous inflationary models predict an enhancement in small-scale power [27–31, 38–40, 49, 51–53, 56, 69–81]. Certain nonstandard thermal histories, such as an early matter-dominated era [181–183, 224] or an era dominated by a fast-rolling scalar field [191], also enhance small-scale fluctuations. Thus, probing the small-scale power spectrum is key to understanding early-Universe physics.

Unfortunately, at sub-Mpc scales, we only have upper bounds on density fluctuations, which are

---

[1]The content of this chapter was previously published in Physical Review D as Refs. [26, 226] and is copyright © 2018 American Physical Society. The original references are as follows: M. S. Delos, A. L. Erickcek, A. P. Bailey, and M. A. Alvarez, *Are ultracompact minihalos really ultracompact?*, Physical Review D **97**, 041303(R) (2018); M. S. Delos, A. L. Erickcek, A. P. Bailey, and M. A. Alvarez, *Density profiles of ultracompact minihalos: Implications for constraining the primordial power spectrum*, Physical Review D **98**, 063527 (2018).

obtained through the absence of secondary effects. Density contrasts of order 0.3 at horizon entry would form primordial black holes, so constraints on their abundance constrain $\mathcal{P}_\zeta(k) \lesssim 3 \times 10^{-2}$ over a wide range of scales [252]. An excess of integrated power would imprint distortions onto the CMB blackbody spectrum, so their nonobservation constrains $\mathcal{P}_\zeta(k) \lesssim 2 \times 10^{-5}$ for $k \lesssim 10^4 \text{ Mpc}^{-1}$ [19]. However, UCMHs supply the strongest constraints. The nondetection of gamma rays from dark matter annihilation in UCMHs constrains $\mathcal{P}_\zeta(k) \lesssim 3 \times 10^{-7}$ for $k \lesssim 10^7 \text{ Mpc}^{-1}$ [234].

2.1.1 The $\rho \propto r^{-9/4}$ density profile

With one recent exception [232], all constraints derived from UCMHs have been calculated assuming they develop the $\rho \propto r^{-9/4}$ density profile, which is drawn from analytic radial infall theory [203, 253] and taken to apply to halos forming at $z \gtrsim 1000$ due to the small velocity dispersion at those times [202]. This profile has a much steeper inner form than is typically observed in simulations (e.g., [194]), a property that enhances the observational signatures of UCMHs, but it is derived in an idealized picture satisfying spherical symmetry, radial motion, and (after halo collapse) self-similarity, or the absence of a scale length. It has been reproduced in N-body simulations from carefully constructed self-similar initial conditions [254, 255] but not from more realistic conditions [256–258]. In contrast, dark matter halos at galaxy scales form by hierarchical clustering, and simulations of this scenario yield halo density profiles of the Navarro-Frenk-White (NFW) form [205, 259, 260],

$$\rho(r) = \frac{\rho_s}{(r/r_s)(1 + r/r_s)^2}, \tag{2.1}$$

with a $\rho \propto r^{-1}$ inner profile. A slightly steeper profile arises in simulations with a free-streaming cutoff scale below which there are no fluctuations: halos at that scale form by steady accretion and develop $\rho \propto r^{-3/2}$ inner profiles [261–266]. Neither of these pictures comes close to reproducing the UCMH density profile. However, previous numerical experiments did not explore the collapse of an extreme density fluctuation at $z \simeq 1000$, and prior UCMH analyses have assumed that the combination of small velocity dispersion and isolation associated with a halo forming at such early times will suffice to yield the $\rho \propto r^{-9/4}$ profile.

Recent simulation work in Ref. [267] explicitly explored the UCMH formation scenario and called the applicability of the $\rho \propto r^{-9/4}$ profile into question. This work simulated early structure growth from a power spectrum with a narrow boost (which we will call a "spike") and concluded that the

resulting halos have NFW profiles. However, Ref. [267] failed to rule out UCMHs with the $\rho \propto r^{-9/4}$ profile because it did not select for extreme density peaks, instead simulating a typical box whose largest peak corresponded to a 4.3σ fluctuation (smoothed at the scale of the spike). Moreover, Ref. [267] claimed that the absence of $\rho \propto r^{-9/4}$ profiles owes to the lack of spherical symmetry and isolation in realistic conditions. Since Refs. [254, 255] observed (and we confirm) that spherical symmetry is unnecessary for the $\rho \propto r^{-9/4}$ profile, this claim suggests that halos forming from peaks rarer than 4.3σ could be sufficiently isolated to develop it. Reference [234] used peaks as extreme as 6σ to derive observational constraints, above the 5σ level that Ref. [267] claimed based on idealized simulations to not produce the $\rho \propto r^{-9/4}$ profile.

Our approach differs in that we search millions of density fields to find a sufficiently extreme peak. We simulate 6.8σ peaks collapsing at $z \simeq 1000$ in a more weakly boosted power spectrum than that of Ref. [267]. This level of statistical extremity corresponds to a UCMH mass fraction $f \simeq 10^{-9}$ in the analysis of Ref. [234], which is well below constrained levels[2], implying that our density peak is rarer than any level hitherto assumed to suffice for development of the $\rho \propto r^{-9/4}$ profile. We also consider an alternative power spectrum amplification—a step instead of a spike—and show that the density profile depends on the shape of the power spectrum. In particular, the spiked power spectrum produces isolated halos with $\rho \propto r^{-3/2}$ inner density profiles, while the step-enhanced spectrum produces halos by hierarchical assembly that develop NFW profiles. Lastly, we use idealized simulations to argue that self-similarity is necessary to produce the $\rho \propto r^{-9/4}$ profile, which would definitively rule out its appearance in a Gaussian random field.

2.1.2 Modeling halo populations to probe the primordial power spectrum

We also introduce a new model for predicting, based on their formation times, the density profiles of minihalos that form from spiked power spectra. Spectral spikes can arise from steps in the inflaton potential [27–30] or from particle production during inflation [49, 51, 52]. Near the free-streaming cutoff, the power spectrum imprinted by an early matter-dominated era is also similar to a spike [181–183, 224]. Moreover, spiked power spectra are less well constrained than flatter power spectra by CMB spectral distortions, which limit the power integrated over a broad range in k-space [19].

---

[2]While our power spectrum spike peaks above the generalized constraint in Ref. [234], it is not ruled out because it is not locally scale invariant.

In this chapter, we begin an investigation of halos forming from spiked power spectra that we will expand upon in Chapter 4.

Finally, we discuss the impact of our result on the capacity for minihalos to constrain the primordial power spectrum. We use our model to calculate an upper bound on the amplitude of spiked power spectra that incorporates the new shallower minihalo density profiles. This upper bound is based on limits from Fermi-LAT [268] on gamma rays from dark matter annihilation. Despite the reduced annihilation rate implied by the shallower profile, this constraint is stronger than an equivalent UCMH constraint derived using the $\rho \propto r^{-9/4}$ density profile. Our model provides a stronger constraint because it accounts for all halos, whereas the old UCMH model only counted halos forming at $z \gtrsim 1000$. Our calculation demonstrates the continued viability of minihalos as probes of the small-scale power spectrum, and we discuss future avenues for improvement.

2.2 Simulation preparation

We carry out simulations of halos forming at $z \simeq 1000$ from extreme peaks in the density field. This picture is intended to match the UCMH formation scenario [202], and we aim to show conclusively that the $\rho \propto r^{-9/4}$ single-power-law density profile does not arise in halos forming due to an enhancement of the primordial power spectrum.

2.2.1 Power spectrum

In order to perform numerical experiments on such early-forming minihalos, we must start with an enhanced power spectrum. Inflationary models supply a rich phenomenology in this respect. Steps, kinks, or second-derivative jumps in the inflaton potential would imprint spikes, steps, or bends, respectively, on the primordial power spectrum [27–31]. Particle production during inflation can produce a spike in the power spectrum [49, 51, 52], while multifield inflation can imprint steps [38–40] or oscillations [53, 56]. Inflation aside, an early matter-dominated era enhances perturbations that enter the horizon prior to the onset of radiation domination [181–183, 224], and an era dominated by a fast-rolling scalar field generates a similar enhancement [191].

For our simulations, we consider two examples from these possible power spectrum enhancements. First, we consider a narrow spike in the power spectrum. This shape has possible inflationary origins, as discussed above, and is also qualitatively similar to the enhancement generated by an early matter-dominated era at scales close to the free-streaming cutoff. Next, we consider a step in the power spectrum, intended to represent the opposite extreme where fluctuations are enhanced
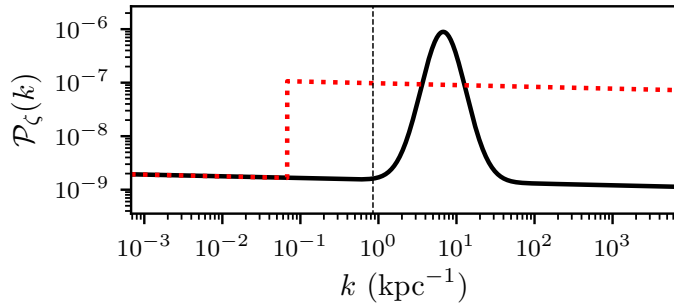
Figure 2.1: The dimensionless primordial power spectrum of curvature fluctuations used in our UCMH simulations. The solid line shows the spike modification, while the dotted line shows the step. The vertical dashed line indicates the smallest k (largest scale) accessible in the simulations.

over a broad range of scales. The two power spectra are plotted in Fig. 2.1. We superpose these modifications on a conventional power spectrum with amplitude $\mathcal{A}_s = 2.142 \times 10^{-9}$ and spectral index $n_s = 0.9667$ [16]. The spike contains 90% of its added power inside 1 e-fold in k, while the step amplifies fluctuations over the full range of scales accessible to the simulation. We will focus on the spiked power spectrum for most of Sec. 2.3 and return to the step in Sec. 2.3.5.

Halos forming from more extreme density contrasts are both more spherically symmetric [269] and less affected by nearby structure. To best simulate the UCMH formation scenario, we tune our power spectra so that halos forming by $z = 1000$ are exceedingly rare. In particular, the spiked power spectrum is tuned so that a 6.8σ fluctuation is necessary to seed such early collapse, and we generate a large number of random fields in order to obtain a handful of boxes to use as initial conditions for our simulations. This procedure may be contrasted with that of Ref. [267], who simulated a typical box whose most extreme peak was 4.3σ. UCMHs forming from peaks as extreme as 6σ are employed to derive observational constraints [234], so we wish to exceed this amplitude to conclusively rule out the $\rho \propto r^{-9/4}$ profile.

2.2.2 Simulation setup

A matter power spectrum is calculated at $z = 1000$ from the primordial power spectrum using the Boltzmann code CAMB SOURCES [270, 271]. To match simulation behavior, this power spectrum is evolved back to an earlier time using the Mészáros equation [272]

$$\frac{d^2\delta}{dy^2} + \frac{2 + 3y}{2y(y+1)}\frac{d\delta}{dy} - \frac{3}{2y(y+1)}\delta = 0, \tag{2.2}$$

18

which describes the subhorizon (Newtonian) evolution of dark matter density perturbations when baryons and radiation fluctuations are neglected. Here $y \equiv a/a_{\mathrm{eq}}$, where a_{eq} is the scale factor at matter-radiation equality. The physical solution to this equation is obtained by matching its general solution to the asymptotic behavior $\delta \propto \ln(0.44a/a_H)$ during radiation domination, where a_H is the scale factor when the perturbation mode enters the horizon. This physical solution is [273]

$$\delta \propto \left[\ln\left(\frac{k}{0.12h \ \mathrm{Mpc}^{-1}} \right) - \ln\left(\frac{\sqrt{1+y}+1}{\sqrt{1+y}-1} \right) \right] \left(y + \frac{2}{3} \right) + 2\sqrt{1+y}, \tag{2.3}$$

which provides a convenient prescription for calculating the evolution of a density contrast δ at linear order during mixed matter-radiation domination.

We choose to study fluctuations of order 0.2 kpc, so the spectral spike of Fig. 2.1 is centered at wavenumber $k_s = 6.8 \ \mathrm{kpc}^{-1}$. The starting redshift is chosen to be $z = 8 \times 10^6$ so that a density contrast that collapses at $z \simeq 1000$ is initially of order 0.1. We do not expect our results to depend significantly on either of these choices. We fix a comoving box size of 7.4 kpc and search periodic Gaussian random fields generated at the initial redshift for candidate peaks to collapse near $z = 1000$. Our search proceeds by first generating a Gaussian random field on a grid at the initial redshift using our spiked power spectrum. We then linearly evolve that field to $z = 1000$ and check whether the evolved density field has a peak[3] with $\delta > 1.686$, the linear threshold for collapse. If so, we use that grid, and if not, we generate a new one. Once we have a suitable density field, we use the Zel'dovich approximation to perturb a particle grid into a corresponding initial particle distribution. Since our simulations begin while the Universe is radiation-dominated, initial velocities are computed by differentiating Eq. (2.3); see Appendix A.1 for details.

For the spiked power spectrum shown in Fig. 2.1, we generate 2.3 million random density fields. Nine of them meet the collapse criterion, so we use these as the initial density fields and simulate them to $z = 50$. We also pick out one such density field, which we label the primary, to simulate at higher resolution and perform convergence tests; a slice of its initial density field is shown in Fig. 2.2. Notice how extreme the most overdense region is compared to its surroundings: this is indeed a rare

---

[3]For simplicity, we require $\delta > 1.686$ in one grid-cell in our 512^3-cell density field, which corresponds to a smoothing scale of 0.014 kpc. Because the power is concentrated in the spike, the precise choice of smoothing scale is unimportant.
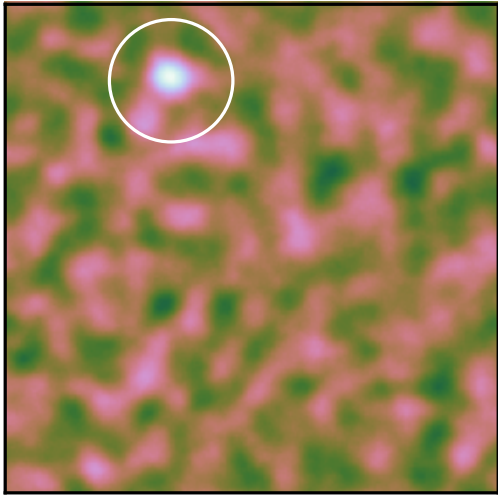
Figure 2.2: A slice of the 7.4 kpc density field used as initial conditions for the primary simulation run. Lighter regions are denser. The circle indicates the spherical region for a high-particle-density simulation.

event.

We also resimulate each of these density fields with increased simulation-particle density by resampling the initial field at higher resolution and including only a sphere of radius 0.93 kpc (with vacuum boundary conditions) around the most overdense point. This cut-out region is drawn in Fig. 2.2. This procedure allows us to probe smaller scales, and in Appendix A.2, we demonstrate that it does not change the density profile of the UCMH in the primary density field at $z = 100$. This convergence does not hold for the UCMHs in all nine fields: some of them begin to be influenced by structure outside the sphere as early as $z \sim 200$. Consequently, we only carry out these cut-out simulations up to $z = 400$ for the other eight density fields.

2.2.3 N-body code

We use the cosmological simulation code GADGET-2 [274, 275] for our numerical experiments. GADGET-2 is a hybrid N-body code that computes short-range forces using a tree method and long-range forces using Fourier techniques on a mesh. A discussion on our choices of simulation parameters can be found in Appendix A.2, along with convergence studies. We also model all matter as collisionless dark matter with $\Omega_m = 0.3089$ [16]: at the scales we study, dark matter halos cannot capture significant baryon content.

In order to accurately simulate a halo collapse at $z \simeq 1000$, our experiments must begin during radiation domination, so our N-body code must account for radiation. However, fluctuations in the radiation density field decay rapidly after horizon entry (see e.g. [276]), so it is only necessary to model the effect of a smooth radiation component on the expansion rate. We modified the publicly available release of GADGET-2 to include such a radiation component. Tests of the accuracy of this code can be found in Appendix A.1.

2.3   Simulation results

A visual inspection of the primary simulation box yields some key insights. First, we note that our criterion for early collapse, that the linear density contrast be $\delta > 1.686$ by $z = 1000$, has worked as expected. Figure 2.3 shows a slice of the density field evolving from $z = 1255$ to $z = 941$ at the location of the extreme density peak where we expect the UCMH to form, and we see that the density at the central point grows astronomically around $z = 1000$, an indication of collapse. To emphasize the rarity of this event, we also show the density field at $z = 715$: the UCMH is still the only halo to have collapsed by this redshift.

Next, we look at the density field at a much later redshift. Figure 2.4 shows the density field at $z = 100$ projected along one axis. The imprint of the spike in the power spectrum is evident, for we see an almost uniform distribution of halos with no large-scale structure. This is quite unlike a hierarchical growth picture (cf. Fig. 2.10). There is also minimal small-scale structure: these halos appear generally isolated and are only linked by filaments. These points are emphasized in the enhanced pictures of the main halo, where we see more clearly the lack of small-scale structure. We also see the beginning of fragmentation of the filaments into halos, but this fragmentation is a numerical artifact; see Appendix A.2.

According to the ROCKSTAR halo finder [277], there are 530 halos with masses above $1.5M_{\odot}$ at $z = 100$, and these halos contain 24% of the total mass of the simulation box within their virial radii. Such an abundance of halos is clearly expected in any picture that can produce a halo that collapses by $z \simeq 1000$, but later halos have been neglected in prior UCMH treatments because they are expected to be less compact. We will explore in Sec. 2.3.4 whether younger halos have the same structure as the oldest ones.
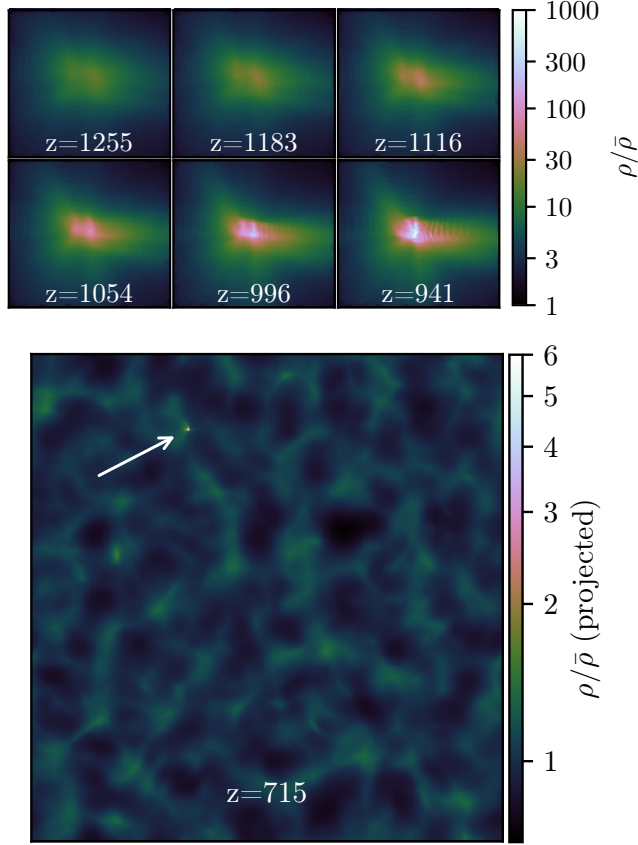
Figure 2.3: The density field for the primary run at different redshifts. Top: A $(0.24 \text{ kpc})^2 \times 0.06$ kpc slice showing the collapse of the UCMH near $z = 1000$. The color scale is logarithmic in units of the background matter density. Bottom: The full $(7.4 \text{ kpc})^3$ projected density field at $z = 715$. There is still only one halo, a testament to its rarity.

2.3.1 Density profiles

We now study the spherically averaged density profiles of the UCMHs. We simulated the UCMH in the primary simulation box at the highest particle density (see Appendix A.2 for details), so we first focus our study on that halo. This halo has mass $M = 31 M_\odot$ at $z = 100$, and Fig. 2.5 shows its density profile at $z = 50$, $z = 100$, $z = 200$, and $z = 400$ plotted in physical (not comoving) coordinates. We first note that this halo clearly does not follow a $\rho \propto r^{-9/4}$ or similar single-power-law form, contradicting the assumption made in prior UCMH treatments. We have conducted extensive convergence testing to confirm the validity of this result, as described in Appendix A.2. The actual density profile is shallower, which will substantially reduce the observational signals of these halos, as we discuss in Sec. 2.5. However, the inner profile is still steeper than the $\rho \propto r^{-1}$ behavior of the
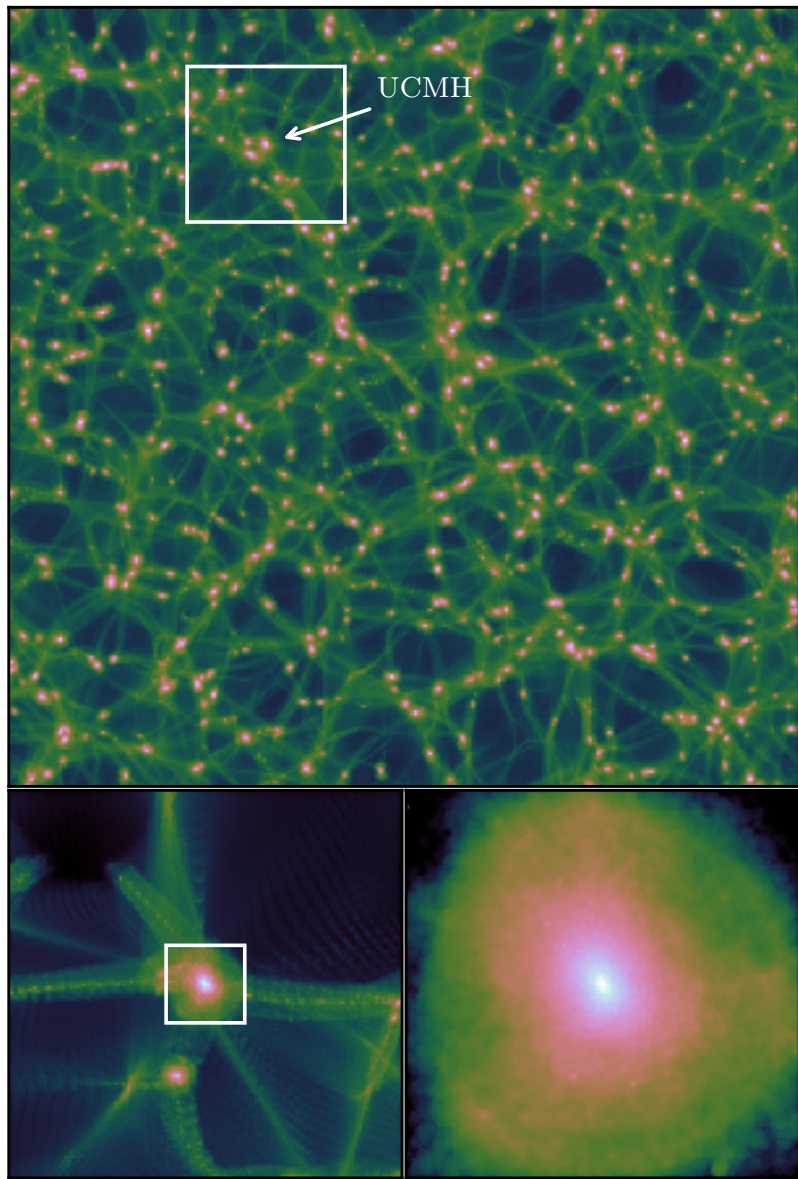
Figure 2.4: The projected density field of the primary simulation box at $z = 100$. Top: The full 7.4 kpc field. Bottom: Expanded pictures of the UCMH. The left (right) panel shows the projected density field for the surrounding 1.5 kpc (0.3 kpc) cube. Note that the expanded pictures do not fully match the white boxes because they are projected over smaller depths.
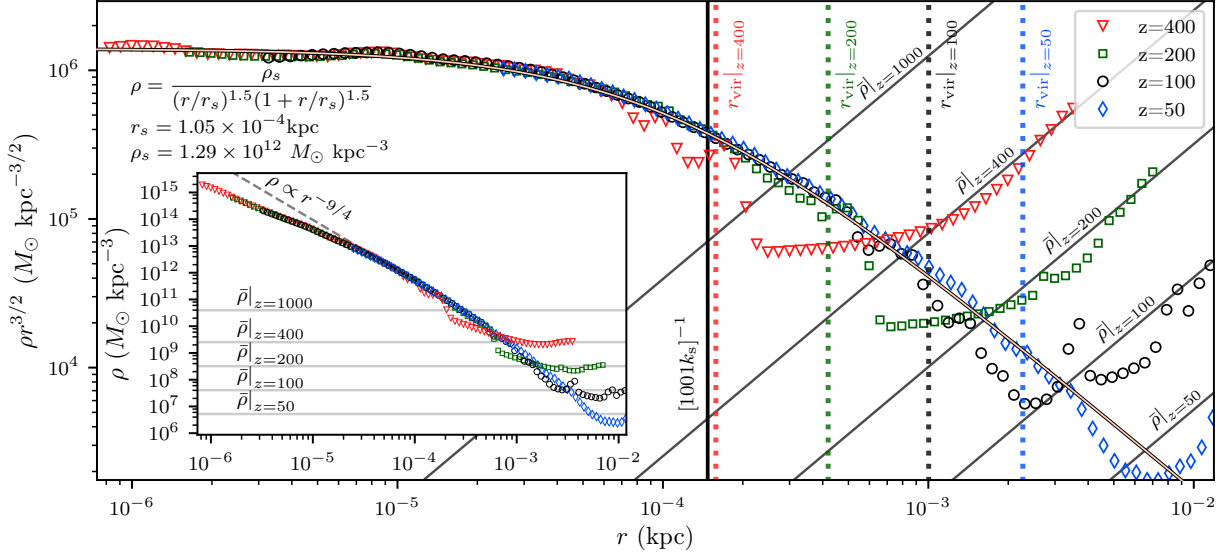
Figure 2.5: The spherically averaged density profile of the UCMH in the primary density field at $z = 400$, $z = 200$, $z = 100$, and $z = 50$. The vertical axis is scaled by $r^{3/2}$ to reduce the vertical range and better exhibit asymptotic behaviors; this practice will be adopted without remark in later figures. The density profile approaches $\rho \propto r^{-3/2}$ at small r and $\rho \propto r^{-3}$ at large r and is fit well by Eq. (2.4) (solid curve). The solid vertical line shows the physical scale of the power spectrum spike at $z = 1000$, while the vertical dashed lines show the halo virial radius at different redshifts. Inset: The same plot without y-axis scaling. A $\rho \propto r^{-9/4}$ curve is shown for comparison. We plot physical, not comoving, quantities. We show results from the vacuum-bounded sphere inside $r_{\rm vir}$ for $z \leq 100$, and results from the full box otherwise. The smallest radius at each redshift is set by $r > 2.8\epsilon$, where ϵ is the force-softening length parameter (see Appendix A.2), and contains $N > 3000$ particles.

NFW profile given by Eq. (2.1). In fact, the inner density profile approaches $\rho \propto r^{-3/2}$, and the full density profile is fit well by the double-power-law form

$$\rho(r) = \frac{\rho_s}{(r/r_s)^{3/2}(1 + r/r_s)^{3/2}} \tag{2.4}$$

which scales as $\rho \propto r^{-3/2}$ at small r and $\rho \propto r^{-3}$ at large r. We will call Eq. (2.4) the Moore profile due to its similarity to the form in Ref. [278].

Inner profiles $\rho \propto r^{-\gamma}$ with index γ ranging from 1.3 to 1.5 have previously been observed in the smallest halos forming above a cutoff in the power spectrum [262–266], and Ref. [261] found that the emergence of $\rho \propto r^{-3/2}$ is connected to the presence of a uniform-density core in the precursor density peak. In this light, it is not surprising that $\rho \propto r^{-3/2}$ arises in our spiked power spectrum, since like a cutoff power spectrum, it lacks power below the scale of the spike and produces cored peaks in the
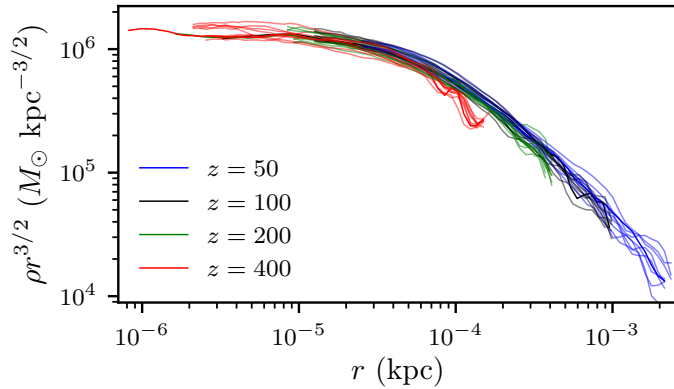
Figure 2.6: Radial density profiles at $z = 400$, $z = 200$, $z = 100$, and $z = 50$ of all nine UCMHs. These density profiles are cut off above the virial radius at each redshift. Evidently, all of our UCMHs possess similar density profiles to the one depicted in Fig. 2.5 (which is also plotted here).

primordial density field. The physical origin of the $\rho \propto r^{-3/2}$ profile is not well understood, but it is known to be markedly less rotationally supported than the NFW profile [261].

We next remark that the inner density profile does not appear to change in time: observe the remarkable concordance between the inner density profiles at different redshifts. This behavior was noticed in the radial infall solution [203, 253], and it is explained in that context by the steepness of the potential well: newly accreted matter passes through the central regions too quickly to significantly affect the density there. This effect is only enhanced in a three-dimensional picture, where newly accreted matter is likely to possess too much angular momentum to pass through the central parts of the halo at all. The stability of the density profile in time is important to us for two reasons. First, it allows us to use the measurement of the inner density profile at an early redshift as a proxy for the inner density profile at a later redshift, when the expansion of the comoving coordinates has brought the inner profile beyond our resolution limits (due to force softening; see Appendix A.2). In other words, we view the innermost points in Fig. 2.5, present only at high z, as also representing the density profile at later z, e.g. $z = 50$. This argument allows us to claim that we have probed radii down to $10^{-3.5} r_{\text{vir}}$ at $z = 50$, where r_{vir} is the UCMH virial radius. (If one does not accept this argument, we have still probed radii down to $10^{-2.5} r_{\text{vir}}$ at $z = 100$.) Second, this stability means we can study the density profile at redshifts of order $z \sim 100$ and assume that—in the absence of disruptive events—the profile is the same today. Observational signals can therefore be calculated using this profile (see Sec. 2.5).
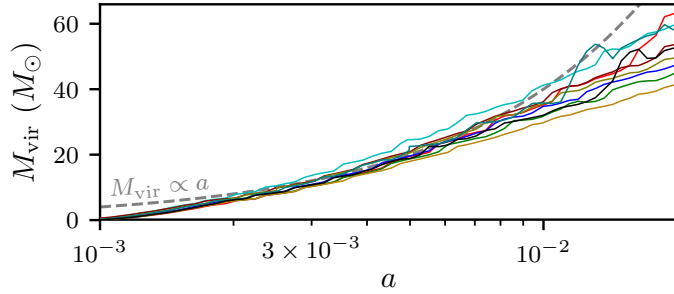
Figure 2.7: The virial mass $M_{\rm vir}$ plotted against the scale factor a for all nine UCMHs. For $a \gtrsim 2.5 \times 10^{-3}$ ($z \lesssim 400$), the growth appears logarithmic, presenting as a straight line on this plot. A $M_{\rm vir} \propto a$ reference curve is shown as a dashed line: these halos are growing more slowly than $M_{\rm vir} \propto a$.

Finally, we remark on the fitting parameters ρ_s and r_s of the Moore profile [Eq. (2.4)] for the UCMH shown in Fig. 2.5. The scale radius r_s that separates the $\rho \propto r^{-3/2}$ behavior from the $\rho \propto r^{-3}$ behavior appears to be set by the physical scale associated with the spike in the power spectrum at $z = 1000$, obeying $r_s \simeq 0.7[(1 + z)k_s]^{-1}$. Similarly, the scale density ρ_s is close to the background physical density at $z = 1000$, obeying $\rho_s \simeq 30(1 + z)^3 \bar{\rho}_0$, where $\bar{\rho}_0$ is the background matter density today. These correlations suggest that the $\rho \propto r^{-3/2}$ inner profile is set during the earliest stages of the halo's growth while the $\rho \propto r^{-3}$ outer profile grows during late accretion. We will develop these ideas in more detail in Sec. 2.3.4.

All of these results come from the UCMH in the primary simulation run. We also simulated eight other UCMHs, and we show the density profiles of all nine of them in Fig. 2.6. All of these halos collapsed near $z = 1000$, and there is clearly little deviation in the structure of these halos. In particular, all of them exhibit the same $\rho \propto r^{-3/2}$ inner density profile, providing further evidence that the $\rho \propto r^{-9/4}$ pure power law density profile does not arise in a realistic formation scenario.

2.3.2 Mass accretion

We briefly remark on the mass accretion history of the UCMHs. UCMHs have been previously assumed to grow as $M \propto a$ [202], but this is a result from radial infall theory [203]. This theory describes an overdense region in an unperturbed background, which is very different from the Gaussian random field from which a realistic halo would form.

Figure 2.7 shows the growth of our UCMHs in virial mass $M_{\rm vir}$. For $z \lesssim 400$ ($a \gtrsim 2.5 \times 10^{-3}$), the mass of these halos appears to be logarithmic in a. We do not claim that this logarithmic behavior
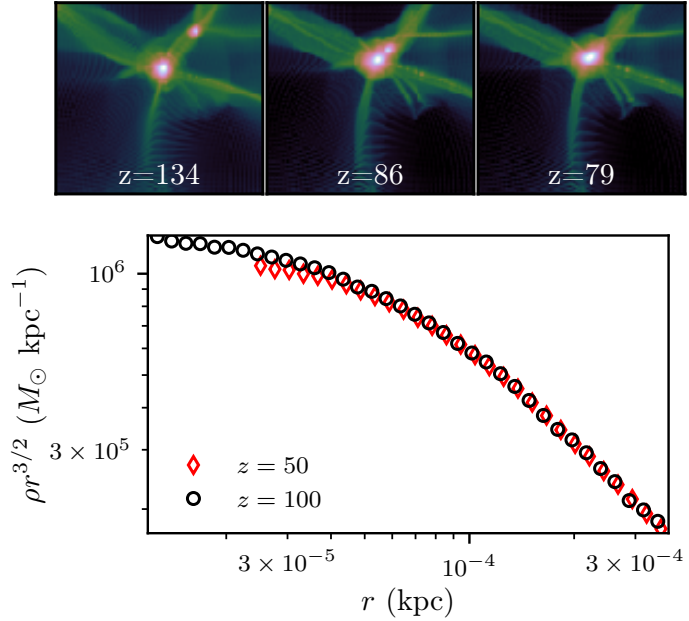
Figure 2.8: A merger event and its result. Top: A $(1.5 \text{ kpc})^2 \times 0.7$ kpc (projected) region showing the first merger event experienced by the larger halo, which formed at $z \simeq 1000$. Bottom: The change in the density profile of this UCMH as a result of the merger. Mass is dispersed from the inner region.

necessarily continues to later times: halos that form from flatter power spectra have been observed to grow with redshift z as $M \propto \mathrm{e}^{-\alpha z}$ for some α [279], which becomes slower than logarithmic, and halos in a spiked power spectrum could exhibit similar growth. However, we have confirmed that these halos grow much more slowly than prior UCMH treatments have assumed.

2.3.3 Mergers

We noted earlier that halo density profiles are expected to remain stable over time in the absence of disrupting events. Halo mergers, however, are disruptive events and may be expected to alter the inner density profile. In fact, this topic has been already explored in the context of the steeper inner profiles ($\rho \propto r^{-\gamma}$ with $\gamma > 1$) that arise in the smallest halos above a cutoff in the power spectrum [280]. Consecutive mergers cause these halos to relax toward shallower $\rho \propto r^{-1}$ inner density profiles. However, these simulations used halos with concentration parameter $c = r_{\text{vir}}/r_s \simeq 2$, where r_{vir} is the halo virial radius and r_s is the scale radius. Halos forming in a spiked power spectrum are sufficiently isolated that they may be expected to have concentration parameters of order 10 or higher by the time a merger takes place. A systematic study of the effect of halo mergers on highly

concentrated halos is beyond the scope of this work, but we will briefly discuss in this section the effect of a merger on one of our UCMHs.

Three of our nine UCMHs underwent mergers between $z = 100$ and $z = 50$, with another two impending. One such event occurring at $z \simeq 86$ is depicted in the upper panel of Fig. 2.8. The UCMH had concentration $c = 12$ at this time. The lower panel shows the density profile of this halo at $z = 100$ and $z = 50$ before and after the merger takes place, and we see that this event has been energetic enough to disperse mass out of the center of the halo and make the inner profile shallower. Unfortunately, we do not have the resolution at these redshifts to determine the slope of the inner profile after the merger, but the fact that the density profile at $r < r_s$ is altered indicates that the stability we observed in Sec. 2.3.1 does not hold after mergers.

2.3.4 Other minihalos

So far, we have studied only the exceptionally rare halos that form at $z \simeq 1000$. In this section, we explore a sample of other halos in the simulation box shown in Fig. 2.4. We pick 10 halos, including the UCMH, with masses evenly distributed between 3 $M_\odot$ and 32 $M_\odot$ at $z = 100$. Figure 2.9 shows the density profiles of these halos. As we discussed in Sec. 2.3.1, we expect that each halo will obey

$$r_s \propto a_{\rm c} k_s^{-1} \tag{2.5}$$

$$\rho_s \propto a_{\rm c}^{-3} \bar{\rho}_0, \tag{2.6}$$

where $a_{\rm c}$ is the scale factor at the halo's formation. To test this hypothesis, we must determine $a_{\rm c}$ for each halo. We do so using linear theory in the following way. We find the earliest time at which ROCKSTAR identifies the halo and map the location of the halo at this time onto the initial density grid. Then we walk from this grid-cell to a local maximum in the density field by successively moving to the densest neighboring cell. This local maximum is taken to be the amplitude $\delta_{\rm pk}$ of the protohalo peak. Finally, we evolve the grid using linear theory, Eq. (2.3), and find the time at which $\delta_{\rm pk} = 1.686$, the linear threshold for collapse. The scale factor at this time is taken to be $a_{\rm c}$.

With a formation time $a_{\rm c}$ now associated with each halo, we test Eqs. (2.5) and (2.6) by plotting in Fig. 2.9 the same density profiles with ρ scaled to $a_c^{-3} \bar{\rho}_0$ and r scaled to $a_c k_s^{-1}$ for each halo. We
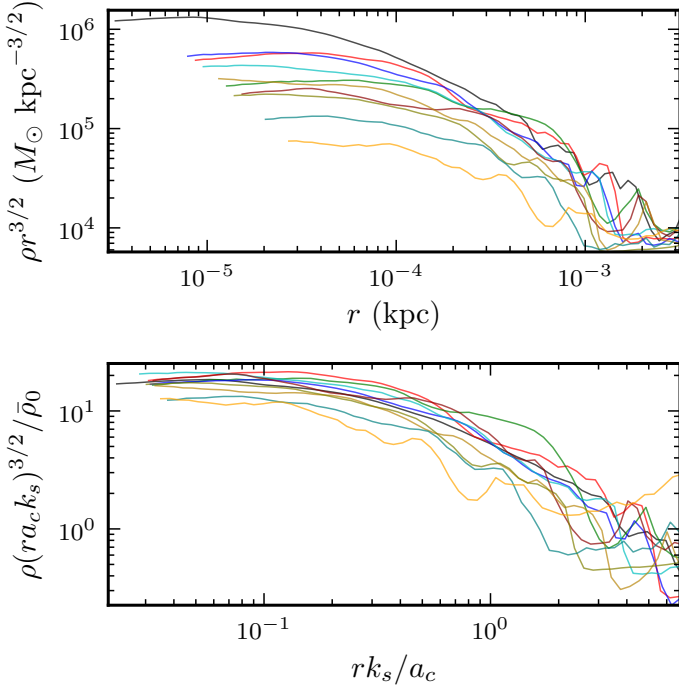
Figure 2.9: The density profiles of a sample of 10 halos in the same simulation box at $z = 100$. Top: The density profiles in physical coordinates. Bottom: The density profiles scaled to each halo's formation time using Eqs. (2.5) and (2.6).

find that the scatter in the density profiles is greatly reduced, with the bulk of the halos obeying

$$\rho_s r_s^{3/2} \simeq 17 \bar{\rho}_0 k_s^{-3/2} a_{\rm c}^{-3/2} \tag{2.7}$$

($\rho_s r_s^{3/2}$ is the $r \ll r_s$ asymptote of $\rho r^{3/2}$ for a Moore profile). The two halos lying farthest below this line have formed only slightly before the time $z = 100$ at which we are seeing them, so it is plausible that their inner profiles are still growing.

We do not attempt to study the scaling of ρ_s and r_s separately because this requires fitting functional forms to the density profiles, which is unreliable with the resolution to which we are limited here. However, $\rho_s r_s^{3/2}$ alone is a useful combination because it determines most of the annihilation signal of the halo (see Sec. 2.5). Our ultimate goal is to predict halo density profiles from the power spectrum in order to place constraints thereon, and we find the spread in $\rho_s r_s^{3/2}$ to be well within a factor of 2 of Eq. (2.7), which is promising. However, our halo sample is small and we are biased by resolution toward larger halos. We are also limited to a single power spectrum. We
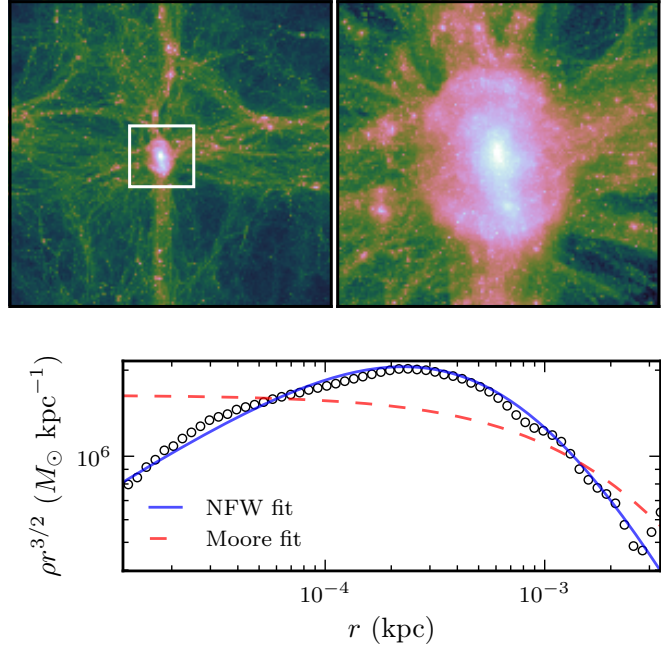
Figure 2.10: A halo at $z = 100$ that collapsed at $z \simeq 1000$ from the step power spectrum shown in Fig. 2.1. Top: The projected full $(7.4 \text{ kpc})^3$ density field and an expanded picture of the 1.5 kpc cube surrounding the UCMH. Bottom: The density profile of this halo. It is fit well by the NFW profile.

will carry out in Chapter 4 a more systematic study of the density profiles of halos forming from spiked power spectra.

2.3.5 Power spectrum with step

We finally step away from the spiked power spectrum to verify that a picture with power evenly distributed across scales still produces NFW halos even in the UCMH scenario involving the early collapse of rare extreme overdensities. We used the step power spectrum shown in Fig. 2.1 and prepared a set of initial conditions in a $(7.4 \text{ kpc})^3$ periodic box using the procedure described in Sec. 2.2. Boxes were repeatedly generated until the $z = 1000$ collapse criterion was met, which occurred after about 2300 boxes. We began the simulation run at $z = 8 \times 10^6$ and ended it at $z = 100$; the resulting UCMH at $z = 100$ is shown in Fig. 2.10. It is evident from the density field that this is a very different picture from what we have seen with our spiked power spectrum. The large-scale power has caused much of the mass within the box to collapse into the UCMH, while at the same time, the small-scale power has given this halo abundant substructure.

Figure 2.10 also shows the radial density profile of this halo. It follows the NFW form well, and does not fit the Moore form at all. Moreover, we resolve an inner density profile that is at least as shallow as $\rho \propto r^{-1}$. Even halos that collapse near $z \simeq 1000$ still possess the shallow inner profiles characteristic of hierarchical clustering.

A natural question to ask is how the density profiles behave in the transition between a spiked and a scale-invariant power spectrum. A careful treatment is beyond the scope of this work, but we will see in Chapter 4 that the answer is ultimately related to mergers. As we discussed in Sec. 2.3.3, mergers induce shallowing of the inner density profile toward $\rho \propto r^{-1}$. Meanwhile, mergers occur more frequently when the power spectrum spike is wider, culminating in the hierarchical clustering characteristic of conventional power spectra. These concepts explain, at least qualitatively, the shift from $\rho \propto r^{-3/2}$ to $\rho \propto r^{-1}$ inner profiles when the spike in the power spectrum is replaced by a step.

As a final remark, we have found between the spiked and step power spectra that UCMHs develop the same density profiles as halos that form at much later times. The spike produces UCMHs with similar density profiles to those of the smallest halos forming above a free-streaming cutoff, while the step produces UCMHs with density profiles resembling those of the galactic halos created by hierarchical clustering. In retrospect, this is not surprising. Ref. [202] conceived of UCMHs as the late stage of rare non-Gaussian density fluctuations, so they assumed a conventional (unenhanced) power spectrum when calculating the velocity dispersion at $z \simeq 1000$. The small velocity dispersion that resulted was the basis for the argument that radial infall theory would apply, but this velocity dispersion would be increased by any power spectrum enhancement. There is no difference, aside from the emerging dominance of a radiation or dark energy component, between halos forming from a boosted power spectrum at early times and halos forming from a conventional power spectrum at late times. However, the velocity dispersion is not the only obstacle to the $\rho \propto r^{-9/4}$ profile, as we discuss next.

2.4 Conditions for the $\rho \propto r^{-9/4}$ density profile

We now check whether we can produce the ultracompact $\rho \propto r^{-9/4}$ density profile from an initially uniformly overdense ellipsoid. We construct the initial peak at $z = 18\,000$ to collapse near $z = 1000$, and we evolve it under matter domination (so radiation is neglected) to $z = 200$, at which time its radial density profile is plotted in Fig. 2.11. We find that the density profile is well described by a pure power law $\rho \propto r^{-\alpha}$ with $\alpha > 2$. While the power-law index α is not exactly $-9/4$, the

best-fit α is even steeper at $\alpha \simeq 2.38$. We conclude that our simulation parameters are sufficient to produce such steep cusps, and that it is for physical reasons that they do not appear in realistic simulations. This test also confirms the finding of Refs [254, 255] that spherical symmetry is not important to the production of the $\rho \propto r^{-9/4}$ density profile.

Let us recount three scenarios under which the $\rho \propto r^{-\alpha}$ similarity solution has been reproduced in three-dimensional simulations. The first, presented in Refs. [254, 255], used carefully constructed initial conditions to match the structure of the analytic similarity solution of Ref. [253]. The second, presented in Ref. [267], begins with an initial peak in the shape of a radial Gaussian function. The third, presented here, begins with a uniformly overdense ellipsoid. The key feature shared between these scenarios is self-similarity, or the absence of a scale length. This is obvious in the first case but more subtle in the other two. A uniform ellipsoid or radial Gaussian clearly has a scale length, but only within a finite (or effectively finite) region. This initial structure does not significantly affect the final density profile because it collapses as the halo first forms, and outside of it, the fractional mass excess contained within a given radius obeys $\delta M/M \propto M^{-1}$: it possesses self-similarity of the form treated in Ref. [253]. This common feature between otherwise disparate initial conditions strongly suggests that self-similarity is a necessary condition to produce the $\rho \propto r^{-9/4}$ profile.

It is important to note that this form of self-similarity only holds for uncompensated peaks. Peaks generated by a localized boost to the power spectrum are compensated by a surrounding trough, which maintains the scale length indefinitely. To study how this permanent scale length affects the density profile, we employed the description of Ref. [269] to construct an idealized initial peak drawn from our spiked power spectrum of Fig. 2.1 with amplitude $\delta \simeq 0.1$ constrained in order to effect collapse at $z \simeq 1000$. This peak is necessarily in isolation and possesses no substructure. We simulated it from $z = 8 \times 10^6$ to $z = 100$ and found that it produced the same density profile as Fig. 2.5. This is consistent with the results of Ref. [261], who carried out similarly idealized simulations of halos in a cutoff power spectrum, and we conclude that isolation alone is not sufficient to produce the $\rho \propto r^{-9/4}$ density profile.

While isolation is evidently insufficient to produce the $\rho \propto r^{-9/4}$ profile, it is also clearly necessary. Halos that undergo major mergers develop isotropic velocity fields [281], which produce the $\rho \propto r^{-1}$ inner profile characteristic of hierarchical growth [282]. Ref. [267] also confirmed via idealized simulations that an uncompensated peak must have much greater amplitude than surrounding
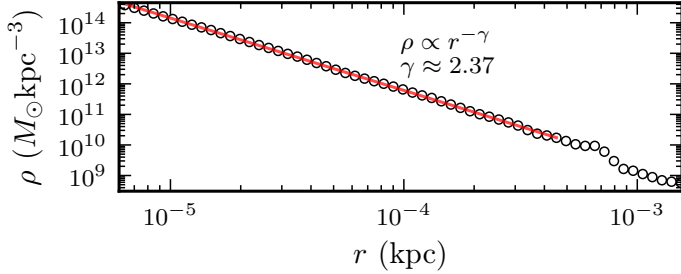
Figure 2.11: The density profile at $z = 200$ of a halo that formed from a uniform ellipsoid. This follows a pure power law $\rho \propto r^{-\alpha}$ (solid line) with $\alpha > 2$, as predicted by radial infall theory.

structure to maintain its $\rho \propto r^{-9/4}$ profile.

We argued in Sec. 2.4 that self-similarity and isolation are both necessary conditions for the development of the $\rho \propto r^{-9/4}$ profile. We now claim that these conditions cannot both be satisfied in a Gaussian density field. Consider first the case where fluctuations are enhanced over a wide range of scales, as in our "step" modification. This picture produces a nearly self-similar peak in the spherical average, but it also generates an abundance of structure at ever smaller scales. Isolation fails here as structure grows hierarchically, resulting in $\rho \propto r^{-1}$ inner profiles. We can instead preserve isolation by suppressing small-scale power by creating a spike (or cutoff) in the power spectrum, but this feature imposes a scale length, breaking self-similarity, and $\rho \propto r^{-3/2}$ profiles result. In no Gaussian formation scenario can both self-similarity and isolation be satisfied, and as a result, the $\rho \propto r^{-9/4}$ similarity solution is not physically realized if fluctuations are Gaussian. We note, however, that an alternative seeding mechanism that generates uncompensated peaks in a relatively smooth background can still yield halos with $\rho \propto r^{-9/4}$ profiles, as demonstrated by the collapse of the uniform ellipsoid described in Sec. 2.4 and of the radial Gaussian overdensity in Ref. [267].

2.5 Constraining the power spectrum

UCMHs have been employed to constrain the primordial power spectrum through nonobservation of their predicted signals in a variety of contexts. For thermal-relic dark matter models, such as the weakly interacting massive particle (WIMP) model [198, 199, 283], the dark matter annihilation rate is greatly increased by the compactness of the assumed $\rho \propto r^{-9/4}$ density profile. The strongest constraints therefore come from nonobservation of the strong gamma-ray [232–234] or neutrino [235, 236] signals that are expected from WIMP annihilation within such dense clumps. These

annihilation signals would also lead to other observable effects, such as heating of the intergalactic medium [238, 239] and galactic gas [240] and interactions with the CMB or other background photons [241–243]. The primordial power spectrum can also be constrained by searching for UCMHs using astrometric microlensing [246] or macrolens distortions [244] or by constraining the UCMH abundance using pulsar timing arrays [245, 249].

However, with the exception of Ref. [232], all of these works used only minihalos that form at $z \gtrsim 1000$ and assumed these halos possessed the $\rho \propto r^{-9/4}$ density profile. We showed in Sec. 2.3 that minihalos forming in an enhanced power spectrum, even UCMHs forming at $z \gtrsim 1000$, develop significantly shallower profiles. We also found that younger minihalos possess the same density profiles as the oldest ones. In this section, we explore the impact of this discovery. The observational signatures of UCMHs forming at $z \gtrsim 1000$ are weakened by the shallower density profile, but our analysis is now able to include minihalos forming at $z < 1000$. As we saw in Fig. 2.4, these younger minihalos are far more abundant than the rare UCMHs.

Broadening to the entire population of minihalos brings new challenges. Minihalo-minihalo mergers will reduce the minihalo count and alter their density profiles [280], and tidal interactions within galactic structures will have more impact on the shallower density profiles [284]. These considerations are beyond the scope of this chapter, but to motivate further study, we calculate in this section how the new minihalo picture directly alters previous constraints on the power spectrum derived from UCMHs. To this end, we focus on the upper bound derived by Bringmann, Scott, and Akrami [234] (hereafter BSA) based on the gamma-ray signal from WIMP annihilation within UCMHs. In our calculation, we adopt our new minihalo model from Sec. 2.3.4 but otherwise replicate BSA's calculation as closely as possible. In particular, we employ the same Fermi-LAT data and, like BSA, when deriving bounds from diffuse emission, we consider only a Galactic contribution and neglect the possibility of improving constraints by including extragalactic sources (e.g., Refs. [229, 232]).

The derivation of a constraint on the power spectrum using WIMP annihilation in minihalos proceeds in three steps:

1. The annihilation signal of a minihalo is calculated.

2. A constraint on the number density of minihalos is calculated from the nonobservation of such

an annihilation signal.

3. The number density constraint is converted into a constraint on the primordial power spectrum using the statistics of Gaussian random fields.

In past studies, such as BSA, UCMHs are assumed to collapse at $z \simeq 1000$, so the UCMH luminosity is solely a function of its size. We now have the machinery to study minihalos collapsing at any redshift, so we calculate the minihalo luminosity L as a function of both its formation time and the scale of the density fluctuation that sourced it.

2.5.1 Halo luminosity

We assume that the density profile of a minihalo follows the Moore fitting form given by Eq. (2.4). In addition, we found in Sec. 2.3 that the Moore fitting parameters r_s and ρ_s can be predicted from the halo formation time as

$$r_s = f_1 k_s^{-1} a_c$$
$$\rho_s = f_2 \bar{\rho}_0 a_c^{-3}, \tag{2.8}$$

where $\bar{\rho}_0 = \Omega_c \rho_{\mathrm{crit}}$ is the background dark matter density today, k_s is the (comoving) wavenumber associated with the spike in the power spectrum, and a_c is the halo formation time in a spherical collapse model. The coefficients f_1 and f_2 are determined from simulations; they possess some scatter between halos, but we will neglect that scatter for the purpose of this calculation. The annihilation signal of the Moore profile depends dominantly on the combination $f_2^2 f_1^3$ and only logarithmically on f_2 alone, so we will use $f_2 f_1^{3/2} = 17$ from Eq. (2.7), which was derived from a sample of halos forming at different times, along with the more approximate value $f_2 \simeq 30$ derived from the UCMHs alone.

The gamma-ray signal L of a halo with density profile $\rho(r)$ may be calculated as

$$L = 4\pi g \int_0^R r^2 \rho^2(r) \mathrm{d}r, \tag{2.9}$$

where R is the radius of the halo and g is a factor related to the annihilation mechanism. For

threshold photon energy E_{th},

$$g = \sum_k \int_{E_{\text{th}}}^{m_\chi} E \frac{\mathrm{d}N_k}{\mathrm{d}E} \mathrm{d}E \frac{\langle \sigma_k v \rangle}{2m_\chi^2}, \tag{2.10}$$

where $\mathrm{d}N_k/\mathrm{d}E$ is the differential photon yield of the kth annihilation channel and $\langle \sigma_k v \rangle$ is its cross section. Equation (2.10) describes the energy flux; for the photon flux, the factor of E is removed from the integrand.

For now, we keep our calculations model-independent and return to Eq. (2.9). Equation (2.9) diverges for a $\rho \propto r^{-3/2}$ profile, but this implies that annihilations would have smoothed out the central cusp within some small radius. We use the standard estimate [285]

$$\rho_{\text{max}} = \frac{m_\chi}{\langle \sigma v \rangle (t - t_{\text{i}})} \tag{2.11}$$

for the maximum density at time t in a structure that formed at t_{i}, where m_χ is the mass of the WIMP and $\langle \sigma v \rangle$ is its thermally averaged velocity-weighted cross section (in the zero-velocity limit). Note that $t - t_{\text{i}} \simeq t$ today if halo formation occurs at $z \gtrsim 10$, and we will see in Sec. 2.5.4 that this is true for the minihalos relevant to power spectrum constraints. Thus, we take $t - t_{\text{i}}$ to be the age of the Universe today, making ρ_{max} the same for all minihalos. For a canonical WIMP with $\langle \sigma v \rangle = 3 \times 10^{-26}$ cm^{3}s^{-1} and $m_\chi = 1$ TeV, $\rho_{\text{max}} \sim 10^{16} \bar{\rho}_0$.

We now evaluate Eq. (2.9) for a Moore profile as given by Eq. (2.4) modified to have maximum density ρ_{max}. The choice of radius R has negligible impact as long as $R > r_s$, so taking $R \to \infty$, we obtain

$$L = 4\pi g \rho_s^2 r_s^3 \left[\frac{1}{3} + \ln(1 + D) - \frac{3 + 2D^{-1}}{2(1 + D^{-1})^2} \right], \tag{2.12}$$

where $D \equiv (\rho_{\text{max}}/\rho_s)^{2/3} = (f_2^{-1}\rho_{\text{max}}/\bar{\rho}_0)^{2/3} a_c^2$. For halos collapsing at $z \lesssim 1000$, we find that $D \gtrsim 10^4 \gg 1$ for a canonical WIMP, so Eq. (2.12) simplifies to

$$L \simeq B k_s^{-3} a_c^{-3} \ln(\beta a_c) \tag{2.13}$$

with

$$B \equiv 8\pi g f_2^2 f_1^3 \bar{\rho}_0^2, \quad \beta \equiv \mathrm{e}^{-7/12} \left(\frac{\rho_{\text{max}}}{f_2 \bar{\rho}_0} \right)^{1/3}. \tag{2.14}$$

B and β are independent of the scale k_s of the spike in the power spectrum, and since we are

neglecting scatter in f_1 and f_2, they are the same for all halos. We remark that since $\beta \sim 10^5$, the logarithmic dependence on a_c is weak for $a_c \gtrsim 10^{-3}$. If halos relax to a $\rho \propto r^{-1}$ inner profile due to mergers or other disruptive dynamics, a similar calculation with the NFW profile yields $L \simeq B k_s^{-3} a_c^{-3}/6$, which is smaller by a factor of ~ 30 for formation time $z \sim 100$. In this case, Eq. (2.9) converges, so the effect of $\rho_{\max}$ is negligible.

2.5.2 Halo abundance

We use observational detection limits to constrain the minihalo number density based on the luminosity we computed above. Following BSA, we employ two approaches that utilize different observations and yield different constraints. First, we treat the minihalos as point sources and use their nonobservation to constrain their number density. Next, we consider the diffuse background flux from minihalos within the Milky Way and use the observed background gamma-ray flux to constrain the minihalo number density.

Point sources The gamma-ray flux $\mathcal{F}$ from a point source is related to its luminosity L and distance d by $\mathcal{F} = L/(4\pi d^2)$. If our detecting instrument has flux sensitivity $\mathcal{F}_{\min}$ to point sources, then this imposes a maximum observable distance $d_{\mathrm{obs}} = \sqrt{L/(4\pi \mathcal{F}_{\min})}$ corresponding to the observable volume

$$V_{\mathrm{obs}} = \frac{1}{3\sqrt{4\pi}} \frac{L^{3/2}}{\mathcal{F}_{\min}^{3/2}}. \tag{2.15}$$

If V_{obs} were the same for all halos, then the expected number of observable objects would be $\lambda = n V_{\mathrm{obs}}$, where n is the halo number density, and we could use Poisson statistics to constrain n from our knowledge of V_{obs}. However, in our model, L, and hence V_{obs}, is a function of the formation time a_c of the minihalo. Instead of the total number density n, we must consider the differential number density $\mathrm{d}n/\mathrm{d}a_c$ of minihalos forming at $a = a_c$. The expected number of observable minihalos is now

$$\lambda = \int_0^1 \mathrm{d}a_c \left(\frac{\mathrm{d}n}{\mathrm{d}a_c} \right)_{\mathrm{obs}} V_{\mathrm{obs}}(a_c), \tag{2.16}$$

where we write $(\mathrm{d}n/\mathrm{d}a_c)_{\mathrm{obs}}$ to clarify that we are referring to the number density of minihalos within V_{obs}, which in general differs from the cosmological mean $\mathrm{d}n/\mathrm{d}a_c$.

From Poisson statistics, the probability that there is at least one observable object is $P(N_{\mathrm{obs}} > 0) = 1 - \mathrm{e}^{-\lambda}$. If the confidence level associated with the flux threshold $\mathcal{F}_{\min}$ is x, then the probability of observing at least one object is $P_{\mathrm{obs}} = x(1 - \mathrm{e}^{-\lambda})$. If we observe no objects, an upper bound on λ

with confidence level y is obtained by setting $P_{\text{obs}} \leq y$, implying $\lambda \leq -\ln(1 - y/x)$. Combining this result with Eqs. (2.15) and (2.16), we find

$$\int_0^1 \mathrm{d}a_c \left(\frac{\mathrm{d}n}{\mathrm{d}a_c}\right)_{\text{obs}} L^{3/2}(a_c) \leq -3\sqrt{4\pi}\ln(1 - y/x)\mathcal{F}_{\min}^{3/2}, \tag{2.17}$$

which gives us the prescription for constraining the local number density of minihalos based on the nonobservation of point sources. Due to the dependence of a minihalo's luminosity on its formation time, we constrain a formation time-weighted density instead of a total UCMH density.

To complete the calculation, we need to relate $(\mathrm{d}n/\mathrm{d}a_c)_{\text{obs}}$ to the cosmological mean $\mathrm{d}n/\mathrm{d}a_c$ that is predicted by the power spectrum. To do this, we assume that the spatial distribution of minihalos is proportional to that of dark matter at large[4]; that is, $n(\boldsymbol{x}) \propto \rho(\boldsymbol{x})$. We define $\mu(d) \equiv 3M(d)/(4\pi d^3 \bar{\rho}_0)$ as the ratio of the dark matter mass $M(d)$ contained within distance d from Earth to the cosmological mean dark matter mass contained within an equal volume. Then the mean minihalo number density within d_{obs} is related to the cosmological mean by the factor $\mu(d_{\text{obs}})$, implying

$$\left(\frac{\mathrm{d}n}{\mathrm{d}a_c}\right)_{\text{obs}} = \mu\left(\sqrt{\frac{L(a_c)}{4\pi\mathcal{F}_{\min}}}\right)\frac{\mathrm{d}n}{\mathrm{d}a_c}. \tag{2.18}$$

We evaluate $\mu(d)$ in Appendix A.3 and plot it in Fig. 2.12 assuming an NFW profile for the Milky Way with parameters from Ref. [286]. For $d_{\text{obs}} \lesssim 8$ kpc, the distance to the Galactic center, $\mu(d_{\text{obs}}) \simeq 2 \times 10^5$ is approximately constant.

Diffuse flux The calculation is simpler for the case of a diffuse gamma-ray flux. If $\mathrm{d}\mathcal{F}/\mathrm{d}\Omega$ is the upper bound on the observed differential gamma-ray flux that can be attributed to minihalos, then we can relate this to the differential flux summed over all minihalos along the line of sight,

$$\frac{\mathrm{d}\mathcal{F}}{\mathrm{d}\Omega} \geq \int_0^\infty s^2 \mathrm{d}s \int_0^1 \mathrm{d}a_c \frac{\mathrm{d}n}{\mathrm{d}a_c}\frac{\rho(s)}{\bar{\rho}_0}\frac{L(a_c)}{4\pi s^2}, \tag{2.19}$$

---

[4]Galactic tides and other disruptive processes would realistically alter the spatial distribution of minihalos, but we neglect them here.
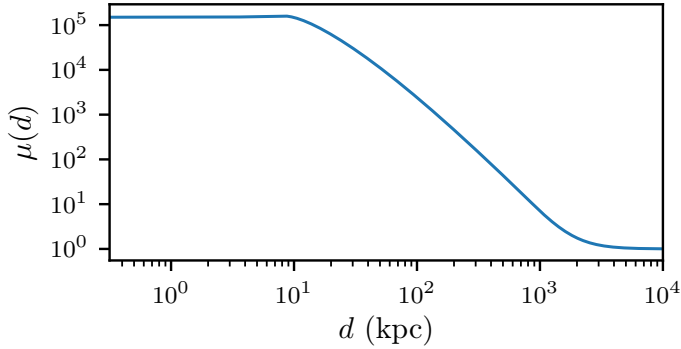
Figure 2.12: The ratio $\mu(d) = 3M(d)/(4\pi d^3 \bar{\rho}_0)$ of the dark matter mass $M(d)$ within distance d of Earth to the cosmological mean dark matter mass in an equal volume. An NFW profile is assumed for the Milky Way with parameters from Ref. [286]. Minihalos are assumed to follow this spatial distribution.

where s is the line-of-sight distance. Here we have inserted the factor $\rho(s)/\bar{\rho}_0$ to account for the Milky Way density field at distance s from Earth. Following BSA, we are only interested in the Galactic contribution to the diffuse flux, so we truncate the density field beyond the Milky Way, eliminating the need to redshift distant sources. The minihalo abundance constraint from the diffuse flux at angle θ to the Galactic center now becomes

$$\int_0^1 da_c \frac{dn}{da_c} L(a_c) \leq \frac{4\pi}{K(\theta)} \frac{d\mathcal{F}}{d\Omega}, \tag{2.20}$$

where

$$K(\theta) \equiv \int_0^\infty ds \frac{\rho_{\mathrm{MW}}(\sqrt{s^2 + r_0^2 - 2sr_0 \cos\theta})}{\bar{\rho}_0}, \tag{2.21}$$

$\rho_{\mathrm{MW}}(r)$ is the Milky Way density profile, and r_0 is the solar orbital radius.

2.5.3 The power spectrum

Finally, we must find the relationship between dn/da_c and the power spectrum $\mathcal{P}(k)$. The standard way to relate a halo population to a power spectrum is Press-Schechter theory [287]. For any power spectrum with a small-scale cutoff, including a spiked power spectrum, it is necessary to employ a sharp k-space smoothing filter to avoid overpredicting structure below the cutoff scale [288–290]. However, there are additional challenges in adapting Press-Schechter theory to our purposes. Halo formation times can be obtained from the conditional mass function [291], but these yield the average formation time of progenitor halos. It is necessary to construct merger trees to

39

study the first progenitor. Also, Press-Schechter theory always destroys a halo when two halos merge. For unequal-mass mergers, a remnant of the smaller halo is generally expected to survive as a subhalo with its central structure intact [284].

For our calculation, we employ a more direct approach. Bardeen, Bond, Kaiser, and Szalay [269], hereafter BBKS, formulated a description of the statistics of peaks in a Gaussian random field. In this approach, each peak in the primordial density field is to be identified with a halo at late times. Spiked power spectra are very natural arenas for peak theory because they possess finite integrated power and generate peaks around a particular scale, so it is not necessary to use any smoothing filter. To represent a spike centered at wavenumber k_s, we consider a delta-function matter power spectrum of the form $\mathcal{P}(k) \propto D(a)^2 k_s \delta(k - k_s)$, where $D(a)$ is the linear growth function. We will see in Sec. 2.5.4 that the minihalos contributing to our power spectrum constraint form in matter domination, so $D(a) = a$, and we may write

$$\mathcal{P}(k) = \mathcal{A}a^2 k_s \delta(k - k_s), \tag{2.22}$$

where $\mathcal{A}$ parametrizes the integrated area of the spike. We use the BBKS formalism to calculate the number density of peaks with $\delta > \delta_c$, where $\delta_c = 1.686$ is the linear collapse threshold. The identification of these peaks with halos leads to a number density n that increases in time solely due to halo formation, implying we can differentiate it with respect to scale factor a to obtain the distribution of halos by formation time. A disadvantage to this procedure is that minihalo-minihalo mergers are not automatically accounted for and must be handled separately, a task that is beyond the scope of this work[5].

As detailed in Appendix A.4, we obtain

$$\frac{\mathrm{d}n}{\mathrm{d}a_c} = \frac{k_s^3}{a_c} \, h\left(\frac{\delta_c}{\mathcal{A}^{1/2} a_c}\right), \tag{2.23}$$

where $h(\nu)$ is the distribution of peak heights given by Eq. (A.10) (see Fig. A.8). With the minihalo

---

[5]However, as we will see in Chapter 4, mergers become rare as the power spectrum spike is narrowed. With a delta-function spike in the primordial power spectrum, we suspect that they are negligible.

signal given by Eq. (2.13), the abundance constraints given in Eqs. (2.17) and (2.20), and this relation between dn/da and the power spectrum, we can place an upper bound on the amplitude $\mathcal{A}$ of the spike in the matter power spectrum. The final step is to convert this bound into a bound on the primordial curvature power spectrum. We adopt a similar delta-functional form for the primordial power spectrum,

$$\mathcal{P}_\zeta(k) = \mathcal{A}_0 k_s \delta(k - k_s), \tag{2.24}$$

with amplitude $\mathcal{A}_0$. The transfer function given by Eq. (A.14) converts the bound on $\mathcal{A}$ into a bound on $\mathcal{A}_0$.

To carry out the calculation, we assume a canonical WIMP with cross section $\langle \sigma v \rangle = 3 \times 10^{-26}$ cm^{3}s^{-1} and mass $m_\chi = 1$ TeV that annihilates into $b\bar{b}$ pairs. We take the Fermi-LAT point-source sensitivity for energies above 100 MeV to be $\mathcal{F}_{\max} = 4 \times 10^{-9}$ cm^{-2}s^{-1} for a 5σ detection, and we set $y = 0.95$ in Eq. (2.17) for a 95% confidence limit. For the diffuse flux, we use $d\mathcal{F}/d\Omega = 1.2 \times 10^{-5}$ GeVcm^{-2}s^{-1}sr^{-1} as the 2σ limit (with systematic error alone) in the energy flux from the Galactic poles as measured by Fermi-LAT [292]. Finally, we take the Milky Way to have an NFW density profile with parameters determined in Ref. [286]. All of these choices are picked solely for parity with BSA, and further detail can be found there.

Figure 2.13 shows the resulting upper bound on the integrated area $\mathcal{A}_0$ of a spike in the primordial curvature power spectrum if the spike is located at wavenumber k_s. We show the constraints from point sources and diffuse flux separately, and the shaded regions are forbidden. We wish to compare this constraint to the upper bound derived in BSA under the UCMH picture, but BSA assumed a locally scale-invariant power spectrum for their analysis. Therefore, we employ the UCMH abundance constraints in BSA to derive a constraint on the spiked power spectrum of Eq. (2.22). This calculation is detailed in Appendix A.5, and the results are plotted on Fig. 2.13 as dashed lines. Evidently, new minihalo constraints can be stronger than old UCMH constraints despite employing shallower density profiles. For comparison, we also show as dotted lines the upper bounds that employ the shallower density profiles while restricting to UCMHs forming by $z \geq 1000$. These bounds are calculated by altering the upper limit of the integrals in Eqs. (2.17) and (2.20). Evidently, the shallower density

Figure 2.13: The upper bound on the integrated area $\mathcal{A}_0$ of a spike in the primordial curvature power spectrum centered at scale wavenumber k_s. Black curves use point sources, while red curves employ the diffuse flux. The shaded regions are ruled out in the new minihalo picture with shallower density profiles. The dashed lines show the corresponding constraints in the old UCMH model calculated using the abundance constraints in BSA. As another comparison, the dotted lines show the constraints using shallower density profiles while still restricting to UCMHs forming at $z \geq 1000$. While the new density profiles slightly weaken the upper bound, the inclusion of all minihalos ends up leading to stronger constraints.

profiles weaken the upper bound on the power spectrum by roughly a factor of two[6]. The inclusion of all minihalos, instead of only the rare UCMHs that form by $z = 1000$, more than compensates for this loss.

2.5.4 Discussion

To develop a better understanding of the power spectrum constraints in this new minihalo picture, we specialize to the diffuse flux and to point sources in the small-object limit where d_{obs} is sufficiently short that $\mu(d_{\mathrm{obs}}) \equiv \mu$ is constant[7]. In these cases, it is possible to derive the analytic constraints

---

[6]In contrast, the signal from each UCMH is reduced by a factor of about 200. In the next section, we discuss why power spectrum constraints derived from UCMHs are so insensitive to reductions in the UCMH signal. This feature is a consequence of the restriction to halos forming at $z \geq 1000$ and is no longer applicable once all minihalos are included.

[7]The small-object limit produces the power-law branch of the point-source constraint in Fig. 2.14, implying that this limit corresponds to $k_s \gtrsim 20$ Mpc^{-1}.

(see Appendix A.4)

$$\mathcal{A} \left(\ln \frac{\beta \delta_c}{\mathcal{A}^{1/2}} \right)^{2/9} \left[\left(\ln \frac{\beta \delta_c}{\mathcal{A}^{1/2}} \right) I_{3/2} - J_{3/2} \right]^{4/9} \leq \left(\frac{-3\sqrt{4\pi} \ln(1 - y/x)}{\mu} \right)^{4/9} \left(\frac{\delta_c^3 k_s \mathcal{F}_{\min}}{B} \right)^{2/3} \quad (2.25)$$

for point sources in a uniform field with μ times the background density and

$$\mathcal{A} \left[\left(\ln \frac{\beta \delta_c}{\mathcal{A}^{1/2}} \right) I_1 - J_1 \right]^{2/3} \leq \left(\frac{4\pi \delta_c^3}{K(\theta) B} \frac{\mathrm{d}\mathcal{F}}{\mathrm{d}\Omega} \right)^{2/3} \quad (2.26)$$

for diffuse sources. Here, $I_{3/2} = 0.228$, $J_{3/2} = 0.370$, $I_1 = 0.0477$, and $J_1 = 0.0478$ are different moments of the peak height distribution $h(\nu)$.

We first note that if we neglect logarithms[8], the constraint on $\mathcal{A}$ is proportional to $B^{-2/3}$ and hence to the $-2/3$ power of the WIMP annihilation rate within minihalos [see Eq. (2.13)]. This relationship implies that the upper bound on $\mathcal{A}$ is highly sensitive to the WIMP model. For example, if the annihilation cross section $\langle \sigma v \rangle$ were increased by a factor of 8, the upper bound on $\mathcal{A}$ would be reduced by a factor of 4. This behavior is a stark contrast to that of constraints in the old UCMH picture, which exhibit a very weak dependence on WIMP model (see BSA Fig. 5).

The same distinction arises when considering the observational flux constraint $\mathcal{F}_{\min}$ or $\mathrm{d}\mathcal{F}/\mathrm{d}\Omega$. The upper bound on $\mathcal{A}$ is more sensitive to these observational constraints in the new minihalo picture than in the old UCMH picture. Therefore, improved observational limits are far more valuable in the new picture. This property is also responsible for how, as depicted in Fig. 2.13, the point-source constraint in the new picture exhibits markedly stronger k_s-dependence: larger objects are more visible, and this heightened visibility now significantly strengthens the upper bound on the power spectrum on the corresponding scales. Likewise, we saw in the last section that reducing the UCMH gamma-ray signal by a factor of 200 only weakens the UCMH-derived power spectrum bounds by a factor of two. A similar change to the luminosity of all minihalos would weaken the bounds in the new picture by a factor of 34.

These differences in sensitivity can be understood in the following way. Upper bounds on minihalo abundance (f in BSA; n or $\mathrm{d}n/\mathrm{d}a_c$ here) are always highly sensitive to minihalo signals

---

[8]Using Fig. 2.14, $\beta \sim 10^5 \gg \mathcal{A}^{1/2}$, so the logarithmic dependence of Eqs. (2.25) and (2.26) on $\mathcal{A}$ is weak.

and observational flux constraints, whether we restrict to UCMHs or not; compare Eqs. (2.17) and (2.20) to BSA Eqs. (26) and (29). However, the sensitivity of a power spectrum bound to these abundance constraints depends on the types of minihalos that contribute. In the old UCMH picture, constraints were dominated by halos forming from initial overdensities that correspond to 5σ-6σ fluctuations. These peaks are so far out in the Gaussian tail of the density distribution that altering their abundance only marginally changes the distribution's spread[9]. In the new minihalo picture, constraints are influenced by the bulk of the peaks, so an alteration to the abundance of these peaks now changes the spread of the distribution more drastically. We also remark on another consequence of this difference in statistics: the constraints will no longer be as sensitive to possible small deviations from Gaussianity that would significantly affect the tails of the distribution [293].

The influence of the peak population on the power spectrum constraint is encoded in the moments $I_{3/2}$, $J_{3/2}$, I_1, and J_1 of the peak distribution. These are integrals over peak height $\nu = \delta/\sigma$, and their integrands exhibit most of their support between $\nu = 2$ and $\nu = 4$ (see Appendix A.4). Consequently, the integrals in Eqs. (2.17) and (2.20) that determine the upper bounds on the power spectrum are dominated by peaks with amplitudes between 2σ and 4σ, which confirms the difference in statistics from the old UCMH picture. We can also use this information to find the formation times of the corresponding halos. The upper bound on $\mathcal{A}$, which parametrizes the matter power spectrum, is shown in Fig. 2.14 and lies between 3×10^2 and 6×10^4. The root-mean-squared density variance of the spiked power spectrum is $a\mathcal{A}^{1/2}$ at scale factor a, implying that the collapse time a_c of a peak with amplitude ν is $a_c = \delta_c/(\nu\mathcal{A}^{1/2})$. It follows that peaks contributing significantly to the power spectrum constraint would have formed between $z = 20$ and $z = 600$, confirming that matter domination was a valid approximation.

Finally, we remark on a similar constraint that was recently published by Nakama, Suyama, Kohri, and Hiroshima in Ref. [232] (hereafter NSKH). Unlike previous UCMH works, this work did not employ the $\rho \propto r^{-9/4}$ density profile. Instead, NSKH assumed that minihalos developed NFW density profiles, and like us, they constrained a delta-spiked power spectrum. Thus, a comparison is

---

[9]The (differential) abundance of a density excess δ is proportional to $\exp\left(-\frac{1}{2}\delta^2/\sigma^2\right)$ if δ is distributed with spread σ. If δ/σ is large, then a large change in the abundance—the quantity constrained by observations—corresponds to a small change in σ, which sets the power spectrum normalization. (This is just an illustration: to be precise, we should use the cumulative distribution function.)
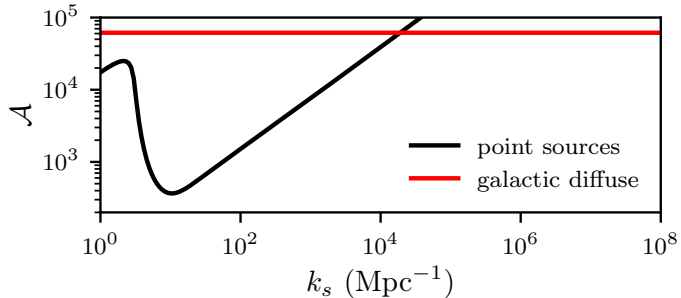
Figure 2.14: The constraint on the integrated area $\mathcal{A}$ of the spiked matter power spectrum Eq. (2.22). Note that this is not the primordial power spectrum; see Fig. 2.13 for that constraint.

warranted: despite assuming shallower density profiles, NSKH were able to derive comparable or stronger constraints on the integrated area $\mathcal{A}_0$ ($\mathcal{A}^2$ in their paper) of the power spectrum spike.

To model the NFW fitting parameters for their minihalos, NSKH assumed that halo concentrations $c = r_{\mathrm{vir}}/r_s$ grow at the rate $c \propto a^{1.575}$. However, as we discussed in Sec. 2.3, the inner profiles of dark matter halos tend to remain stable in time in the absence of disruptive events. Under the same conditions, the virial radius r_{vir} in physical coordinates grows approximately as a. If the concentration is growing much faster than a, then this implies that the physical scale radius is shrinking in time and the halo center is becoming denser. Our simulations suggest that this is not the case: the concentrations of our minihalos grow as $c \propto a$. The rate $c \propto a^{1.575}$ was drawn from a previous work [294] that simulated structure growth from scale-free power spectra. With these power spectra, halo mergers are common, and these can cause halo physical virial radii r_{vir} to grow significantly faster than a. This fact may explain the large concentration growth rate: it reflects rapid growth in virial radius r_{vir} rather than shrinkage in scale radius r_s. Since halos that form from a spiked power spectrum do not experience these mergers, their concentrations grow more slowly.

Their assumption of a faster concentration growth rate likely explains why the constraints in NSKH are so strong. The annihilation rates within such concentrated minihalos would be greatly enhanced. However, NSKH also employed the diffuse gamma-ray flux from extragalactic sources, whereas we, for parity with BSA, assumed only Galactic sources. This could contribute to the strength of their constraints: as we discuss above, the upper bound on the power spectrum is now highly sensitive to observational limits on the gamma-ray flux.

2.6 Conclusion

We have shown that the minihalos that form due to a power spectrum enhancement do not develop the single-power-law $\rho \propto r^{-9/4}$ density profile even when they form by $z = 1000$ from extremely rare (6.8σ) peaks. Instead, they develop density profiles with inner power-law indices between $-3/2$ and -1, depending on the range of scales that are enhanced. This finding contradicts the assumption made by previous UCMH work [204, 233–236, 246–250], throwing into question power spectrum constraints that have been derived from this theory. However, we have also offered hope. We constructed a new model based on our simulation results for minihalos that form from a spiked power spectrum, and we calculated a new power spectrum constraint in this model using Fermi-LAT constraints on gamma rays from WIMP annihilation. The resulting upper bound on the primordial power spectrum is stronger than an equivalent constraint derived in the old UCMH picture. It turns out that the drop in signal from each early-forming halo is more than compensated by the vast increase in the number of halos that contribute to the expected gamma-ray signal.

Our constraint is specialized to a power spectrum enhanced over a narrow range of scales. Such spiked power spectra have motivations in inflationary phenomenology [27–30, 49, 51, 52] and in nonstandard thermal histories of the Universe [181–183, 224], but halos forming from these spectra have not been numerically studied prior to this work and Refs. [226, 267]. Our model for halos forming from spiked power spectra predicts halo density profiles based on their formation time: the characteristic density is set by the background density at formation, while the characteristic scale is set by the spike scale at formation. However, we developed this model based a single power spectrum. We also neglected any scatter in the density profiles of halos forming at the same time. In Chapter 4, we will extend this model by quantifying its scatter and its applicability to different power spectra.

Inflationary phenomenology also includes less scale-localized power spectrum boosts such as steps or bends [27–31, 38–40]. We have found that the halos forming from a stepped power spectrum develop the same density profiles as later-forming galaxy-scale halos. Consequently, there is already a vast body of literature on modeling the density profiles of these halos (e.g. [205, 260, 294–318]), and we expect that these results may be adapted toward constraining steps or bends in the power spectrum.

Our constraint also employed only gamma rays from WIMP annihilation in Galactic or near-Galactic sources. We made this restriction in order to facilitate a direct comparison between an

upper bound on the power spectrum derived in the shallower minihalo picture and an equivalent bound derived using the results of Ref. [234], which made the same restriction, used UCMHs forming at $z \geq 1000$, and assumed the $\rho \propto r^{-9/4}$ profile. As a result, we have left open the possibility of immediately improving the power spectrum constraints by considering the diffuse annihilation signal from extragalactic minihalos as Refs. [229, 232] do. We have also not explored the impact of the shallower density profiles on gravitational probes such as astrometric microlensing [246] and pulsar timing arrays [245, 249].

Most pressingly, we neglected the influence of disruptive events on the minihalo abundance and their density profiles. Minihalo-minihalo mergers are one such disruptive event. They can be counted by means of Press-Schechter theory [291][10] with a sharp k-space filter [288–290], but their physical impact, especially on minihalos with $\rho \propto r^{-3/2}$ inner profiles, is not yet well understood. Reference [280] simulated controlled halo mergers and observed that successive mergers cause the inner density profiles of these halos to relax toward shallower forms, an effect that we confirmed. However, they also found that the merger product can have a higher central density than its progenitor halos. Moreover, for highly unequal-mass mergers, a remnant of the smaller halo is expected to survive within the larger one [284].

Figure 2.15 illustrates the possible impact of mergers on the minihalo-derived constraints on the primordial power spectrum. If we naively assume that minihalos develop NFW profiles with the same scale parameters r_s and ρ_s, then the shallower inner profiles weaken the power spectrum bound by roughly a factor of 10. If mergers additionally halve the minihalo count, the constraint is weakened by another factor of 1.6. We suspect that this latter constraint, depicted as the red curve in Fig. 2.15, represents a pessimistic estimate of how mergers may weaken the upper bound on the power spectrum. First, we neglected the increased central densities that can result from mergers. Second, we assumed that all halo profiles fully relax to NFW form, while Ref. [280] showed that such relaxation is a gradual process occurring over multiple mergers. Finally, mergers are relatively rare in spiked power spectra, and even if more than half of the minihalo population is ultimately destroyed by mergers (not even becoming subhalos), smaller halos, which contribute less

---

[10]However, the self-consistency of Press-Schechter merger rates is questioned in Ref. [319]; see also Ref. [320] for a counterpoint.
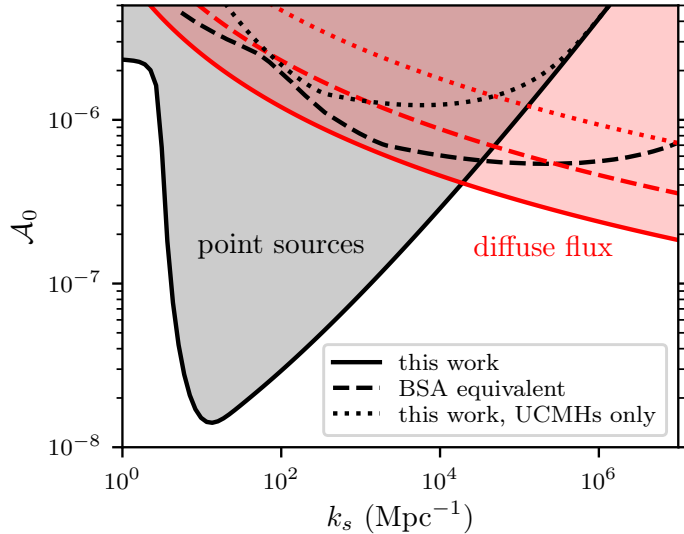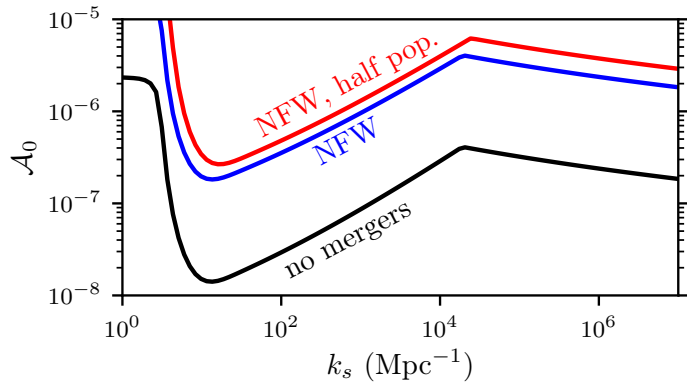
Figure 2.15: Possible upper bounds on the integrated area $\mathcal{A}_0$ of a spike in the primordial curvature power spectrum centered at scale wavenumber k_s when mergers are taken into account. The black curve shows the bound with mergers neglected, which is the same constraint shown in Fig. 2.13. The blue curve shows the bound if minihalos develop NFW profiles with the same scale parameters r_s and ρ_s, while the red curve additionally halves the number of halos.

to observational signals, are preferentially destroyed. Hence, we expect that a careful accounting of mergers will produce a result between the black and red curves of Fig. 2.15.

Disruption of minihalos can also occur by the tidal influence of larger galactic potentials or by high-speed encounters with objects, such as other substructure or stars, within these galactic potentials. This topic has been studied in a number of previous works, such as Refs. [321–327], and a recent overview of such disruptive processes can be found in Ref. [328]. It is also possible to bypass the issue of galactic disruption by only considering minihalos that have not accreted onto galactic halos, as Ref. [232] does.

Our goal in this chapter was to show that despite them not possessing the $\rho \propto r^{-9/4}$ density profiles that were previously assumed, minihalos are still able to yield competitive constraints on the primordial power spectrum. The plethora of minihalos that now contribute to observational signals counteracts the loss of signal from the rarest of these halos. This finding motivates their further study, and we have discussed avenues for future work. With a better understanding of disruptive processes, minihalos can become strong and robust cosmological probes.

CHAPTER 3:
FORMATION OF MINIHALOS BEFORE THE MATTER-DOMINATED EPOCH[1]

3.1 Introduction

While dark matter's abundance has been established through the study of its gravitational influence, the identity of its constituent particles remains a major unsolved problem. Experiments impose two key conditions that dark matter must satisfy.

(1) Dark matter must interact with ordinary matter in some nongravitational way in order to be produced cosmologically by known mechanisms, and moreover, the details of this interaction are tightly constrained by the requirement that dark matter achieve its observed abundance of roughly 26% of the present-day energy density of the Universe [208].

(2) Dark matter's interactions with ordinary matter must be sufficiently rare to explain why we have not produced dark matter in particle colliders, such as the Large Hadron Collider [138–144], or detected its pervasive presence directly [329–331].

A popular solution to these competing requirements, which also has motivations in string theory, is to propose that dark matter belongs to a *hidden sector* [146–151]. Instead of interacting directly with ordinary matter, dark matter interacts with a heavy mediator particle that in turn couples to ordinary matter. The weight of this mediator suppresses any manifestation of dark matter in laboratory experiments.

However, for a range of hidden-sector theories, the mediator particle would naturally dominate the energy density of the Universe during a fraction of the Universe's first second, leading to an

---

[1]Some of the content of this chapter was previously published in Physical Review D as Ref. [206] and is copyright © 2019 American Physical Society. The original reference is as follows: C. Blanco, M. S. Delos, A. L. Erickcek, and D. Hooper, *Annihilation signatures of hidden sector dark matter within early-forming microhalos*, Physical Review D **100**, 103010 (2019).

early matter-dominated era (EMDE) [153, 154]. This EMDE would amplify small-scale density variations dramatically, potentially causing overdense regions to collapse before the onset of the last matter-dominated epoch, which began at redshift $z \simeq 3400$. In this chapter, we explore the extent to which regions that collapse during radiation domination can form gravitationally bound dark matter halos. Structure evolves by particle drift alone when matter is subdominant, and drift velocities are set during the EMDE. Thus, to ensure correct evolution for the hidden-sector EMDE cosmology, we begin our analysis during the EMDE.

We consider an era dominated by a heavy particle, Z', that decays into radiation with rate $\Gamma_{Z'}$. Note that $\Gamma_{Z'}$ is uniquely associated with the reheat temperature T_{RH}, the temperature at which early matter domination gives way to radiation.[2] In the hidden-sector picture, dark matter froze out from the thermal plasma before the EMDE began, so only Z' and the radiation bath evolve nontrivially in the cosmological mean. For simplicity, we neglect changes in the composition of the radiation bath. The average radiation density $\bar{\rho}_{\mathrm{r}}$ and Z' density $\bar{\rho}_{Z'}$ evolve according to the system[3]

$$
\begin{aligned}
H \frac{\mathrm{d}(\bar{\rho}_{Z'} a^3)}{\mathrm{d} \ln a} &= -\Gamma_{Z'} \bar{\rho}_{Z'} a^3 \\
H \frac{\mathrm{d}(\bar{\rho}_{\mathrm{r}} a^4)}{\mathrm{d} \ln a} &= \Gamma_{Z'} \bar{\rho}_{Z'} a^4,
\end{aligned}
\tag{3.1}
$$

where H is the Hubble rate at scale factor a. Finally, the trajectories are fixed by picking initial conditions at some time during the EMDE. The initial radiation density is of little consequence and may be taken to be zero, but the initial $\bar{\rho}_{Z'}$ must be numerically tuned to yield a final radiation density that matches the observed cosmic microwave background temperature.[4]

We now explore the growth of structure in this scenario. We begin by analytically characterizing the evolution and collapse of overdense regions. When matter dominates, collapse precipitates bound halo formation, but this is not necessarily true when radiation dominates. Thus, we subsequently use numerical simulations to explore the connection between collapse and halo formation.

---

[2]T_{RH} is conventionally defined as the temperature at which $\Gamma_{Z'} = \tilde{H}$, where $\tilde{H}$ is the Hubble rate (as a function of temperature) if there were no EMDE.

[3]Note that $H \frac{\mathrm{d}}{\mathrm{d} \ln a} = \frac{\mathrm{d}}{\mathrm{d}t}$.

[4]Up to factors of order unity and powers of the effective number of relativistic degrees of freedom g_* at reheating, $\bar{\rho}_{Z'} \sim \Omega_r^{3/4} \rho_{\mathrm{crit}} \sqrt{\Gamma_{Z'}/H_0}\, a^{-3}$. Here, H_0 is the Hubble rate today and Ω_r is the radiation density today in units of the critical density ρ_{crit}. This relation arises from matching the Z' density to the radiation density at reheating.

3.2 Analytic growth and collapse

We first explore dark matter structure growth during and after the EMDE, beginning in the regime where density variations are subdominant. We take $\bar{\rho}_{\mathrm{m}}$ to be the average dark matter density. The system of equations describing the subhorizon growth of the dark matter density contrast $\delta \equiv \delta\rho_{\mathrm{m}}/\bar{\rho}_{\mathrm{m}} = \delta\rho_{Z'}/\bar{\rho}_{Z'}$, at linear order in δ and neglecting radiation fluctuations, is

$$
H\frac{\mathrm{d}\delta}{\mathrm{d}\ln a} = -\frac{u}{a},
$$
$$
H\frac{\mathrm{d}u}{\mathrm{d}\ln a} = -Hu - 4\pi G a\left(\bar{\rho}_{Z'} + \bar{\rho}_{\mathrm{m}}\right)\delta, \tag{3.2}
$$

where $u \equiv ikv$ is the (Fourier-transformed) divergence of the velocity field. The first equation is a continuity equation, while the second equation combines the Poisson and Euler equations to describe the response of the velocity field to the matter distribution. For a given initial $\delta_i \ll 1$ at scale factor a_i (with Hubble rate H_i), the initial velocity is given by

$$
u_i = -H_i a_i \delta_i \tag{3.3}
$$

during the EMDE.

In order to explore gravitational collapse, we next consider the nonlinear growth of an overdense region in a spherically symmetric picture. A sphere initially containing average density contrast δ_i and having radius r_i evolves in radius r and radial velocity v (in physical, not comoving coordinates) according to the equations[5]

$$
H\frac{\mathrm{d}r}{\mathrm{d}\ln a} = v
$$
$$
H\frac{\mathrm{d}v}{\mathrm{d}\ln a} = -\frac{4\pi G}{3}r\left[\left(\bar{\rho}_{Z'} + \bar{\rho}_{\mathrm{m}}\right)\left(\frac{ar_i}{a_i r}\right)^3(1 + \delta_i) + 2\bar{\rho}_{\mathrm{r}} - 2\bar{\rho}_{\Lambda}\right] \tag{3.4}
$$

($\bar{\rho}_{\Lambda}$ is the dark energy density). The second equation comes from the second Friedmann equation but can also be understood as Newtonian gravitation with a pressure correction. For a given initial

---

[5]If we were to account for changes in the radiation's composition, it would be necessary to replace $2\bar{\rho}_{\mathrm{r}}$ with $\bar{\rho}_{\mathrm{r}} + 3\bar{P}_{\mathrm{r}}$ in Eq. (3.4), where $\bar{P}_{\mathrm{r}}$ is the average radiation pressure.
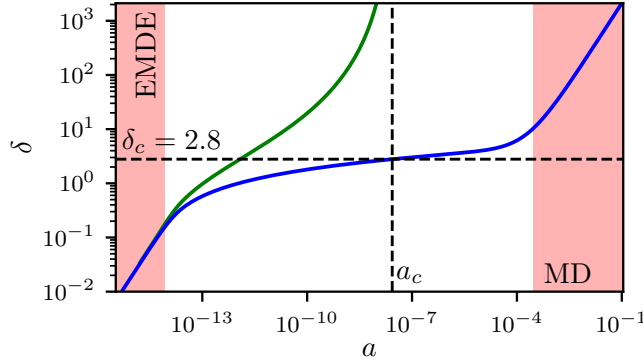
Figure 3.1: Growth of fractional density contrasts after an EMDE. The blue curve shows the linear-theory result (valid for $\delta \ll 1$), while the green curve shows the nonlinear evolution assuming spherical symmetry, evaluated for the same example initial conditions. Density contrasts grow rapidly during both the EMDE and the last matter-dominated (MD) epoch and much more slowly during radiation domination (white region), at least in linear theory. In the nonlinear calculation, the density contrast collapses ($\delta \to \infty$) during radiation domination when the linear-theory density contrast reaches a critical value of about $\delta_c = 2.8$, a larger value than the standard $\delta_c = 1.686$ that holds during matter domination.

radius r_i, the initial velocity v_i may be set using the Zel'dovich approximation [332] if $\delta_i \ll 1$ so that

$$v_i = H_i r_i (1 - \delta_i/3). \tag{3.5}$$

We may now numerically integrate the full system Eqs. (3.1), (3.2), and (3.4) with the initial conditions Eqs. (3.3) and (3.5) set during the EMDE. The initial radius r is arbitrary, while the initial $\delta \ll 1$ is tuned to yield collapse during radiation domination. Figure 3.1 shows a representative result. The blue line shows the linear theory prediction for δ, valid only for $\delta \ll 1$, while the green line shows the prediction δ_{sc} of the spherical collapse model, calculated as

$$\delta_{\text{sc}} = \left(\frac{ar_i}{a_i r}\right)^3 (1 + \delta_i) - 1. \tag{3.6}$$

We see that despite gravitational potentials being negligible during radiation domination, gravitational collapse still occurs, but it occurs at a larger linear $\delta = \delta_c$ than during matter domination. We discuss in Appendix B the behavior of δ_c during radiation domination and present a convenient fitting function.

Evidently, overdense regions can collapse during radiation domination. However, where radiation dominates, matter particles cannot experience net forces, so this collapse must occur by drift alone.

Dark matter particles were attracted toward overdense regions during the EMDE, and they continue drifting in the same directions after Z' domination gives way to radiation.[6]. While these drifting particles may eventually converge, producing a collapse event, it is not clear that they can form bound structures. To determine when a halo can form, we turn to numerical simulations.

3.3 Numerical simulations

3.3.1 Simulation methods

We use the cosmological simulation code GADGET-2 [274] to study gravitational collapse during radiation domination. We modified the code to include both radiation and a decaying Z' matter component. These components are modeled at the homogeneous level by adding corresponding terms to the Hubble rate appearing in the time integrands used for particle drifts and gravitational kicks. Meanwhile, the clustering capacity of the decaying Z' component is modeled by scaling the mass m of each simulation particle as

$$m = \frac{\bar{\rho}_{Z'} + \bar{\rho}_{\mathrm{m}}}{\bar{\rho}_{\mathrm{m}}} m_0, \tag{3.7}$$

where m_0 is the particle mass at late times, as in Refs. [333, 334]. Effectively, each simulation particle is representing Z' particles and dark matter particles together. As a technical matter, this modification is also implemented by modifying a time integral; in particular, the time integrand used for gravitational kicks is scaled by m/m_0, as in Ref. [335]. This implementation is necessary to maintain accuracy near reheating, when the particle mass changes rapidly over a single time integration step. Figure 3.2 demonstrates the accuracy of this modification. A periodic box with small initial density fluctuations is simulated through reheating and matter-radiation equality, and the growth of the square root of the (dimensionless) power spectrum in the simulation, measured at a particular wavenumber, is compared to the growth of δ in linear theory [Eq. (3.2)]. The two match closely as long as the power spectrum (and hence δ) remain inside the linear regime.

---

[6]In fact, this observation readily explains the logarithmic growth of small density contrasts during radiation domination. Comoving velocities decay as a^{-2}, so the comoving displacement $\boldsymbol{s}$ of a particle is proportional to $\int a^{-2} dt = \int a^{-2} da/(aH) \propto \int da/a$ since $H \propto a^{-2}$ during radiation domination. Thus, $\boldsymbol{s} \propto \ln a$, and since $\delta = -\nabla \cdot \boldsymbol{s}$ at linear order, $\delta \propto \ln a$.
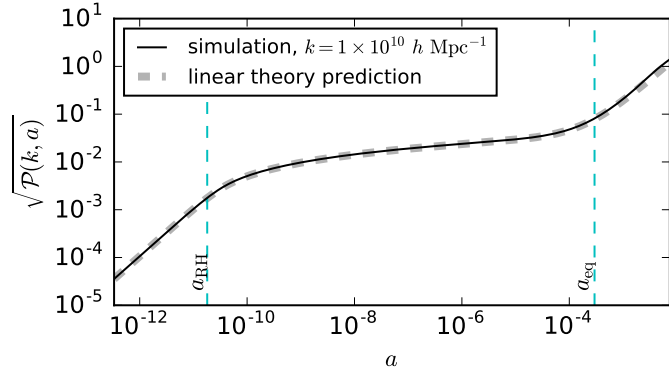
Figure 3.2: Demonstration of our modification to GADGET-2 to represent an EMDE. We simulated a periodic box with small Gaussian initial density variations beginning during the EMDE, and we plot the evolution of the dimensionless power spectrum $\mathcal{P}$ evaluated at a fixed wavenumber. The simulated growth of density contrasts (solid line), which are proportional to $\sqrt{\mathcal{P}}$, matches the linear-theory prediction for δ (dashed line).

3.3.2 Simulating collapse during radiation domination

We now use our custom simulation code to study whether collapsed regions can become bound during the radiation-dominated era. For simplicity, we study the collapse of individual density peaks instead of full Gaussian fields. We fix an EMDE cosmology with $T_{\mathrm{RH}} = 22$ MeV, corresponding to radiation domination beginning at the scale factor $a = 10^{-11}$ (where $a = 1$ today). To generate density peaks, we consider a dimensionless power spectrum that scales as

$$\mathcal{P}(k) \propto \ln(k/k_0)^2 \tag{3.8}$$

with $k_0 = 4 \times 10^6$ Mpc^{-1}; that is, we consider scales that entered the horizon during a prior period of radiation domination. We now draw individual proto-halo density peaks from the Gaussian-filtered power spectrum

$$\mathcal{P}_{\mathrm{f}}(k) = \mathcal{P}(k) \exp(-R_{\mathrm{f}}^2 k^2) \tag{3.9}$$

using the density profiles of Ref. [269] with smoothing scale $R_f = 1.5 \times 10^{-11}$ Mpc. To add some realism to this otherwise smooth density peak, we also superpose small-scale Gaussian noise drawn from the oppositely filtered power spectrum

$$\mathcal{P}_{\mathrm{cf}}(k) = \mathcal{P}(k) \left[1 - \exp(-R_{\mathrm{f}}^2 k^2) \right]. \tag{3.10}$$

54
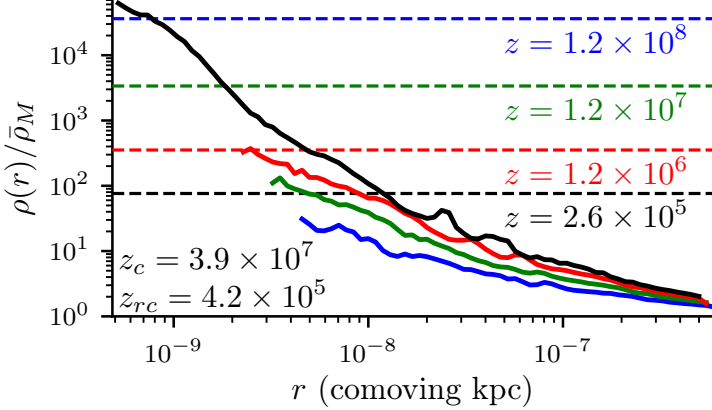
Figure 3.3: Formation of a bound halo during radiation domination. The solid lines show the spherically averaged dark matter density profile at four different times, all during radiation domination, as simulated from an isolated initial density excess. The dashed lines show the density of the homogeneous radiation background at the same times. We plot all density values in units of the background dark matter density $\bar{\rho}_{\mathrm{m}}$. The spherical collapse model described in Sec. 3.2 predicts that the overdense region collapses at $z_c = 3.9 \times 10^7$, but a bound structure does not form at that time. Instead, the dark matter density grows slowly until it locally exceeds the radiation density, at redshift $z_{rc} = 4.2 \times 10^5$. At that time, still long before matter-radiation equality, a bound halo forms (black solid line). The minimum radius plotted at each redshift is set to contain 100 simulation particles.

Finally, we impose vacuum boundary conditions at the comoving radius 7×10^{-10} Mpc and begin the simulation at $a = 3 \times 10^{-13}$.

We tested a variety of initial peak density profiles, three-dimensional shapes, and amplitudes (corresponding to collapse times). The general outcome for peaks collapsing deep in radiation domination is that after collapse, the structure develops a shallow cusp with $\mathrm{d}\ln\rho/\mathrm{d}\ln r \simeq -1$. Eventually, this structure recollapses to form a bound halo, and this process happens at roughly the time of *local* matter-radiation equality. That is, recollapse occurs when the matter density within the structure exceeds the homogeneous radiation density, typically around redshift $z \sim (2-5) \times 10^5$. The characteristic density of the resulting halo is determined by the recollapse time, rather than the initial collapse. Figure 3.3 illustrates this process using one of our simulations.

Figures 3.4 and 3.5 show the density profiles arising from a variety of initial peaks after collapse but before recollapse. We find that the size of the collapsed structure is proportional to the size of the initial peak, or equivalently the smoothing scale R_f, while the density of the structure scales as $\ln(a/a_c)$ where a_c is the scale factor of collapse predicted by the spherical collapse model. Shape parameters describing the three-dimensional shape and density profile of the initial peak, on the
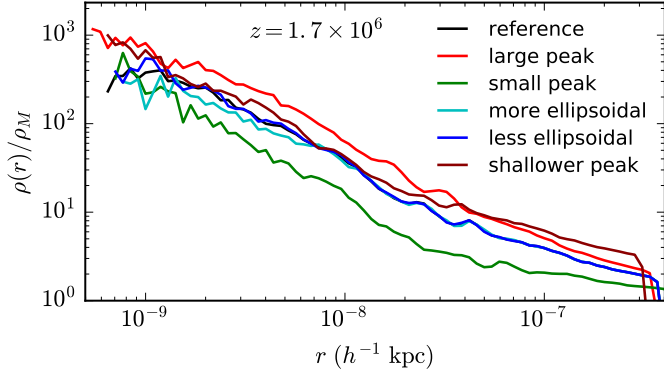
Figure 3.4: Dependence of the collapsed structure during radiation domination on properties of the initial peak. The larger and smaller peaks differ by a factor of 2 in their initial size (measured by $|\delta/\nabla^2\delta|^{1/2}$ at the peak), which roughly matches the difference in the size of the density profile after collapse. More and less ellipsoidal peaks vary derivatives $\partial_i\partial_j\delta$ at the peak while holding $\nabla^2\delta$ fixed. Evidently, three-dimensional shape has minimal effect. The shallower peak employs a smaller k_0 in the power spectrum of Eq. (3.8). All peaks have the same filtering scale.

other hand, appear to have minimal effect.[7] We found the expression

$$\rho(r) = \left[A\ln\left(\frac{a}{a_{\rm c}}\right) + B\right]\bar{\rho}_{\rm m}\frac{R_f}{r},$$
(3.11)
$$A \simeq 8.4, \quad B \simeq 12.4.$$

to provide a reasonable fit to this density profile.[8] If we now posit that recollapse occurs when the mean matter density within R_f exceeds the radiation density, then this leads to the condition

$$\left[A\ln\left(\frac{a_{\rm rc}}{a_{\rm c}}\right) + B\right]a_{\rm rc} = \frac{2}{3}a_{\rm eq}$$
(3.12)

for the recollapse scale factor $a_{\rm rc}$, where $a_{\rm eq}$ is the scale factor of matter-radiation equality. Equation (3.12) turns out to be approximately correct in predicting $a_{\rm rc}$ in the simulations. We note that

---

[7]The density profile of the initial peak has minimal effect as long as it remains self-similar, as in a nearly scale-invariant power spectrum. Peaks drawn from a small range of k-modes (rather than associated with power at all scales) were found to develop constant-density cores in radiation domination instead of r^{-1} cusps.

[8]We suspect it would be feasible to derive the density profile by using an ellipsoidal collapse model before reheating and letting all particles freely drift afterward. With the removal of gravitation, a Lagrangian map (between initial and final particle positions) should remain only two-valued. However, ellipsoidal collapse is necessary. This calculation carried out under spherical symmetry yields $\rho \propto r^{-2}$, which is steeper than the profile we obtained in simulations.
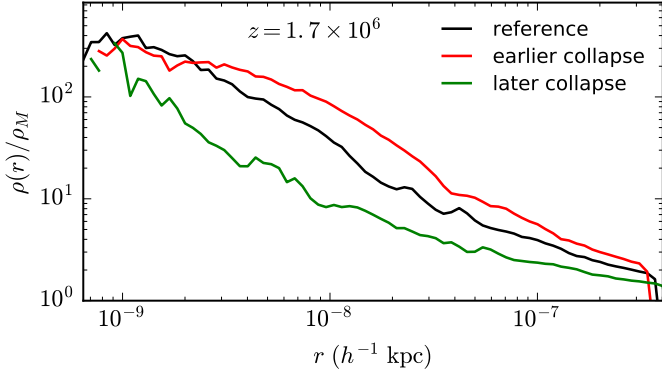
Figure 3.5: Dependence of the collapsed structure during radiation domination on the collapse time. We depict the density profiles of collapsed structures arising from peaks that collapse at scale factors 2.6×10^{-8}, 2.5×10^{-9}, and 1.0×10^{-6}, respectively, as predicted by the spherical collapse model. (The last collapse is later than the time of the plot, but due to the ellipsoidal shape, one axis collapses significantly earlier than the spherical collapse model predicts.) The difference between the three structures is fully explained by their logarithmic growth over time as per Eq. (3.11).

if Eq. (3.12) predicts $a_{rc} < a_c$, then the collapsed region is immediately dense enough to recollapse. In this case, a bound structure simply forms at scale factor a_c.

We remark that structures collapsing too soon after reheating did not recollapse at all, owing to the high particle velocities induced by the collapse. The precise threshold for this effect was not explored. At the other extreme, highly spherically symmetric peaks can collapse much deeper into radiation domination owing to their ability to concentrate infalling matter into a much smaller region. Such peaks are very rare, however.

While simulations of isolated density peaks allow for easy control of variables, they recover poorly the detailed structure of halos arising from a nearly scale-invariant power spectrum. This structure is fundamentally linked to halo mergers. For this reason, we do not attempt to measure the characteristic density (or concentration parameter) of the halos that arose in our simulations. Additionally, the recollapse time cannot be precisely measured because we did not develop an exact definition for this quantity. Future work should carry out simulations of full density fields in order to test Eq. (3.12) and determine the precise connection between a halo's internal structure and its recollapse time.

3.4   Conclusion

For a wide range of parameters, hidden-sector dark matter theories predict an EMDE that could boost small-scale dark matter density variations dramatically. In these cosmologies, overdense regions could begin to collapse prior to the last matter-dominated epoch. In order to estimate the properties of the minihalos that arise in these scenarios, we studied the behavior of regions sufficiently overdense that they collapse during the radiation-dominated epoch. The collapse time of an overdense region can be predicted using a spherical collapse model even during radiation domination, and we supplied in Appendix B a fitting function that relates this spherical collapse to linear theory. The critical linear density contrast δ_c is larger than its value during matter domination, rising as high as about 3.

However, during radiation domination, collapse does not directly correlate with the formation of a bound structure. To address this ambiguity, we used a customized version of the Gadget-2 simulation code to simulate the collapse of isolated density peaks during radiation domination. We found that regions become gravitationally bound when their matter density locally exceeds the radiation density. Additionally, we found a fitting function that describes the structure of a collapsed (but not bound) region as a function of its collapse time. Using this fit, it is straightforward to predict when the matter density locally exceeds the radiation density, and thus when a collapsed structure recollapses to become gravitationally bound. Our fitting function successfully predicts this recollapse time. These results were used in Ref. [206] to develop new observational constraints on hidden-sector dark matter theories.

Further research is necessary to fully understand the properties of halos that form during radiation domination. We simulated only isolated overdense regions, but halos that arise from density variations at all scales are fundamentally shaped by mergers with other halos, which our simulations do not represent. Full Gaussian density fields must be simulated in order to precisely study these halos.

Another valuable research avenue would be to study halo formation during the EMDE. Halos that arise during an EMDE would largely evaporate as the Z' particle decays, leaving the dark matter that resided within them gravitationally heated [206]. This effect could suppress subsequent structure formation. However, since only a fraction of the dark matter is gravitationally heated, the extent of this suppression is unclear. Numerical simulations could resolve this uncertainty.

CHAPTER 4:
PREDICTING THE DENSITY PROFILES OF THE FIRST HALOS[1]

4.1 Introduction

Decades of work have been devoted to understanding the halos that form by the gravitational collapse of collisionless dark matter. In the cold dark matter (CDM) model, N-body simulations have demonstrated that the radial density profiles $\rho(r)$ of these halos are well described by a remarkably universal form, known as the Navarro-Frenk-White (NFW) profile [205, 260], which is a double power law that transitions from $\rho \propto r^{-1}$ at small radii to $\rho \propto r^{-3}$ at large radii. This profile has received only minor corrections since its introduction (e.g., Ref. [337]). In the CDM picture, all halos form by hierarchical clustering of smaller halos, and the NFW profile appears to be the generic consequence.

CDM represents an idealized scenario, however. In reality, dark matter particles are expected to have a nonzero temperature, and the corresponding random particle motions wash out density fluctuations smaller than a characteristic free-streaming scale. The first halos form by direct collapse of overdense regions at this scale, and N-body simulations with sufficient resolution show that these halos possess a markedly different density profile that asymptotes to $\rho \propto r^{-3/2}$ at small radii [261–266]. This profile is stable; it does not relax to the NFW profile, at least in the absence of halo mergers.

The first halos subsequently merge to produce successively larger halos, and Refs. [262, 280] find that these mergers gradually drive the halos' density profiles toward the NFW form. As these works argue, the shallowing of the inner density profile is likely a consequence of violent relaxation [338] during merger events. However, there are multiple lines of evidence suggesting that such relaxation does not erase the memory of prior states. For nearly equal-mass mergers, the density profile of the

---

merger remnant depends sensitively on the profiles of its progenitors [262, 266]. Successive mergers either raise or leave unaltered a halo's characteristic density [262, 280, 339]; since the first halos are the densest, this trend preserves them. Finally, for highly unequal-mass mergers, the smaller halo is generally expected to survive as a subhalo of the larger [284]. The smaller halo's central density profile may even be mostly unaffected by the merger [340–342].

In this way, it is broadly plausible that the dense central regions of the first halos survive the hierarchical clustering process. These halos, forming during a denser epoch, should be the densest dark matter objects in the Universe, and such density leads to observational prospects. Signals from dark matter annihilation are dramatically enhanced by the high density within these halos (e.g., Refs. [343–348]). Gravitational signatures, whether through microlensing (e.g., Refs. [349–352]), timing delays (e.g., Ref. [353]), or stellar dynamics (e.g., Refs. [200, 201, 354]), are also enhanced. Meanwhile, since these halos form by direct collapse from overdense patches, they carry sensitive information about the primordial density field on scales that are inaccessible to other probes. Our goal is to develop a model that extracts this information; we aim to connect the properties of the first halos to the statistics of the primordial matter density field.

The matter density field is intimately connected to some of the most fundamental questions of cosmology. The power spectrum $\mathcal{P}(k)$, which quantifies the power in density fluctuations at scale wave number k, has been precisely measured at scales above approximately 1 Mpc using the cosmic microwave background [251] and the Lyman-α forest [15]. However, with a few exceptions [19, 252], it is largely unconstrained at submegaparsec scales. Since density fluctuations are thought to have been seeded during inflation, $\mathcal{P}(k)$ serves as a valuable probe of inflationary models [4]. The power spectrum is also sensitive to the thermal history of the Universe after inflation. An early matter-dominated era (EMDE), driven by an unstable heavy relic, would amplify small-scale density fluctuations [181–183, 224], as would a period of domination by a fast-rolling scalar field [191]. The power spectrum $\mathcal{P}(k)$ thereby supplies one of the few windows into the Universe prior to big bang nucleosynthesis. Separately, its sensitivity to the free-streaming scale makes it a probe of the nature of dark matter.

Numerous previous works have explored the prospects of using the first dark matter halos to probe the small-scale primordial power spectrum [232–236, 246–249]. However, most treatments assumed that these halos, if they form sufficiently early, possess a particularly compact $\rho \propto r^{-9/4}$

density profile [202] derived from self-similar theory [203]. References [267] and [226] used N-body simulations to show that this profile does not arise from a realistic formation scenario. In Chapter 2, we showed that, despite possessing shallower $\rho \propto r^{-3/2}$ density profiles, the first halos can still supply competitive constraints on the power spectrum through nondetection of their observable signals. In that work, we used scaling arguments to model the population of the first halos given a particular family of power spectra. Each peak in the density field was mapped to a collapsed halo at later time.

Our present work represents a natural extension of that model to arbitrary power spectra. It is based on the notion that the density profile of a halo forming by direct collapse is uniquely related to the properties of its precursor density peak. Numerous prior works have explored the problem of explaining a halo's density profile in terms of the structure of the density peak whence it collapsed. In work that pioneered the so-called spherical infall model, Refs. [355, 356] approximated the density profile of a collapsed halo by employing the simplifying assumption that particle orbits are unaltered after accretion. Subsequent works extended this model by including the contraction of orbiting material due to new accretion [203, 253, 357–362], relaxing the assumption of spherical symmetry [363, 364], and modeling nonradial motions [282, 365–370]. Because of the difficult, nonlinear nature of the matter infall problem, every treatment employs simplifying assumptions. Exact solutions only exist for the self-similar case [203, 253, 363, 364], in which the primordial mass excess is a power law in radius. More general treatments employ Ansätze related to angular momenta and orbital contraction. As an alternative to tracking each orbit, other works have employed an Ansatz related to virialization [371, 372].

Whereas spherical infall models relate halo density profiles to the precursor mass distribution, a complementary paradigm empirically studies the distribution of halo density profiles as a function of cosmology and redshift. In this paradigm, cosmological N-body simulations are used to tune a parametric model that describes the density profile of a halo as a function of its mass, and models built in this paradigm are known as concentration-mass relations.[2] The distribution of halo masses can be subsequently obtained using Press-Schechter theory [287, 373, 374], so these models can predict the full population of halos and their density profiles. Concentration-mass relations have been

---

[2]The concentration is a parameter in the NFW profile (and extended to other profiles) describing how centrally distributed the halo's mass is.

studied extensively. The simplest models describe the halo distribution in a particular cosmological scenario and at a particular time of interest [295, 299–305, 310, 312, 317, 318, 375–380]. Other works have framed a halo's density profile in terms of its age or assembly history [205, 260, 279, 294, 296–298, 306, 309, 313, 315, 381, 382], and progress has been made in isolating the physical variables most directly relevant for predicting density profiles [307, 314, 316, 383]. Nevertheless, due to their empirical nature, concentration-mass relations do not readily extend beyond the cosmological scenarios, times, and halo-mass ranges over which they are tuned.

Broadly, spherical infall models attempt to explain the structures of halos from first principles, while concentration-mass relations endeavor to predict these structures pragmatically. Our analysis constitutes a hybrid between these two procedures that is specialized to the first halos. Forming by direct collapse, these halos are well suited to the spherical infall description. At the smallest radii, we use ellipsoidal collapse arguments [373, 374, 384] to predict the coefficient of the $\rho \propto r^{-3/2}$ inner profile. Beyond the inner asymptote, we employ the simplest spherical infall models to predict the larger profile, parametrized by the maximum circular velocity $v_{\max}$ and the radius $r_{\max}$ at which it is attained [385]. By building from such first-principles descriptions, our predictive models are valid in any cosmological scenario; we demonstrate this by validating and tuning the models using six high-resolution cosmological N-body simulations carried out in wildly disparate cosmological scenarios. Our models nominally predict a halo's density profile from the density peak whence it collapsed. However, modulo the influence of halo mergers (which we discuss), the statistics of peaks [269] may be applied to thereby predict the full halo population at a given time.

4.2 Simulations

We first build a halo catalogue on which to test our model. For this purpose, we simulated six different simulation boxes drawn from different initial power spectra. These power spectra are shown in Fig. 4.1. Three of these power spectra are constructed as "spikes" centered at the scale $k_s = 6.8$ kpc^{-1} with the form

$$\mathcal{P}(k) = \frac{\mathcal{A}}{\sqrt{2\pi}w} \exp\left[-\frac{1}{2}\left(\frac{\ln(k/k_s)}{w}\right)^2\right] \tag{4.1}$$

for different values of w. These spectra are primarily intended as artificial test beds for halo formation, but they do have qualitative motivations in inflationary phenomenology [27–30, 49, 51, 52, 73, 76, 78]. A fourth power spectrum represents the impact of an EMDE with reheat temperature $T_{\mathrm{RH}} = 100$
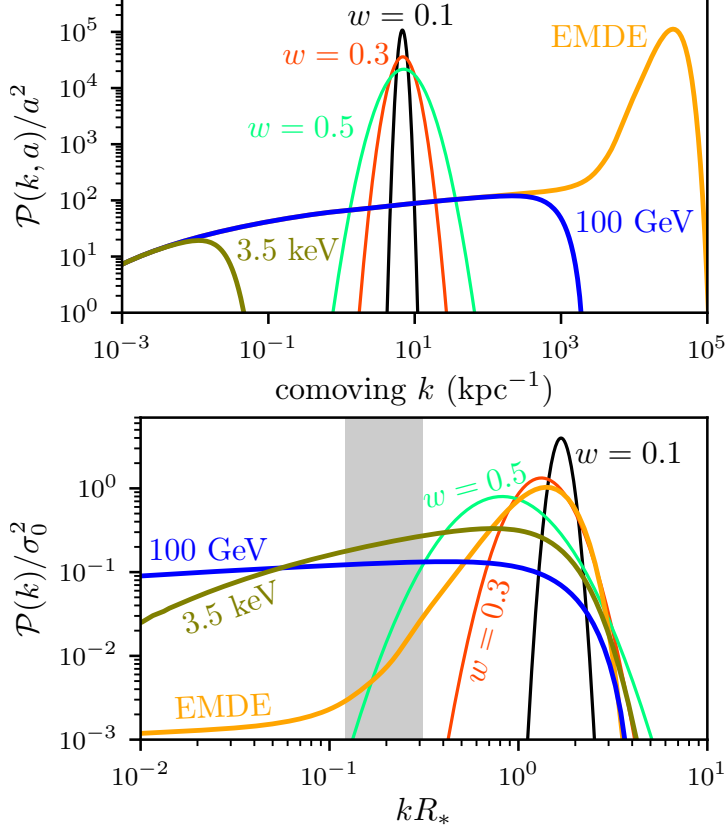
Figure 4.1: Top: The (linear-theory) dimensionless matter power spectra of our six simulations during matter domination. In linear theory, $\mathcal{P}(k,a) \propto a^2$ when matter dominates, which motivates the y-axis scaling (with $a = 1$ today). Bottom: The same power spectra, but each is scaled to its density variance and characteristic correlation length (see the text). The shaded region marks the range of box sizes for the six simulations: larger modes (smaller k) have wavelengths longer than the simulation box, so they are not sampled.

MeV and ratio $k_{\rm cut}/k_{\rm RH} = 20$ between the free-streaming cutoff and the largest scale affected by the EMDE (see Ref. [224]). Finally, the last two power spectra include only the free-streaming cutoffs associated with cold dark matter with mass $m_\chi = 100$ GeV and kinetic decoupling temperature $T_{\rm kd} = 33$ MeV (corresponding to a typical weakly interacting massive particle [283]) and warm dark matter (WDM)[3] with mass $m_\chi = 3.5$ keV (close to lower bounds from the Lyman-α forest [387]), respectively. The particular parameter choices for these power spectra are intended to represent very different cosmological scenarios so that we can test the broad applicability of our models.

We generate the three spiked power spectra from Eq. (4.1) at a starting redshift of $z = 10^4$,

---

[3]For WDM, we also take the dark matter particle to be fermionic with 2 degrees of freedom (so, $g_X = 1.5$ in Ref. [386]).

normalizing $\mathcal{A} = 2 \times 10^{-7}$ at this time in order to effect abundant halo formation by $z \sim 100$. To generate the latter three power spectra, we begin with a primordial curvature power spectrum of amplitude $\mathcal{A}_s = 2.142 \times 10^{-9}$ and spectral index $n_s = 0.9667$ [16]. We then use the Boltzmann solver CAMB SOURCES [270, 271] to produce a matter power spectrum at $z = 500$ in a scenario with no thermal dark matter motion. Next, we apply transfer functions from Refs. [224], [388], and [386] to create, respectively, the EMDE, CDM, and WDM spectra. Finally, we use linear theory [273] to evolve these power spectra to their initial redshifts. Note that we include radiation in our simulations, and the linear evolution accounts for this; see Chapter 2 for details.[4] We also include a cosmological constant, although it is of minimal relevance.

The starting redshift z_{init}, ending redshift z_{final}, and periodic box size of each simulation are listed in Table 4.1. Also listed are the rms density variance σ_0 and comoving characteristic correlation length R_* associated with each power spectrum in linear theory. These spectral parameters are defined as [269]

$$\sigma_j = \left(\int_0^\infty \frac{dk}{k} \mathcal{P}(k) k^{2j} \right)^{1/2} \tag{4.2}$$

$$R_* = \sqrt{3} \frac{\sigma_1}{\sigma_2}. \tag{4.3}$$

To illustrate the significance of these quantities, Fig. 4.1 also shows the correspondingly rescaled power spectra. This rescaling is useful because it factors out the scale differences between the spectra, leaving only their shapes. For this reason, we will use these spectral parameters as our units. The mass unit is $m_{\mathrm{unit}} \equiv \bar{\rho}_0 R_*^3$, where $\bar{\rho}_0$ is the background matter density today. Meanwhile, the physical distance unit is $r_{\mathrm{unit}} \equiv [a/\sigma_0(a)]R_*$, where $\sigma_0(a)$ is evaluated using linear theory during matter domination (so $\sigma_0 \propto a$) and $a = 1$ today. For each simulation, the ending redshift is tuned so that $\sigma_0 \sim 3$ (in linear theory) at simulation termination, and the comoving box size is tuned to be roughly 30 to 80 times R_*. The initial redshift is chosen so that the largest fractional density excesses $\delta \equiv (\rho - \bar{\rho})/\bar{\rho}$ are of order 0.2 or smaller.

For each simulation, we draw a random density field from the matter power spectrum at z_{init}

---

[4]Modes that were subhorizon during an EMDE grow in an altered way during radiation domination [224], and we modify the linear growth function for this scenario accordingly.

Table 4.1: The simulation list with basic parameters. Also listed are σ_0, the rms density variance, and R_*, the comoving characteristic correlation length, both calculated in linear theory. When matter dominates, $\sigma(a) \propto a$, which motivates the scaling in this column (with $a = 1$ today).

Simulation	z_{init}	z_{final}	Box (kpc)	$\sigma_0(a)/a$	R_* (kpc)
$w = 0.1$	10^4	50	7.4	164	0.25
$w = 0.3$	10^4	50	7.4	164	0.19
$w = 0.5$	10^4	50	7.4	164	0.12
EMDE	3×10^4	100	1.5×10^{-3}	330	4.1×10^{-5}
100 GeV	500	9	0.15	30	1.9×10^{-3}
3.5 keV	150	2	4.4×10^3	7.6	66

and generate initial conditions using the Zel'dovich approximation modified to account for radiation as described in Chapter 2.[5] Finally, we carry out the simulations using a version of the cosmological simulation code GADGET-2 [274, 275] that we modified to include the effects of radiation (see Chapter 2). All simulations employed 1024^3 particles and a comoving force softening length set at 3% of the initial interparticle spacing (with forces becoming non-Newtonian at 2.8 times this length).

Figure 4.2 shows the initial and final density fields for three of these simulations. This sample illustrates the characteristic differences between the density fields and halo populations that result from the different power spectra. The $w = 0.1$ spectrum produces fluctuations only on a characteristic scale, and the resulting halo population is relatively uniform in size and separation. Meanwhile, the $w = 0.5$ spectrum produces fluctuations on a wider range of scales, yielding very small halos as well as larger halo clusters and voids. Finally, the 100 GeV power spectrum includes fluctuations at scales up to and exceeding the box size.[6] Accordingly, the bulk of the halos in the box reside within a few clusters, and some halos are growing exceedingly large.

At the final redshift of each simulation, we use the ROCKSTAR halo finder [277] to identify every halo with mass larger than a cutoff $M_{\text{cut}} = (4\pi/3)k_{\text{max}}^{-3}\bar{\rho}_0$, where k_{max} is the wave number k at which $\mathcal{P}(k)$ is maximized. This cutoff is intended to exclude most of the artificial fragments [389, 390] that are normally expected to appear in simulations with a small-scale cutoff in density fluctuations.

---

[5]For the EMDE, the methods in Chapter 2 were adapted to the post-EMDE growth function.

[6]In fact, the entire boxes of the 100 GeV and 3.5 keV simulations should be collapsing by the final redshift, a fact that cannot be reflected in these simulations. Thus, we do not expect these two simulations to accurately capture the large-scale dynamics; for example, halo mergers are probably under-represented. We focus on understanding the halos that form by direct collapse from peaks in the density field, so we do not expect this shortcoming to impact our main results.
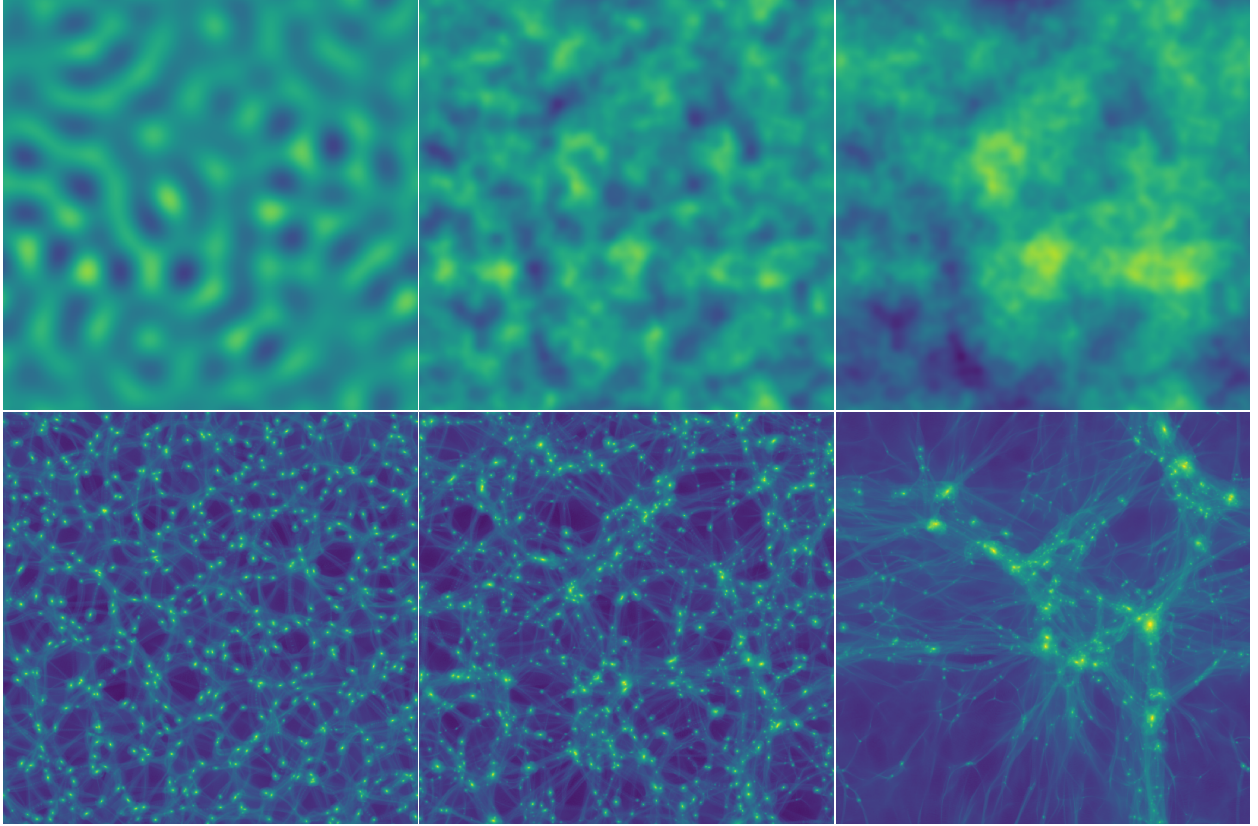
Figure 4.2: The projected initial (top) and final (bottom) density fields for the $w = 0.1$ (left), $w = 0.5$ (middle), and $m_\chi = 100$ GeV (right) simulations. The color scale is logarithmic; lighter is denser.

Roughly speaking, fluctuations at the scale $k_{\max}$ are the first to collapse, so we do not expect to find many real halos at smaller scales. Table 4.2 lists the number N_{halo} of such halos found in each simulation.

Next, we wish to associate each halo with the density peak whence it collapsed. To do this, we use ROCKSTAR to generate halo catalogues at intervals of roughly 5% in the scale factor, and we use the CONSISTENT TREES merger tree code [391] to improve the consistency of halo tracking through time. Starting at the final redshift, we trace each halo back to its formation time, defined as the time when its mass first exceeded M_{cut}. In case of a merger, we follow the larger progenitor. We then identify all particles in the halo at its formation time, find their positions in the initial particle grid at z_{init}, and compute the center of mass $\boldsymbol{x}_{\text{CM}}$ and rms spread r_{CM} of these positions. Finally, we consider the initial grid $\delta(\boldsymbol{x})$ of fractional density contrasts and find the largest value of $\delta(\boldsymbol{x})$ within a sphere of radius r_{CM} about $\boldsymbol{x}_{CM}$. If this maximum is also a local maximum in $\delta(\boldsymbol{x})$ (a condition that could fail if the maximum lies at the sphere's boundary), we take it to be the initial

Table 4.2: For each simulation, we list the halo count N_halo above the mass cutoff at the final redshift, the number of peaks N_peak in the linear density field, and the number N_match of successful halo-peak matches. Of these matches, also listed are the number N_A with density profiles resolved at small radii, the number N_r with $r_\mathrm{max} < r_\mathrm{vir}$, and the subsets $N_\mathrm{A}^{<3\mathrm{MM}}$ and $N_\mathrm{r}^{<3\mathrm{MM}}$ that also underwent fewer than three major mergers.

Simulation	N_halo	N_peak	N_match	N_A	$N_\mathrm{A}^{<3\mathrm{MM}}$	N_r	$N_\mathrm{r}^{<3\mathrm{MM}}$
$w = 0.1$	696	439	411	408	350	404	347
$w = 0.3$	801	933	565	561	481	537	457
$w = 0.5$	1011	3896	795	790	683	738	634
EMDE	610	730	424	416	366	388	339
100 GeV	216	6108	157	153	141	82	73
3.5 keV	581	4401	463	455	430	322	303

density peak for this halo. Otherwise, we discard the halo from further consideration, suspecting it to be an artificial fragment.[7] Moreover, when this procedure associates multiple halos in the final box with the same initial peak, we discard all but the most massive halo. Table 4.2 lists both the number N_peak of peaks in the initial density field and the number N_match of peak-halo identifications made through this procedure.

To test our models, we must still make further cuts to the halo-peak population. For the small-radius asymptote of the density profile (Sec. 4.3), we consider the subset of our peak-matched halos that have well-resolved inner density profiles[8]. The number N_A of such halos in each simulation is listed in Table 4.2. Moreover, Ref. [280] found that successive major mergers alter the inner asymptote of a halo's density profile, and we confirm this effect in Sec. 4.5.2. We aim to model the initial density profile of a halo before it undergoes any disruptive dynamics, leaving a treatment of mergers for future work.[9] Thus, we also restrict our sample to halos that underwent fewer than three major mergers, which we define to be mergers between two halos with a mass ratio smaller than 3. The number $N_A^{<3\mathrm{MM}}$ of these halos is also listed in Table 4.2. The particular threshold of three major mergers is chosen as a compromise between minimizing the impact of mergers on our

---

[7]We explored the alternative procedure of following the density gradient to a local maximum, but the only consequence was the introduction of unphysically distant halo-peak associations.

[8]In particular, we require that at least 100 particles reside within the simulation softening length. Otherwise, the central density is small, usually implying that the density profile was not centered on the halo's cusp, which is only true of a handful of halos not found by Rockstar but filled in by Consistent Trees. Due to the minuscule fraction of halos affected, we did not make further efforts to find the true center.

[9]We prefer to exclude the impact of mergers in this work because mergers are a continuing process, so their impact is sensitive to the arbitrarily chosen simulation termination redshift.

results and maximizing the sample of halos from which our results are drawn. As we will see in Sec. 4.5.2, the first two major mergers only marginally alter halo density profiles.

Meanwhile, for the larger-radius density profile (Sec. 4.4), we consider the subset of our peak-matched halos that have r_{max}, the radius at which the circular velocity is maximized, inside their virial radius, defined as the radius r_{vir} enclosing average density 200 times the background.[10] The number N_{r} of these halos is listed for each simulation in Table 4.2. Mergers only minimally alter r_{max} (see Sec. 4.5.2), so when testing models for r_{max}, it is not necessary to restrict to halos that underwent few mergers. However, mergers can significantly alter the mass $M(r_{\mathrm{max}})$ enclosed within r_{max} (or equivalently v_{max}), so to test our mass predictions, we restrict the sample to the subset $N_{\mathrm{r}}^{<3\mathrm{MM}}$ of halos that underwent fewer than three major mergers. This number is also listed in Table 4.2. Altogether, it is evident from Table 4.2 that only a small fraction of the full peak and halo populations is used to test our models. Section 4.5 explores the impact of these restrictions by returning to the full peak and halo populations.

We now have a catalogue that matches peaks in an initial density field to collapsed halos at a much later time. All that remains is to collect the halo density profiles and the parameters of each peak, and we detail these processes in Appendixes C.1 and C.2, respectively. With these data, we are now prepared to test any model relating the structure of a dark matter halo to its precursor density peak. In the following sections, we develop such a model.

4.3   Density profile at small radii

We first study the coefficients A of the $\rho = Ar^{-3/2}$ asymptotes of the density profiles of the first halos. It is of prime importance to accurately predict the density profiles in this regime because these radii source the bulk of the prospective signal from dark matter annihilation, and this remains true even if these halos relax toward $\rho \propto r^{-1}$ profiles due to mergers. Moreover, there is another reason to study small radii separately: the $\rho \propto r^{-3/2}$ inner density profile is established almost immediately after collapse. To illustrate this fact, we simulate[11] the collapse of the isolated density peak shown in

---

[10]The requirement $r_{\mathrm{max}} < r_{\mathrm{vir}}$ culls a significant fraction of the halo population in the 100 GeV simulation, but this is not a serious concern. It turns out that the models we discuss predict very large r_{max} for these halos as well, and $r_{\mathrm{max}} > r_{\mathrm{vir}}$ only implies that the halo's outermost profile has not yet steepened to the point that $\mathrm{d}\ln M/\mathrm{d}\ln r < 1$.

[11]This simulation employed about 9 million particles in a comoving vacuum-bounded sphere of radius 1.5 kpc. The starting redshift was $z = 10^6$.
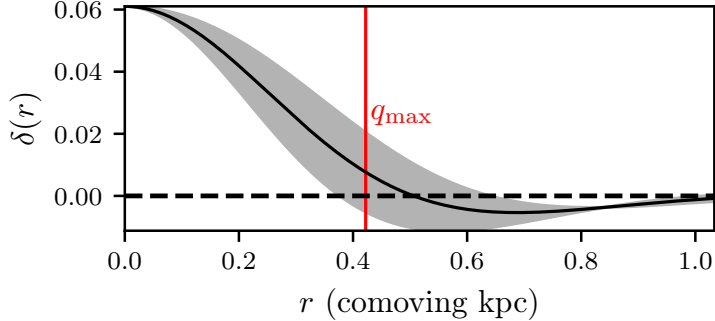
Figure 4.3: The radial profile of a density peak drawn from the $w = 0.3$ power spectrum at redshift $z = 10^6$. The peak is ellipsoidal, and the shading indicates the variation in the profile along different axes. The vertical line marks $q_{\max}$ computed using the turnaround model (Sec. 4.4.1).

Fig. 4.3. This peak represents a typical 3σ peak drawn from the $w = 0.3$ power spectrum using the statistics of peaks as described in Ref. [269]. The shallowing of this profile toward $r = 0$ is associated with the absence of small-scale fluctuations, and this is the single feature common to density peaks drawn from all of the power spectra we are studying. Indeed, it has been suggested that this feature is responsible for the development of the $\rho \propto r^{-3/2}$ profile [261].

Figure 4.4 shows the halo resulting from this initial peak in the moments after collapse. We also compute the expected collapse time from the initial peak using both the spherical collapse model, $\delta(a_{\mathrm{sc}}) = 1.686$, and the ellipsoidal collapse model described in Ref. [373]. The redshifts z_{sc} and z_{ec} of spherical and ellipsoidal collapse, respectively, are indicated in Fig. 4.4. The critical observation is that the $\rho \propto r^{-3/2}$ asymptote of the density profile develops almost immediately after collapse, matching closely the late-time density profile as early as $a \simeq 1.15 a_{\mathrm{ec}}$. Subsequently, the profile grows outward in radius alone, gradually steepening as accretion of new material slows. The interval $\Delta a/a \simeq 0.15$ over which the profile develops is not arbitrary. The characteristic dynamical time $\Delta t = \sqrt{3\pi/(16G\rho)}$ [392] of a virialized region with density 200 times the background is $\Delta t = 0.16/H$, where H is the Hubble rate. This interval corresponds to $\Delta a/a = 0.16$, implying that the inner density profile develops over a single dynamical time interval.

4.3.1 Spherical collapse

The rapid development of a halo's inner $\rho = A r^{-3/2}$ profile implies that the coefficient A can only be influenced by the immediate neighborhood of the precursor density peak. To make this

69
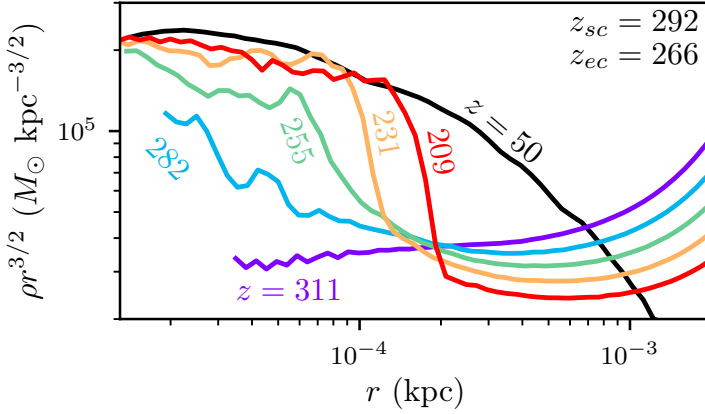
Figure 4.4: The density profile of the resulting halo during and after collapse of the peak in Fig. 4.3. The numbers denote the redshifts z at which the density profile is plotted, while z_{sc} and z_{ec} are the redshifts of spherical and ellipsoidal collapse, respectively, computed from the initial peak. The black curve shows the density profile long after collapse.
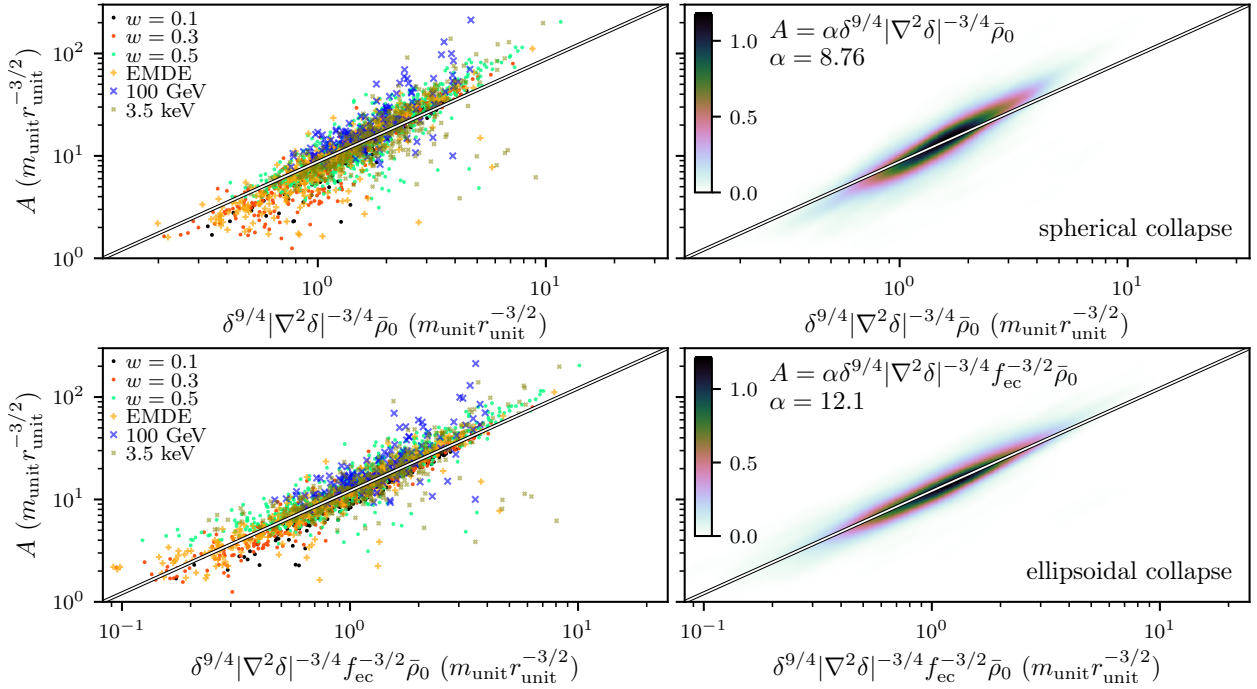
Figure 4.5: The coefficient A of the $\rho = Ar^{-3/2}$ density profile asymptote, plotted against the prediction from our models. Top: The spherical model, Eq. (4.5). Bottom: The ellipsoidal model, Eq. (4.7). The left panels plot all of the halos, while the right panels plot a density estimate: the color scale indicates the density $f(\ln A, \ln A_{\mathrm{pred}})$ of the distribution, where A_{pred} is the x-axis quantity. We also plot the line corresponding to the median proportionality constant for each model.

argument precise, we define[12]

$$\tilde{\delta}(\boldsymbol{x}) \equiv \delta(\boldsymbol{x}, a)/a, \tag{4.4}$$

where $\delta(\boldsymbol{x}, a)$ is evaluated using linear theory during matter domination (when $\delta \propto a$). Here, $\boldsymbol{x}$ is a comoving coordinate, and we define $a = 1$ today. We now claim that the inner $\rho \propto r^{-3/2}$ asymptote is only sensitive to the local properties $\tilde{\delta}$ and $\partial_i \partial_j \tilde{\delta}$ of the precursor density peak. If we neglect deviations from spherical symmetry, the peak reduces to two parameters: its amplitude $\tilde{\delta}$ and curvature $|\nabla^2 \tilde{\delta}|$. During matter domination, spherical collapse theory implies that $a_{\rm sc} \propto \tilde{\delta}^{-1}$. Meanwhile, $|\nabla^2 \tilde{\delta}|$ defines a comoving length scale $q_{\rm pk} \equiv (\tilde{\delta}/|\nabla^2 \tilde{\delta}|)^{1/2}$ associated with the peak. At the time of collapse, this comoving length corresponds to the physical length scale $a_{\rm sc} q_{\rm pk} \propto (\tilde{\delta}|\nabla^2 \tilde{\delta}|)^{-1/2}$. There is also a physical density scale $\bar{\rho}_0 a_{\rm sc}^{-3} \propto \bar{\rho}_0 \tilde{\delta}^3$, i.e., the cosmological background density at collapse. If these are the only scales, then up to a constant coefficient, there is a unique prediction for the coefficient A of the $\rho = A r^{-3/2}$ asymptote of the density profile,

$$A = \alpha \bar{\rho}_0 \delta^{9/4} |\nabla^2 \delta|^{-3/4}, \tag{4.5}$$

where α is a proportionality constant. We omit the tildes in Eq. (4.5), but all quantities related to the linear density field are understood to be evaluated on $\tilde{\delta}(\boldsymbol{x})$. This convention applies to the remainder of this work. The parameter α must be calibrated by simulations, but this calibration is only necessary once; it should be the same for any power spectrum.

We test this model on the $N_A^{<3\rm MM}$ peak-matched halos in each simulation that have well-resolved inner density profiles and underwent fewer than three major mergers (see Sec. 4.2). For these halos, Fig. 4.5 plots the left-hand side against the right-hand side of Eq. (4.5) in order to test the model. Evidently, our model works well for how simple it is, predicting the asymptotes with reasonable success in all six simulations. There does, however, appear to be a correlated effect wherein halos with the densest predicted asymptotes tend to exceed that prediction, and vice versa at the less dense end. In fact, this effect is caused by the assumption of spherical collapse. Peaks of smaller

---

[12]After this section, we will omit the tilde, and any quantity related to the linear density field should be understood to be evaluated on the scaled linear density field $\tilde{\delta}(\boldsymbol{x})$ unless otherwise specified.
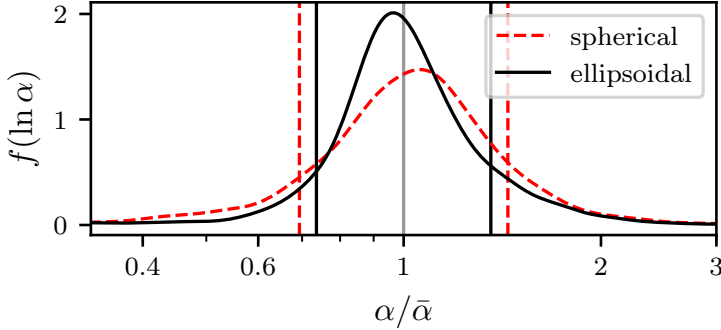
Figure 4.6: A comparison of the scatter from the two asymptote models. For each model, we plot a histogram of the coefficient α between the asymptote A and its model prediction, scaled to the mean coefficient for all halos. Vertical lines mark 1σ deviations from the mean, computed in log space.

amplitude tend to be less spherical, thereby collapsing later and forming less dense halos than their amplitude would suggest. We next account for this effect.

4.3.2 Ellipsoidal collapse

Equation (4.5) neglects deviations from spherical symmetry. However, it can be immediately generalized in the following way. Since $A \propto a_{\text{sc}}^{-3/2}$, we can use the theory of ellipsoidal collapse [373, 374, 384] to predict how the three-dimensional shape of a peak alters its collapse time. In particular, ellipsoidal collapse occurs later than spherical collapse by a factor $f_{\text{ec}}(e, p) \equiv a_{\text{ec}}/a_{\text{sc}}$, which is a function of the ellipticity e and prolateness p of the gravitational potential ϕ in the vicinity of the peak (see Appendix C.2 for definitions). To compute f_{ec}, we use the approximation [373]

$$f_{\text{ec}}(e, p) = 1 + 0.47 \left[5(e^2 - p|p|) f_{\text{ec}}^2(e, p) \right]^{0.615}. \tag{4.6}$$

Accounting for ellipsoidal collapse,

$$A = \alpha \bar{\rho}_0 \delta^{9/4} |\nabla^2 \delta|^{-3/4} f_{\text{ec}}^{-3/2}(e, p), \tag{4.7}$$

where α is a proportionality constant.

Figure 4.5 compares the predicted asymptotes in the ellipsoidal collapse model to their measured values. The correlated scatter associated with the spherical model is no longer apparent, confirming that the spherical collapse assumption was the source. Figure 4.6 compares the overall scatter between these two models; the ellipsoidal collapse model is clearly superior. We remark that not

all of the scatter depicted is physical; there is numerical noise in our simulated density profiles and finite density grids. Nevertheless, there are still clear sources of physical scatter. Absent an understanding of why the $\rho \propto r^{-3/2}$ profile develops, we constructed our model using purely scaling arguments, and these arguments can break down in two ways. First, the inner profile does not develop instantly, so it is sensitive to a small region about the density peak instead of only its immediate neighborhood. Also, as depicted in Fig. 4.4, the inner asymptote is not completely static but instead grows marginally after it develops, implying that it exhibits some sensitivity to the larger density field. Second, we only accounted for nonspherical peak shapes by altering the time of collapse. The sensitivity of the asymptotic coefficient A to the shape of the peak may be more complicated.

Nevertheless, it is a significant success to obtain a mere approximately 30% scatter across such a broad range of cosmologies from a model as simple as the one presented here. The proportionality coefficients and their statistics for our models are summarized in Table 4.3. Thus calibrated, the model developed in this section may be employed to predict the inner asymptotes of the first halos' density profiles in any cosmological scenario.

4.4 Density profile at large radii

We next study the density profile beyond the inner $\rho \propto r^{-3/2}$ asymptote. These larger radii, containing the bulk of the halo mass, are relevant to gravitational lensing signatures as well as to the dynamical evolution of the halo through mergers and tidal stripping. In this section, we discuss and validate models that can predict the density profile at large radii. We focus on three physical models:

(1) a "turnaround" model, tracing back to Ref. [355], in which each mass shell freezes at a fraction of its turnaround radius, or the radius of first apocenter;

(2) a "contraction" model, expressed most concisely by Ref. [362], that accounts for contraction of halo particle orbits due to subsequent infall;

(3) a "virialization" model, put forward by Ref. [371], in which the final radius of a mass shell is determined by enforcing that the shell's enclosed energy be distributed according to the virial theorem.

All of these models rely on the assumption that material is accreted gradually. Hence, they are not applicable to the density profiles at small radii, and none of them predicts the $\rho \propto r^{-3/2}$

asymptote. We will explore in Sec. 4.4.4 precisely where these models are accurate. In the meantime, we validate and tune the models by using them to predict the radius r_{max} at which the halo's circular velocity is maximized along with the mass $M(r_{\mathrm{max}})$ within this radius. The maximum circular velocity itself follows as $v_{\mathrm{max}} = \sqrt{GM(r_{\mathrm{max}})/r_{\mathrm{max}}}$.

The radius r_{max} characterizes where the profile bends away from its inner asymptote.[13] It is more common in the literature to study the scale radius r_s, often defined to be where $\mathrm{d}\ln\rho/\mathrm{d}\ln r = -2$, instead of r_{max}, which is where $\mathrm{d}\ln M/\mathrm{d}\ln r = 1$. However, we favor r_{max} over r_s for several reasons. First, r_{max} can be read from a simulation more robustly than r_s, since the mass profile is less noisy than the density profile. Second, r_{max} turns out to be cleaner to predict from the linear density field. Finally, since r_{max} characterizes the total mass rather than the local density, it is the more relevant quantity for understanding halo dynamics [385] and for predicting gravitational lensing signatures. The combination of A and r_{max} serves to mostly characterize the density profile of a halo, and the mass $M(r_{\mathrm{max}})$ (or velocity v_{max}) supplies an additional constraint.

4.4.1 Turnaround

To develop a model that can predict the full density profile of a collapsed halo, we must relate this profile to the spherically averaged fractional density excess profile $\delta(q)$, where q is the comoving radius, about the corresponding peak in the linear density field. Following the convention established in Sec. 4.3, we define $\delta(q) \equiv \delta(q, a)/a$ evaluated in linear theory during matter domination (with $a = 1$ today). We will also use

$$\Delta(q) = \frac{3}{q^3} \int_0^q \delta(q') q'^2 \mathrm{d}q', \tag{4.8}$$

the fractional enclosed mass excess defined under the same convention. As in Ref. [355], we consider the simplified spherical infall model in which each spherical shell freezes at a fixed fraction of its turnaround radius. A mass shell initially at comoving radius q turns around at physical radius $r_{\mathrm{ta}} = (3/5)q/\Delta(q)$. Hence, the final physical radius r of this shell is

$$r = \beta q/\Delta(q), \tag{4.9}$$

---

[13]For example, if $\rho(r) = \rho_s (r/r_s)^{-3/2}(1 + r/r_s)^{-3/2}$ [226, 278] (where ρ_s and r_s are scale parameters), $r_{\mathrm{max}} = 1.055 r_s$.

where β is a proportionality constant to be measured in simulations. But in this model, mass shells never cross, so the mass enclosed within this shell, now at r, is still

$$M(q) = \beta_M \frac{4\pi}{3} q^3 \bar{\rho}_0 \qquad (4.10)$$

(at zeroth order in Δ) with $\beta_M = 1$. This equation gives the mass profile $M(r)$ of the collapsed halo if q is obtained from r by inverting Eq. (4.9).

To find $r_{\max}$ (up to the proportionality constant β), we may maximize $M(r)/r$. Alternatively, we can write

$$\frac{\mathrm{d}\ln M}{\mathrm{d}\ln r} = \frac{3}{1 + 3\epsilon(q)}, \qquad (4.11)$$

where we define[14]

$$\epsilon(q) \equiv -\frac{1}{3}\frac{\mathrm{d}\ln\Delta}{\mathrm{d}\ln q} = 1 - \frac{\delta(q)}{\Delta(q)}. \qquad (4.12)$$

In this case, $r_{\max}$ is obtained as the solution to $\mathrm{d}\ln M/\mathrm{d}\ln r = 1$ or, equivalently, $\epsilon(q_{\max}) = 2/3$ with $r_{\max}$ computed from $q_{\max}$ using Eq. (4.9).

This model, at first glance, seems to be far divorced from a realistic description. However, it turns out to be a reasonable approximation of late accretion. At late times, halo density profiles are stable in time; see, e.g., Chapter 2. This observation is explained by noting that once the halo is established and accretion begins to slow, newly accreted mass only contributes significantly to the outskirts of the halo; there is too little new matter, spending too small a fraction of its orbital period at small radii, to substantially raise the interior density. Since the density profile is static, a newly accreted particle settles into a stable orbit with time-averaged radius proportional to its orbital apocenter, the turnaround radius.[15] The final radius in this model is to be understood as that orbital average.

We test this model on the N_r peak-matched halos for which $r_{\max} < r_{\mathrm{vir}}$ (see Sec. 4.2). In the top panel of Fig. 4.7, we plot the measured $r_{\max}$ against the prediction from this model. The model

---

[14]We define $\epsilon(q)$ as a generalization of the index ϵ of $\delta M/M \propto M^{-\epsilon}$ in the self-similar theory [253]. Consequently, Eq. (4.11) has exactly the same form as its analogue in the self-similar theory.

[15]The orbital apocenter actually decays over time, an effect for which the contraction model accounts.

Figure 4.7: For the turnaround model, this figure plots the values of $r_{\max}$ measured in our simulations against the predicted values. For visual reference, an example proportionality curve is plotted (not a fit). The model dramatically overpredicts $r_{\max}$ for a subpopulation of the halos, a problem that we attribute to the finite time at which the simulated density profiles are measured (see the text).

appears to work well for the bulk of the halos. However, there is a significant population of halos, especially coming from the broader 100 GeV, 3.5 keV, EMDE, and $w = 0.5$ power spectra, for which the predicted $r_{\max}$ is much larger than the measured value. In fact, in these simulations, there are many peaks for which the mass shell with $\epsilon = 2/3$ has not yet accreted onto the halo by the final redshift. In these cases, it makes no sense to use the properties of this shell to predict $r_{\max}$.

A minimal correction, for these halos, is to instead relate $r_{\max}$ to the outer boundary of the halo. In the spherical collapse model, a mass shell virializes when it falls to half of its turnaround radius; at this point, its energy is distributed according to the virial theorem. The halo's outer boundary may be taken to be the physical radius of the last shell to virialize in this way, and we define q_v to be the Lagrangian radius of this shell. If we are considering the halo population at scale factor a, then q_v is the smallest q that satisfies $\Delta(q, a) = a\Delta(q) \leq \delta_v$, where $\delta_v = 1.583$. If $r_{\max}$ is proportional to the halo boundary so defined, then

$$r_{\max} = \beta' q_v / \Delta(q_v), \tag{4.13}$$

where β' is another proportionality constant, and this model is understood to apply only to the halos of which the $\epsilon = 2/3$ mass shells have not yet virialized, i.e., $q_{\max} > q_v$. In Fig. 4.8, we plot the turnaround model for only those halos of which the $\epsilon = 2/3$ shells have virialized, separately plotting the q_v model for the remainder of the halos. Evidently, the halos of which the $\epsilon = 2/3$ shells had not yet virialized were indeed the population of which the $r_{\max}$ was severely overpredicted, and the $\epsilon = 2/3$ model exhibits significantly less scatter with them excluded. Meanwhile, using q_v to
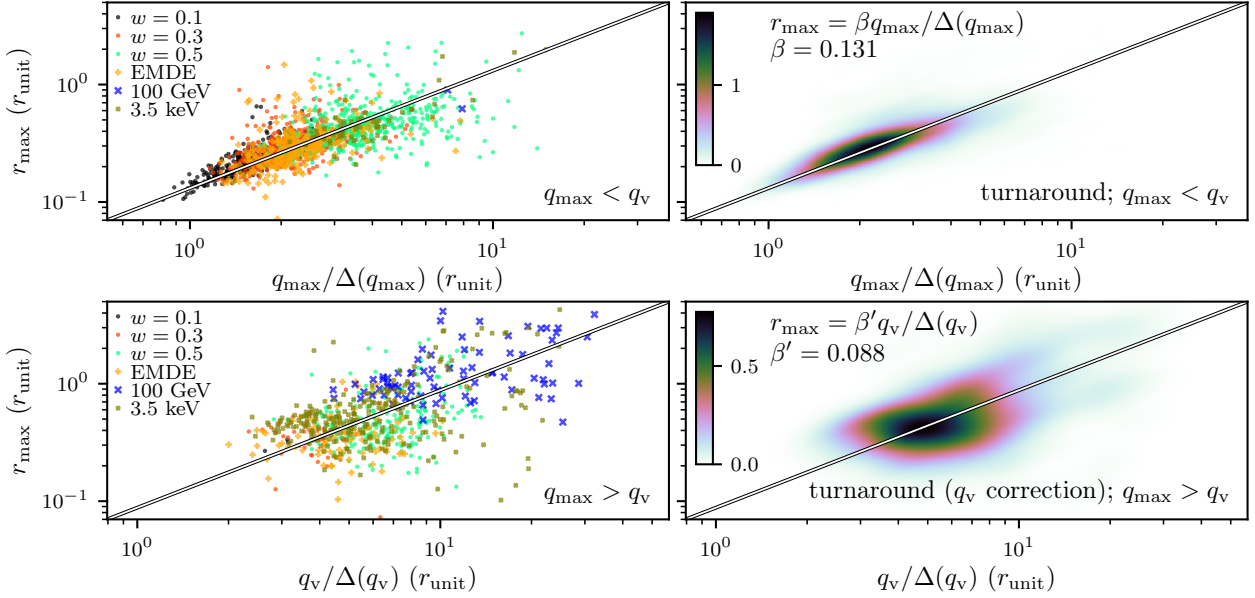
Figure 4.8: For the corrected turnaround model, we plot the values of r_{max} measured in our simulations against the predicted values. At the top, we show the turnaround model with halos with $q_{\text{max}} > q_{\text{v}}$ excluded, while at bottom, we use q_{v} to predict r_{max} for the previously excluded halos. This separation corrects the discrepancy seen in Fig. 4.7. The left panels plot all of the halos, while the right panels show density estimates; the color scale indicates the density $f(\ln r_{\text{max}}, \ln r_{\text{max,pred}})$ of the distribution, where $r_{\text{max,pred}}$ is the x-axis quantity. The solid line corresponds to the median proportionality constant.

predict r_{max} for these halos works reasonably well, although the scatter here is significantly larger. The top panel of Fig. 4.9 depicts these differences in scatter more transparently.

Finally, we test how well this model predicts $M(r_{\text{max}})$ in similar fashion by using Eq. (4.10) and allowing β_M to float. In this case, we employ the $N_r^{<3\text{MM}}$ halos with $r_{\text{max}} < r_{\text{vir}}$ that also underwent fewer than three major mergers (see Sec. 4.2). As above, we set $q = q_{\text{max}}$ when $q_{\text{max}} < q_{\text{v}}$ and $q = q_{\text{v}}$ otherwise. The bottom panel of Fig. 4.9 shows the scatter in these predictions. For both r_{max} and $M(r_{\text{max}})$, Table 4.3 lists the tuned coefficients β and β_M and their statistics.

4.4.2 Contraction

The turnaround model assumed that each new shell freezes at a fixed fraction of its turnaround radius, contributing mass to that radius alone. In reality, a shell contributes mass to a large range of radii. Figure 4.10 shows the density profiles[16] laid down by a range of initial mass shells. These shells

---

[16]This figure depicts a halo that collapsed from an isolated 3σ peak drawn from the $w = 0.3$ power spectrum. This peak was simulated with about 70 million particles in a comoving vacuum-bounded sphere of radius 1 kpc.
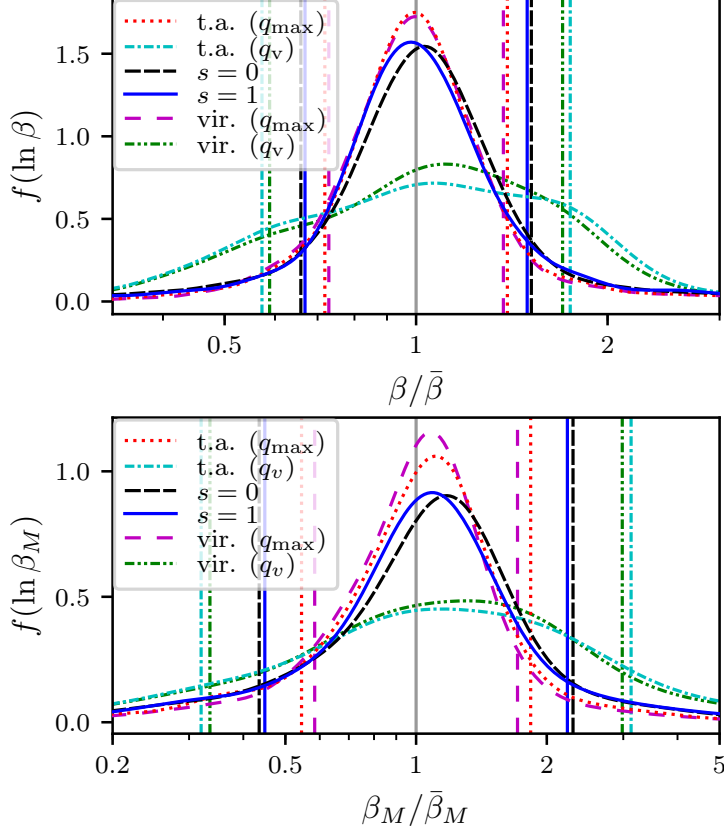
Figure 4.9: Comparisons of the scatter in the r_{max} (top) and $M(r_{max})$ (bottom) predictions. For each model, we plot the distribution of the coefficient β or β_M between the halo quantity and its model prediction, scaled to the mean coefficient for all halos. "t.a. (q_{max})" and "t.a. (q_v)" denote the turnaround models using q_{max} and q_v and applied only to halos with $q_{max} < q_v$ and $q_{max} > q_v$, respectively. "$s = 0$" and "$s = 1$" denote the respective contraction models. "vir. (q_{max})" and "vir. (q_v)" denote the virialization models using q_{max} and q_v and applied only to halos with $q_{max} < q_{ta}$ and $q_{max} > q_{ta}$, respectively. Note that the contraction models have more scatter than the turnaround and virialization (q_{max}) models only because the latter describe a smaller range of halos; see the footnotes in Table 4.3.

consist of successive factors of 1.5 in initial radius, so that the lowest shell contains the mass initially in the comoving radius band 0.044 to 0.066 kpc; the second shell contains the mass initially in the band 0.066 to 0.10 kpc; and so on. Notably, each shell has a characteristic radius within the final halo below which it contributes roughly constant density. As Ref. [362] argues, the constant-density contribution follows from the notion that particles from large-radius mass shells cross the lower radii at such high velocity that their motions are effectively unaccelerated.

Consider a halo particle initially orbiting with apocenter radius r that encloses halo mass $M(r)$. As time goes on, newly accreted shells contribute to the enclosed mass, increasing $M(r)$. In a
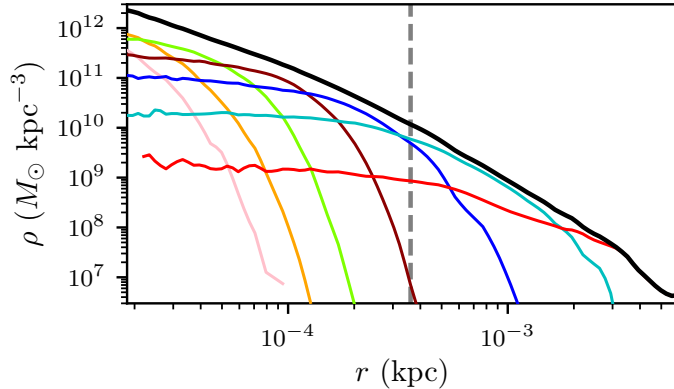
Figure 4.10: The density profile of a halo (black curve) along with the density profiles contributed by different initial mass shells (colored curves). The lowest shell contains the mass initially in the comoving radius band 0.044 to 0.066 kpc, the second shell corresponds to the band 0.066 to 0.10 kpc, and so on. The dashed vertical line marks r_{max}.

spherically symmetric and self-similar system, the quantity $\oint v_r dr \propto [M(r)r]^{1/2}$ is an adiabatic invariant, implying that as the enclosed mass grows r shrinks as $r \propto 1/M(r)$. While the quantity Mr need not be conserved in a more general picture, Ref. [364] found that it remains nearly invariant for each particle even with spherical symmetry relaxed.

For a mass shell with apocenter r', let $f(r, r')$ be the fraction of the shell's mass that is within r. It is readily seen that the mass enclosed within a shell with Lagrangian radius q and final apocenter $r(q)$ increases by the factor

$$X(q) \equiv 1 + \frac{3}{q^3} \int_q^{q_{\mathrm{v}}} q'^2 \mathrm{d}q' f\left[r(q), r(q')\right] . \tag{4.14}$$

due to the contribution of shells with $q' > q$. As before, q_{v} is the Lagrangian radius of the latest shell to virialize; it is the smallest q that satisfies $a\Delta(q) \leq \delta_v$, where a is the scale factor at which we wish to characterize the halo population (and $a = 1$ today). If orbital apocenters shrink according to $r \propto 1/M$, then

$$r(q) = \beta \frac{q}{\Delta(q)} \frac{1}{X(q)} \tag{4.15}$$

describes the apocenter of the q shell after contraction, with $\beta = 3/5$.

As a simple model, let us assume that each shell contributes density $\rho(r) \propto r^{-s}$ below its apocenter radius and 0 above it, so $f(r, r') = (r/r')^{3-s}$. With this shell profile, Eq. (4.14) yields the
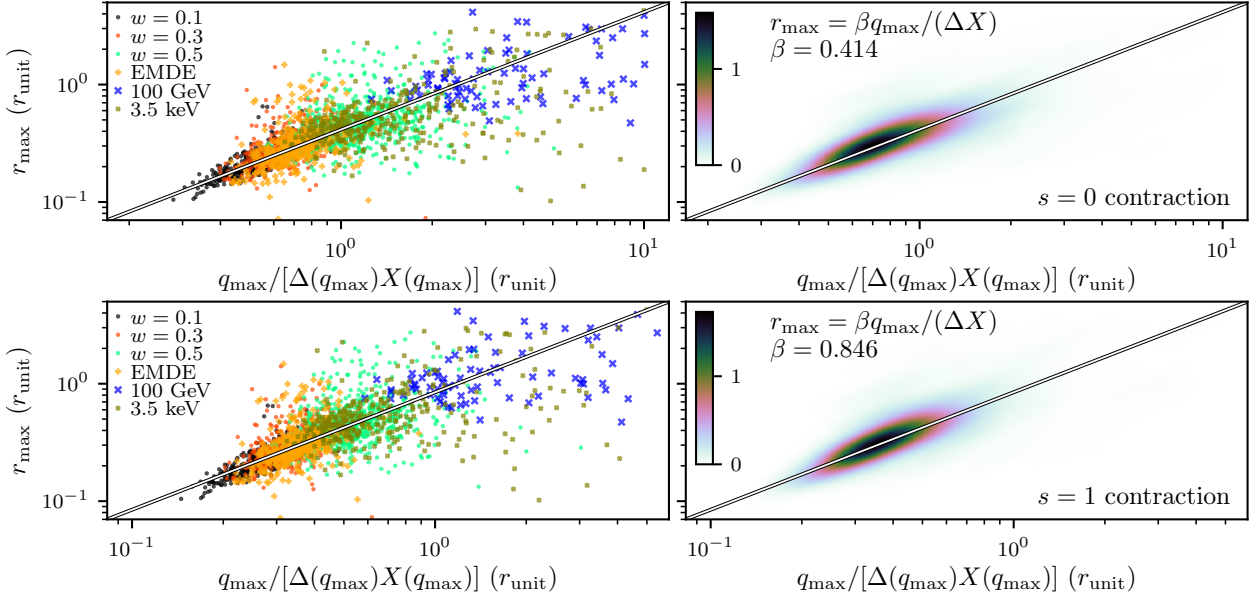
Figure 4.11: For the $s = 0$ (top) and $s = 1$ (bottom) contraction models, this figure plots the values of r_{max} measured in our simulations against the predicted values. The left panels plot all of the halos, while the right panels show density estimates; the color scale indicates the density $f(\ln r_{\mathrm{max}}, \ln r_{\mathrm{max,pred}})$ of the distribution, where $r_{\mathrm{max,pred}}$ is the x-axis quantity. The solid line corresponds to the median proportionality constant.

ordinary differential equation

$$\frac{\mathrm{d}\ln X}{\mathrm{d}\ln q} = -\frac{3 - [3(3-s)\epsilon(q) - s](X-1)}{1 + (4-s)(X-1)} \tag{4.16}$$

with initial condition $X(q_{\mathrm{v}}) = 1$. This equation is equivalent to the simpler expression in Ref. [362], but since it is expressed with respect to the variable q, it is more straightforward to integrate over a numerically tabulated peak profile $\epsilon(q)$. The enclosed mass profile after contraction is now

$$M(q) = \beta_M (4\pi/3) q^3 \bar\rho_0 X(q) \tag{4.17}$$

(to zeroth order in Δ) with $\beta_M = 1$. Note that X ranges from 1 (at q_{v}) to $\mathcal{O}(10)$. Using these equations, one may maximize $M(q)/r(q)$ to obtain q_{max}, after which r_{max} and $M(r_{\mathrm{max}})$ are obtained immediately. Alternatively,

$$\frac{\mathrm{d}\ln M}{\mathrm{d}\ln r} = \frac{3 + \mathrm{d}\ln X/\mathrm{d}\ln q}{1 + 3\epsilon(q) - \mathrm{d}\ln X/\mathrm{d}\ln q} \tag{4.18}$$

with $\mathrm{d}\ln X/\mathrm{d}\ln q$ given in Eq. (4.16), so one may solve $\mathrm{d}\ln M/\mathrm{d}\ln r = 1$ to obtain q_{max}. Finally,

since we do not expect to employ the correct form of $f(r, r')$, we will allow β and β_M to vary, tuning them to simulations.

We test the contraction model using $s = 0$ as well as $s = 1$. While Fig. 4.10 suggests that $s = 0$ at small radii, a nonzero choice of s is motivated by noting that for a given mass shell q most of the enclosed mass contributed by higher shells comes from shells just slightly above q. Meanwhile, Fig. 4.10 shows that the density profile contributed by a mass shell does not level off to a constant value until well below its apocenter radius. Therefore, the bulk of the mass contribution comes from shell density profiles $\rho \propto r^{-s}$ with $s > 0$. The particular choice $s = 1$ is partly arbitrary, but it is roughly the slope of the shell profiles in Fig. 4.10 slightly below their apocenters.[17]

Figure 4.11 plots $r_{\max}$ against its model prediction for both contraction models using the N_r halos with $r_{\max} < r_{\mathrm{vir}}$. Both models successfully predict, with some scatter, the values of $r_{\max}$ for the halos in all six simulations. In fact, both models work equally well, as Fig. 4.9 demonstrates. Moreover, comparing the results of these models to those of the turnaround models, which used the $\epsilon = 2/3$ or q_{v} shells to predict $r_{\max}$, we see that the main difference is that the contraction models can handle all of the halos in a single model requiring just one tuned parameter. Adiabatic contraction can produce a bend in the density profile, and hence an $r_{\max}$, near the halo outskirts because the outskirts are uncontracted while the rest of the halo is contracted. Other than this, there is no significant advantage to the contraction models for predicting $r_{\max}$, as the top panel of Fig. 4.9 shows.

We also use the $s = 0$ and $s = 1$ contraction models to predict $M(r_{\max})$ using Eq. (4.17) with β_M allowed to float. For this test, we employ the $N_r^{<3\mathrm{MM}}$ halos with $r_{\max} < r_{\mathrm{vir}}$ that underwent fewer than three major mergers. The scatter in these predictions is depicted in the bottom panel of Fig. 4.9. The tuned values of β and β_M and their statistics are listed in Table 4.3.

4.4.3 Virialization

Reference [371] developed a model for halo density profiles in which a mass shell freezes where its enclosed energy is virialized.[18] In this model, the final radius of the q shell is $r(q) =$

---

[17]The choice $s = 1$ also corresponds roughly to the $\rho^{1/2}$ model in Ref. [362], since ρ is approximately proportional to r^{-2} at $r = r_{\max}$.

[18]Note that a model in which a shell freezes where *its own* energy is virialized is equivalent to the turnaround model above.
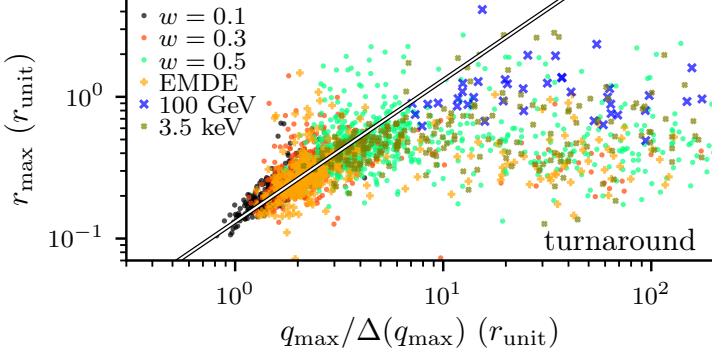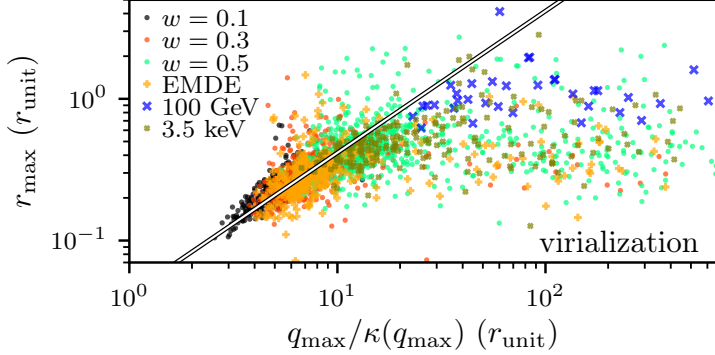
Figure 4.12: For the virialization model, this figure plots the values of r_{max} measured in our simulations against their predicted values. For visual reference, an example proportionality curve is plotted (not a fit). Like the turnaround model, this model dramatically overpredicts r_{max} for a subpopulation of the halos, a discrepancy that can be corrected in a similar fashion (see the text).

$-(3/10)GM(q)^2/E(q)$, where $M(q)$ and $E(q)$ are, respectively, the mass and energy enclosed within the q shell in the linear density field. This model may be expressed as

$$r(q) = \beta \frac{q}{\kappa(q)}, \quad \kappa(q) \equiv \frac{2}{q^5} \int_0^q q'^4 dq' \Delta(q') \tag{4.19}$$

with $\beta = 3/10$ and $M(q)$ defined as in Eq. (4.10). For this model, $d \ln M/d \ln r = 3/[6 - 2\Delta(q)/\kappa(q)]$. As before, q_{max} is obtained by maximizing $M(q)/r(q)$ or by solving $d \ln M/d \ln r = 1$. We test this model in a similar fashion, allowing β to float and plotting in Fig. 4.12 the simulated r_{max} against the model prediction (using the N_r halos with $r_{max} > r_{vir}$). Evidently, this model performs similarly to the turnaround model. Again, there is a multitude of halos of which the q_{max} shells have not yet accreted, leading to dramatically overpredicted values of r_{max}. In this case, the $q_{max} < q_v$ condition turns out to be too restrictive; it eliminates too many halos. Instead, we require $q_{max} < q_{ta}$, where q_{ta} is Lagrangian radius of the last shell to turn around. In particular, q_{ta} is the smallest q satisfying $a\Delta(q) \leq \delta_{ta}$, where $\delta_{ta} = 1.062$ and a is the scale factor at which we are studying the halo population. If $q_{max} < q_{ta}$, we use q_{max} to predict r_{max} using Eq. (4.19); otherwise, we use q_v to predict r_{max} using Eq. (4.13). We also use this model to predict $M(r_{max})$ in a similar fashion (again using the $N_r^{<3MM}$ halos that also underwent fewer than three major mergers), allowing β_M to float. The scatter and

82

Table 4.3: A summary of the predictive models along with their simulation-tuned coefficients. In each model, the halo quantity is proportional to the peak quantity with the given coefficient between them. The mean and rms deviation σ in the proportionality coefficient are computed in log space. We express the spread as a ratio: in particular, the middle 50% spread is the ratio between the 75th and 25th percentiles, while the 1σ spread is the ratio corresponding to the log-space σ. We also list the number of halos contributing to the coefficient statistics.

Halo quantity	Peak quantity	Model[a]	median coef.	mid. 50% spread	mean coef.	1σ spread	sample size	section ref.
A	$\bar{\rho}_0\delta^{9/4}\lvert\nabla^2\delta\rvert^{-3/4}$	SC	8.76	1.43	8.50	1.44	2451	4.3.1
A	$\bar{\rho}_0\delta^{9/4}\lvert\nabla^2\delta\rvert^{-3/4}f_{\mathrm{ec}}^{-3/2}$	EC	12.1	1.31	12.2	1.36	2450[b]	4.3.2
$r_{\max}$	$q_{\max}/\Delta(q_{\max})$	TA, $q_{\max} < q_{\mathrm{v}}$	0.131	1.34	0.132	1.39	1759	4.4.1
$r_{\max}$	$q_{\mathrm{v}}/\Delta(q_{\mathrm{v}})$	TA, $q_{\max} > q_{\mathrm{v}}$	0.088	2.18	0.085	1.75	712	4.4.1
$r_{\max}$	$\frac{q_{\max}}{\Delta(q_{\max})X(q_{\max})}$	$s = 0$ AC	0.414	1.40[c]	0.406	1.52	2471	4.4.2
$r_{\max}$	$\frac{q_{\max}}{\Delta(q_{\max})X(q_{\max})}$	$s = 1$ AC	0.846	1.39[d]	0.848	1.49	2471	4.4.2
$r_{\max}$	$q_{\max}/\kappa(q_{\max})$	Vir., $q_{\max} < q_{\mathrm{ta}}$	0.042	1.36	0.042	1.37	1578	4.4.3
$r_{\max}$	$q_{\mathrm{v}}/\Delta(q_{\mathrm{v}})$	Vir., $q_{\max} > q_{\mathrm{ta}}$	0.092	1.95	0.087	1.70	893	4.4.3
$M(r_{\max})$	$(4\pi/3)q_{\max}^3\bar{\rho}_0$	TA, $q_{\max} < q_{\mathrm{v}}$	0.273	1.64	0.258	1.84	1514	4.4.1
$M(r_{\max})$	$(4\pi/3)q_{\mathrm{v}}^3\bar{\rho}_0$	TA, $q_{\max} > q_{\mathrm{v}}$	0.134	2.97	0.123	3.13	639	4.4.1
$M(r_{\max})$	$(4\pi/3)q_{\max}^3\bar{\rho}_0 X(q_{\max})$	$s = 0$ AC	0.441	1.76	0.396	2.30	2153	4.4.2
$M(r_{\max})$	$(4\pi/3)q_{\max}^3\bar{\rho}_0 X(q_{\max})$	$s = 1$ AC	0.658	1.73	0.619	2.23	2153	4.4.2
$M(r_{\max})$	$(4\pi/3)q_{\max}^3\bar{\rho}_0$	Vir., $q_{\max} < q_{\mathrm{ta}}$	0.150	1.59	0.145	1.71	1341	4.4.3
$M(r_{\max})$	$(4\pi/3)q_{\mathrm{v}}^3\bar{\rho}_0$	Vir., $q_{\max} > q_{\mathrm{ta}}$	0.143	2.79	0.129	2.98	812	4.4.3

[a] Abbreviations refer to spherical collapse, ellipsoidal collapse, turnaround, adiabatic contraction, and virialization.

[b] One peak is so ellipsoidal that Eq. (4.6) has no solution, so this peak is discarded from analysis.

[c] The $s = 0$ coefficient has spread 1.33 and 1.74 over halos for which the turnaround model predicts $q_{\max} < q_{\mathrm{v}}$ and $q_{\max} > q_{\mathrm{v}}$, respectively, implying that the contraction model is superior or comparable to the turnaround model in both cases.

[d] Similarly, the $s = 1$ coefficient has spread 1.33 and 1.68 in these two cases.

statistics of these predictions[19] are shown in Fig. 4.9 and Table 4.3, and we find that this model's scatter is comparable to that of the turnaround model.

4.4.4 Discussion

Table 4.3 summarizes the $r_{\max}$ and $M(r_{\max})$ models and the statistics of their simulation-tuned parameters. Evidently, all of these models exhibit similar scatter. For instance, when $q_{\max} < q_{\mathrm{v}}$ or q_{ta}, each model's predicted $r_{\max}$ exhibits about 30% scatter in the middle half of its predictions. These similarities suggest there may be a statistical floor limiting the precision of all three models equally. We propose two sources of such a floor. The first is artificial discreteness noise in our simulations. As noted in Chapter 2, there is discreteness noise in each radial bin of the density profile that is significantly larger than Poisson noise and may be associated with the accretion of artificial fragments. Our procedure of averaging radial profiles over a finite time interval (see Appendix C.1)

---

[19]We remark that the optimal $\beta \simeq 0.042$ is much smaller than the exact value 3/10 claimed in Ref. [371].

mitigates but does not eliminate this noise.[20]

The other probable source of a statistical floor is physical and owes to a simplifying assumption common to all three models: spherical symmetry. Observe in Fig. 4.3 that at the initial radius of the q_{max} shell the density profile of the peak that is depicted—a typical peak drawn from the $w = 0.3$ power spectrum—is highly ellipsoidal. It is likely that a substantial fraction of the approximately 30% scatter in r_{max} results from deviations from spherical symmetry in the initial density peaks. To correct this, models must be employed that move beyond the assumption of spherically symmetric initial conditions, perhaps employing ellipsoidal collapse arguments [373, 374, 384] or drawing from nonspherical self-similar infall theory [363, 364]. The principal difficulty in moving beyond spherical symmetry is that the three-dimensional shape of a peak is different at each radius, an effect for which no model has accounted (to our knowledge). However, the spherical models presented here exhibit just approximately 30% scatter in r_{max} and approximately 60% scatter in $M(r_{max})$ over the full range of cosmologies we simulated, a success that should not be understated. As we will see in Sec. 4.5, halo mergers present a larger source of error.

Beyond predicting r_{max} and $M(r_{max})$ (or equivalently v_{max}), we may ask how well the spherical infall models can predict the full density profiles of the first halos. No model successfully predicts $\rho \propto r^{-3/2}$ at small radii[21], and this is not surprising because in the moments after halo collapse the accretion of new material is not adiabatic with respect to the orbits of the already bound material. Nevertheless, we may explore the radial range over which the spherical infall models do accurately predict the density profiles. Figure 4.13 compares the mass profiles of a small halo sample to their predicted profiles using the median proportionality coefficients in Table 4.3. Evidently, the turnaround and virialization models do not accurately predict the density profile below r_{max}, although they may succeed at larger radii. The $s = 0$ and $s = 1$ contraction models, and especially the latter, more accurately capture the shape of the profile at smaller radii. However, as shown

---

[20]There are other sources of discreteness noise in our analysis, but they are minor. The binning of our density profiles in factors of 1.1 introduces artificial scatter, but this scatter does not exceed 5% in r_{max} and is further reduced by our use of interpolation (see Appendix C.1). There is also noise in the predicted values of r_{max} because they arise from a finite density grid, but since q_{max} is typically much larger than a grid cell [so $\delta(q_{max})$ averages over a large number of cells], the resulting scatter is small.

[21]An $s = 3/2$ contraction model predicts $\rho \propto r^{-3/2}$ at small radii, but only in a contrived way; the adiabatic approximation is not valid when this part of the profile develops.
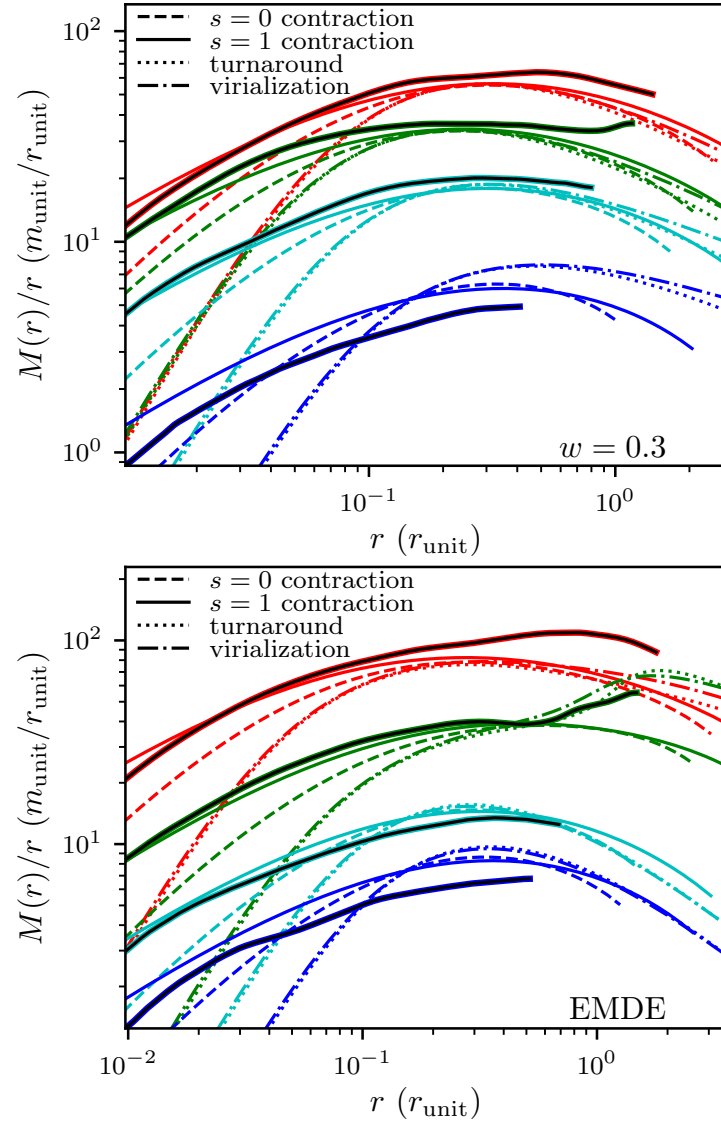
Figure 4.13: The mass profiles (thick, dark lines) of a few halos in the $w = 0.3$ (top) and EMDE (bottom) simulations compared to their model predictions (thin lines). This figure is intended to depict how the shapes of the profiles compare, so the sample was selected to have little discrepancy in the overall normalization of M/r. The simulated profiles are plotted out to their virial radii. The turnaround and virialization model predictions largely overlap.

in Fig. 4.10, the true density profile of a mass shell is more complicated than $\rho \propto r^{-s}$, so a more sophisticated model for a shell's density profile should yield still better results.

In this section, we presented models that can predict the outer portions of the density profiles of the first halos in any cosmology. While the models themselves are not new, our calibrations enable their use as predictive tools. Moreover, our simulations demonstrate the universality of these models by showing that they succeed across wildly dissimilar cosmological scenarios.

4.5 Predicting halo populations

So far, we have studied the relationship between a density peak and its resulting halo. However, our ultimate goal is to study the larger populations. Recall from Sec. 4.2 that not all peaks matched to halos in our simulations and not all halos matched to peaks. These discrepancies are reflected in Table 4.2 and may arise from physical processes, such as halo mergers, or numerical artifacts in our simulations. We have shown that if we know that a peak developed into a halo that persisted to some later redshift then we can predict the properties of that halo from the properties of the peak. Ultimately, however, we wish to predict an entire population of halos directly from a population of peaks. In light of the halo- and peak-count discrepancies, can our models proceed in this way?

4.5.1 Population comparisons

We first study the population of halos distributed in the asymptote A. In Fig. 4.14, we compare the entire halo population found in our simulations to the population predicted by accounting for every peak in the initial density fields that would have collapsed by simulation termination. We use the ellipsoidal collapse model. Generally, we see that for the narrower $w = 0.1$, $w = 0.3$, and EMDE power spectra the predicted population matches the simulated population reasonably well. In these scenarios, our model underpredicts halos at the low-density end, a surprising result that may be due to artificial fragmentation. In simulations with a small-scale power-spectrum cutoff (like ours; see Fig. 4.1), discreteness noise causes filamentary structures to fragment into halos even below the scales of the smallest density fluctuations. These halos have been shown to be unphysical simulation artifacts [389, 390], but they could contribute to the excess of less-dense halos in our simulations relative to model predictions in the cases of the narrower power spectra.

Otherwise, Fig. 4.14 shows a tendency for the model to overpredict halos at the middle-density range and underpredict at the highest-density range. This discrepancy can be attributed to mergers, for which our model does not account. Halo mergers reduce the number of halos while raising the

central density of the merger remnants. For the broader $w = 0.5$, 100 GeV, and 3.5 keV power spectra (bottom panel of Fig. 4.14), the merger-based discrepancy is amplified: the model underpredicts the densest halos and dramatically overpredicts the rest. Evidently, while our model can predict the density profiles of individual halos, an understanding of halo mergers is necessary to accurately predict halo populations in scenarios with more broadly supported power spectra. We will return to this point.

We next study the distribution in the radius r_{max}. Many of the simulated halos had $r_{\mathrm{max}} > r_{\mathrm{vir}}$, and while we discarded those halos from previous analyses, doing so now would alter the populations. Instead, we account for this problem here by substituting r_{vir} for r_{max} in those cases. As Fig. 4.15 shows, the $s = 0$ contraction model predicts the r_{max} distribution reasonably well for the narrow power spectra, with the bulk of the discrepancy arising from overprediction of the total halo count due to halo mergers. The predicted distributions are also more sharply peaked, an effect that may owe to the model's neglect of spherical asymmetry (see Sec. 4.4.4). For the broader power spectra, the halo count discrepancy is magnified due to the much larger frequency of mergers. However, unlike in the case of the asymptote A, we will soon see that the radius r_{max} does not significantly increase due to mergers beyond what the models already predict. Hence, there is no significant underprediction of the largest-radius halos.

We can also ask how well our models predict aggregate observational signals. If we assume that all halos have $\rho \propto r^{-3/2}$ inner density profiles, then the total dark matter annihilation rate in halos is proportional to the sum $\sum A^2$ over all halos.[22] In Table 4.4, we show how accurately the ellipsoidal collapse model predicts the aggregate annihilation signal. Remarkably, despite not accounting for halo mergers, we successfully predict the annihilation signal to within a factor of 1.3 for all simulations. The increased central density within merger remnants has compensated for the drop in halo count. One caveat is that in this calculation, we did not account for changes in the slope γ of the $\rho \propto r^{-\gamma}$ inner profile resulting from mergers. This change must be accounted for separately and will significantly reduce the annihilation signal (see Chapter 2).

We also consider an aggregate microlensing signal. The apparent image of a background star

---

[22]There is a logarithmic sensitivity to r_{max}, which we neglect. Also, note that there is a density cap imposed by annihilations [285], so the signal converges even for $\rho \propto r^{-3/2}$.
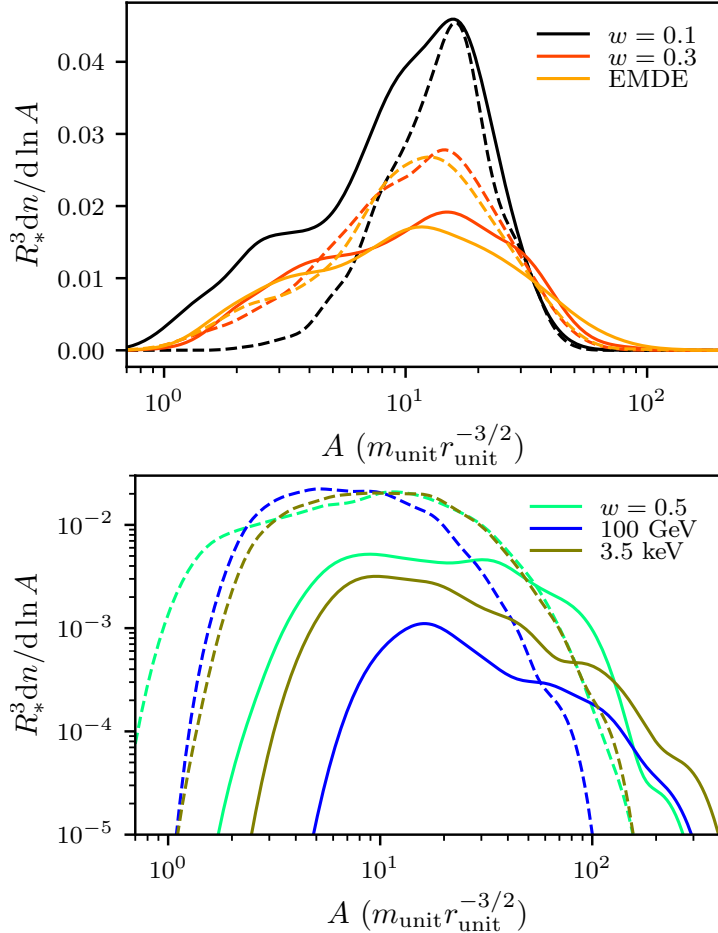
Figure 4.14: A comparison between the simulated halo population, as solid lines, and the population predicted from the peaks in the linear density field, as dashed lines, distributed in the inner asymptotic coefficient A. We use the ellipsoidal collapse model to predict A. Top: The three simulations with narrower power spectra. Bottom: The three simulations with broader power spectra. The vertical axis is logarithmic here to accommodate the differences in scale. We find that our model can capture halo populations arising from more narrowly supported power spectra, but it does not describe well the populations arising from broader power spectra because of the predominance of halo mergers in those scenarios.
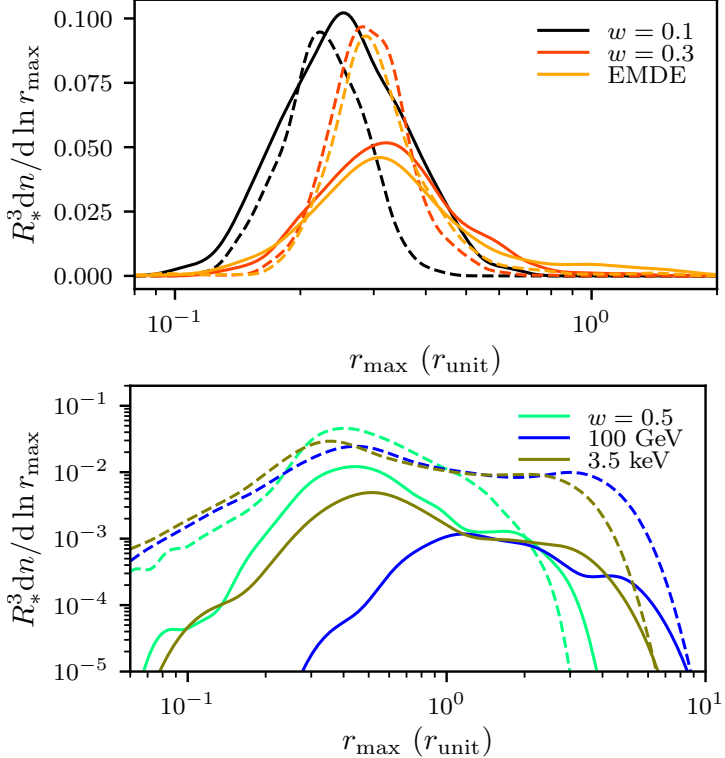
Figure 4.15: Similar to Fig. 4.14, but studying the halo population distributed in the radius $r_{\max}$ instead. We use the $s = 0$ contraction model. As in Fig. 4.14, we find that our model describes the halo populations arising from more narrowly supported power spectra with reasonable success, although the predicted distributions tend to be more sharply peaked. However, halo mergers greatly alter the halo populations in scenarios with broader power spectra.

is deflected by an angle proportional to $M_{2D}(\xi)/\xi$, where $M_{2D}(\xi)$ is the projected mass enclosed within impact parameter ξ. As an approximation, we claim that the deflection due to a halo is proportional to $M(r_{\max})/r_{\max}$ and a function related to the impact parameter. Integrating over impact parameters introduces a factor $r_{\max}^2$, the characteristic area of the halo. Hence, for a halo population, the aggregate lensing signal, considered as the expected deflection of a given image, is proportional to $\sum M(r_{\max}) r_{\max}$ summed over all halos.

In Table 4.4, we show how accurately the $s = 0$ contraction model predicts this signal. We find that our models predict the lensing signal significantly worse than the annihilation signal, although in four of the simulations, the prediction still agrees to about a factor of 2. For the simulations drawn from the 3.5 keV and 100 GeV power spectra, however, the model overpredicts the lensing signal by an order of magnitude. These power spectra yield the greatest prevalence of halo mergers, and unlike in the case of annihilations, mergers do not sufficiently boost the remnant's lensing signal

Table 4.4: This table shows how accurately our models predict aggregate halo signals. We consider simplified aggregate signals $\sum A^2$ for annihilation and $\sum M(r_\mathrm{max})r_\mathrm{max}$ for lensing, each summed over the population of predicted or simulated halos. In each case, we list the ratio of the signal predicted from the linear density field to the signal aggregated over halos in the simulation box. We use the ellipsoidal collapse and $s = 0$ contraction models.

Simulation	$\sum A^2$	$\sum M(r_\mathrm{max})r_\mathrm{max}$
$w = 0.1$	0.91	0.56
$w = 0.3$	0.89	0.69
$w = 0.5$	0.91	2.2
EMDE	0.78	0.66
100 GeV	1.15	33
3.5 keV	1.16	14

relative to its model prediction to compensate for the loss of halo count in mergers. Hence, the lensing signal in the simulations is much smaller than that predicted from the linear density field. We remark, however, that the story may change if instrument sensitivities are taken into account. Mergers predominantly destroy smaller halos, and their signals may have been beyond sensitivity limits regardless.

It is clear from these results that an accurate accounting of halo mergers is necessary to predict a halo population in any generality. However, for narrower power spectra such as our $w = 0.1$, $w = 0.3$, or EMDE cases, mergers are subdominant, and our models can predict the populations reasonably well. Moreover, when considering aggregate annihilation signals, halo mergers may not have a significant impact beyond altering the slope γ of the $\rho \propto r^{-\gamma}$ inner density profiles. For these uses, we describe in Appendix C.3 a method to sample the halo population directly from the matter power spectrum $\mathcal{P}(k)$, bypassing the step of drawing a density field $\delta(\boldsymbol{x})$. Halo populations predicted using this method are slightly different from those predicted using our density fields, but we propose that they are more accurate; the method we describe can easily sample a much larger number of peaks, and it is not subject to errors related to the finite size and finite grid spacing of a sampled density field.[23]

---

[23]If sampling directly from the power spectrum is more accurate, one may wonder why we chose to compare our simulation results to those predicted from the less-accurate finite density fields (Figs. 4.14 and 4.15). The reason for this choice is that it leads to a more explicit test of our model. Since we compare a simulation's results to model predictions using the same simulation's initial density field, any discrepancy that is not a simulation artifact can be attributed to the model.

4.5.2 Halo mergers

A full treatment of mergers is beyond the scope of this work, but we are poised to make some observations. Our procedure for matching a halo to its predecessor density peak involved tracking each halo backward through time. During this process, we counted the number of major mergers this halo underwent, which we define to be a merger between two halos with mass ratio smaller than 3. Over half of our halos with well-resolved asymptotes experienced at least one major merger, and 12% experienced at least three.

In an effort to find a simple way to cull halos that end up merging, we explored cutting out density peaks that were too close to an earlier-collapsing density peak. We considered two characteristic comoving length scales below which to make these cuts: the scale q_{pk} associated with the density peak (see Sec. 4.3) and the scale q_{max} where $\epsilon(q_{max}) = 2/3$ (see Sec. 4.4.1). Unfortunately, neither of these cuts produced sensible results. The q_{pk} cut culled far too few halos, while the q_{max} cut culled far too many. Ultimately, we expect that a more sophisticated accounting of mergers will be necessary, possibly following along the lines of extended Press-Schechter theory [291] or the PEAK PATCH algorithm [384, 393, 394].

Another question is how halo density profiles change due to mergers. Reference [280] found that successive mergers cause the slope γ of the small-radius asymptote of the density profile, $\rho \propto r^{-\gamma}$, to become shallower than its initial value of $\gamma = 3/2$. The same work also found that successive mergers increase the central density. Figure 4.16 shows that both of these results are borne out in our own simulations as well. There is a clear trend wherein more major mergers lead to successively denser[24] but shallower inner structures. On the other hand, we also see in Fig. 4.16 that major mergers do not significantly increase r_{max} beyond what our models already predict, although they do increase $M(r_{max})$.

4.6 Conclusion

The first halos form by direct collapse of peaks in the primordial density field. If some of these halos survive the subsequent hierarchical clustering process, as evidence suggests [262, 266, 280, 284, 339–342], then they would be the densest dark matter objects in the Universe. In this work, we presented

---

[24]While the coefficient A is only well defined if $\gamma = 3/2$, our procedure for measuring A (see Appendix C.1) obtains a logarithmically averaged value of $\rho r^{3/2}$ over the inner density profile regardless.
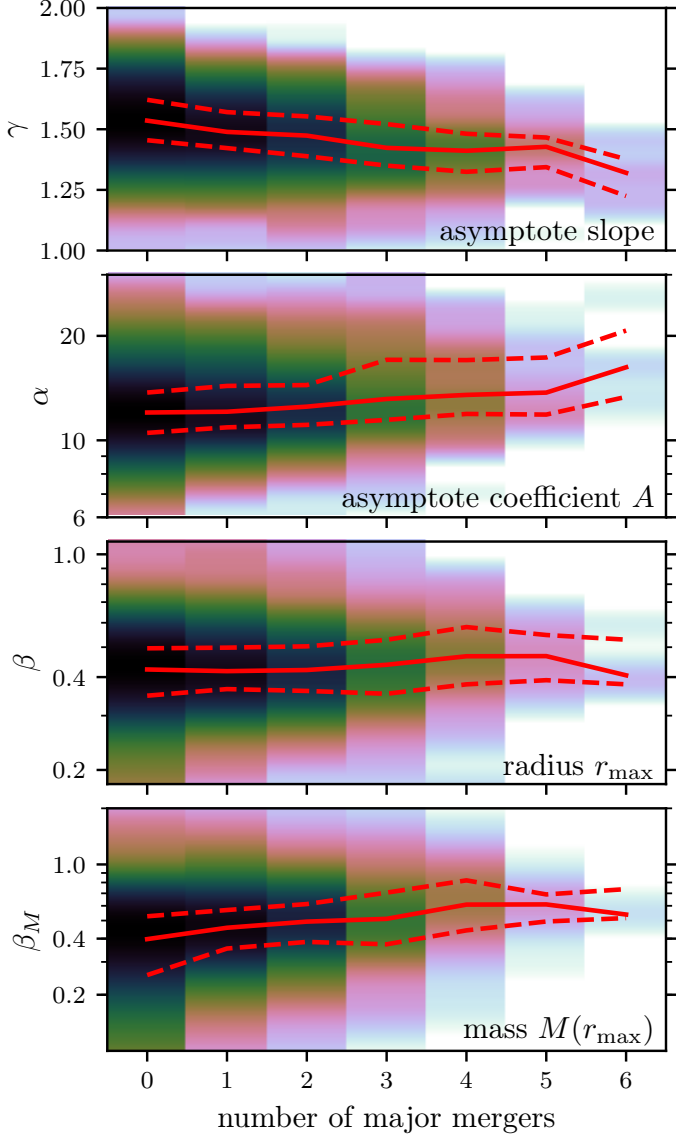
Figure 4.16: The impact of major mergers on the density profiles in our simulations. Top: The effect on the power-law index γ of the $\rho \propto r^{-\gamma}$ inner asymptote. Since we do not resolve these radii well, much of the scatter likely arises from numerical noise. Middle to bottom: The effects on the asymptote A, radius $r_{\max}$, and mass $M(r_{\max})$, respectively, plotted as the ratio between the measured value and the prediction using our models. For the asymptote, we use the ellipsoidal collapse model, while for $r_{\max}$ and $M(r_{\max})$, we use the $s = 0$ contraction model. The color scale, which is logarithmic, represents a density estimate (in log space for α, β, and β_M; darker is denser), while the lines mark the median and the 25th and 75th percentiles at each merger count.

models that predict the density profiles of these halos directly from the properties of the density peaks that formed them, and we used high-resolution cosmological simulations in a variety of different scenarios to tune and validate these models. The models are described in Secs. 4.3 and 4.4 and summarized in Table 4.3. They have simulation-tuned parameters, but these parameters are independent of cosmology and do not need to be retuned to accommodate different scenarios.

We treated small and large radii separately, with the understanding that these regimes form under radically different circumstances. At small radii, the first halos develop $\rho = Ar^{-3/2}$ density profiles [26, 226, 261–266], and our model predicts the coefficient A with remarkable success. Over the full range of cosmologies we explored, the scatter from our model is only in the vicinity of 30%-40%, and it is likely that a significant fraction of that scatter arises from numerical noise in our simulations. The density profiles at large radii are more varied, but we parametrize them using the radius $r_{\max}$ at which the circular velocity is maximized along with the mass $M(r_{\max})$ enclosed within that radius. For this regime, we employ models already present in the literature [355, 362, 371], but we supply calibrations that enable their use as predictive tools applicable to any cosmology. The scatter from our models is roughly 40%-50% in $r_{\max}$ and a factor of 2 in $M(r_{\max})$, and, similarly, not all of this scatter is physical.

In this way, the models we presented can predict the halo arising from a given density peak. Our goal, however, is to predict populations of halos. For a power spectrum of density fluctuations that is narrowly supported, such as the spectrum imprinted by an EMDE [181–183, 224] or certain inflationary models [27–30, 49, 51, 52, 73, 76, 78], our models replicate the entire halo population reasonably well. Thus, our models can serve as a tool to predict the observational signals of such cosmologies. However, for more broadly supported power spectra, such as those arising from a scale-invariant initial spectrum, halo mergers dramatically alter the halo population, causing the populations that arise in our simulations to differ substantially from the populations our models predict. Interestingly, modulo changes in the slopes γ of the $\rho \propto r^{-\gamma}$ inner density profiles, dark matter annihilation signals seem to be sufficiently close to additive in halo mergers that our models still predict the aggregate annihilation signal to within 30% in every cosmology we tested.

Nevertheless, it is not clear that this additivity in the annihilation signal should extend beyond the timescales spanned by our simulations. More broadly, our models predict the initial halo population, but a proper understanding of halo mergers is needed in order to robustly connect it to

the population today. It is necessary to understand both how mergers are distributed across halos and time and how they impact halo density profiles. Methods exist that can predict the distribution of mergers, the most prominent of which is the extended Press-Schechter theory [291]. The PEAK PATCH algorithm [394] represents a method that may be easier to adapt, among other advantages, if more computationally expensive to apply. Meanwhile, the larger challenge is to predict how halo mergers alter density profiles. References [262, 280, 339] (for major mergers) and [340–342] (for minor mergers) represent steps toward this goal, but there is not, as yet, a sufficiently general model.

Moreover, there is room for improvement in our models themselves. In predicting the density profiles at large radii, we assume that each mass shell contributes density in a profile that is a single power law up to a maximum radius. In reality, shell profiles follow more complicated forms that are sensitive to the total density profile; see Fig. 4.10 and Refs [362, 364]. Utilizing more accurate shell profiles would likely improve the model predictions for the density profile, especially in predicting its broader shape rather than only $r_{\max}$ and $M(r_{\max})$. Also, our model for the density profile at large radii completely discounts any deviations from sphericity in the initial peak. Another avenue for improvement may be to incorporate ellipsoidal collapse. At small radii, the reason the $\rho \propto r^{-3/2}$ profile arises is not well understood, and its accuracy has only been confirmed down to the resolution limits of N-body simulations. A physical understanding must be developed of the mechanism by which this profile arises in order to confirm whether the profile truly extends to arbitrarily small radii.

The primordial density field and its power spectrum of density fluctuations comprise a valuable window into the early Universe and the nature of dark matter. Our work in this chapter was carried out as part of an effort to use the observational signatures of dark matter halos to probe these fluctuations. Further research is still needed to understand the impact of mergers on halo populations before these signatures, or their nonobservation, can be employed to robustly constrain cosmology. Nevertheless, the models presented here, which predict the initial halo population, represent a step forward in our capacity to use this probe.

CHAPTER 5:
TIDAL EVOLUTION OF DARK MATTER ANNIHILATION RATES IN SUBHALOS[1]

5.1 Introduction

Despite overwhelming evidence for the existence of dark matter (e.g., Refs. [16, 192, 193]), its microphysical details remain unknown. Numerous models have been considered, but none have been experimentally confirmed (see Refs. [195–199] for reviews). However, to explain the present abundance of dark matter, a large class of models, including the popular weakly interacting massive particle [283], propose that dark matter was pair produced from the thermal plasma in the hot early Universe. In this scenario, the dark matter can annihilate back into standard-model particles today, leading to prospects for the detection of high-energy gamma rays or other annihilation products (e.g., Ref. [344]).

The rate of dark matter annihilation scales as the square of the dark matter density, so it is strongly sensitive to the spatial distribution of the dark matter. At galactic scales and above, this spatial distribution is well understood. Initially overdense patches in the Universe collapse into gravitationally bound dark matter halos, which thereafter merge to produce successively larger structures. Numerical simulations demonstrate that the spherically averaged mass distributions of the resulting dark matter halos are well described by the NFW density profile [205, 260],

$$\rho(r) = \frac{\rho_s}{(r/r_s)(1 + r/r_s)^2},\tag{5.1}$$

which has scale parameters r_s and ρ_s. Baryonic effects may subsequently alter this density profile (e.g., Ref. [396]).

---

[1]This chapter was previously published in Physical Review D as Ref. [395] and is copyright © 2019 American Physical Society. The original reference is as follows: M. S. Delos, *Tidal evolution of dark matter annihilation rates in subhalos*, Physical Review D **100**, 063505 (2019).

However, at subgalactic scales, the spatial distribution of the dark matter is less clear. As a halo is built up through hierarchical merging, it accretes smaller halos that survive as subhalos within the larger host. These subhalos gradually lose mass due to the influence of tidal forces from the host (e.g., Refs. [392, 397]), surviving until either they are completely stripped or dynamical friction causes them to sink into the host's center [398]. However, for sufficiently small subhalos dynamical friction is inefficient [397]. Moreover, numerous analyses have found that if the subhalos possess divergent central density, as in the NFW profile, then tidal forces may never fully strip them [284, 325, 341, 399].

Thus, a galactic-scale dark matter halo is likely to possess a multitude of subhalos. This substructure can significantly boost the rate of dark matter annihilation, depending on the scale of the smallest halos and when they form [263–265, 284, 321, 345, 347, 400–407] (see Ref. [348] for a recent review). When the smallest halos are microhalos of roughly earth mass, annihilation rates may be boosted by a factor of about 10 [405, 407] relative to those expected in the absence of substructure, assuming that these halos arise from primordial density fluctuations comparable to the large-scale fluctuations inferred from the cosmic microwave background (e.g., Ref. [16]). Moreover, this boost can be raised by orders of magnitude by cosmological scenarios that amplify small-scale density fluctuations and thereby lead to earlier and more abundant microhalo formation. Such scenarios include a period of domination by a heavy species [181–183, 224] or a fast-rolling scalar field [191] prior to nucleosynthesis, along with a variety of inflationary models [27–31, 38, 40, 49, 51–53, 56, 69–71, 73–76, 78–81]. In these cases, the high density within these microhalos causes them to completely dominate any dark matter annihilation signal (e.g., Refs. [26, 206, 234]).

Unfortunately, all estimates of the substructure's boost to annihilation rates are subject to uncertainties about the impact of tidal effects on subhalos. Cosmological simulations cannot resolve subhalos that are much smaller than the host, and those that are resolved are prone to artificial destruction [328, 408, 409]. Numerous semianalytic models have been developed to describe the dynamical evolution of subhalos; Refs. [410–417] model a subhalo's loss of mass due to tidal stripping, and Refs. [340, 341] predict the impact of this mass loss on the halo's density profile. However, these models are typically tuned to the results of cosmological simulations, so their predictions are affected by the artificial subhalo disruption occurring therein. They cannot fully reproduce the results of idealized simulations [328, 342].

Meanwhile, calculations of the dark matter annihilation rate in the substructure have employed a number of different treatments of tidal evolution. Some, such as Refs. [347, 407], employ a combination of the models above to predict the time evolution of subhalo density profiles. Others, such as Refs. [224, 404–406], employ simpler models, often either truncating subhalos at a characteristic tidal radius or formulating a destruction condition for subhalos and assuming the survivors are unaltered. Still others, such as Refs. [26, 206, 234, 263, 265, 401, 402] neglect the tidal disruption of the substructure altogether.

Our work is motivated by this context. Since cosmological simulations cannot resolve the smallest substructures, we follow Refs. [340–342, 409, 418, 419] in using idealized simulations of an N-body subhalo inside an analytic galactic potential. However, unlike these works, we focus on understanding the impact of tides on the subhalo's annihilation rate, a goal that requires significantly better resolution than has been attained in previous studies. Moreover, previous works have focused on understanding the evolution of subhalos of scales resolvable in cosmological simulations, such as halos associated with dwarf galaxies within a galactic halo. Accordingly, they probe only the subhalo properties and orbits that are found in such simulations. For instance, Ref. [342] only studies subhalos orbiting above the host's scale radius. In contrast, we seek to probe the full range of subhalos down to the smallest microhalos, which span a far broader range of properties and orbits.

Using the results of 52 high-resolution N-body simulations, we develop a physically motivated model that can predict the time evolution of a subhalo's annihilation rate due to tidal effects. In the process, we isolate three physical variables that determine this evolution:

(1) The energy injected by tidal forces into subhalo particles over the course of each orbit about the host, in units of the particle's binding energy to the subhalo;

(2) The ratio of stretching (radial) tidal forces to compressive (tangential) tidal forces;

(3) The range of radii in the subhalo across which material is heated by tidal forces, which is set by the shape of the subhalo's orbit.

This model predicts the suppression of a subhalo's annihilation rate, characterized by its J factor[2]

$$J \equiv \int \rho^2 \mathrm{d}V, \tag{5.2}$$

as a function of its orbit about the host. To assist the application of our model, we supply convenient fitting functions.

This chapter is organized as follows. In Sec. 5.2, we detail how we carry out our N-body simulations. Section 5.3 qualitatively discusses the trajectory of a subhalo's J factor, interpreting simulation trends physically and motivating our model. In Sec. 5.4, we develop our predictive model for the evolution of a subhalo's J factor, and Sec. 5.5 summarizes the model and discusses limitations and extensions. In Sec. 5.6, we compare the model's predictions to those of previous semianalytic models. Section 5.7 concludes, and we supply a variety of appendixes in Appendix D. Appendix D.1 supplies further details about our simulations, while Appendix D.2 quantifies the range of subhalo sizes over which the results of these simulations are applicable. Appendix D.3 presents fitting formulas and other computational details that aid in applying our model. Appendix D.4 tests our model against a publicly available simulation library [342]. Finally, in Appendix D.5, we observe that our model can be adapted to describe the evolution of subhalo properties beyond the J factor.

5.2 Simulations

Owing to the difference in scales between a host and its smallest subhalos, the computational challenge in simulating subhalo evolution in a cosmological context is formidable. A number of previous works have addressed this problem by simulating an N-body subhalo inside an analytic host potential [340–342, 409, 418, 419]; our approach is similar but differs in one key step. Instead of placing a subhalo in orbit about the host potential, we subject the subhalo directly to the time-dependent tidal force field experienced by an analytic orbit about the host. This procedure minimizes the impact of numerical precision errors that can result from differences in scale between the subhalo's orbital and internal dynamics. In this section, we detail that procedure and present qualitative results.

---

[2]We assume the dark matter annihilation cross section is velocity independent in the nonrelativistic limit.

We assume that both the host and the subhalo possess the NFW density profile given by Eq. (5.1). While there is evidence that many galactic halos possess constant-density cores instead of the NFW profile's cusp [420], at least some galactic halos appear to be cuspy [421]. Additionally, while microhalos are expected to form with $\rho \propto r^{-3/2}$ inner profiles [26, 226, 261–266, 336], it is likely that mergers will drive their inner cusps toward the $\rho \propto r^{-1}$ of the NFW profile [262, 280, 336].

To model the host's tidal field we begin with an analytically computed orbit, described by the time-dependent vector $\boldsymbol{R}(t)$ pointing from host center to subhalo center. The tidal acceleration at position $\boldsymbol{r}$ relative to the subhalo center is[3]

$$\boldsymbol{F}_{\text{tidal}}(\boldsymbol{r}) = -\frac{\mathrm{d}F}{\mathrm{d}R}(\boldsymbol{r} \cdot \hat{\boldsymbol{R}})\hat{\boldsymbol{R}} - F(R)\frac{\boldsymbol{r} - (\boldsymbol{r} \cdot \hat{\boldsymbol{R}})\hat{\boldsymbol{R}}}{R} \tag{5.3}$$

at linear order in r/R, where $F(R)$ is the force profile of the host, $R = |\boldsymbol{R}|$, and $\hat{\boldsymbol{R}} = \boldsymbol{R}/R$. We modified the GADGET-2 N-body simulation code [274, 275] to include this tidal acceleration.

We prepare the initial N-body subhalo with an NFW profile by drawing particles from an isotropic distribution function computed using the fitting form in Ref. [422]. Additionally, we sample the subhalo's central region at increased resolution; particles whose orbital pericenters are below $r_s/3$, where r_s is the subhalo scale radius, have $1/64$ the mass and 64 times the number density of the other particles. Appendix D.1 demonstrates that there is no significant relaxation associated with the use of particles of different masses. We cut off the density profile at $r = 500r_s$; subhalo particles this far out are stripped immediately, so as long as the cutoff radius is much larger than r_s, the precise choice makes no difference.[4] We represent the subhalo using a total of 8×10^6 particles, and roughly 70% of them, carrying roughly 4% of the total mass, are high-resolution particles. All of our subhalos have $r_s \simeq 10^{-6}R_s$, where R_s is the scale radius of the host, but as we will soon discuss, the precise choice of r_s has no impact on dynamics.

For our simulations, we consider a variety of orbits about the host. An orbit in a spherically

---

[3]We experimented with using the full tidal force $\boldsymbol{F}_{\text{tidal}}(\boldsymbol{r}) = \boldsymbol{F}(\boldsymbol{R}+\boldsymbol{r}) - \boldsymbol{F}(\boldsymbol{R})$, but because $r \ll R$ in our simulations, it offers no advantage; moreover, it is less numerically stable due to the subtraction of two close numbers.

[4]The natural place to cut off the density profile would be where the density reaches that of the subhalo's background: the host. However, tidal forces automatically truncate a subhalo's density profile at roughly the radius where its average density equals that of the host [see, e.g., Eq. (5.24)], so it is not necessary to tune a cutoff radius by hand.

symmetric potential is characterized by two parameters: energy E and angular momentum L or, equivalently, a scale parameter and a shape parameter. For convenience, we use the circular orbit radius[5] R_c, defined as the radius of the circular orbit with energy E, and the "circularity" $\eta = L/L_c$, where L_c is the angular momentum of the circular orbit with the same energy. In each simulation the subhalo begins at its orbital apocenter.

Figure 5.1 illustrates a simulation executed through this arrangement. The host has scale radius $R_s = 0.8$ kpc and scale density $P_s = 5 \times 10^7$ $M_\odot/\text{kpc}^3$, while the N-body subhalo is initially a microhalo with scale radius $r_s = 6 \times 10^{-7}$ kpc that has $\rho_s/P_s = 1285$ times the scale density of the host. The subhalo orbit has $R_c = 0.15$ kpc and $\eta = 0.5$. The simulation runs through 18 orbits about the host, and Fig. 5.2 plots the density profile of the subhalo at each apocenter. Consistently with the results of other works, such as Refs. [284, 325, 341, 399], we find that this subhalo's central cusp is highly resistant to disruption by the host's tidal forces. 91% of the subhalo's mass is stripped by simulation termination, but its central density profile is largely unscathed.

Our goal in this work is to understand how the annihilation signal decays due to tidal effects. For this purpose, we consider the J factor, Eq. (5.2), integrated over the subhalo mass distribution. This J factor is the factor in the annihilation rate that depends on mass distribution, and Appendix D.1 discusses our procedure to extract it from the simulations. We also show in Appendix D.1 that the resulting J-factor trajectories are converged with respect to simulation parameters.

Finally, we conclude this section by discussing the applicability of our simulation results. The linearized tidal force in Eq. (5.3) is valid for $r \ll R$, and in Appendix D.2 we show that it yields accurate results in simulations as long as

$$r_s \lesssim 0.1 R_c. \tag{5.4}$$

Our simulation results are only applicable if this condition is satisfied. Additionally, since we do not simulate the host halo's dynamics, we cannot account for dynamical friction. Reference [342] found

---

[5]Note that R_c is roughly the time-averaged radius; for a power-law potential $\phi(R) \propto R^n$, $R_c = \langle R^n \rangle^{1/n}$. See Appendix D.3 for a more precise relationship for NFW profiles.
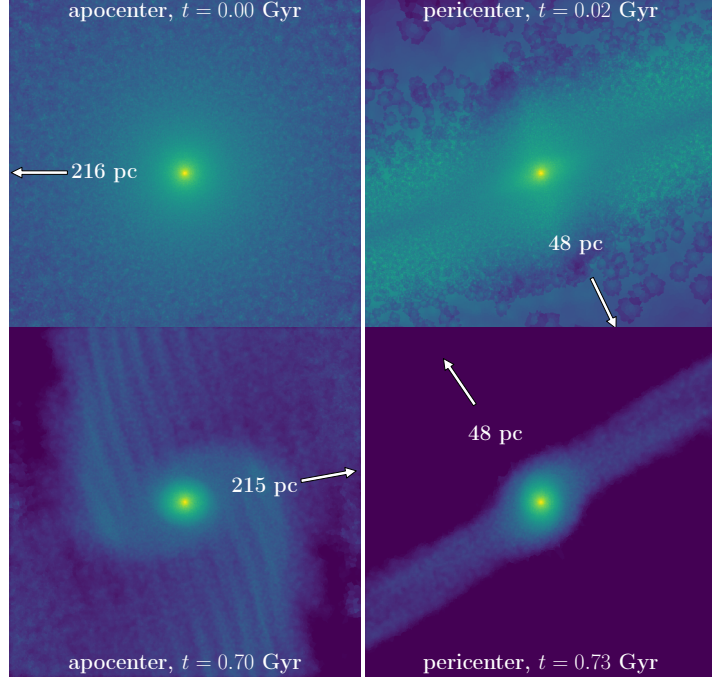
Figure 5.1: The projected density field of a microhalo simulated in orbit about a galactic halo. The width of each frame is 0.03 pc, and the arrow indicates the direction and distance to the host center. The density is computed using a k-nearest-neighbor density estimate with $k = 50$ and is plotted with a logarithmic color scale (lighter is denser).

that dynamical friction[6] has minimal impact on a subhalo's mass evolution for host-to-subhalo mass ratios $M/m \gtrsim 100$. However, since subhalos relevant to dark matter annihilation may orbit over significantly longer timescales than considered in Ref. [342], it is also useful to have an analytic estimate for when dynamical friction can be neglected. It follows from the analysis in Ref. [397] that for a subhalo that accretes onto a host at redshift z, dynamical friction can be neglected as long as the host-to-subhalo mass ratio M/m satisfies

$$\frac{M/m}{\ln(M/m)} \gtrsim 10(1+z)^{3/2}. \tag{5.5}$$

Our results may be considered applicable as long as Eqs. (5.4) and (5.5) are satisfied, but we remark that if one is satisfied, then the other likely is too.

---

[6]Specifically, Ref. [342] studied dynamical self-friction, or the dynamical friction that results from the subhalo's own tidal tail. This friction can be considerably more efficient than that resulting from the host's material alone [423, 424].
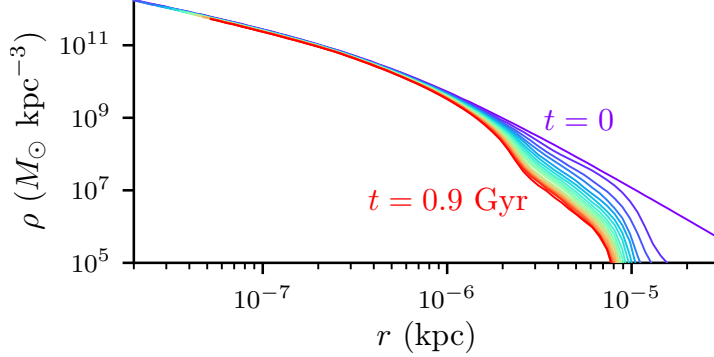
Figure 5.2: The density profile evolution of the halo depicted in Fig. 5.1. 91% of the initial mass of the microhalo is stripped by $t = 0.9$ Gyr, but the central density profile is largely unaffected.

5.3 Trends in the tidal evolution

In this section, we explore trends in the evolution of J as a function of system and time and attempt to explain them physically. Our goal is to find the J factor as a function of time t, orbital parameters R_c and η, subhalo parameters r_s and ρ_s, and host parameters R_s and P_s. The dimensionality of this space is large, but some immediate simplifications are evident:

(1) As long as the subhalo is much smaller than its orbit, or $r_s \ll R_c$, the value of r_s has no impact on dynamics.[7] All of our simulated subhalos have $r_s \simeq 10^{-6} R_s$, which leads to $r_s \ll R_c$ for all orbits we consider.

(2) If instead of time t we use the orbit count $n = t/T$, where T is the orbital period, then the overall density scale has no impact on dynamics, and only the ratio ρ_s/P_s enters.

(3) The overall size of the host-subhalo system is irrelevant, so only the ratio R_c/R_s affects dynamics.

We have verified that all of these simplifications are borne out in our simulations. Hence, if J_{init} is the initial J factor, then J/J_{init} is now a function of time $n = t/T$ and just three system parameters: ρ_s/P_s, R_c/R_s, and η. Notably, the tidal evolution is independent of the subhalo's mass, a property also noted in prior works (e.g., Ref. [342]).

---

[7]For fixed density, the internal velocities of particles in a subhalo are proportional to its radius. Since the tidal acceleration in Eq. (5.3) is also proportional to the radius, fractional velocity changes induced by tidal forces are independent of the subhalo's radius.
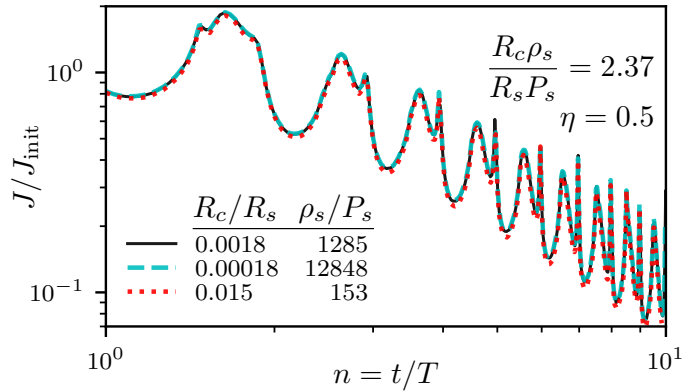
Figure 5.3: Trajectories of the J factor for different systems with the same $\tilde{x} = \frac{R_c\rho_s}{R_sP_s}$ and η. Scaled to the orbital period, these systems all have the same trajectory.

5.3.1 Trends in the simulations

We first inspect the results of selected simulations in order to find trends in the behavior of J. As a further simplification, we focus on the $R_c \ll R_s$ regime. The host potential is self-similar in this regime, reducing the tidal evolution problem in two additional ways:

(1) The orbital radius R_c is degenerate with properties of the host and subhalo. For instance, reducing the orbital radius is equivalent to making the host denser.

(2) Orbits with the same circularity η have the same shape; they are rescaled versions of one another.

The first simplification further reduces the parameter space so that in this self-similar regime, there are only two parameters,[8]

$$\tilde{x} \equiv \frac{R_c\rho_s}{R_sP_s} \tag{5.6}$$

and η. Figure 5.3 shows the success of this parameter reduction; different systems with the same $\tilde{x}$ and η follow precisely the same $J(n)$ trajectories. Meanwhile, the second simplification allows us to isolate the impact of these two parameters; we can vary the "reduced orbital radius" $\tilde{x}$ without altering the orbit's shape.

We first investigate the impact of orbit shape. Figure 5.4 shows the trajectory of the J factor

---

[8]We reserve x (without the tilde) for later use as a modified version of $\tilde{x}$.

for several values of η. We see immediately that the J factor oscillates with the orbital period with a larger amplitude for more eccentric orbits. This trend is explained by noting that all tidal forces are compressive in the self-similar regime,[9] so the subhalo becomes most compact near the orbital pericenter. The subhalo's J factor, being proportional to its mass-weighted average density [e.g., Eq. (D.3)], is maximized at this point. The precise appearance of these oscillations can be complicated because a subhalo's response to these tidal forces is delayed; for instance, double peaks in Fig. 5.3 arise because the subhalo and its unbound tidal stream are maximally compressed at different times. However, these oscillations are relatively unimportant. If subhalos are at random points in their orbits, then the J factor averaged over an orbital period suffices to predict the aggregate signal from a population of subhalos. We discuss this point further in Sec. 5.5.

More interesting trends arise in the broader time evolution. Figure 5.5 plots the running power-law index $\mathrm{d}\ln J/\mathrm{d}\ln t$ of the J factor with time, and the equation

$$\frac{\mathrm{d}\ln J}{\mathrm{d}\ln t} = -bn^{1-c} \tag{5.7}$$

describes the evolution of this index reasonably well as long as $|\mathrm{d}\ln J/\mathrm{d}\ln t| < \mathcal{O}(1)$. Here, $b > 0$ and $c > 0$ are constant parameters, and c is smaller for more eccentric orbits. Figures 5.4 and 5.5 also show fits to the J-factor trajectories using this form, which determines $J(n)$ up to a constant multiple. The exponent in Eq. (5.7) is so defined because it leads to the more evocative expression

$$\frac{1}{J}\frac{\mathrm{d}J}{\mathrm{d}n} = -bn^{-c}. \tag{5.8}$$

If $c = 0$, this equation tells us that the J factor would decay by the same factor e^{-b} over each orbit. The parameter c, when $c > 0$, accommodates some physical process by which tidal effects lose efficiency over time.

We show the impact of the orbital radius in Fig. 5.6, which plots the trajectories of J and $\mathrm{d}\ln J/\mathrm{d}\ln t$ for a variety of reduced orbital radii $\tilde{x}$ ranging from 0.7 to 230. Evidently, $\tilde{x}$ affects the

---

[9]Tangential tidal forces are always compressive, while radial tidal forces are negligible when $R_c \ll R_s$; see Sec. 5.4.1 for further discussion.
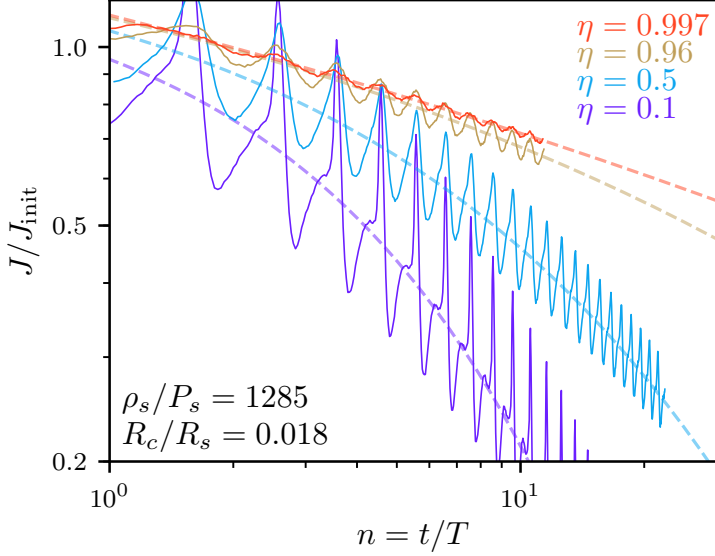
Figure 5.4: Trajectories of the J factor for different orbital shapes. The J factor oscillates with the orbital period; the dashed lines show fits using Eq. (5.7) (for $|\mathrm{d}\ln J/\mathrm{d}\ln t| < 1$).

initial decay rate of the J factor, described by the parameter b in Eq. (5.7), without altering the rate at which the decay slows over time. This figure also shows more clearly that there is a steepness limit to the decay of the J factor:

$$\frac{\mathrm{d}\ln J}{\mathrm{d}\ln t} \simeq -\min\left\{bn^{1-c}, B\right\}, \tag{5.9}$$

where $B \sim \mathcal{O}(1)$.

5.3.2 Physical interpretation

Behavior similar to that of Eq. (5.9) can be reproduced in a toy model. Suppose the subhalo has potential $\phi(r) \propto r^{\gamma}$ up to an additive constant; for instance, an NFW profile would have $\gamma = 1$ for $r \ll r_s$. Now discretize time, perhaps as a count of orbits, letting r_n be the radius of the subhalo's outer boundary at time t_n. Any material outside r_n at time t_n is free, fixing the additive constant in the potential such that $\phi_n(r) \propto r^{\gamma} - r_n^{\gamma}$ (where $\phi \geq 0$ implies freedom). Now suppose that at each time step, particles in the subhalo experience an injection of energy $\Delta E \propto r^{\alpha}$ due to tidal forces, and any radius with $\Delta E + \phi > 0$ no longer belongs to the halo. For instance, if the time step is constant, then $\alpha = 2$ since the energy injection is proportional to the square of the tidal force, which is in turn proportional to the radius. This tidal heating rule leads to the evolution equation

105
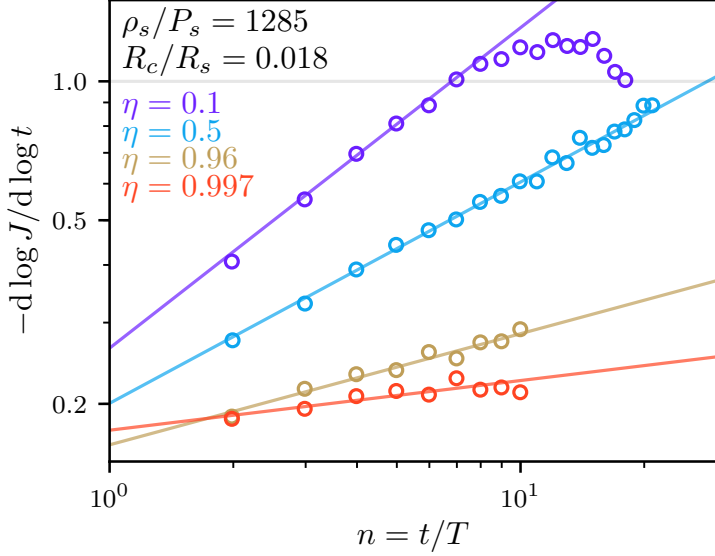
Figure 5.5: The impact of orbit shape on the J-factor trajectory. This figure plots the logarithmic slope of the orbital period-averaged trajectory to make the trends clearer. Notably, the slope runs more rapidly for more eccentric orbits. The points show the simulation results, while the lines correspond to fits using Eq. (5.7) (for $|d \ln J/d \ln t| < 1$).

$\phi_n(r_{n+1}) + \Delta E(r_{n+1}) = 0$, or

$$r_{n+1}^{\gamma} - r_n^{\gamma} + f r_{n+1}^{\alpha} = 0, \tag{5.10}$$

where f incorporates all of the proportionality constants.

For simplicity, we may assume $r_0 = 1$, absorbing its dimensionful value into f. For $\alpha > \gamma$, Eq. (5.10) obeys

$$\frac{\Delta \ln r}{\Delta \ln n} \simeq \begin{cases} -fn/\gamma, & fn \ll 1, \\ -1/(\alpha - \gamma), & fn \gg 1, \end{cases} \tag{5.11}$$

where Δ denotes the discrete difference across time steps. If $J \propto r^{\beta}$, then

$$\frac{\Delta \ln J}{\Delta \ln n} \simeq -\min\{bn, B\} \tag{5.12}$$

with $b = \beta f/\gamma$ and $B = \beta/(\alpha - \gamma)$. The quantity fn can be understood as (up to factors of order unity) the ratio of the tidal energy injection to the subhalo's internal energy. The two separate regimes arise physically because when $fn \ll 1$, the total radius change $|r_n - r_0| \ll r_0$. Since the radius does not change appreciably, the efficiency of tidal heating does not change, so r and J drop
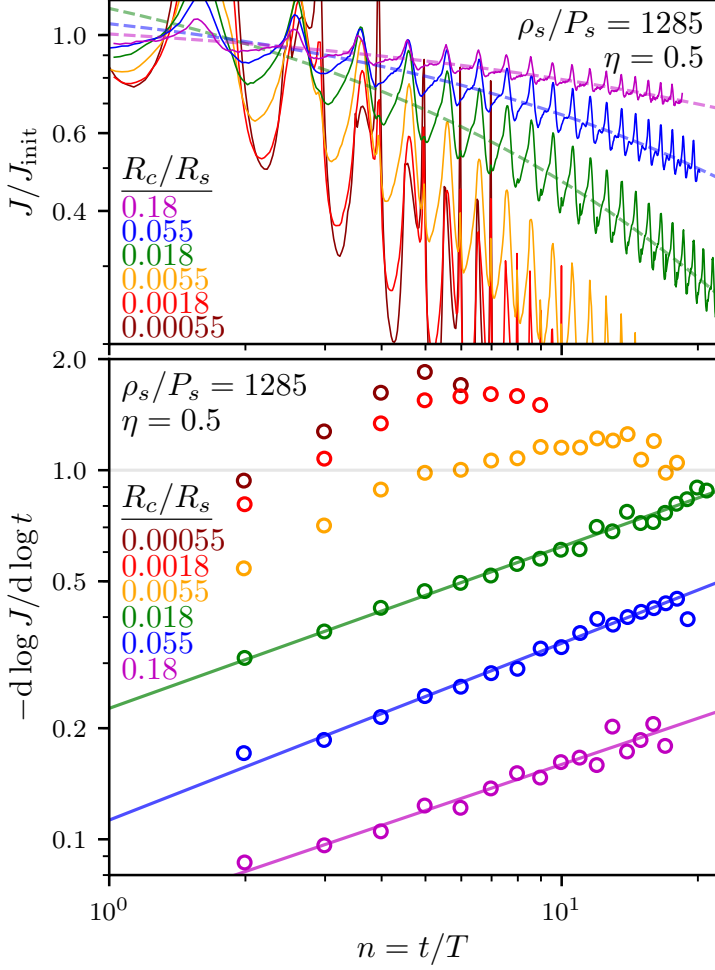
Figure 5.6: The impact of the orbital radius on the J-factor trajectory. Top: The J-factor trajectory as in Fig. 5.4 (solid lines); the dashed lines show fits using Eq. (5.7). Bottom: The logarithmic slope of the orbital period-averaged trajectory, as in Fig. 5.5; the points show the simulation results, while the lines correspond to the fits. We only fit the trajectories that do not pass $|\mathrm{d}\ln J/\mathrm{d}\ln t| = 1$.

by the same fraction in each orbit. However, when $fn \gg 1$, $|r_n - r_0| \sim r_0$. In this case, the radius is decreasing significantly, which implies that the density at the halo's shrinking outer boundary is increasing and hence that the halo is becoming more difficult to strip.

This toy model has reproduced Eq. (5.7) with $c = 0$, successfully explaining the apparent upper limit in $|\mathrm{d}\ln J/\mathrm{d}\ln t|$. We remark, however, that there is another, completely different, physical reason to expect an upper limit in $|\mathrm{d}\ln J/\mathrm{d}\ln t|$: an unbound tidal stream grows in length L as $L \propto t$. Hence, its volume grows as $V \propto t$, so its J factor drops as $J \propto M^2/V \propto t^{-1}$. Once a subhalo has been stripped to the point that its own J factor is dwarfed by that of its tidal stream, the J factor of the subhalo remnant decays as $J \propto t^{-1}$. The combination of these two processes—the increasing

density of the subhalo as its radius drops and the J factor of its tidal stream—may explain the behavior in Figs. 5.5 and 5.6 wherein $|\mathrm{d}\ln J/\mathrm{d}\ln t|$ initially shallows toward some value larger than 1 before subsequently returning back to 1. Note, however, that the precise evolution of the J factor in the $|\mathrm{d}\ln J/\mathrm{d}\ln t| \sim 1$ regime is of little consequence. By this point, the subhalo has already lost most of its J factor and contributes little to annihilation signals.

The physical explanation for the $c > 0$ behavior observed in the simulations remains unclear. However, it is necessarily connected to how the shape of the subhalo's density profile changes in response to tidal effects (see Fig. 5.2), which the toy model does not account for. In a more complete picture, the rate $\mathrm{d}J/\mathrm{d}n$ of tidal evolution should be sensitive only to the instantaneous host-subhalo system with no explicit dependence on the time n. Hence, it should be possible to replace the factor n^{-c} in Eq. (5.8) with a function of the subhalo's density profile (and other properties of the system). However, in the $|\mathrm{d}\ln J/\mathrm{d}\ln t| < 1$ regime, the total change in J is much smaller than J itself, and if we neglect changes in the shape of the density profile, then any parameter of the density profile (e.g., ρ_s or r_s) must experience a similarly small change. Since the factor n^{-c} can change by an order of magnitude in the same regime, it is not possible, except in a very contrived way, to replace this factor with a function of the density profile.

Thus, the $c > 0$ behavior must follow from changes in the density profile's shape. As a result of these changes, the density profile picks up new parameters that can potentially vary wildly without significantly altering J, and the factor n^{-c} can be replaced with a function of those parameters. For instance, by introducing a new parameter q, we can write

$$\frac{1}{J}\frac{\mathrm{d}J}{\mathrm{d}n} = -bq, \qquad \frac{1}{q}\frac{\mathrm{d}q}{\mathrm{d}n} = -cq^{1/c}. \tag{5.13}$$

This system no longer has explicit time dependence, but if $q = 1$ when $n = 1$, then it is equivalent to Eq. (5.8).

5.4 Modeling the tidal evolution

Motivated by the results of the previous section, we seek a model of the form

$$\ln \frac{J}{J_{\mathrm{init}}} = b\left[a - \frac{1}{1-c}\left(n^{1-c} - 1\right)\right] \tag{5.14}$$
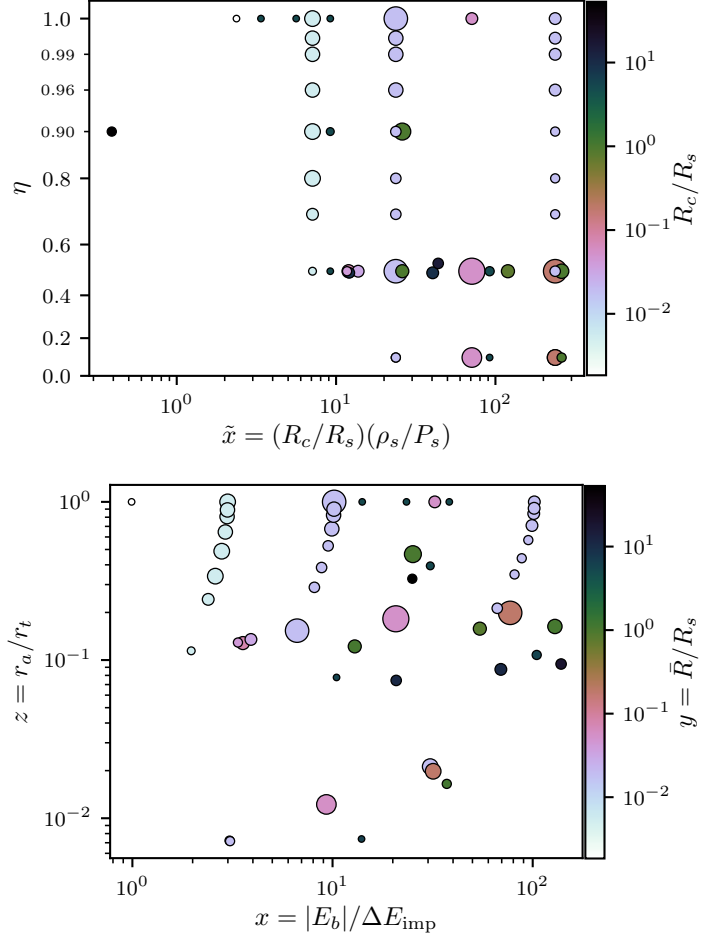
Figure 5.7: These figures summarize the 52 simulations we use to tune our model. Top: The simulations distributed in the host-subhalo system parameters. Bottom: The simulations distributed in the reduced parameters x, y, and z (see the text). Simulations with $x \lesssim 1$ are not included in this sample because they lead to $|\mathrm{d} \ln J / \mathrm{d} \ln t| \geq 1$ too quickly. The radius of each marker is proportional to the number of orbital periods, which ranges from 5 to 20.

for the case where $|\mathrm{d} \ln J / \mathrm{d} \ln t| < 1$. The parameters b and c follow immediately from Eq. (5.7), and we have inserted another parameter a to fix the overall normalization. Our goal is now to relate a, b, and c to the parameters of the host-subhalo system. For this purpose, we use the results of 52 idealized N-body simulations that we carried out as described in Sec. 5.2. The parameter space covered by these simulations is depicted in Fig. 5.7.

For each simulation we obtain the trajectory of the subhalo's J factor, stopping if $|\mathrm{d} \ln J / \mathrm{d} \ln t| \geq 1$ or otherwise at an arbitrarily chosen simulation termination time. As we discussed in the previous section, the evolutionary behavior changes markedly when $|\mathrm{d} \ln J / \mathrm{d} \ln t| \geq 1$, but precise predictions in this regime are unnecessary. Next, we convolve the J-factor trajectory in log space with a top-hat
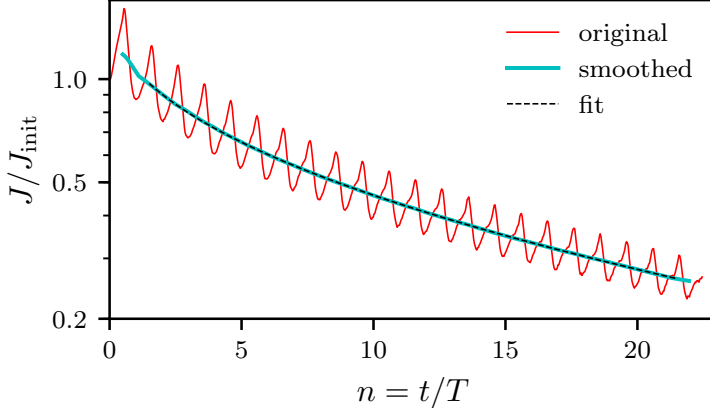
Figure 5.8: Demonstration of the fitting procedure for J-factor trajectories. The trajectory (thin oscillating line) obtained from the simulation is smoothed (thick line) using a top-hat filter with width equal to the orbital period. Equation (5.14) is fit (dashed line) to the smoothed trajectory.

filter of width equal to the radial (apocenter-to-apocenter) orbit period.[10] This step suppresses the influence of the periodic oscillatory behavior observed in Sec. 5.3; we are effectively finding the moving logarithmic average of J over this period. Finally, we fit Eq. (5.14) to this smoothed trajectory of J, but we only employ times after the end of the first radial period (so the first point is at $n = 1.5$, whose corresponding J factor averages from $n = 1$ to $n = 2$). This restriction is intended to remove the influence of any transient effects associated with suddenly turning on the tidal field. Additionally, in case the smoothing procedure fails to fully suppress periodic effects, we minimize any resulting bias by ending the fit at an integer number of orbits (so for instance, we might end at $n = 15.5$, corresponding to the average J from $n = 15$ to $n = 16$). The number of radial orbits fit through this procedure is represented in Fig. 5.7 as the marker size; this number is a proxy for how much information that simulation provides.[11] Figure 5.8 illustrates the procedure; the smoothing filter suppresses oscillations quite effectively.

5.4.1 Parameter b: The initial J-factor decay rate

From Fig. 5.6 we anticipate that b should depend strongly on the orbital radius. For simplicity we first study the self-similar regime, $R_c \ll R_s$. The upper panel of Fig. 5.9 plots b against the reduced orbital radius $\tilde{x}$ for the 36 of our simulations that satisfy $R_c/R_s < 0.3$. While b is strongly

---

[10]For circular orbits the radial orbit period is ill defined, and we substitute its limit as the orbit approaches circular as obtained using the fitting form in Appendix D.3.

[11]When performing fits, we weight a simulation spanning n orbits by $\sqrt{n}$.
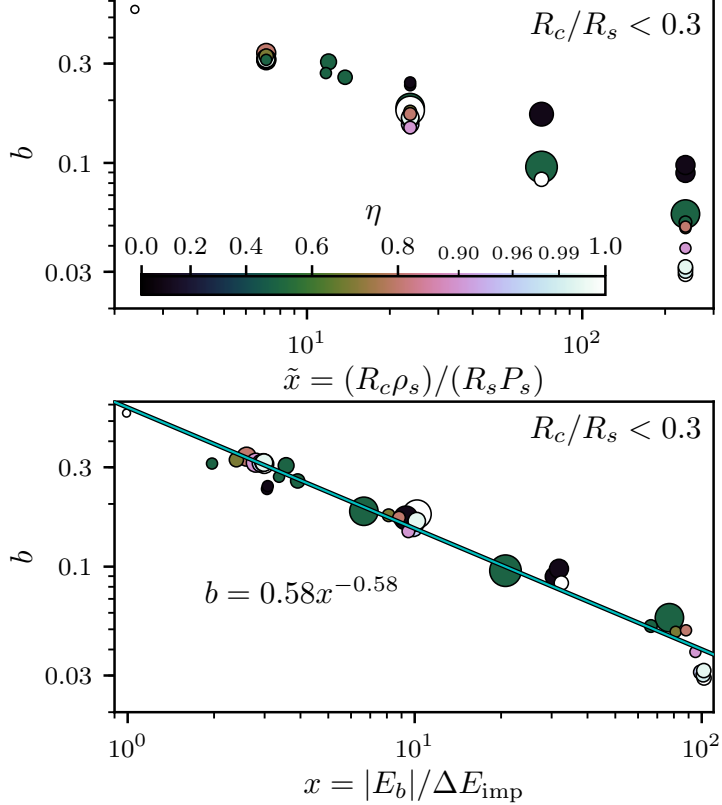
Figure 5.9: The dependence of the trajectory parameter b on system parameters in the self-similar regime ($R_c/R_s \ll 1$). Top: There is a trend between b and $\tilde{x}$, but it is polluted by residual sensitivity to the orbit-shape parameter η. Bottom: b is a power law in x with little residual sensitivity to the orbit shape, and the best fit is plotted as a solid line. The color scale is the same for both panels. Each marker is a simulation, and the marker radius is proportional to the number of orbital periods, which ranges from 7 to 20 for this sample.

sensitive to $\tilde{x}$, there is also significant sensitivity to the orbital shape, parametrized by η. However, it turns out that we can eliminate the shape dependence of b by defining the reduced orbital radius more carefully.

We first remark that $\tilde{x} \sim |E_b|/\Delta E$, where E_b is the binding energy of a particle at the subhalo's initial scale radius r_s and ΔE is the energy injected into that particle by tidal forces over the subhalo's orbital period. To see this, observe that the particle's binding energy is

$$E_b = -4\pi(\ln 2)G\rho_s r_s^2 \tag{5.15}$$

(per mass). Meanwhile, the tidal acceleration on this particle is roughly $(r_s/R)F$, where R is the subhalo's orbital radius and F is the host force (per mass) at radius R. In the self-similar regime,

$F \sim GP_s R_s$. The total velocity injected into the particle is $\Delta v \sim FT$, where T is the subhalo orbital period. Since $T \sim \sqrt{R/F}$, the energy injection (per mass) is $\Delta E \sim (\Delta v)^2 \sim GP_s R_s r_s^2/R$, and since $R \sim R_c$, this leads to $|E_b|/\Delta E \sim \tilde{x}$.

With this motivation, we define

$$x \equiv |E_b|/\Delta E_{\mathrm{imp}} \tag{5.16}$$

as a more exact version of $\tilde{x}$. Here, ΔE_{imp} is the energy injection per orbit on a particle at r_s computed using the impulse approximation as in Ref. [425]. In this approximation, the subhalo particle is treated as stationary while Eq. (5.3) is integrated to find the velocity (and hence energy) injection. We supply a fitting formula for ΔE_{imp} in Appendix D.3 for convenience. As intuition, x is of order the ratio

$$x \sim \rho_s/\bar{P}(<R_c) \tag{5.17}$$

between the subhalo's density and the average host density within the subhalo's orbital radius, a connection that follows from the observation that $\Delta E_{\mathrm{imp}}/r_s^2 \sim F(R_c)/R_c$ (see Appendix D.3). In the bottom panel of Fig. 5.9 we plot b against x for the self-similar regime. Evidently, our definition of x captures most or all of the sensitivity of the parameter b to the orbit shape, and

$$b = b_0 x^{-b_1}, \text{ if } R_c \ll R_s, \tag{5.18}$$

with $b_0 = 0.58$ and $b_1 = 0.58$. This success is remarkable; the approximation that subhalo particles are stationary during the application of tidal forces can only be valid for highly eccentric orbits, and yet the impulsive energy calculation accurately predicts the tidal evolution for more circular orbits as well.

To complete our understanding of the parameter b we must move beyond the self-similar regime. In the upper panel of Fig. 5.10, we plot b against x for all of our simulated subhalos. The color scale indicates the time-averaged orbital radius $\bar{R}$ in units of R_s. It appears that the effect of leaving the self-similar regime is to alter the normalization of b while keeping the power-law sensitivity to x unchanged. In particular, we may write

$$b = b_0 x^{-b_1} \left[1 + b_2 f(y) \right], \tag{5.19}$$
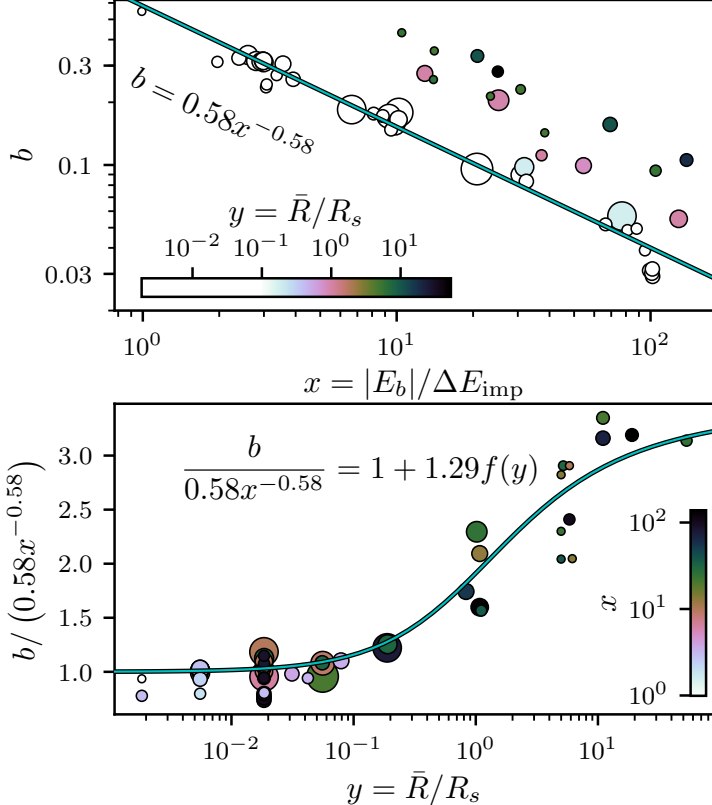
Figure 5.10: The dependence of b on x and y. Top: At each radius $y = \bar{R}/R_s$, b appears to follow a similar power law in x with a different normalization. The solid line is duplicated from Fig. 5.9. Bottom: Scaling of the normalization of b with radius y. The best fit is plotted, with $f(y)$ defined in Eq. (5.21). Each marker is a simulation, and the marker radius is proportional to the number of orbital periods, which ranges from 5 to 20.

for some function $f(y)$ and parameter b_2, where we define

$$y \equiv \bar{R}/R_s. \tag{5.20}$$

For convenience, we supply a fitting formula for $\bar{R}$ in Appendix D.3. While we could use the circular orbit radius R_c instead, we favor $\bar{R}$ because its physical significance is clearer.

To define the function $f(y)$, we consider the physical impact of leaving the self-similar regime. The magnitudes of the tidal forces are altered, but this effect should be accounted for by the definition of x. However, the directions of the tidal forces also change. In particular, Eq. (5.3) implies that there are stretching tidal forces proportional to $\mathrm{d}F/\mathrm{d}R$ along the radial axis from the host and compressive tidal forces proportional to F/R along the perpendicular directions. When the host force

profile $F(R)$ is self-similar, the ratio between the stretching and compressive forces is fixed.[12] Beyond the self-similar regime, however, the ratio between these forces can change. With this motivation, we define $f(R/R_s) \equiv (\mathrm{d}F/\mathrm{d}R)/(F/R)$ as this ratio. For the NFW profile this definition implies that

$$f(y) = \frac{2\ln(1+y) - y(2+3y)/(1+y)^2}{\ln(1+y) - y/(1+y)}.$$

(5.21)

In the bottom panel of Fig. 5.10, we plot $b/(b_0 x^{-b_1})$ against y for the purpose of tuning the parameter b_2 in Eq. (5.19). We find that this equation[13] works reasonably well, and we obtain $b_2 = 1.29$. The introduction of stretching tidal forces increases the efficiency of tidal effects, which is reflected as an increase in the decay rate b of the J factor.

5.4.2   Parameter a: The J-factor normalization

We next handle the overall normalization of J/J_{init}. According to Eq. (5.14), the J factor changes by the factor e^{ab} after the first orbit, which is sensitive to a second parameter: a. Because of the way we defined this parameter, it turns that a is almost wholly sensitive to $y = \bar{R}/R_s$ alone. Figure 5.11 plots a against y for all of our simulations, and we find that with only moderate scatter,

$$a = a_0 - a_1 f(y)$$

(5.22)

with $a_0 = 0.44$ and $a_1 = 1.32$.

In some sense, the parameter a describes the initial behavior of the subhalo as it equilibrates—to the extent that this is possible—into the tidal field generated by the host. When $y \ll 1$ all nonzero tidal forces are compressive, so the J factor is initially slightly boosted ($a > 0$). However, when $y \gtrsim 1$, the stretching tidal forces cause the J factor to be initially suppressed ($a < 0$). Note that the trajectory given by Eq. (5.14) is only valid after this equilibration takes place, so it is not valid for $n < 1$.

---

[12]In fact, for an NFW profile, $\mathrm{d}F/\mathrm{d}R = 0$ when $R \ll R_s$.

[13]The force-ratio argument motivates any expression of the form $[1 + b_2 f(y)^\alpha]^\beta$, but we assume for simplicity that $\alpha = \beta = 1$.
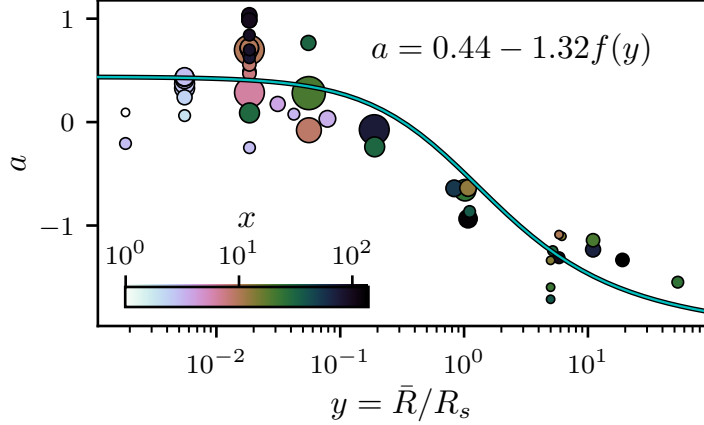
Figure 5.11: The dependence of the trajectory parameter a on the orbital radius parameter y. The best-fitting curve is plotted as a solid line using the definition of $f(y)$ in Eq. (5.21). Each marker is a simulation, and the marker radius is proportional to the number of orbital periods, which ranges from 5 to 20.

5.4.3 Parameter c: The loss of tidal efficiency

Finally, we address the parameter c that characterizes the drop in the efficiency of tidal effects over time. As we found in Sec. 5.3, c is sensitive to the orbit shape; more eccentric orbits yield smaller values of c while more circular orbits yield larger values. In the self-similar regime we could write c as a function of η, since η completely describes the orbit shape. However, beyond this regime, orbits with the same η could have different shapes. Thus, to accurately describe the sensitivity of the parameter c to the host-subhalo system, it is necessary to find the correct orbit-shape parametrization.

We argued in Sec. 5.3 that the loss of tidal efficiency encoded in c is related to changes in the shape of the subhalo density profile. The connection to the orbital shape is that circular orbits tidally heat material more predominantly in the outskirts of the subhalo, while eccentric orbits can alter the density profile further inward. This tendency is illustrated in Fig. 5.12, which depicts the tidally altered density profiles of two subhalos with different orbit shapes. The subhalo on the circular orbit loses more material from its outskirts, while the subhalo on the eccentric orbit loses more material from its interior.

Differences in the radii at which material is heated can be understood in terms of adiabatic shielding (e.g., Refs. [426–429]). Deep within the subhalo, the internal dynamical timescale is much shorter than the timescale over which the external tidal field changes. In this case, the conservation of adiabatic invariants prevents any energy injection by tidal forces; these radii are adiabatically
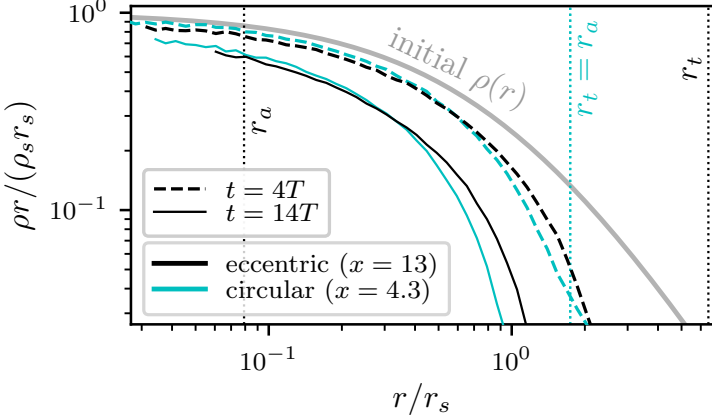
Figure 5.12: The influence of the shape of a subhalo's orbit on its density profile after tidal evolution. One subhalo is on a highly eccentric orbit ($\eta = 0.1$) while the other its on a circular orbit; we plot the density profiles after 4 and 14 orbits. The key difference is that the circular orbit strips material primarily from the outskirts, while the eccentric orbit strips more material from the interior. This difference can be understood in terms of the adiabatic shielding radius r_a and its comparison to the tidal radius r_t (see the text), shown as dotted lines for both orbits. The subhalos are chosen to yield similar density profiles and do not have the same energy parameter x.

shielded. Meanwhile, adiabatic shielding is connected to the shape of the subhalo's orbit. The timescale over which tidal forces change is related to the timescale of the pericenter passage, which can be very short for highly eccentric orbits.

Up to factors of order unity, the subhalo's internal dynamical timescale is $t_{\rm dyn} \sim (Gm(r)/r^3)^{-1/2}$ at radius r, where $m(r)$ is the subhalo mass profile [392]. Meanwhile, the pericenter passage timescale is $t_p \sim R_p/V_p$, where R_p and V_p are the radius and velocity at the pericenter, respectively. To make precise the connection between the orbit shape and the radii at which tidal heating is efficient, we define the adiabatic shielding radius r_a as the radius at which $t_{\rm dyn} = t_p$. This definition motivates a characteristic density scale

$$\rho_a \equiv \frac{V_p^2}{GR_p^2} = \eta^2 \frac{M(R_c)R_c}{R_p^4}, \tag{5.23}$$

so that r_a is the radius at which $m(r_a)/r_a^3 = \rho_a$. Note that we used the definitions of the circular orbit radius R_c and orbit circularity η to eliminate V_p from Eq. (5.23); $M(R)$ is the host mass profile at radius R.

To quantify changes in the shape of the subhalo density profile, we can compare the radius r_a below which material is shielded to the tidal radius r_t above which all material is stripped. The tidal radius is the radius above which the tidal force from the host exceeds the gravitational force

from the subhalo. There are several definitions of the tidal radius in the literature, but they are all related to the expression [430, 431] $r_t = R[m(r_t)/M(R)]^{1/3}$ by (possibly nonconstant) factors of order unity (see, e.g., Ref. [328]). The tidal radius is only well defined for circular orbits, but it is common to apply the concept to eccentric orbits as well [328]. In particular, if we seek the radius above which all material is stripped, we can define the tidal radius r_t using the orbital apocenter radius R_a. In this case, there is a characteristic density scale

$$\rho_t \equiv M(R_a)/R_a^3, \tag{5.24}$$

and r_t is the solution to $m(r_t)/r_t^3 = \rho_t$.

Anticipating that the drop in the efficiency of tidal effects encoded in the parameter c is a consequence of changes to the shape of the subhalo density profile, we may hypothesize that c is sensitive to the ratio

$$z \equiv r_a/r_t, \tag{5.25}$$

which ranges from 0 for radial orbits to 1 for circular orbits. For simplicity, in defining z we employ the subhalo's initial NFW mass profile [see Eq. (D.6)]. Figure 5.13 shows the relationship between c and z; there is some scatter, but the trend is that[14]

$$c = c_0 z^{c_1} \tag{5.26}$$

with $c_0 = 0.73$ and $c_1 = 0.21$. Note that z is not solely a function of the subhalo's orbit. Because it depends on the subhalo mass profile $m(r)$, it is also sensitive to the density ratio ρ_s/P_s. We explored using ρ_t/ρ_a, a purely orbital parameter, instead of r_a/r_t. This parameter exhibited a similar power-law relationship with c, but it left significant residual sensitivity to the parameter x, which is related to ρ_s/P_s. Using $z = r_a/r_t$ mostly eliminates that sensitivity.

---

[14]We argued in Sec. 5.3.2 that $c > 0$ is connected to changes in the density profile's shape. In this light, Eq. (5.26) implies that in the limit $z = 0$ where the tidal energy injection is completely impulsive, the shape of the density profile does not change over successive orbits. This notion is consistent with the results of Ref. [432], which found that impulsive point-object encounters yield a universal density profile.

117
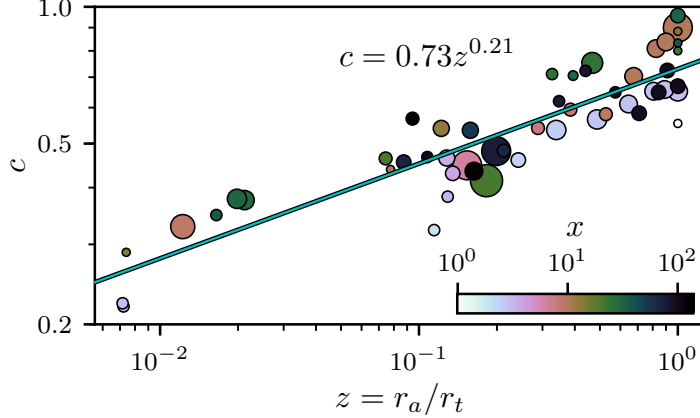
Figure 5.13: The dependence of the trajectory parameter c on the system parameter $z = r_a/r_t$. With moderate scatter, c follows a power law in z, shown as the solid line. Each marker is a simulation, and the marker radius is proportional to the number of orbital periods, which ranges from 5 to 20.

5.5 Model summary and discussion

In the last section, we developed a model for the evolution of a subhalo's J factor due to tidal effects as a function of parameters of the host-subhalo system. As long as the J factor decays slower than $|\mathrm{d}\ln J/\mathrm{d}\ln t| = 1$, its trajectory is well fit by the expression

$$\ln \frac{J}{J_{\text{init}}} = b \left[a - \frac{1}{1-c} \left(n^{1-c} - 1 \right) \right]. \tag{5.14}$$

Here, $n = t/T$ is the number of subhalo orbits, and a, b, and c are parameters that depend on the host-subhalo reduced system parameters x, y, and z through

$$a = a_0 - a_1 f(y), \tag{5.22}$$

$$b = b_0 x^{-b_1} \left[1 + b_2 f(y) \right], \tag{5.19}$$

$$c = c_0 z^{c_1} \tag{5.26}$$

with $a_0 = 0.44$, $a_1 = 1.32$, $b_0 = 0.58$, $b_1 = 0.58$, $b_2 = 1.29$, $c_0 = 0.73$, and $c_1 = 0.21$. In Appendix D.3, we detail how to compute x, y, z, and T from the subhalo parameters r_s and ρ_s, host parameters R_s and P_s, and orbital parameters R_c and η.

Equation (5.14) applies only when $|\mathrm{d}\ln J/\mathrm{d}\ln t| < 1$. The J factor's precise behavior when $|\mathrm{d}\ln J/\mathrm{d}\ln t| \gtrsim 1$ is of little consequence, as the subhalos in this regime contribute only minimally to aggregate annihilation signals. Nevertheless, it is useful to have an approximate treatment in

this regime. As we discussed in Sec. 5.3, when $|\mathrm{d}\ln J/\mathrm{d}\ln t| \geq 1$ it is a reasonable approximation to enforce $-\mathrm{d}\ln J/\mathrm{d}\ln t = 1$, i.e., $J \propto n^{-1}$. We define

$$n_1 = b^{1/(c-1)} \tag{5.27}$$

as the orbit count at which $-\mathrm{d}\ln J/\mathrm{d}\ln t = 1$. Additionally, when $b > 1$ (so $n_1 < 1$), we cannot expect our treatment of the normalization of J (Sec. 5.4.2) to be accurate. To handle these issues, we can write

$$\frac{J}{J_{\mathrm{init}}} = \begin{cases} \exp\left\{b\left[a - \frac{1}{1-c}\left(n^{1-c}-1\right)\right]\right\}, & \text{if } n \leq n_1, b < 1, \\ \exp\left\{b\left[a - \frac{1}{1-c}\left(\frac{1}{b}-1\right)\right]\right\}\frac{n_1}{n}, & \text{if } n > n_1, b < 1, \\ \mathrm{e}^a/n, & \text{if } b \geq 1, \end{cases} \tag{5.28}$$

where the last case follows from continuity considerations. We further note that this equation is valid only when $n \geq 1$ (see Sec. 5.4.2).

One can now use our model to understand the emission from a host halo due to dark matter annihilation in subhalos. In particular, one can sample subhalos from an orbital distribution in R_c and η (e.g., Refs. [408, 413, 433–436]). Accounting for tidal evolution, each subhalo's contribution to the dark matter annihilation signal is then scaled by the orbit-dependent function given by Eq. (5.28). In Ref. [437] (in preparation), we will use this model to study the annihilation signature arising from the extreme-density microhalos that result from certain early-Universe scenarios. In this case, the orbital distribution of subhalos is the same as that of particles, and one may employ the host halo's distribution function (e.g., Ref. [422]) to sample subhalo orbits.

Our model does not include the periodic oscillations in the J factor observed in Sec. 5.3. These oscillations do not affect the overall annihilation rate in subhalos, but they still introduce a systematic biasing effect where subhalos at smaller radii have larger J, and this effect can alter the morphology of an annihilation signal. However, we remark that these oscillations only have a significant amplitude in the $R_c \ll R_s$ regime, when all tidal forces are compressive, and at small $x \lesssim 10$. Because of these restrictions, we anticipate that their impact is minor. However, in forthcoming work [437] we will quantify the impact of these oscillations.

We also address another potential limitation to our model. The differential equation driving

it, Eq. (5.8), has explicit time dependence in the factor n^{-c}, so the resulting tidal evolution is not completely determined by the system's instantaneous state. Physically, we view n^{-c} as a proxy for unknown physical variables [e.g., Eq. (5.13)], and as long as the host halo's density profile and the subhalo's orbit are static, this formulation poses no difficulty. Since halos grow from the inside outward, subsequent accretion is not expected to significantly alter the density profile of a host halo at the radii of already-present subhalos, so the host halo is generally expected to remain static. Moreover, if dynamical friction is negligible [see Eq. (5.5)], the subhalo's orbit is also static. However, there is a scenario where a subhalo's host is expected to change dramatically. If the host is itself a satellite of a larger host halo, then the subhalo may be tidally stripped from its host, becoming itself a satellite of the superhost. In this scenario, it is not obvious how to continue the subhalo's tidal evolution.

If the initial host-subhalo system yields trajectory parameters a', b', and c' and the new host-subhalo system yields parameters a, b, and c, then a self-consistent way to treat this problem is to substitute the factor n^{-c} in Eq. (5.8) with $(n + n'^{c'/c})^{-c}$ and integrate the resulting expression. This treatment follows from the assumption that the parameter $q = n^{-c}$ in Eq. (5.13) is a function of the subhalo alone. Additionally, the J factor should be rescaled by $e^{ba - b'a'}$, a consideration motivated by the discussion in Sec. 5.4.2. However, it turns out that while this treatment works reasonably well for a portion of the a', b', c', a, b, c parameter space, it does not accurately predict every scenario; the parameter q in Eq. (5.13) is not a function of the subhalo alone. We leave a detailed investigation of this problem to future work.

As another caveat, the long-term accuracy of the trajectory in Eq. (5.14) relies on the assumption that the efficiency of tidal effects follows precisely the power law n^{-c}, as described by Eq. (5.8). While such a power law is a natural assumption [e.g, Eq. (5.13)] and is borne out in our simulations, it does not have a direct physical motivation; tidal heating models considered in Sec. 5.3.2 and elsewhere [416] can only reproduce $c = 0$. Without such motivation it is unclear that this power-law behavior should extend beyond the $n = 20$ orbits of our longest simulations. Also, the system parameter $z = r_a/r_t$ that sets the power-law index c is defined based on two concepts that are not themselves entirely well defined: the adiabatic shielding radius r_a and the tidal radius r_t. Moreover, since our model does not predict the larger evolution of the subhalo density profile, we use the subhalo's initial density profile to define r_a and r_t even though the density profile quickly begins to

change. For these reasons, we anticipate that it is possible to find a better-motivated parameter to replace $z = r_a/r_t$.

Nevertheless, this model describes the results of our simulations with remarkable success. As further validation, we consider the library of idealized subhalo simulations, called DASH (for dynamical aspects of subhaloes), published by Ref. [342]. These simulations have a lower resolution than ours, but because of the extraordinary volume of this library, it still supplies a valuable test for our model. In Appendix D.4 we verify that modulo substantial scatter and certain systematic effects associated with their lower resolution, the DASH simulations are consistent with our model.

5.6 Comparison to previous work

Numerous prior works have endeavored to model the impact of tidal effects on a subhalo's dynamical evolution [340, 341, 410–417]. In this section, we explore how our results compare to those of previous studies. Motivated primarily by simulations, our model is based on the notion that a subhalo's J-factor evolution is determined by

$$\frac{1}{J}\frac{\mathrm{d}J}{\mathrm{d}n} = -bn^{-c}, \tag{5.8}$$

where b and c are functions of the host-subhalo system and n counts the number of orbits. In contrast to our focus on the J factor, previous works have largely focused on the evolution of a subhalo's total bound mass m_{bound} and of its maximum circular velocity v_{max} and corresponding radius r_{max}. However, the general form of our model is not specific to the J factor, and we show in Appendix D.5 that it can also describe the evolution of v_{max}, r_{max}, and m_{bound}.

Despite the broad applicability of our model suggested by Appendix D.5, no prior work (to our knowledge) has proposed tidal evolution of the form given in Eq. (5.8). Broadly, prior models of tidal evolution fall into two main categories, although a given work may employ more than one:

(1) Tidal stripping models, where material outside the characteristic tidal radius [e.g., Eq. (5.24)] is assumed to be stripped over some time period;

(2) Tidal heating models, where energy injected by tidal forces heats subhalo material, causing it to rise and possibly become freed from the subhalo.

We found in Sec. 5.4.1 that the parameter b in Eq. (5.8), which characterizes the rate of tidal

121

evolution, is tightly sensitive to the energy injected by tidal forces (see Fig. 5.9). Additionally, we observed in Sec. 5.3 that the tidal evolution in our simulations closely resembles that predicted by a toy model of tidal heating. Consequently, we anticipate that of the two classes of models, tidal heating models should yield results most similar to those of our model. We will first compare the results of our model to those of the tidal heating model developed by Ref. [416], hereafter P14.

However, prior treatments of dark matter annihilation within subhalos predominantly treat the impact of the host halo's tidal forces using models based on tidal stripping [224, 347, 348, 404–407]. Tidal stripping models cannot prescribe how to change a subhalo's density profile below the tidal radius, but it is possible to apply a simulation-tuned prescription for how the density profile responds to mass loss [340, 341]. We will subsequently compare the results of our model to those of a tidal stripping model developed by Ref. [417] (hereafter J16), using the prescription of Ref. [341] (hereafter P10) to predict the subhalo's density profile. This pair of models has been employed by Refs. [347, 407] to predict dark matter annihilation rates in subhalos.

5.6.1 Comparison to a tidal heating model

We first compare our model's predictions to those of the analytic tidal heating model given in P14. In the tidal heating picture, energy injected by tidal forces causes subhalo material to move to higher radii, and P14 employed the assumption of virial equilibrium to predict this change in radius and consequently the subhalo's new density profile. We follow the prescription in P14[15] to compute the evolution of a subhalo's density profile, subsequently integrating it to obtain the J factor. Figure 5.14 shows a sample of the resulting J-factor trajectories, and we compare those trajectories to our model's predictions and to the results of our simulations. Generally, we find that for a model constructed from first principles, the P14 model is remarkably accurate. However, it does not fully capture the sensitivity of tidal evolution to system parameters, a matter we explore next.

The quantity $Q = \Delta E/r^2$ employed by P14 is related to host-subhalo system parameters by $Q/(G\rho_s) = 4\pi(\ln 2)N/x$, where N is the number of orbits over which the energy injection is taken and x is the system parameter (see Sec. 5.4). For our comparison, we take $N = 1$ and iterate the

---

[15]For simplicity, we compute the energy injection ΔE directly using the impulse approximation (Appendix D.3), neglecting additional corrections suggested in P14; these corrections will not qualitatively alter the results.
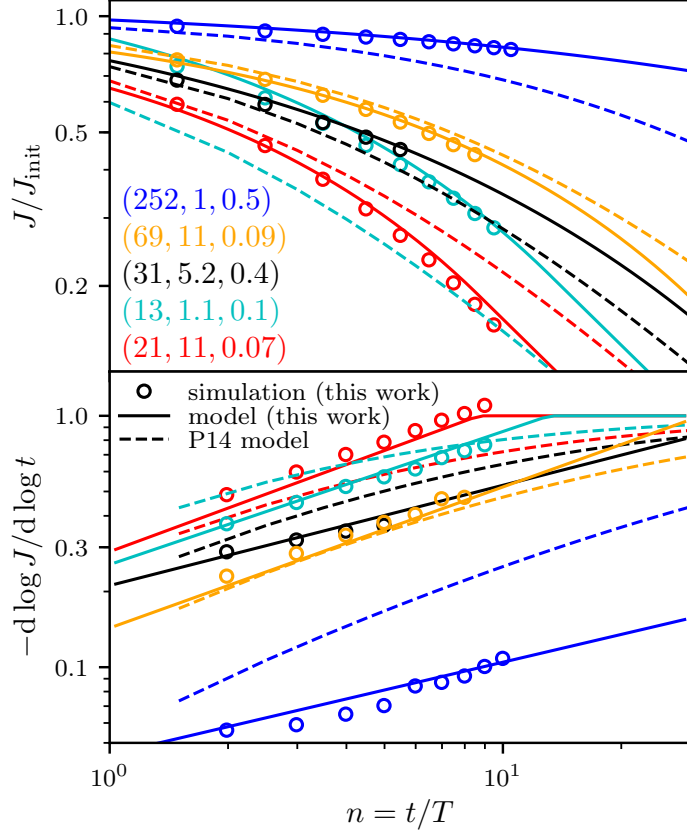
Figure 5.14: A comparison between our tidal evolution model (solid lines) and the analytic tidal heating model developed in Ref. [416] (P14, dashed lines). This figure shows the J-factor trajectory and its logarithmic derivative for different host-subhalo parameters (x, y, z), listed on the figure. We also show our simulation results (as circles) for these parameters. The P14 predictions exhibit the correct trends, but they are only reasonably accurate for a small range of host-subhalo system parameters.

calculation, assuming the halo revirializes during each orbit. Since the density profile evolution in P14 is only sensitive to the ratio $Q/(G\rho_s)$, we see immediately that this model's predictions are sensitive only to the system parameter x and are insensitive to y and z. Additionally, the J-factor evolution predicted by P14 turns out to be only sensitive to x in the combination n/x, where $n = t/T$ is the number of orbits, so every system follows the same trajectory rescaled in time. In this respect, the P14 model is similar to the toy model we explored in Sec. 5.3.2, which was only sensitive to the combination fn of system parameters f and orbit count n. In fact, the P14 model approximately obeys the toy model solution Eq. (5.12) with $b \simeq 3.2/x$ and $B = 1$, but it can potentially transition between the $n/x \ll 1$ and $n/x \gg 1$ regimes extremely slowly, and all behavior seen in Fig. 5.14 is in the intermediate regime.

The combination of its single time-rescaled trajectory and its insensitivity to y and z leaves the P14 model unable to accurately predict tidal evolution in the full host-subhalo parameter space. We see evidence of this deficiency in Fig. 5.14, but we further note that we did not plot any subhalos in the $y \ll 1$ regime. In this regime, the P14 model dramatically overestimates the impact of tidal stripping since it does not account for the directions of tidal forces, which are encapsulated in the parameter y. While the P14 model yields reasonably accurate predictions over a small range of host-subhalo system parameters, our model can accurately predict the evolution of a much broader variety of systems.

5.6.2 Comparison to a tidal stripping model

Finally, we compare our model to a semianalytic model of tidal stripping that has been employed in previous calculations of annihilation rates in the substructure [347, 407]. This semianalytic model uses the tidal stripping model in J16 to characterize a subhalo's mass loss, subsequently using the results of P10 to connect this mass loss to the subhalo's density profile and hence annihilation signal. In J16, the rate of mass loss for subhalos of mass m inside a host halo of mass M, averaged over subhalo orbits, is modeled using

$$\frac{\mathrm{d}m}{\mathrm{d}t} = -\mathcal{A}\frac{m}{t_{\mathrm{dyn}}}\left(\frac{m}{M}\right)^{\zeta}. \tag{5.29}$$

Here, $\mathcal{A}$ and ζ are simulation-tuned parameters and t_{dyn} is the host's dynamical timescale at its virial radius (e.g., Ref. [392]). For this comparison we adopt J16's central values $\mathcal{A} = 0.86$ and $\zeta = 0.07$.

In P10, it is shown that the subhalo's maximum circular velocity v_{max} and the radius r_{max} at which it is attained are related to the fraction m/m_{acc} of the subhalo's mass that remains gravitationally bound, where m_{acc} is the subhalo's virial mass at accretion. We confirm in Appendix D.5 that these relations are reasonably accurate if $y > 1$ and the subhalos have concentration $r_{\mathrm{vir}}/r_s \simeq 20$ at accretion. If we assume that subhalos possess NFW profiles, then the mass fraction m/m_{acc} predicted by J16 thereby determines each subhalo's J factor.

To compare our model, we employ the same subhalo orbital distribution considered in J16, which is drawn from Ref. [413]. The circular orbit radius R_c is taken to be uniformly distributed between $0.6R_{\mathrm{vir}}$ and R_{vir}, where R_{vir} is the host's virial radius. Meanwhile, the circularity η is distributed proportionally to $\sin \pi \eta$, and we assume that the distributions of R_c and η are independent. By
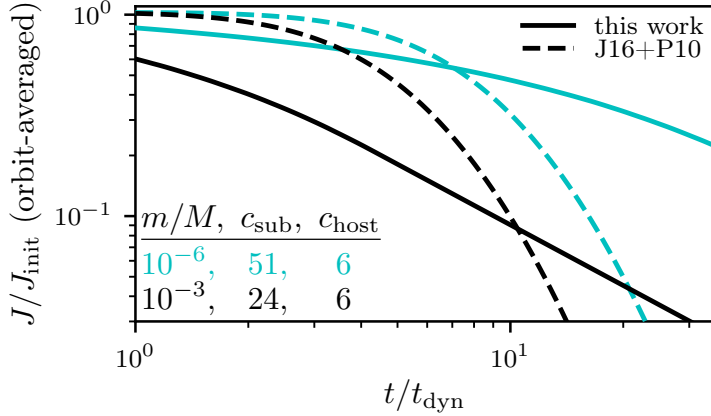
Figure 5.15: A comparison between our tidal evolution model and the semianalytic model developed in Refs. [417] (J16) and [341] (P10). This figure shows the orbit-averaged J-factor trajectory of subhalos of mass m and concentration c_{sub} within a host halo of mass M and concentration c_{host}. Compared to our model, the semianalytic model underestimates the impact of tidal stripping early on while overestimating its impact at late times. Since the plotted trajectories are averaged over subhalo orbits, we cannot plot simulation results for comparison; nevertheless, Fig. 5.14 illustrates that our model matches simulation results reasonably well.

drawing subhalo orbits from this distribution, we are able to compute the orbit-averaged[16] value of J/J_{init} using our model given in Eq. (5.28). In Fig. 5.15, we plot the resulting orbit-averaged J-factor trajectories along with those predicted by the semianalytic model of J16 and P10. We consider two different host-subhalo systems, listed on the figure, and since the semianalytic model is sensitive to the total virial masses of the host and subhalo, we employ the concentration parameter $c \equiv r_{\mathrm{vir}}/r_s$ to describe these systems; c_{host} is the host halo's concentration, while c_{sub} is the subhalo's concentration when it is accreted.

Compared to our model, Fig. 5.15 shows that the semianalytic model underestimates the impact of tidal forces early on while overestimating their impact at late times. These discrepancies arise from several sources. As we show in Appendix D.5, a subhalo's J factor after tidal evolution is about 30% smaller than what would be predicted from its parameters r_{max} and v_{max} assuming an NFW profile. However, this source of error is relatively minor. The main differences arise from the model in J16 given by Eq. (5.29). Since this model does not account for the subhalo's density profile, it takes too long to strip the subhalo's weakly bound outskirts (beyond r_s) that contribute little to

---

[16]Specifically, we take the median J/J_{init} at each time, but using the mean or the logarithmic mean instead does not significantly alter the results.

annihilation rates.[17] This behavior partially explains why the semianalytic model underestimates the early impact of tidal effects. Meanwhile, for small $\zeta \ll 1$, Eq. (5.29) describes nearly exponential decay, analogous to our model, Eq. (5.8), with $c = 0$. Without the braking behavior contributed by $c > 0$ (and attributed to changes in the shape of the subhalo's density profile; see Sec. 5.3) along with the limiting $|\mathrm{d}\ln J/\mathrm{d}\ln t| \sim 1$ behavior, the semianalytic model overestimates the impact of tidal effects at late times. For these reasons, our simulation-tuned model supplies significantly more accurate predictions of subhalo annihilation rates.

5.7   Conclusion

In this work, we used 52 idealized N-body simulations to develop a model that can predict the impact of a host halo's tidal forces on the rates of dark matter annihilation within its subhalos. Our model is given by Eq. (5.28) and summarized in Sec. 5.5, and it predicts the evolution of the subhalo's J factor, the factor in the annihilation rate that depends on mass distribution, as a function of the subhalo's orbit and other properties of the host-subhalo system. These properties are distilled into three physically motivated variables x, y, and z that characterize the energy injected by tidal forces, the ratio of stretching to compressive tidal forces, and the radial distribution of tidally heated material, respectively. Appendix D.3 details how to compute these variables from standard properties of the host-subhalo system.

Our model is based on the notion that for sufficiently small changes in J, the J factor evolves according to

$$\frac{1}{J}\frac{\mathrm{d}J}{\mathrm{d}n} = -bn^{-c}, \tag{5.8}$$

where $n = t/T$ is the time in units of the subhalo's orbital period and b and c are parameters that depend on the system. If $c = 0$, Eq. (5.8) states that the subhalo loses a fixed fraction e^{-b} of its J factor in each orbit. The parameter $c \geq 0$ is motivated by simulation results and adds a braking mechanism to the J factor's decay. To our knowledge, a model of this form has not previously been put forward, even though we find that it can also describe other structural properties of the

---

[17]For the two cases shown in Fig. 5.15, it takes, respectively, 6 and 3 dynamical times for the J16 model to bring the subhalo's bound mass below its initial $m_{\max}$, the mass enclosed within the radius $r_{\max}$ at which the maximum circular velocity is attained. As we find in Appendix D.5 (see Fig. D.6), the drop in the J factor is minimal above this mass threshold.

subhalo. We also find that our model predicts significantly different J-factor trajectories than prior semianalytic models. We further validate our model by testing it against the publicly available DASH library of subhalo simulations [342], finding reasonable agreement.

Our model has limitations. As presented, it is restricted to host-subhalo systems in which both halos possess NFW density profiles. The NFW profile (possibly with minor corrections; e.g., Ref. [337]) arises generically in dark matter simulations of halos built by hierarchical clustering [205, 260]. However, the smallest subhalos, forming by direct collapse, exhibit steeper density profiles [26, 226, 261–266, 336]. Additionally, the density profiles of many galactic halos (but not all [421]) are inferred to be shallower than the NFW profile, an observation that may be explained by baryonic effects or unknown dark matter properties (see Refs. [396, 438] for reviews). Despite being developed using NFW profiles, we anticipate that the physical manner in which we defined the model parameters x, y, and z implies that our model can be adapted to accommodate different host or subhalo density profiles.

Also, our model only accounts for tidal forces from the host halo. Subhalos can also be disrupted by encounters with other subhalos, but the results of Ref. [328] suggest that this effect is subdominant. More importantly, subhalos can be affected by baryonic content residing within the host, such as stars (e.g., Refs. [264, 322–327, 400, 432, 439]) or a disk (e.g., Refs. [322, 327, 405, 410, 439–445]). These effects are not included in our model and must be accounted for separately. However, we remark that many of the dwarf spheroidal galaxies, already some of the most promising targets for dark matter annihilation searches [344], have such little baryonic content (e.g., Ref. [446]) that it may be possible to neglect the influence of this content on their subhalos.

Despite these limitations, we anticipate that our model will prove useful in understanding the annihilation signals of dark matter substructure. In Chapter 7, we will explore the consequences of our model by using it to study microhalo-dominated annihilation signals in nearby dwarf galaxies. Such signals are expected to arise from certain cosmological scenarios, such as an early matter-dominated era prior to nucleosynthesis, and our model enables precise characterization of the magnitude and morphology of these signals.

CHAPTER 6:
EVOLUTION OF DARK MATTER MICROHALOS THROUGH STELLAR ENCOUNTERS[1]

6.1   Introduction

Dark matter structure grows through hierarchical assembly; the smallest halos form first, and larger halos grow through subsequent mergers and accretion of smaller halos. The latter are not destroyed by this assembly process but instead broadly survive as subhalos of their new hosts, and cosmological simulations reveal copious substructure within each dark matter halo (e.g., Refs. [447–452]). In the cold dark matter scenario, the smallest halos may be earth mass or smaller [321, 388, 453], and many of these microhalos are expected to persist today within galactic halos [264, 321, 325, 327].

The present-day abundance and structure of dark matter microhalos are important to astrophysical dark matter detection efforts. Thanks to their early formation, these halos would possess the highest characteristic density of any dark matter objects, making them important contributors to prospective signals from dark matter annihilation [263–265, 284, 321, 345, 347, 400–407, 454, 455] (see Ref. [348] for a review). Their high density also makes them promising targets for gravitational searches, whether through microlensing (e.g., Refs. [349, 351, 352, 456]), timing delays (e.g., Refs. [353, 457, 458]), or the dynamics of stars or other astrophysical systems (e.g., Refs. [200, 201, 354, 459, 460]). Conversely, any observational constraints on the structure and abundance of these microhalos serve as cosmological probes. The mass scale of the smallest halos directly reflects the free-streaming scale of the dark matter particle. Meanwhile, the abundance and internal structures of microhalos are closely linked to the statistics of the primordial density fluctuations from which they formed [336] (see also Refs. [314, 316, 382, 383]), and these fluctuations are sensitive to the details of both inflation (e.g., Refs. [27–31, 38, 40, 49, 51–53, 56, 69–71, 73–76, 78–81]) and the postinflationary

---

cosmic history (e.g., Refs. [181–183, 191, 206, 224]).

However, microhalos are subjected to complex dynamical processes after accretion onto a host halo, and the impact of these processes must be understood in order to accurately predict microhalo populations. These microhalos experience gradual disruption by means of tidal forces from the host, encounters with other substructures, and dynamical friction. Subhalo survival prospects resulting from these processes have been widely studied (e.g., Refs. [284, 325, 328, 340–342, 395, 399, 408–417]). Additionally, within galaxies microhalos are susceptible to encounters with individual stars. The objective of this work is to develop a general framework, applicable to a wide variety of systems, that can predict the evolution of a microhalo's density profile through stellar encounters.

Previous works have explored the impact of stellar encounters on dark matter microhalos. A common strategy (e.g., Refs. [323–325, 327, 439]) is to compare the total energy injected by a stellar encounter to the total binding energy of the microhalo. However, as Ref. [328] has noted, this comparison is not directly connected to the question of halo survival because such energy injections are not distributed efficiently; the least bound particles, at large radii, receive the most energy. Prior works have also employed semianalytic models [326] and numerical simulations [264, 322, 324, 327] to study the impact of stellar encounters. However, the scopes of these investigations have been limited; they typically aim to understand the microhalo's energy injection or mass loss or focus on the survival of microhalos near the solar neighborhood. Our work is much more general. We study the evolution of a microhalo's full density profile due to an arbitrary series of stellar encounters.

The smallest microhalos are expected to form with $\rho \propto r^{-3/2}$ inner density profiles [26, 226, 261–266, 336, 454], but successive mergers tend to shallow their inner cusps toward $\rho \propto r^{-1}$ [262, 280, 336]. Accordingly, we study microhalos that initially possess the Navarro-Frenk-White (NFW) density profile [205, 260],

$$\rho(r) = \frac{\rho_s}{(r/r_s)(1 + r/r_s)^2}, \tag{6.1}$$

which has scale parameters r_s and ρ_s and a $\rho \propto r^{-1}$ cusp. We use high-resolution N-body simulations of 96 stellar encounters to explore the parameter space of encounters with these microhalos, and we consider both first and successive encounters. For validation we also simulate randomized realistic sequences of encounters. The framework we develop predicts the density profile of a microhalo after arbitrarily many stellar encounters predominantly as a function of the energy injected by each

encounter. We also find that the density profile after stellar encounters is nearly universal, which simplifies the problem considerably.

This chapter is organized as follows. In Sec. 6.2, we detail how our simulations are carried out. Section 6.3 develops a parametrization of stellar encounters and shows how our simulated encounters are distributed. In Sec. 6.4, we use our simulation results to develop a model for the impact of distant encounters, where the impact parameter is much larger than the halo, and we consider both initial and successive encounters. Section 6.5 discusses the impact of closer encounters. In Sec. 6.6, we explore the application of our model to microhalos passing through fields of stars. Section 6.7 concludes. Finally, Appendix E.1 explores the range of validity of the impulse approximation that we employ throughout this work, while Appendix E.2 explores the impact of encounters occurring in close succession.

6.2   Simulations

We follow Refs. [264, 322, 324, 327] in using N-body simulations to study a microhalo's response to a stellar encounter. We prepare the microhalo with an NFW density profile using the same procedure as Ref. [395]. We draw particles from an isotropic distribution function computed using the fitting formula in Ref. [422]. Additionally, to better resolve the microhalo's central region, we sample particles whose orbital pericenters are below $r_s/3$, where r_s is the microhalo's scale radius, with 64 times the number density and 1/64 the mass of the other particles.[2] We cut off the density profile at $r = 500r_s$; subhalo particles this far out are completely stripped by even a glancing encounter, so as long as the cutoff radius is much larger than r_s, the precise choice makes no difference. We represent the subhalo using a total of 8×10^6 particles, and roughly 70% of them, carrying roughly 4% of the total mass, are high-resolution particles.

To simulate a stellar encounter, we follow Refs. [264, 322] in perturbing the velocities of microhalo particles using the impulse approximation, in which these particles are treated as stationary while the passing star exerts a tidal acceleration on each particle. Consider an encounter with impact parameter b and relative velocity V, and center a coordinate system on the microhalo such that

---

[2]Mixing particles of different masses can induce a discreteness artifact wherein two-body interactions transfer energy from heavy to light particles [461]. However, this effect is suppressed in our halo construction by the high particle count and the initial radial segregation between the particle types. Reference [395] verified that there is no tendency for the heavier particles to sink to lower radii within our halos even after hundreds of dynamical time intervals.

the star is at position $(-Vt, b, 0)$ at time t. Since a microhalo is typically much larger than a solar system (e.g., Sec. 6.6), the star can be accurately treated as a point mass. By integrating the tidal acceleration it is straightforward to show that a particle at position (x, y, z) experiences velocity injection

$$\Delta \boldsymbol{v} = -\frac{2GM_*}{V} \frac{1}{(y-b)^2 + z^2} \left(0, \frac{(y-b)y + z^2}{b}, z \right), \tag{6.2}$$

where M_* is the mass of the star.

Application of the impulsive velocity injections given by Eq. (6.2) is computationally faster and more numerically stable than adding a new particle to the simulation to represent the star, owing to the star's immense velocity and mass compared to those of microhalo particles. Moreover, we expect the impulse approximation to be valid in most scenarios because due to the size difference, a microhalo's internal velocity dispersion is typically much smaller than that of its host. A passing star's relative velocity is thus expected to be much greater than that of microhalo particles. However, to clarify the conditions under which the impulse approximation is valid, we explicitly simulate a passing star in Appendix E.1; we find that the approximation yields accurate results as long as

$$t_{\text{dyn}} \gtrsim 5b/V, \tag{6.3}$$

where t_{dyn} is the initial microhalo's dynamical timescale given by [392]

$$t_{\text{dyn}} \equiv \sqrt{3\pi/(16G\rho_s)}. \tag{6.4}$$

Here, ρ_s is the microhalo's scale density.

After perturbing the velocities of microhalo particles, we use the N-body simulation code GADGET-2 to simulate the microhalo's response. The force-softening length is set at $\epsilon = 0.003r_s$, a small value that allows radii as small as $2.8\epsilon \simeq 0.01r_s$ to be resolved. When studying microhalo density profiles, we use the procedure in Ref. [395] to set the resolution limit as the largest of the limits set by the softening length, Poisson noise, and artificial relaxation.

Each microhalo may experience a large number of stellar encounters, so it is necessary to also study a microhalo's response to successive encounters. To prepare a stellar encounter after the first, we extract the self-bound remnant of the microhalo at the end of a prior simulation using an

131
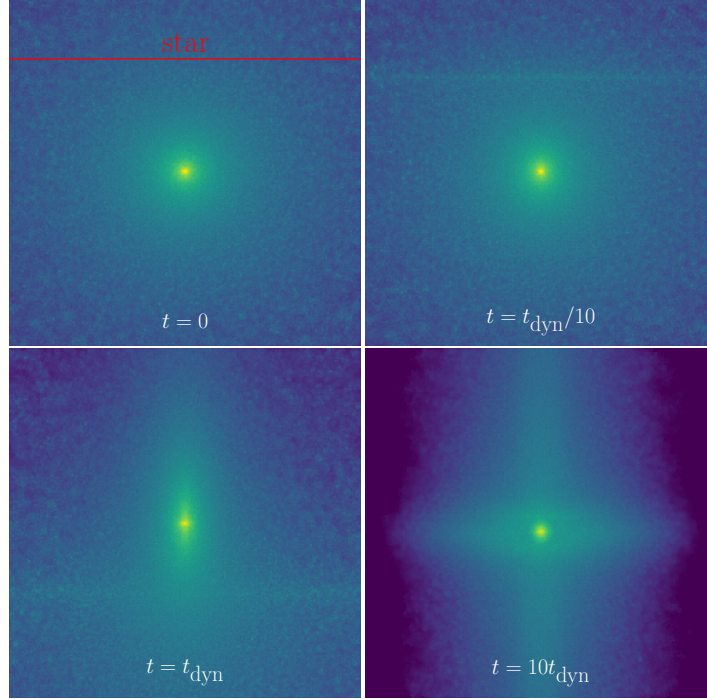
Figure 6.1: The projected density field of a microhalo subjected to a stellar encounter. Each panel has width $50r_s$, where r_s is the microhalo scale radius. The density is computed using a k-nearest-neighbor density estimate with $k = 50$ and is plotted with a logarithmic color scale (lighter is denser).

iterative procedure detailed in Ref. [395]. We compute the potential energy of each particle due to other bound particles and use that energy to determine whether each particle is bound; this process is iterated until the number of bound particles converges. The resulting bound remnant is then subjected to a stellar encounter using Eq. (6.2).

Figure 6.1 illustrates a stellar encounter with an NFW microhalo simulated in this way. 96% of the initial mass of the microhalo is freed by the encounter, but a highly dense remnant remains. While the final system is significantly nonspherical, the dense remnant itself is highly spherical, and Fig. 6.2 shows the evolution of the microhalo's spherically averaged density profile. The central profile stabilizes over the course of a single dynamical time interval t_{dyn}, and the stable region grows over time. The final density profile is well fit by

$$\rho = \rho_s' \frac{r_s'}{r} \exp\left[-\frac{1}{\alpha}\left(\frac{r}{r_s'}\right)^{\alpha}\right] \tag{6.5}$$

with different scale parameters r_s' and ρ_s' and an additional parameter $\alpha = 0.78$. For this profile,
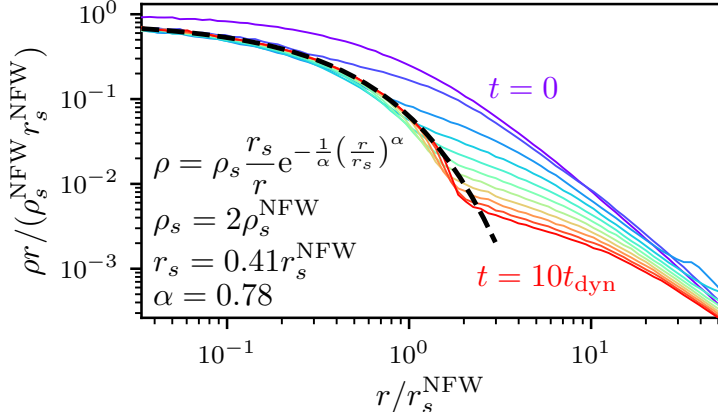
Figure 6.2: The density profile of the microhalo depicted in Fig. 6.1. Each curve indicates the passage of a single dynamical time $t_{\rm dyn}$ given by Eq. (6.4). This profile, initially an NFW profile with parameters $\rho_s^{\rm NFW}$ and $r_s^{\rm NFW}$, stabilizes into the form given by Eq. (6.5) with fitting parameters shown. All particles are plotted, not only particles bound to the halo, and beyond the stable part of the density profile the mean radial motion is typically outward.

ρ_s' and r_s' are defined analogously to the parameters of the NFW profile: r_s' is the radius at which $\mathrm{d}\ln\rho/\mathrm{d}\ln r = -2$, and at small radii, the profile asymptotes to $\rho(r) = \rho_s' r_s'/r$. However, the profile in Eq. (6.5) decays much more rapidly than the NFW profile at large radii. In this respect it is similar to density profiles proposed to result from tidal evolution within host halos (e.g., Refs. [340, 341, 462]), although its functional form is more closely inspired by the Einasto profile [463], which differs only in lacking the r_s'/r factor.

We simulated a variety of stellar encounter scenarios, including up to five successive encounters with a single microhalo.[3] In each case, we simulated the microhalo for the same duration of $10t_{\rm dyn}^{\rm NFW}$, where $t_{\rm dyn}^{\rm NFW}$ is the dynamical timescale of the initial NFW halo.[4] We find that the density profile of a microhalo subjected to any number of stellar encounters almost universally follows Eq. (6.5) with the same $\alpha = 0.78$. In subsequent sections, we will demonstrate the near universality of this profile and discuss when it fails to apply.

---

[3]Successive encounters are cosmologically relevant. For instance, we find in Sec. 6.6 that microhalos in the solar vicinity are expected to have experienced potentially thousands of stellar encounters, although the precise number depends on the threshold impact parameter for inclusion.

[4]Stellar encounters raise the characteristic density of the subhalo remnant by stripping its less-dense outskirts, thereby reducing its dynamical timescale. Hence, our simulations always last at least 10 times the dynamical timescale of the initial microhalo, even when the initial microhalo has already experienced an encounter.

6.3 Parametrization of encounters

Our goal is to understand the impact of a stellar encounter with mass M_*, relative velocity V, and impact parameter b on a microhalo with scale density ρ_s and scale radius r_s. The stellar encounter is characterized by these five parameters, but they exhibit substantial degeneracy. Equation (6.2) implies that for a halo of characteristic size r_s, velocity injections are proportional to a characteristic velocity injection

$$\Delta v \equiv \frac{GM_*}{Vb^2} r_s f\left(\frac{r_s}{b}\right),\tag{6.6}$$

where $f(x) = 1 + \mathcal{O}(x)$ is a nonlinear function. Meanwhile, particle velocities within a halo of characteristic scale r_s and density ρ_s are proportional to a characteristic velocity $v \equiv r_s\sqrt{G\rho_s}$, so

$$\frac{\Delta v}{v} = \sqrt{\frac{G}{\rho_s}}\frac{M_*}{Vb^2} f\left(\frac{r_s}{b}\right)\tag{6.7}$$

is the characteristic relative velocity injection. The dynamical impact of a stellar encounter is thus a function of just two parameters: $\sqrt{G/\rho_s}M_*/(Vb^2)$ and r_s/b.

We are free to choose a parametrization that is any set of independent functions of these two parameters, and we do so in the following way. In the $b \gg r_s$ limit, Eq. (6.2) implies that the energy $(1/2)|\Delta v|^2$ (per mass) injected into a particle at cylindrical radius r_s (in the y-z plane) is

$$\Delta E = \frac{2G^2 M_*^2 r_s^2}{V^2 b^4}.\tag{6.8}$$

The b^{-4} divergence at small b owes to the choice of reference frame: Eq. (6.2) specifies the velocity change relative to that of the initial halo's center. However, to understand the dynamics of the halo remnant, the more relevant energy injection is that relative to the halo remnant's center of mass, whose trajectory may differ from that of the halo's center if $b \lesssim r_s$. Reference [464] found that the energy injected by an impulsive encounter is well fit by a form proportional to $1/[1 + (b/r_s)^4]$. With this scaling, Eq. (6.8) becomes

$$\Delta E = \frac{2G^2 M_*^2 r_s^2}{V^2 \left(b^4 + r_s^4\right)}.\tag{6.9}$$

While Ref. [464] studied star clusters with King density profiles [465] instead of dark matter halos, we will see later that this scaling works well for our simulated dark matter halos.
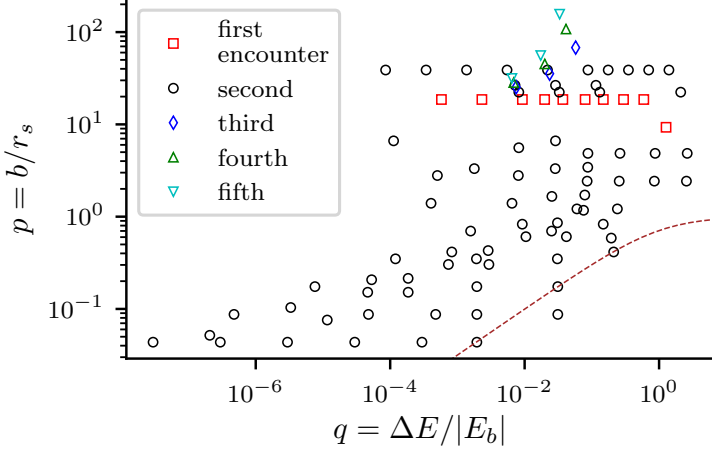
Figure 6.3: The distribution of our 96 stellar encounter simulations. For first encounters, the initial halo has an NFW profile. Higher-order encounters begin with the remnant of a previous encounter. The dashed curve corresponds to $(1 + q^{-1})^{1/2} p = 1$; as we discuss in Sec. 6.5, this outlines the region wherein nonlinearities in the impulsive velocity injections become dominant, typically resulting in disruption of the halo's central cusp. For first encounters, q and p are defined using the results of Sec. 6.4.2.

The characteristic binding energy (per mass) of a particle within a microhalo with scale radius r_s and scale density ρ_s is

$$E_b = -4\pi G \rho_s r_s^2. \tag{6.10}$$

We define one parameter as the encounter's relative energy injection $q \equiv \Delta E / |E_b|$, which implies that

$$q = \frac{G}{2\pi} \frac{M_*^2}{\rho_s V^2 \left(b^4 + r_s^4\right)}. \tag{6.11}$$

We define our second parameter as the relative distance of the encounter,

$$p \equiv b/r_s. \tag{6.12}$$

To probe the impact of stellar encounters, we now explore the q-p parameter space. We carried out 96 simulations using the procedure in Sec. 6.2, and the distribution of these simulations is depicted in Fig. 6.3. The choices of encounters will be motivated in subsequent sections.

6.4   Impact of distant encounters

We begin by studying distant encounters with $b \gg r_s$, and we employ the 36 simulations depicted in Fig. 6.3 for which $p = b/r_s > 8$. In this regime, the nonlinearities (with respect to spatial
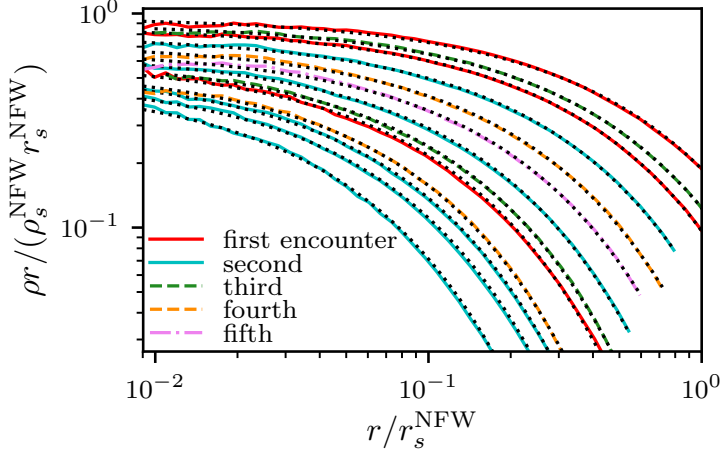
Figure 6.4: A demonstration of the universality of the density profile given by Eq. (6.5) with $\alpha = 0.78$. This figure shows the density profiles (solid, dashed, and dot-dashed lines) resulting from 13 of our 36 simulations with $b \gg r_s$; this sample spans $5 \times 10^{-3} < q < 2$. The dotted lines indicate the fits to each profile using Eq. (6.5) with $\alpha = 0.78$ enforced. Density and radius are expressed in units of the parameters of the original NFW microhalo.

coordinates) in the velocity injections given by Eq. (6.2) are negligible, and the encounter is solely described by the parameter $q = \Delta E/|E_b|$ given by Eq. (6.11). Additionally, the density profile that results from stellar encounters in this regime is universal. Figure 6.4 demonstrates that Eq. (6.5) with $\alpha = 0.78$ can accurately fit the outcome of any succession of stellar encounters. Consequently, it is not necessary to track the full succession of stellar encounters. Instead, we need only to consider two cases:

(1) encounters with microhalos whose density profiles are given by Eq. (6.5) with $\alpha = 0.78$;

(2) encounters with NFW microhalos.

The second case represents a microhalo's first stellar encounter, but it is the more complicated of the two scenarios because it changes the shape of the halo's density profile. We begin by instead studying the first case, which corresponds to successive stellar encounters. This scenario is simple because the microhalo's density profile after an encounter is purely rescaled from its profile beforehand.

6.4.1 Successive encounters

We consider a stellar encounter with a microhalo that already experienced an encounter; that is, a microhalo with a density profile given by Eq. (6.5) with $\alpha = 0.78$. Let r_s and ρ_s be the scale parameters of the microhalo prior to the encounter and r'_s and ρ'_s be its parameters afterward; the
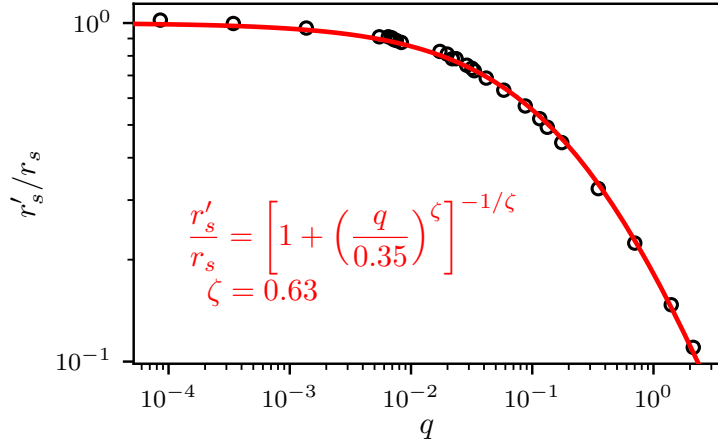
Figure 6.5: The change r'_s/r_s in a microhalo's scale radius in response to an encounter with parameter q. We plot our simulations as circles, and the relationship between r'_s/r_s and q is well fit (solid line) by the equation shown.

encounter parameter q is defined by Eq. (6.11) using r_s and ρ_s. Our objective is to find r'_s and ρ'_s as functions of r_s, ρ_s, and q.

We employ the 26 of our 36 $b \gg r_s$ simulations for which the initial halo is a remnant from a previous encounter. We obtain the scale parameters of the initial and final halos by fitting Eq. (6.5), with $\alpha = 0.78$ enforced, to the stabilized part of the density profile (see Fig. 6.2). In Fig. 6.5, we plot the radius change r'_s/r_s as a function of the relative energy injection q. This relationship is well fit by the remarkably simple form

$$\frac{r'_s}{r_s} = \left[1 + \left(\frac{q}{q_0} \right)^\zeta \right]^{-1/\zeta} \tag{6.13}$$

with just the two fitting parameters $q_0 = 0.35$ and $\zeta = 0.63$. Meanwhile, Fig. 6.6 shows that the density change ρ'_s/ρ_s is a power law in r'_s/r_s,

$$\frac{\rho'_s}{\rho_s} = \left(\frac{r'_s}{r_s} \right)^{-\eta} \tag{6.14}$$

with $\eta = 0.72$.

There is a theoretical reason to expect the behavior in Eq. (6.13) wherein $r'_s \propto q^{-1}$ for $q \gg 1$. In the $q \gg 1$ regime, all material above the halo's scale radius r_s is fully stripped, and only the halo's inner $\rho \propto r^{-1}$ density profile is relevant to dynamics. For this density profile circular velocities scale
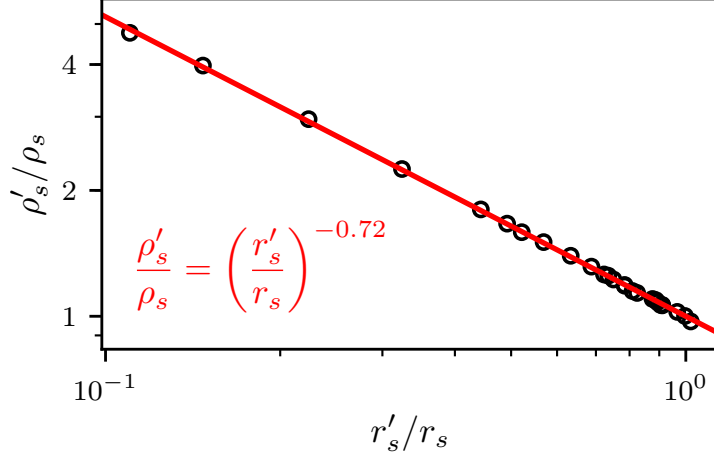
Figure 6.6: The change ρ'_s/ρ_s in a microhalo's scale density in response to an impulsive encounter, as a function of the change r'_s/r_s in its radius. This relationship is evidently a power law (solid line). Each circle represents a simulation.

as $r^{1/2}$, so the characteristic energies of particles at radius r scale as $E \propto r$. Meanwhile, the energy injection ΔE on a particle at radius r is proportional to qr^2. If the radius r'_s of the halo remnant is proportional to the radius r at which $\Delta E = E$, then $r'_s \propto q^{-1}$.

At $q \ll 1$, Eq. (6.13) has another useful interpretation. In this regime,

$$\frac{r'_s}{r_s} = \exp\left[-\frac{1}{\zeta}\left(\frac{q}{q_0}\right)^{\zeta}\right], \text{ if } q \ll 1. \tag{6.15}$$

Consider two successive encounters with the same q, each producing a change r'_s/r_s in the target halo's scale radius. Since the density profile does not change significantly with each encounter, the net change in r_s is $(r'_s/r_s)^2$. Now suppose instead that the two encounters happen simultaneously. While the geometry of the two encounters sets precisely how their velocity injections add together, on average, we expect the energy injection ΔE to double relative to a single encounter.[5] But $q \propto \Delta E$, so Eq. (6.15) implies that the net change in r_s is $(r'_s/r_s)^{2\zeta}$ in this scenario. Since $2^{\zeta} \simeq 1.55 < 2$, this calculation tells us precisely how much less efficiently a halo is altered by simultaneous stellar encounters than by successive ones. A halo's postencounter relaxation makes it more susceptible to subsequent encounters. In Appendix E.2 we show that two encounters can be treated as simultaneous

---

[5]Additivity of energy injections follows from the theory of random walks. If velocity injections are in random directions, then their squared magnitudes are additive, on average.

if they occur within a few dynamical time intervals defined by Eq. (6.4). Section 6.6 will explore how to quantify this behavior more precisely.

Despite the evident precision of the relationships depicted in Figs. 6.5 and 6.6, it is unclear whence the values $\zeta = 0.63$ and $\eta = 0.72$ in Eqs. (6.13) and (6.14) arise. The change in a microhalo's density profile is set by a complicated combination of the initial energy injection and subsequent relaxation. In Appendix E.3 we explore how the distribution of particle energies is altered by a stellar encounter, but we find no simple interpretation that describes it.

6.4.2 First encounter

Next, we explore how an NFW microhalo with parameters ρ_s^{NFW} and r_s^{NFW} evolves through a stellar encounter into a microhalo whose profile is given by Eq. (6.5) with $\alpha = 0.78$ and scale parameters ρ_s' and r_s'. We define the encounter parameter q^{NFW} as the parameter obtained through Eq. (6.11) using ρ_s^{NFW} and r_s^{NFW}. From the results of the previous section, we anticipate that r_s'/r_s^{NFW} and $\rho_s'/\rho_s^{\mathrm{NFW}}$ should follow similar functional forms to Eqs. (6.13) and (6.14). To make the connection explicit, we make the ansatz that the following two scenarios yield a microhalo with exactly the same profile parameters ρ_s' and r_s':

(1) an NFW microhalo with parameters r_s^{NFW} and ρ_s^{NFW} experiencing an encounter with mass M_*, velocity V, and impact parameter b;

(2) a microhalo whose density profile is given by Eq. (6.5) with $\alpha = 0.78$ and scale parameters $r_s = A r_s^{\mathrm{NFW}}$ and $\rho_s = B \rho_s^{\mathrm{NFW}}$ experiencing the same encounter, where A and B are universal.

This ansatz implies $q = B^{-1} q^{\mathrm{NFW}}$ in the $b \gg r_s$ regime. We additionally assume that the two halos have the same asymptote, $\rho_s^{\mathrm{NFW}} r_s^{\mathrm{NFW}} = \rho_s r_s$, which implies $B = A^{-1}$.

Using this ansatz, Eqs. (6.13) and (6.14) imply that

$$\frac{r_s'}{r_s^{\mathrm{NFW}}} = A \left[1 + \left(\frac{q^{\mathrm{NFW}}}{B q_0} \right)^{\zeta} \right]^{-1/\zeta} \tag{6.16}$$

and

$$\frac{\rho_s'}{\rho_s^{\mathrm{NFW}}} = B A^{\eta} \left(\frac{r_s'}{r_s^{\mathrm{NFW}}} \right)^{-\eta} \tag{6.17}$$

with $B = A^{-1}$ and the same $q_0 = 0.35$, $\zeta = 0.63$, and $\eta = 0.72$. We now use our ten simulations of stellar encounters with NFW microhalos to test these relationships. Figure 6.7 shows how the
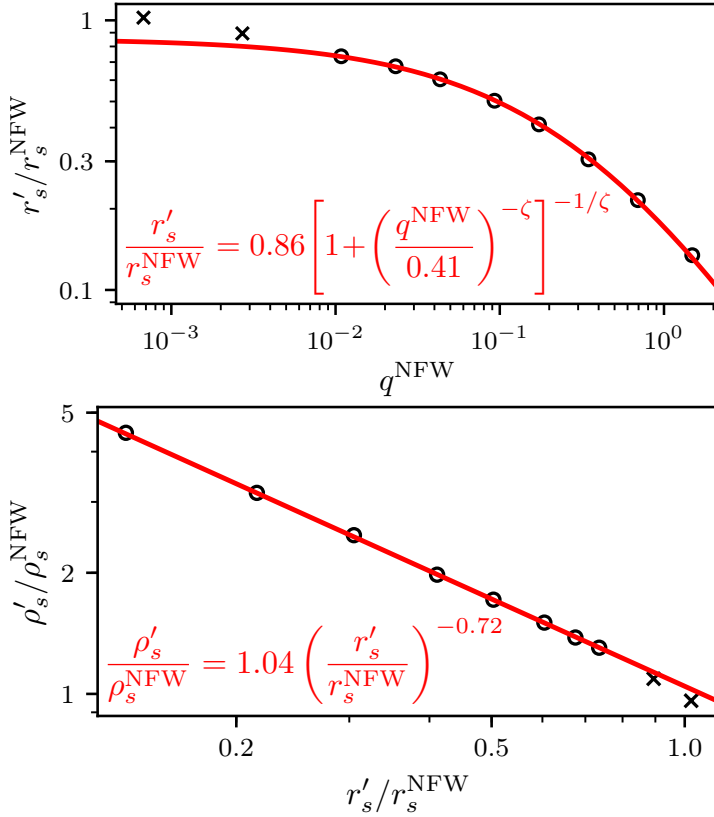
Figure 6.7: Evolution of NFW microhalos through stellar encounters. Top: The sensitivity of the scale radius r_s' of the final halo to properties of the initial halo and the encounter. Bottom: The dependence of the change in scale density on the change in scale radius. For encounters with $q^{\mathrm{NFW}} \gtrsim 10^{-2}$ (circles), we fit Eqs. (6.16) and (6.17) with only one free parameter, as discussed in the text; the fits are shown as solid lines. Encounters with $q^{\mathrm{NFW}} \lesssim 10^{-2}$ (crosses) do not obey the same relationships, an outcome we attribute to the density profile not fully evolving from NFW to the form given by Eq. (6.5).

final density profile depends on r_s^{NFW}, ρ_s^{NFW}, and q^{NFW}. We find that as long as $q^{\mathrm{NFW}} \gtrsim 10^{-2}$ the anticipated relationship is borne out, and by fitting Eqs. (6.16) and (6.17) to this regime, we obtain $A = 0.86$ and $B = A^{-1} = 1.17$. For $q^{\mathrm{NFW}} \lesssim 10^{-2}$, on the other hand, the final density profiles deviate from these relationships. An interpretation of this outcome is that too little energy is injected to fully convert the halo from the NFW profile to the form given by Eq. (6.5).

In conclusion, as long as a microhalo's particles experience minimal energy injections of order 1/100 their binding energy, an NFW microhalo with scale parameters r_s^{NFW} and ρ_s^{NFW} can be treated as having the density profile given by Eq. (6.5) with $\alpha = 0.78$ and scale parameters

$$r_s = 0.86 r_s^{\mathrm{NFW}} \quad \text{and} \quad \rho_s = 1.17 \rho_s^{\mathrm{NFW}}. \tag{6.18}$$

140
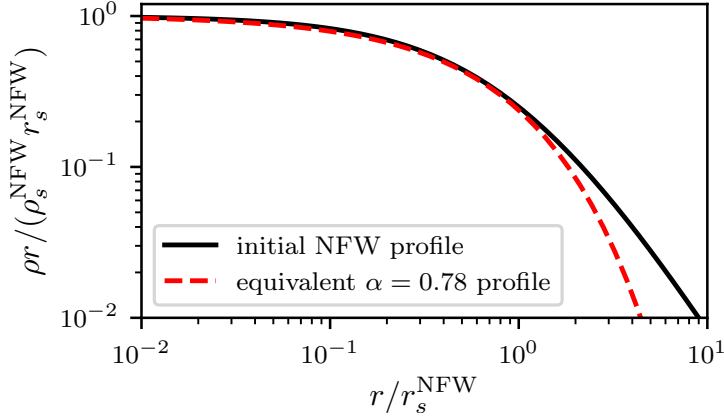
Figure 6.8: A comparison between an NFW profile and the "equivalent" profile (see the text) given by Eq. (6.5) with $\alpha = 0.78$ using the relations in Eq. (6.18). The two profiles are nearly identical except at large radii.

In a realistic scenario in which a microhalo experiences tidal forces not only from stars but also from other substructures and the galactic host, we expect that this condition will usually be satisfied. Figure 6.8 shows a comparison between these two density profiles. The equivalent Eq. (6.5) density profile drops off more quickly than the NFW profile at large radii, but the two profiles are otherwise nearly identical.

6.5   Penetrative encounters

We now turn to penetrative encounters with $b \lesssim r_s$. In this regime, two new effects become important.

(1) Nonlinear terms in the velocity injections given by Eq. (6.2) become significant.

(2) Equation (6.2) no longer accurately describes the velocity injection relative to the halo remnant's center of mass because it describes the velocity injection relative to that on the halo's initial center, whose motion may differ.[6]

We anticipate that our definition of the parameter q in Sec. 6.3 will account for the second effect. However, it is not clear how to account for the first.

We simulated 60 encounters with $p = b/r_s < 8$, as shown in Fig. 6.3. After each encounter, we

---

[6]Equation (6.2) is still suitable for initializing simulations, with the caveat that it can induce a bulk velocity on the halo remnant.

141
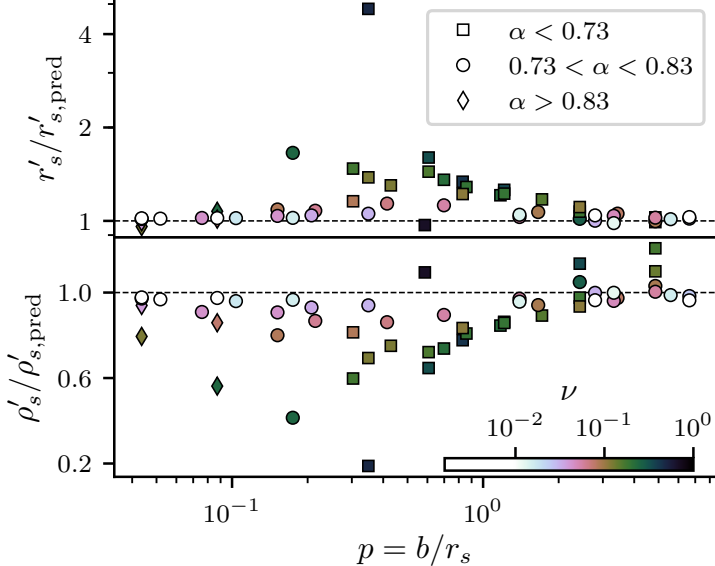
Figure 6.9: A test of the predictions from Eqs. (6.13) and (6.14) for encounters with $b \lesssim r_s$. These predictions work well for a broad range of parameters, but they fail when $\nu = p^{-1}(1+q^{-1})^{-1/2} \gtrsim 0.1$ (color scale). The relative contributions of nonlinear terms in the velocity injections are of order ν, so we find that our predictions are accurate as long as these nonlinear terms can be neglected.

fit Eq. (6.5) to the microhalo's density profile to obtain its scale parameters r_s and ρ_s. Additionally,

we find that it is now necessary to allow the parameter α to vary. Figure 6.9 compares the scale

parameters obtained in these simulations to those predicted from Eqs. (6.13) and (6.14). Evidently,

the model developed for the $b \gg r_s$ regime accurately describes evolution by stellar encounters for a

large portion of the $b \lesssim r_s$ regime, including cases where $b \ll r_s$. However, there are some encounters

for which it predicts wildly inaccurate results.

To understand where our predictions fail, we investigate when nonlinear terms in the velocity

injections become important. For a halo with characteristic internal velocities v, Eq. (6.7) implies

that the characteristic velocity injection is $\Delta v \propto q^{1/2}[1+\mathcal{O}(p^{-1})]v$, which we can separate into linear

part $\Delta v_{\mathrm{lin}} \propto q^{1/2}v$ and nonlinear part $\Delta v_{\mathrm{nl}} \propto q^{1/2}p^{-1}v$. If the nonlinear terms can be neglected,

then the characteristic final velocity is $v'_{\mathrm{lin}} = \sqrt{v^2 + \Delta v_{\mathrm{lin}}^2}$ (where we assume the direction of the

particle's velocity injection is random relative to its velocity). Hence, the relative contribution of

nonlinear terms is of order

$$\Delta v_{\mathrm{nl}}/v'_{\mathrm{lin}} \sim \nu \equiv p^{-1}(1+q^{-1})^{-1/2}. \tag{6.19}$$

We indicate the value of ν in Fig. 6.9 with a color scale, and Fig. 6.10 shows the impacts of the
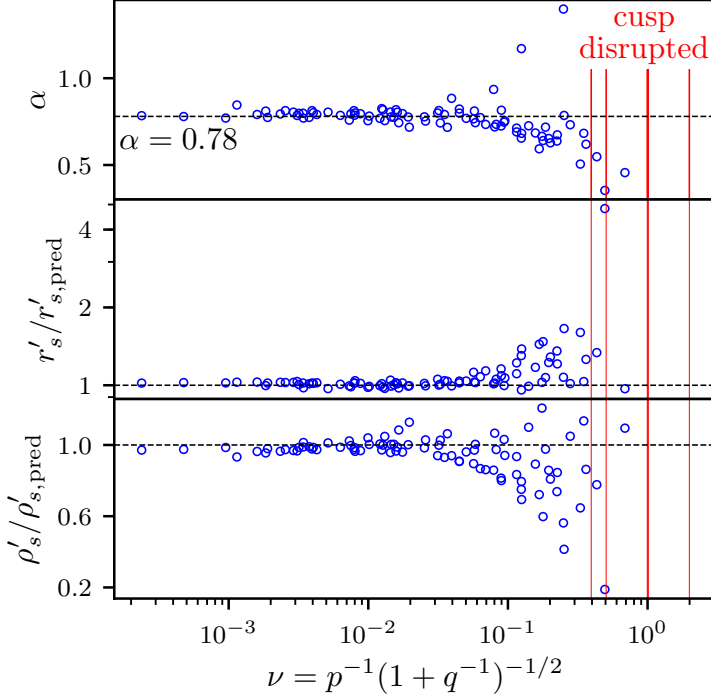
Figure 6.10: The impact of nonlinear terms in the velocity injections, which have relative magnitude of order ν. Top: The parameter α of the best-fitting density profile given by Eq. (6.5). Middle and bottom: Deviations from the predicted values of r_s and ρ_s using Eqs. (6.13) and (6.14). When $\nu \gtrsim 0.1$, deviations start to appear in all three parameters. Additionally, when $\nu \gtrsim 1$, the central $\rho \propto r^{-1}$ cusp can be disrupted (red lines; see Fig. 6.11). There is no fit for these cases.

relative nonlinearity ν more directly. If $\nu \ll 1$, then nonlinear effects are unimportant, and surely enough, we find that deviations from the predictions of Eqs. (6.13) and (6.14) are minimal when $\nu \lesssim 0.1$. On the other hand, when $\nu \gtrsim 0.1$, these deviations can become large. Additionally, the density profile is no longer universal when $\nu \lesssim 0.1$; the best-fitting value of α can deviate significantly from $\alpha = 0.78$. When $\nu \gtrsim 1$, the halo's central $\rho \propto r^{-1}$ density cusp can even be disrupted so that the logarithmic slope γ of its $\rho \propto r^{-\gamma}$ inner profile becomes smaller than 1. In some cases, a uniform-density core ($\gamma = 0$) results. These disruption scenarios are indicated in Fig. 6.10 in red, and Fig. 6.11 shows the resulting density profiles.

The precise sensitivity of the density profile to q and p after an encounter with $\nu \gtrsim 0.1$ is complicated. However, as an approximate treatment, the predictions of Eqs. (6.13) and (6.14) are reasonably accurate for $\nu \lesssim 1/3$, and when $\nu \gtrsim 1/3$, the resulting halo is close to disruption. We will see in the next section that the $\nu \gtrsim 0.1$ regime is relatively unimportant to typical microhalo scenarios.
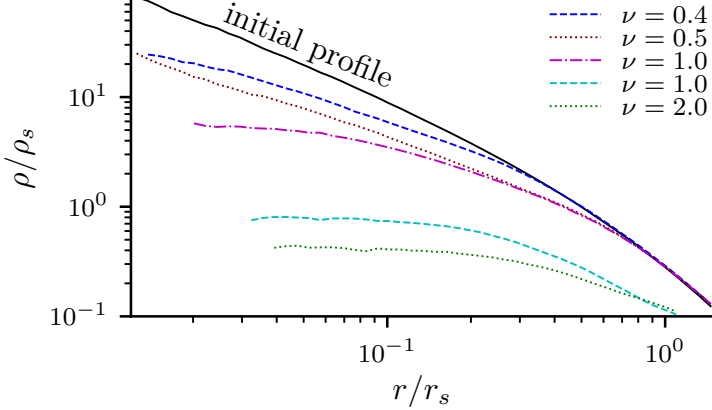
Figure 6.11: The density profiles of microhalos whose central cusps are disrupted by stellar encounters with $\nu = p^{-1}(1 + q^{-1})^{-1/2} \sim 1$. The logarithmic slopes γ of their $\rho \propto r^{-\gamma}$ inner profiles become smaller than 1, and in some cases, a uniform-density core develops ($\gamma = 0$). One disruption scenario, with $\nu = 1$, is excluded from the plot because the resulting core density is too small. The axes units are the scale density and radius of the halo prior to the encounter.

6.6   Stellar fields

We now explore the implications of the model given by Eqs. (6.13) and (6.14) for microhalos passing through fields of stars. As a representative example, we study microhalos traversing the solar neighborhood. We take the microhalos to have NFW scale parameters $\rho_s^{\mathrm{NFW}} = 1.7 \times 10^9 \ M_\odot/\mathrm{kpc}^3$ and $r_s^{\mathrm{NFW}} = 5 \times 10^{-6}$ kpc. These parameters correspond to halos with mass $m_{\mathrm{vir}} = 10^{-6} \ M_\odot$ and concentration $r_{\mathrm{vir}}/r_s = 2$ at redshift $z = 32$, which are typical parameters for the smallest halos in a cold dark matter scenario (e.g., Ref. [454]). Meanwhile, the stellar mass density of the Galactic disk at the sun's altitude is roughly $\rho_* = 4 \times 10^7 \ M_\odot/\mathrm{kpc}^3$ [392]. We assume the microhalos have velocity $V_{\mathrm{halo}} = 200$ km/s relative to the disk while the stars have mass $M_* = 0.5 M_\odot$ and velocity dispersion $\sigma_* = 50$ km/s within the disk. We consider a total duration of $t = 160$ Myr, which is roughly the amount of time microhalos whose orbits cross the solar vicinity are expected to spend inside the disk over the Galactic age [327].[7]

We sample stellar encounter positions uniformly within the cylinder of radius $b_{\mathrm{max}} = 80 r_s$ and length $V_{\mathrm{halo}} t$. For our scenario this choice of b_{max} implies that only encounters with relative energy

---

[7]For clarity, we note that the vast majority of microhalos within the Galactic halo are not expected to encounter a star due to the small relative volume occupied by the disk. In this section we specifically treat microhalos that cross the solar vicinity.

injection $q \lesssim 10^{-7}$ are excluded. A total of 1305 encounters are expected within this volume, and we sample the encounter count from the corresponding Poisson distribution. Each encounter velocity V is the vector sum of V_{halo} and a stellar velocity V_* randomly sampled using the stellar velocity dispersion.

The model developed in the previous sections may now be applied to this scenario, but there is a complication. The dynamical timescale of the initial halo is about 8 Myr, so a large number of stellar encounters are expected to occur within each dynamical time interval. Meanwhile, as we found in Appendix E.2, encounters should be treated as simultaneous if they occur within a few dynamical time intervals t_{dyn} defined by Eq. (6.4). To accommodate this requirement we adopt the following procedure. For an encounter i occurring at time t_i, we consider all n encounters (including the encounter i) within the previous time interval $t_i - \Delta t < t < t_i$, where

$$\Delta t = \lambda t_{\text{dyn}} \tag{6.20}$$

for some number λ. Using these n encounters we compute two effective encounter parameters:

$$q_{\text{eff}}^+ = \sum_{j=i-n+1}^{i} q_j \quad \text{and} \quad q_{\text{eff}}^- = q_{\text{eff}}^+ - q_i. \tag{6.21}$$

q_{eff}^+ is the combined relative energy injection from all encounters within the last time interval Δt including the ith encounter, while q_{eff}^- excludes the ith encounter. Rather than apply the scaling prescribed by Eq. (6.13) using the ith encounter's parameter q_i, we apply this scaling using q_{eff}^+ and the reciprocal scaling using q_{eff}^-. In other words, we take the ith encounter to change the microhalo's scale radius r_s by the factor

$$\frac{r_s'}{r_s} = \left[\frac{1 + (q_{\text{eff}}^+/q_0)^\zeta}{1 + (q_{\text{eff}}^-/q_0)^\zeta} \right]^{-1/\zeta}. \tag{6.22}$$

This procedure treats encounters occurring within the time interval λt_{dyn} as simultaneous in a self-consistent way.[8] We use Eq. (6.18) to initially rescale the microhalo parameters, and for two

---

[8]It is easy to see that this procedure yields the desired results in two limiting cases. If a cluster of encounters occurs within λt_{dyn}, then each encounter cancels the effect of the previous one, and the final encounter applies the scaling given by Eq. (6.13) using the summed energy injection. If an encounter is separated from all others by intervals longer
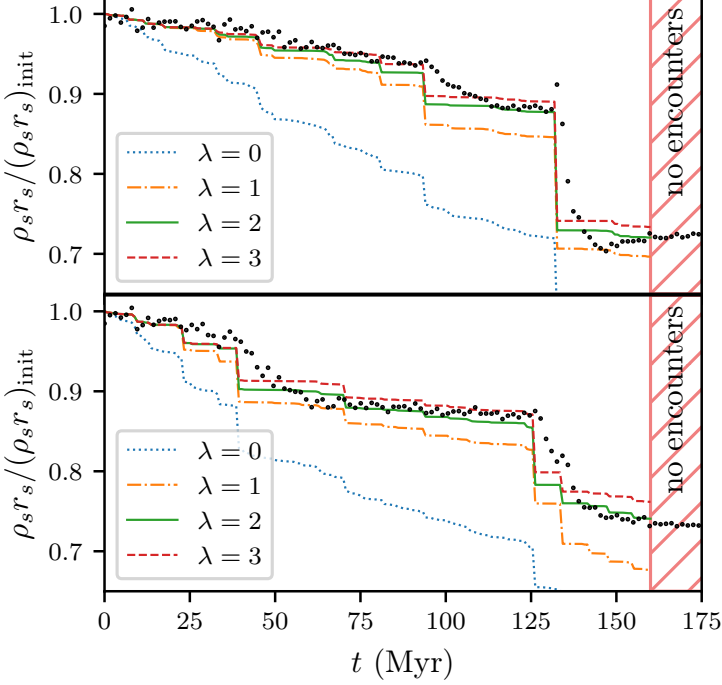
Figure 6.12: Comparing model predictions to simulations for a microhalo traversing a field of stars. We plot the evolution of the density profile asymptote $\rho_s r_s$ for a microhalo crossing two random stellar distributions (upper and lower panels) representative of the solar neighborhood. Predictions using Eqs. (6.22) and (6.14) are shown as solid, dashed, dot-dashed, and dotted lines for various values of the parameter λ (see the text). For comparison, the black circles represent simulation results, where the asymptote is determined by fitting Eq. (6.5) with $\alpha = 0.78$. These points are averaged over ten simulations, each with different randomized encounter orientations, and the simulations continue after the last encounters (hatched region) to allow the halo to relax. The predictions for $\lambda = 2$ match the simulations reasonably well outside of relaxation periods occurring after major encounters. We express the asymptote in units of the initial asymptote $(\rho_s r_s)_{\mathrm{init}}$.

random stellar encounter distributions, Fig. 6.12 shows the predicted microhalo evolution using this procedure for several values of λ.

To test this procedure and tune the parameter λ, we instructed the GADGET-2 simulation code to apply velocity injections given by Eq. (6.2) according to a preset list of stellar encounters. These velocity injections are computed taking the point of least potential as the origin, and each encounter's spatial orientation is randomized. With this arrangement, we carried out numerical simulations of the two stellar field scenarios depicted in Fig. 6.12. In order to facilitate direct comparison, we began the simulations with a microhalo that was a remnant from a previous stellar encounter; this remnant

---

than λt_{dyn}, then $q_{\mathrm{eff}}^- = 0$, and the scaling given by Eq. (6.13) is applied using that encounter's energy injection alone.
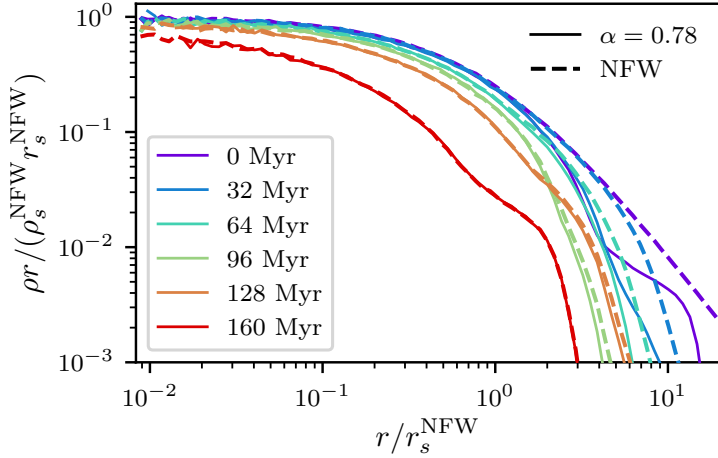
Figure 6.13: Equivalence of the density profile given by Eq. (6.5) with $\alpha = 0.78$ to the NFW density profile, for the purpose of stellar encounters, if the two profiles are related by Eq. (6.18). We subjected microhalos with these two density profiles to the same stellar field scenario (corresponding to the upper panel of Fig. 6.12), and the density profiles that result are identical except at large radii. The profiles plotted here include only particles bound to the halo as computed using the procedure in Sec. 6.2.

was rescaled to have the correct scale parameters predicted by Eq. (6.18). We simulated ten instances of each scenario with different encounter orientations, and Fig. 6.12 shows the orientation-averaged evolution of the microhalo's inner density asymptote $\rho_s r_s$ in these simulations as computed by fitting Eq. (6.5) with $\alpha = 0.78$ to the density profile.[9] Outside of relaxation periods after major encounters, Fig. 6.12 shows that our predictions with $\lambda = 2$ match the simulation results well.

We also subjected a microhalo with an NFW profile to one of the same series of stellar encounters, and we compare this halo's evolution to that of the stellar encounter remnant with the profile given by Eq. (6.5) with $\alpha = 0.78$. Figure 6.13 shows the evolution of the two density profiles. Except at large radii, the resulting halos develop identical density profiles, which further confirms the accuracy of the scaling given by Eq. (6.18).

Finally, to illustrate the power of our predictive framework, we sample 10 000 random sequences of stellar encounters for microhalos traversing the solar neighborhood. Figure 6.14 shows the predicted

---

[9]Specifically, we use the density profile of the instantaneous bound remnant computed using the procedure in Sec. 6.2, and we only fit out to the radius at which $\rho r = \rho_s r_s / 3$. We picked the asymptote $\rho_s r_s$ because it is the quantity least sensitive to details of the fit.
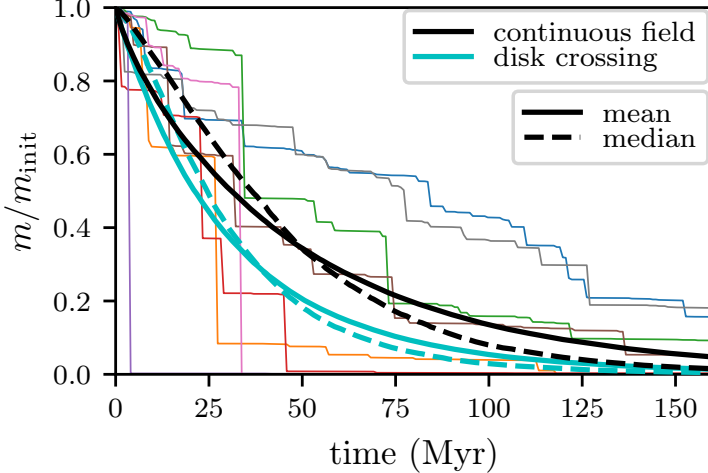
Figure 6.14: Mass evolution for microhalos crossing the solar neighborhood as predicted using Eqs. (6.22) and (6.14). The random distribution of stars induces variance in the mass evolution; we plot eight example mass trajectories along with the mean and median of $10\,000$ trajectories (black curves). The cyan curves represent the trajectories if the halo is allowed to fully relax every 2 Myr, which corresponds to a typical disk-crossing time interval. We express the mass in units of $m_{\rm init}$, which we take to be the mass of the halo after the initial rescaling given by Eq. (6.18).

trajectory of the mass

$$m = 4\pi\alpha^{2/\alpha-1}\Gamma(2/\alpha)\rho_s r_s^3 \simeq 11.9\rho_s r_s^3 \tag{6.23}$$

(for $\alpha = 0.78$; Γ is the gamma function) of microhalos subjected to different sequences. We plot the median and mean mass trajectories along with eight examples. There is substantial variation between halos, but in general, the microhalos lose almost all of their original mass by $t = 160$ Myr. These results are similar to those of Ref. [327], which simulated a similar scenario. We note, however, that in the true solar-neighborhood scenario halos should be allowed to fully relax between disk crossings. In Fig. 6.14, we also plot the mean and median mass trajectories if the halo is allowed to fully relax every 2 Myr; that is, the summation in Eq. (6.22) is made to exclude any encounters prior to the 2 Myr interval. The trajectories change significantly in this scenario, implying it is important to properly account for the halo's relaxation.

Our predictions assume that encounters are

(1) in the impulsive regime with $t_{\rm dyn} \gtrsim 5b/V$; and

(2) in the linear regime with $\nu = p^{-1}(1 + q^{-1})^{-1/2} \lesssim 0.1$.

In the solar neighborhood scenario, all encounters are impulsive with $t_{\rm dyn} \sim 10^3 b/V$, as expected

from the discussion in Sec. 6.2. Roughly half of the microhalo instances experience encounters with $\nu > 0.1$, but their impact turns out to be minimal. We tested an alternative procedure where any encounter with $\nu > 0.1$ was assumed to destroy the halo, and the mean and median trajectories in Fig. 6.14 did not move appreciably. Evidently, the halos that underwent these encounters were already effectively destroyed by them. Thus, neither requirement significantly hinders the model's applicability to this scenario.

6.7   Conclusion

In this chapter, we developed a framework that can predict the evolution of microhalo density profiles as a result of successive stellar encounters. We found that the density profiles of microhalos subjected to stellar encounters follow an almost universal form given by

$$\rho = \rho_s \frac{r_s}{r} \exp\left[-\frac{1}{\alpha} \left(\frac{r}{r_s} \right)^\alpha \right] \tag{6.24}$$

with $\alpha = 0.78$, and Eq. (6.18) describes how this form is related to the initial NFW profile. If each stellar encounter is parametrized by the energy it injects using Eq. (6.11), then Eqs. (6.13) and (6.14) describe the microhalo's response to that energy injection. Successive encounters occurring within roughly $\lambda = 2$ dynamical time intervals should be treated as simultaneous and their energy injections added; Sec. 6.6 discusses how to implement this effect. This framework is accurate assuming that encounters are impulsive [see Eq. (6.3)] and the resulting velocity injections are in the linear regime defined by Eq. (6.19). However, these conditions do not significantly hinder its applicability, as we discuss in Sec. 6.6.

Through Monte Carlo methods, this model can rapidly characterize the impact of stellar encounters on whole ensembles of microhalos. For instance, we were able to generate in minutes 10 000 randomized realizations of a stellar field scenario similar to the single realization simulated in Ref. [327]. In Ref. [437] (forthcoming), we use this model to aid in characterizing the microhalo-dominated dark matter annihilation signals that are expected to arise from certain early-Universe scenarios. In the process, we develop a method to combine the impact of stellar encounters with the subhalo tidal evolution modeled by Ref. [395].

This framework is limited to microhalos initially possessing NFW density profiles. While merger events drive halos' inner density profiles toward the $\rho \propto r^{-1}$ of the NFW profile [262, 280, 336], it is

possible that the smallest halos might retain steeper density cusps today. An exploration of different density profiles is beyond this work's scope, but we anticipate that because of its simplicity, our model will extend readily, albeit with a possibly different universal density profile. Additionally, this model describes microhalos subjected to stellar encounters alone. Further work is needed to precisely understand the combined impact of stellar encounters, galactic tides, and other disruptive processes; Ref. [437] represents a start. Nevertheless, the model presented here will enable more accurate characterizations of the microhalo population within galactic halos.

CHAPTER 7:
BREAKING A DARK DEGENERACY: THE GAMMA-RAY SIGNATURE OF EARLY MATTER DOMINATION[1]

7.1 Introduction

The thermal history of the Universe prior to Big Bang nucleosynthesis (BBN) is largely unprobed. Light-element abundances [6–9], along with density variations inferred from the cosmic microwave background and galaxy surveys [10, 11], demand only that the maximum temperature of the last radiation-dominated epoch be at least 3 MeV. Our sole hint at earlier history is that to solve the horizon and flatness problems and explain the nearly scale-invariant spectrum of primordial density variations, the Universe is believed to have undergone a period of inflation prior to BBN [1–3]. However, the energy scale associated with inflation could be as high as 10^{16} GeV [136, 137], and we have no constraints on the Universe's evolution between inflation and BBN.

There is little reason to assume the Universe was radiation dominated from the end of inflation until BBN (see Ref. [145] for a review of proposed dynamics). Since the energy density of relativistic particles decreases more rapidly than that of nonrelativistic particles, any heavy field left over from the inflationary epoch would naturally come to dominate the energy density of the Universe, leading to an early matter-dominated era (EMDE); such a field is only required to decay into radiation before the onset of BBN. Well motivated examples of such heavy fields include hidden-sector particles [146–158], moduli fields in string theory [159–166], and certain spectator fields invoked to generate primordial curvature variations during inflation [167–170]. After inflation ends, the inflaton itself can also behave as a pressureless fluid before its decay [171–180].

This gap in our understanding of the early Universe gravely impairs our capacity to constrain the properties of thermal-relic dark matter candidates. If the dark matter froze out from the thermal

plasma during the last radiation-dominated epoch, its annihilation cross section must be close to the canonical $\langle \sigma v \rangle = 3 \times 10^{-26}$ cm^{3}s^{-1} in order to produce the observed relic abundance, a value that astrophysical indirect-detection searches have begun to test [209–212]. However, if dark matter froze out during or before an EMDE, its relic density would have been diluted by entropy produced by the decay of the species driving the EMDE. In this scenario, a smaller cross section is required to effect the observed relic abundance, potentially making a broad new range of dark matter candidates viable [213–223].

Fortunately, an EMDE also amplifies the range of dark matter cross sections accessible to indirect-detection searches. Subhorizon density perturbations grow rapidly when pressureless fluids dominate the Universe. Consequently, an EMDE can dramatically enhance small-scale density variations, resulting in the formation of a plethora of highly dense sub-Earth-mass dark matter microhalos long before dark matter halos would otherwise be expected to form [181–183, 206, 224, 225]. These microhalos in turn boost the rate of dark matter annihilation for a given cross section. The purpose of this work is to develop a procedure through which existing indirect-detection experiments can be applied to constrain thermal-relic dark matter candidates that freeze out during or before an EMDE. We improve on previous efforts [206, 224, 225] by employing newly developed models of microhalo formation and evolution to characterize both the magnitude and the morphology of the microhalo-dominated annihilation signals that result from an EMDE.

The signal from annihilation within unresolved microhalos is morphologically similar to that of decaying dark matter; it follows the microhalo distribution, which is similar to the dark matter mass distribution. However, microhalos in dense environments suffer gradual disruption due to tidal effects and encounters with other objects, so their annihilation signal is suppressed within these environments. These effects are particularly important near the centers of host halos, and we account for them in our analysis by employing several recently developed models to characterize the microhalo population. We use the results of Chapter 4 to model the microhalos that result from EMDE scenarios. This work predicts the population of halos and their density profiles given the (linear-theory) power spectrum of density variations. Additionally, we use the results of Chapters 5 and 6 to predict how these microhalos evolve within host halos. Chapter 5 traces the dynamical evolution of subhalos due to tidal forces, while Chapter 6 treats the evolution of microhalos due to encounters with stars.

As a demonstration, we use Fermi-LAT data [268] to derive new constraints on thermal-relic dark matter candidates. We first consider the isotropic gamma-ray background (IGRB), translating published limits on the dark matter lifetime derived therefrom [466, 467] into bounds on dark matter annihilation within unresolved microhalos. These constraints depend strongly on dark matter's free-streaming scale and its relation to horizon scales during the EMDE, but for reasonable sets of parameters, we obtain bounds as small as $\langle \sigma v \rangle \lesssim 10^{-32}$ cm^{3}s^{-1} on dark matter's annihilation cross section. We also consider gamma rays from the Draco dwarf spheroidal galaxy (dSph), employing Fermi-LAT data to derive limits on annihilation within microhalos inside Draco. These limits take into account the unique signal morphology induced by disruptive tidal effects within galactic systems. While Draco yields weaker limits than the IGRB on $\langle \sigma v \rangle$, its signal morphology could potentially discriminate between microhalo-dominated emission and dark matter decay.

This chapter is organized as follows. Section 7.2 reviews the impact of an EMDE on the dark matter abundance and density variations. In Sec. 7.3, we detail how the model in Chapter 4 is employed to predict the microhalo populations resulting from EMDE scenarios. Section 7.4 uses the IGRB to derive limits on dark matter cross sections, while Sec. 7.5 uses gamma rays from the Draco dwarf; in both cases, the suppression of microhalo annihilation rates due to tidal effects is considered in detail. Section 7.6 presents our conclusions. We include further technical details in Appendix F. Appendix F.1 discusses the growth rate of small-scale dark matter density fluctuations and how we account for this growth rate within Chapter 4's halo-formation model. Appendix F.2 details how tidal suppression factors derived from Chapter 5's tidal evolution model are aggregated over a host halo and presents a fitting function for future convenience. Appendix F.3 reanalyzes the simulations in Chapter 5 to present a new refinement to the tidal evolution model, while Appendix F.4 uses a new array of N-body simulations to determine how to combine the effects of galactic tidal forces and stellar encounters. Finally, Appendix F.5 discusses how we estimate Draco's outer density profile.

7.2 Early matter domination

In this section, we review the implications of an EMDE for dark matter; further detail can be found in Refs. [181–183, 206, 213–225]. We denote by ϕ the heavy field that drives early matter domination. The end of an EMDE is characterized by the reheat temperature $T_{\mathrm{RH}} > 3$ MeV at which ϕ domination gives way to radiation. If the EMDE was preceded by another radiation-dominated epoch, then the transition to ϕ domination occurs at an even higher temperature T_{dom}.
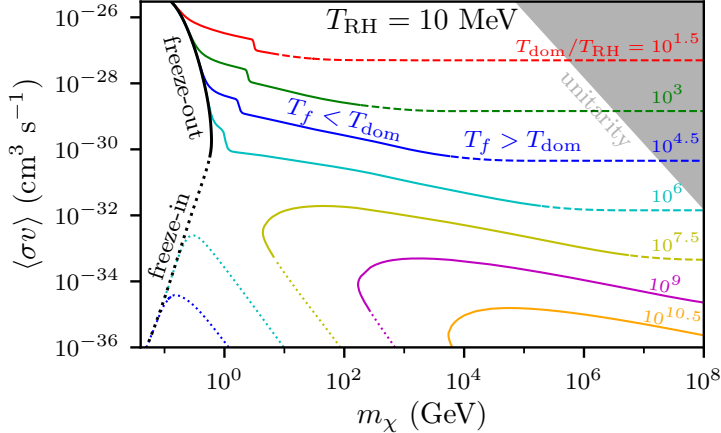
Figure 7.1: Influence of an EMDE on the mass m_χ and annihilation cross section $\langle\sigma v\rangle$ required for thermal-relic dark matter to achieve the observed relic abundance. We show an array of EMDE scenarios with reheat temperature $T_{\mathrm{RH}} = 10$ MeV; one begins at temperature $T_{\mathrm{dom}} \gg T_{\mathrm{RH}}$ (or has no preceding radiation-dominated epoch; thick black curve), while the others (colored curves) have $T_{\mathrm{dom}}/T_{\mathrm{RH}}$ indicated by the numbers on the right. If a colored curve is disconnected from the black curve, then the entire black curve is also viable for that $T_{\mathrm{dom}}/T_{\mathrm{RH}}$. "Freeze-out" (solid and dashed lines) indicates that dark matter dropped out of equilibrium with the thermal bath, while "freeze-in" (dotted lines) corresponds to dark matter never reaching equilibrium; in either case, production and/or annihilation ceases at a temperature T_f closely related to m_χ. Entropy production during the EMDE dilutes the dark matter so rapidly that if there is no radiation from a prior epoch, the dark matter mass cannot exceed $\mathcal{O}(10^2)T_{\mathrm{RH}}$ to have any hope of reaching the observed abundance. On the other hand, the presence of leftover radiation from a prior epoch allows much larger m_χ to still achieve the observed abundance (colored solid curves). Arbitrarily large m_χ can reach the observed abundance by freezing out before the EMDE (dashed curves). Disjointed behavior occurs when the dark matter freezes out close to the QCD phase transition at temperature 170 MeV. The shaded region marks where the dark matter's coupling constant exceeds unity [468].

7.2.1 Relic density of dark matter

The relic density of a dark matter species χ with mass m_χ and annihilation cross section $\langle\sigma v\rangle$ is set by T_{RH} and T_{dom}, and we determine this density by numerically integrating the Boltzmann equations in Ref. [224]. Figure 7.1 illustrates the ways dark matter in an EMDE cosmology can achieve the observed relic density $\rho_\chi/\rho_{\mathrm{crit}} = 0.26$ today, where ρ_{crit} is the critical density. In an EMDE scenario with no prior radiation (thick black curve), the annihilation cross section $\langle\sigma v\rangle$ required to achieve the observed relic abundance depends strongly on m_χ. Dark matter freezes out from thermal equilibrium at a temperature T_f that is approximately proportional to m_χ, so higher m_χ means the dark matter freezes out earlier and consequently suffers more dilution by ϕ decay. To compensate, $\langle\sigma v\rangle$ must be smaller so that the dark matter freezes out at higher density. However, $\langle\sigma v\rangle$ can only become so small before the dark matter never achieves equilibrium in the first place.

Beyond this point, the dark matter is said to freeze in; further reducing $\langle \sigma v \rangle$ now reduces the relic density, requiring smaller m_χ (later freeze-in) to achieve the observed abundance. For $T_{\mathrm{RH}} = 10$ MeV, dark matter with $m_\chi > 100 T_{\mathrm{RH}}$ suffers too much dilution to reach the observed abundance.

The presence of a prior radiation-dominated epoch changes the story considerably (colored curves in Fig. 7.1). While the ϕ decay sources radiation, this production remains subdominant to expansion-induced cooling until late in the EMDE at temperature $T \simeq T_{\mathrm{RH}}^{4/5} T_{\mathrm{dom}}^{1/5}$.[2] Significant entropy production does not begin until that point. Consequently, for $T_f > T_{\mathrm{RH}}$, there are three qualitatively different regimes for dark matter freeze-out. If $T_f \lesssim T_{\mathrm{RH}}^{4/5} T_{\mathrm{dom}}^{1/5}$, then the conditions required for dark matter to achieve the observed abundance are unaffected by the presence of prior radiation. If instead $T_{\mathrm{RH}}^{4/5} T_{\mathrm{dom}}^{1/5} \lesssim T_f \lesssim T_{\mathrm{dom}}$, then the dark matter experiences less dilution than if there were no prior radiation, so it can achieve the observed relic abundance for much larger m_χ than would be possible otherwise. In this regime, the dark matter is diluted by the same factor regardless of its mass, but larger masses m_χ still require smaller $\langle \sigma v \rangle$ to reach the observed abundance because of the influence of the dominant ϕ on the expansion rate.[3] Finally, if $T_f \gtrsim T_{\mathrm{dom}}$, then there is no ϕ-induced boost to the expansion rate and all dark matter masses suffer the same dilution, so the required $\langle \sigma v \rangle$ is independent of m_χ.

Evidently, by tuning T_{dom}, any dark matter candidate that lies to the right of the $T_{\mathrm{dom}} \gg T_{\mathrm{RH}}$ (black) curve in Fig. 7.1 can be brought to the observed relic abundance if $T_{\mathrm{RH}} = 10$ MeV. The story is similar with other reheat temperatures, and we show examples in Fig. 7.2. These figures clearly illustrate the breadth of the degeneracy between dark matter properties and the early thermal history. The $T_{\mathrm{RH}} > 3$ MeV constraint limits $m_\chi \gtrsim 100$ MeV, but otherwise, almost any thermal relic with $\langle \sigma v \rangle \lesssim 3 \times 10^{-26}$ cm^{3}s^{-1} is viable.

7.2.2 Growth of density perturbations

When ϕ dominates, subhorizon dark matter density contrasts grow as $\delta \equiv \delta \rho_\chi / \bar{\rho}_\chi \propto a$, where a is the scale factor, which is significantly faster than the $\delta \sim \log a$ behavior expected when radiation

---

[2]Intuitively, newly sourced radiation may be viewed as remaining subdominant to prior radiation until late in the EMDE, although physically the two cannot be distinguished.

[3]ϕ domination boosts the expansion rate relative to the rate if only radiation were present, and this boost grows in time as ϕ becomes more dominant. Faster expansion means $\langle \sigma v \rangle$ must also be higher to achieve the observed relic abundance. Heavier particles freeze out earlier, so they enjoy less of this boost to the expansion rate and require smaller $\langle \sigma v \rangle$.
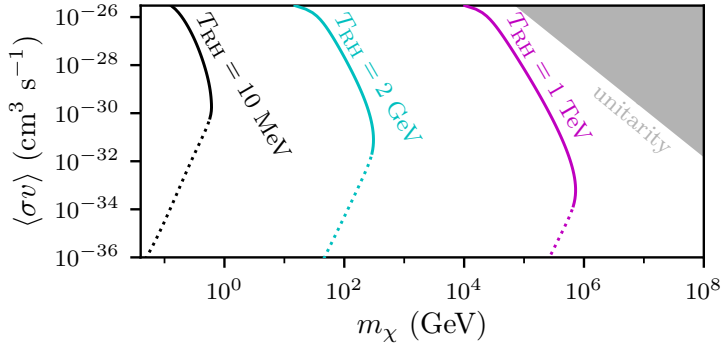
Figure 7.2: Similar to Fig. 7.1, but showing EMDE scenarios with different reheat temperatures T_{RH} and $T_{\mathrm{dom}} \gg T_{\mathrm{RH}}$ (or no prior radiation). For a given T_{RH}, any dark matter candidate that lies to the right of the corresponding curve can be brought to the observed relic abundance by tuning T_{dom}.

dominates. Intuitively, the ϕ particles gravitationally cluster and carry the dark matter with them. Reference [181] determined how the EMDE-boosted growth alters the power spectrum $\mathcal{P}(k)$ of dark matter density variations at later times. $\mathcal{P}(k)$ is influenced by two main parameters: the reheat temperature T_{RH} and the dark matter free-streaming scale, which sets a cutoff wave number k_{cut}. The former is set by properties of the ϕ field, while the latter is determined by the microphysics of the dark matter, namely its interactions with relativistic particles and its residual velocity distribution [388, 469–472]. The kinetic decoupling of dark matter during an EMDE is complicated by the entropy injected by ϕ decay [473], but an EMDE generally leaves dark matter much colder than it would be in the EMDE's absence [474].

Figure 7.3 shows $\mathcal{P}(k)$ for several EMDE scenarios calculated using transfer functions from Ref. [181] as described in Ref. [224]. Fluctuations that were subhorizon during the EMDE are enhanced, so the reheat temperature T_{RH} that marks the end of the EMDE sets the scales at which this enhancement occurs. The smallest scales not suppressed by free streaming are enhanced the most; these are the modes near the wave number k_{cut} associated with the dark matter's free-streaming cutoff.[4] The ratio $k_{\mathrm{cut}}/k_{\mathrm{RH}}$ between this cutoff and the wave number entering the horizon at reheating is significant because it sets the maximum enhancement to $\mathcal{P}(k)$.

These power spectra were derived assuming no prior radiation. To ensure their validity in scenarios with finite T_{dom}, we require that modes entering the horizon prior to the EMDE, at

---

[4]As in Ref. [224], we define k_{cut} such that the matter power spectrum is scaled by $\exp(-k^2/k_{\mathrm{cut}}^2)$.
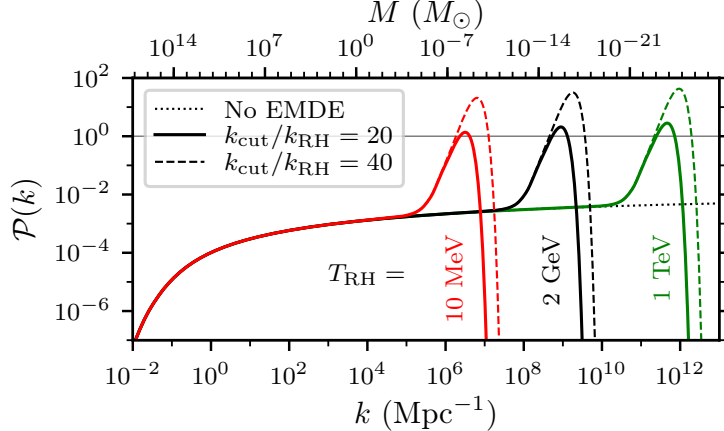
Figure 7.3: The (dimensionless) power spectrum of dark matter density fluctuations at redshift $z = 300$ in several EMDE cosmologies, as computed in linear theory using transfer functions from Ref. [181]. Fluctuations are enhanced on the comoving scales k that were inside the horizon during the EMDE, creating a "bump" in the power spectrum at small scales. To supply intuition, we also plot the mass scale $M = (4\pi/3)\bar{\rho}k^{-3}$ associated with each wave number k, where $\bar{\rho}$ is the cosmological mean dark matter density; M is of order the mass of the halo forming from a density variation of scale k. In all scenarios fluctuations are already nonlinear (horizontal line) by $z = 300$, implying microhalos have begun to form.

temperature $T \gtrsim T_{\mathrm{dom}}$, lie below dark matter's free-streaming scale. To be precise, we demand that the wave number k_{dom} entering the horizon at T_{dom} satisfy $k_{\mathrm{dom}} \gtrsim 3k_{\mathrm{cut}}$, which ensures that the previous radiation epoch's imprint does not reduce the rms density variation in the dark matter by more than about 20%.[5] This requirement is equivalent to

$$T_{\mathrm{dom}}/T_{\mathrm{RH}} \gtrsim 5(k_{\mathrm{cut}}/k_{\mathrm{RH}})^{3/2}. \tag{7.1}$$

Additionally, these power spectra assume that the dark matter froze out early enough before reheating that dark matter density perturbations were able to catch up to those in ϕ. Figure 4 of Ref. [224] suggests that it takes roughly a factor of 5 in a, corresponding to a factor of 2 in T, for a dark

---

[5]We use the zero-baryon transfer function from Ref. [475] to approximate the power spectrum imprinted by an EMDE preceded by a radiation-dominated period, and we test how its rms density variation compares to that associated with a matter-only power spectrum if both have the same k_{cut}. A 20% decrease in the amplitude of a density contrast roughly corresponds to a factor of 2 drop in the corresponding collapsed halo's annihilation rate.

matter density perturbation to settle into $\delta \propto a$ after freeze-out. Thus, we demand

$$T_f \gtrsim 2T_{\mathrm{RH}}. \tag{7.2}$$

7.3   Microhalos and their properties

The density contrasts enhanced by an EMDE can collapse into dark matter microhalos long before the first halos would otherwise be expected to form, and their early formation makes these halos extremely small and dense. In this work, we study scenarios with $20 \leq k_{\mathrm{cut}}/k_{\mathrm{RH}} \leq 40$, for which most microhalos form at redshift $200 \lesssim z \lesssim 3000$. Larger $k_{\mathrm{cut}}/k_{\mathrm{RH}}$ are theoretically plausible [225], especially for hidden-sector dark matter [206]. However, they enhance fluctuations enough to induce collapse prior to matter domination, the study of which is beyond this work's scope.[6] Additionally, we focus on EMDE scenarios with $T_{\mathrm{RH}} = 10$ MeV and $T_{\mathrm{RH}} = 2$ GeV: the former because it is close to the coldest reheat temperature possible without altering BBN, and the latter because it would bring certain supersymmetric dark matter candidates to the observed relic abundance (without assuming prior radiation) [225].

The first microhalos form through the direct collapse of peaks in the density field, so they are expected to possess density profiles that scale as $\rho \propto r^{-3/2}$ at small radii [26, 226, 261–266, 336, 454]. However, successive mergers drive their inner density cusps toward the shallower $\rho \propto r^{-1}$ scaling [262, 267, 280, 336, 454]. Thus, we will assume that microhalos eventually develop density profiles of the Navarro-Frenk-White (NFW) form,

$$\rho(r) = \frac{\rho_s}{(r/r_s)(1 + r/r_s)^2} \tag{7.3}$$

which is a generic outcome of hierarchical halo clustering [205, 260].

---

[6]Sufficiently overdense regions can collapse when radiation dominates due to particle drift alone. If these collapsed regions are locally matter dominated, they form bound halos long before matter-radiation equality; such early formation makes these halos much denser than any halo that forms during matter domination [206]. Regions that are even more overdense can collapse to form halos during an EMDE; these ϕ-dominated halos gravitationally heat the dark matter so that after the ϕ decay destroys them, subsequent structure formation is suppressed [206].

7.3.1 Modeling the microhalo population

We use the framework developed in Chapter 4 to characterize the microhalos that form after an EMDE. This framework maps each peak in the (unfiltered) primordial density field to a collapsed halo, predicting the coefficient A of that halo's inner $\rho = Ar^{-3/2}$ density asymptote, the radius $r_{\max}$ of maximum circular velocity, and the mass $m_{\max}$ that radius encloses. We note that the model predicts a complete mass profile $M(r)$ for each halo, but this profile is only calibrated to agree with simulations at $r = r_{\max}$. By sampling peaks from the density field as described in Appendix C of Chapter 4, we can thereby sample halos. For simplicity, we use the turnaround model in Chapter 4 to predict $r_{\max}$ and $m_{\max}$, but as that work notes, alternate models yield very similar predictions.

We consider a variety of EMDE scenarios, and for each scenario we begin with the power spectrum of density fluctuations. We first use the Boltzmann solver CAMB Sources [270, 271] to compute the power spectrum at redshift $z = 500$ using Planck cosmological parameters [476]. Subsequently, we apply the appropriate transfer function from Ref. [224] to convert this power spectrum into one describing an EMDE scenario. We then use this power spectrum to draw a halo population using the methods of Chapter 4, but there is a complication. Dark matter density contrasts δ at scales $k \gtrsim 10^2$ Mpc^{-1} grow at the suppressed rate $\delta \propto a^{0.901}$ [273], where a is the scale factor, because baryonic matter does not accrete into such small structures [471]. We describe in Appendix F.1 how we adapt the Chapter 4 framework to this growth function.

Using the power spectrum, it is straightforward to apply the methods of Chapter 4 to predict the distribution of the asymptotic coefficient A. However, the application to $r_{\max}$ and $m_{\max}$ demands some care since it requires sampling the profiles $\delta(q)$ of the precursor density peaks at a finite number of comoving radii q. We sample the peaks at 300 radii distributed evenly in log space from $q = 0.03 k_{\mathrm{cut}}^{-1}$ to $q = 3 k_{\mathrm{RH}}^{-1}$; the minimum radius is well below the free-streaming cutoff, while the maximum radius is large enough to ensure that all EMDE-enhanced scales are sampled. The advantage to using the turnaround model is that predictions are insensitive to the choice of maximum radius as long as the initial radius of the mass shell that collapses to $r_{\max}$ is sampled.

We additionally cut off the density profile of each peak when the average enclosed overdensity is either zero or begins to grow. The former scenario implies that no farther mass shells are expected to accrete, while the latter suggests the presence of a denser neighboring structure; such a structure would cause the spherical collapse model that underlies the $r_{\max}$ and $m_{\max}$ predictions to break

down. The cutoff in the peak density profile imposes a cutoff in the predicted mass profile at the collapsed radius of the outermost mass shell, and if the circular-velocity maximum lies at that cutoff (implying it is not a local maximum), then we discard this halo; it is likely too rapidly accreted by a neighboring structure to be relevant.[7] Additionally, we discard peaks for which there is no ellipsoidal collapse solution using the approximation in Ref. [373].[8]

We consider a variety of EMDE scenarios, and we use the above methods to sample 10^6 peaks in each scenario and convert them into predicted halos. As illustration, Fig. 7.4 shows six example mass profiles $M(r)$ predicted for a cosmology with $T_{\mathrm{RH}} = 2$ GeV and $k_{\mathrm{cut}}/k_{\mathrm{RH}} = 20$. We separately show the inner asymptote, set by the prediction of A, and the broader mass profile. The latter is only tuned to be accurate at r_{max}, which is where $M(r)/r$ peaks, and as Chapter 4 notes, it does not produce valid predictions at small r because it is derived under the assumption that mass shells accrete adiabatically.

7.3.2 Annihilation within microhalos

The dark matter annihilation rate within a microhalo is proportional to its J factor,[9]

$$J \equiv \int \rho^2 \mathrm{d}V, \tag{7.4}$$

and is largely set by the inner asymptote A of its density profile. If halos retain $\rho \propto r^{-3/2}$ inner density profiles, then the annihilation rate is proportional to A^2 if we neglect a logarithmic dependence on minimum radius[10] and maximum radius. However, mergers between microhalos are expected to drive these cusps toward the $\rho \propto r^{-1}$ scaling of the NFW profile [262, 267, 280, 336, 454]. Mergers also deplete the microhalo count while making the survivors more dense. To predict the annihilation

---

[7]We reanalyzed the EMDE scenario in Chapter 4 to test the impact of discarding peaks for which r_{max} lies beyond this cutoff in the mass profile. Only 5% of the peaks that matched to simulated halos satisfy the removal criterion, and of those halos, 87% underwent a major merger during the simulation duration.

[8]Only highly aspherical peaks lack a collapse solution. Increased deviation from spherical symmetry causes later collapse, so the absence of a solution may imply these peaks never collapse. Spherical asymmetry is also anticorrelated with the amplitude of a density peak [269], so the collapse of highly aspherical peaks is delayed by both their small amplitude and their asphericity, implying that even if they do collapse they likely do so late enough that their contribution to observables is negligible.

[9]We assume the dark matter annihilation cross section $\langle \sigma v \rangle$ is velocity independent in the nonrelativistic limit.

[10]The annihilation rate from a $\rho \propto r^{-3/2}$ cusp diverges, which implies that the profile would shallow at some minimum radius due to these annihilations.
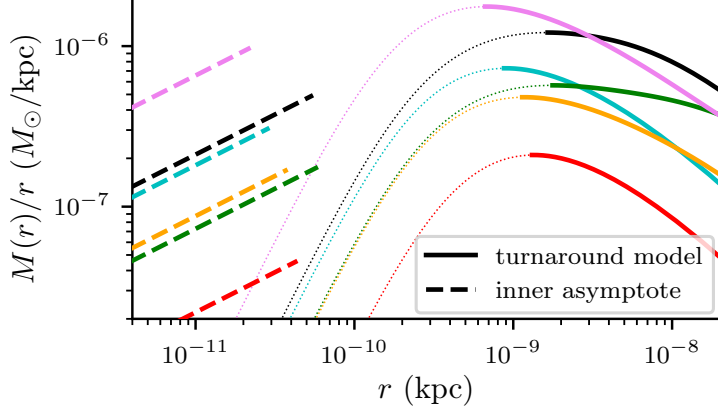
Figure 7.4: Mass profiles of six halos sampled using the methods of Chapter 4 in an EMDE scenario with $T_{\mathrm{RH}} = 2$ GeV and $k_{\mathrm{cut}}/k_{\mathrm{RH}} = 20$. We separately show the inner asymptotes (dashed lines) and the greater mass profiles (solid lines). The greater mass profiles are only tuned to match simulations at $r = r_{\mathrm{max}}$, which is where $M(r)/r$ is maximized. Below r_{max} we plot them as dotted lines; since these profiles are derived assuming gradual mass accretion, they are not expected to be accurate at small r because the mass there accreted rapidly.

signal from microhalos, it is necessary to account for these mergers' impact.

The precise impact of mergers between microhalos on their density profiles, and hence annihilation rates, is yet unclear. However, we can make an estimate in the following way. If a microhalo transitions from a profile with inner density asymptote $\rho = Ar^{-3/2}$ to the NFW profile with scale parameters ρ_s and r_s, then $\rho_s^2 r_s^3 \propto A^2$ from dimensional considerations. Realistically, such a transition occurs simultaneously with mass increases caused by mergers, but we treat the two effects separately for simplicity. The resulting NFW profile's J factor is[11]

$$J = (4\pi/3)\omega A^2, \tag{7.5}$$

where ω is the undetermined proportionality factor acquired in the transition, i.e., $\rho_s^2 r_s^3 = \omega A^2$.

We expect $\omega \gtrsim 1$ from the following examples. If a density profile transitions from $\rho = Ar^{-3/2}$ to $\rho = \rho_s r_s/r$ with mass conserved within the scale radius r_s, then $\rho_s^2 r_s^3 = (4/3)^2 A^2$, i.e., $\omega = (4/3)^2 \simeq 1.8$. Alternatively, suppose a microhalo initially has density profile $\rho = Ar^{-3/2}(1 + r/\tilde{r})^{-3/2}$ [226] or $\rho = Ar^{-3/2}[1 + (r/\tilde{r})^{3/2}]^{-1}$ [278] for some scale radius $\tilde{r}$, each of which appropriately obeys

---

[11]We integrate the NFW profile to radius ∞, but the result is only marginally different if the profile is cut off at any radius $r \gtrsim r_s$.

$\rho = Ar^{-3/2}$ when $r \ll \tilde{r}$. If these profiles transition into NFW profiles while preserving the radius $r_{\max}$ of maximum circular velocity and the corresponding enclosed mass $m_{\max}$, then the transitions are characterized by $\omega = 5.33$ and $\omega = 8.05$, respectively. We conservatively assume $\omega = (4/3)^2$ in line with the first example, but this factor carries cleanly through all calculations.

Chapter 4 found that the sum $\sum A^2$ over all halos is predicted by the model with reasonable accuracy even after mergers take place, which suggests that $J \propto A^2$ is additive in mergers. This property can be understood in light of a conceptual argument. For halos of fixed density profile (e.g., NFW), $J \propto \rho_s M$, where M is halo mass. If halo masses are additive in mergers and characteristic densities ρ_s are not altered,[12] then J factors are also additive. Indeed, Ref. [339] found that in mergers between identical halos, ρ_s tends to either be preserved or grow slightly, and r_s grows roughly as would be expected from the doubling of mass. This finding lends support to the notion that J factors are approximately additive in mergers.

Further work is needed to tease out precisely how mergers alter the annihilation rates in halos, but we exploit the approximate conservation of the sum $\sum J$ to obtain an adequate estimate. We compute the aggregate annihilation signal from microhalos by summing the J factors given by Eq. (7.5) over the previously predicted halo population. If N peaks are sampled to produce the halo population and $\bar{n}$ is the number density of peaks in the primordial density field (computed as in Chapter 4 or Ref. [269]), then the cosmologically averaged squared dark matter density within microhalos is

$$\overline{\rho^2} = \frac{\bar{n}}{N} \sum_i J_i, \tag{7.6}$$

where J_i is the J factor of the ith halo. The mean gamma-ray luminosity expected from microhalos, per cosmological volume, is in turn

$$\overline{\frac{\mathrm{d}L}{\mathrm{d}V}} = \overline{\rho^2} \frac{\langle \sigma v \rangle}{2m_\chi^2} \int_{E_{\mathrm{th}}}^{m_\chi} E_\gamma \frac{\mathrm{d}N_\gamma}{\mathrm{d}E_\gamma} \mathrm{d}E_\gamma, \tag{7.7}$$

for threshold photon energy E_{th}, where m_χ is the mass of the dark matter particle, $\langle \sigma v \rangle$ is its

---

[12]The central cusp can still become denser at a given radius when ρ_s is fixed if r_s grows. Also, we assume that in mergers between halos of different ρ_s, the density of the merger remnant is the mass-weighted average of the densities of the progenitors.
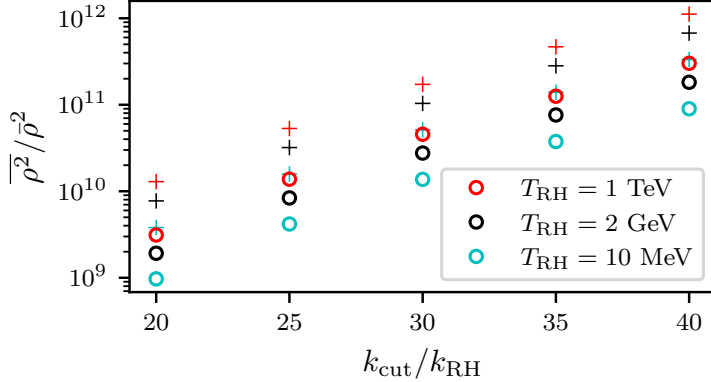
Figure 7.5: The annihilation boost factor (circles) relative to uniform density as a function of EMDE scenario. Annihilation rates are strongly sensitive to $k_{\mathrm{cut}}/k_{\mathrm{RH}}$ and only weakly sensitive to T_{RH}. For comparison, we also plot as crosses the annihilation boost factors computed using the procedure in Refs. [206, 224, 225], which uses Press-Schechter theory as described in the text.

annihilation cross section, and $\mathrm{d}N_\gamma/\mathrm{d}E_\gamma$ is the differential photon yield from annihilation events.

The factor by which dark matter annihilation is boosted, relative to uniform density, is $\overline{\rho^2}/\bar{\rho}^2$, where $\bar{\rho}$ is the mean dark matter density. In Fig. 7.5, we plot this factor (as circles) as a function of EMDE scenario. The annihilation boost is strongly sensitive to $k_{\mathrm{cut}}/k_{\mathrm{RH}}$; this ratio sets the maximum enhancement to density variations, so it strongly influences halo formation times and hence the density within microhalos. T_{RH} also has a small influence on $\overline{\rho^2}/\bar{\rho}^2$ because it sets the duration of the last radiation-dominated epoch, during which the EMDE-enhanced density contrasts grow logarithmically.

For comparison, we also compute the annihilation boost factor using the procedure in Refs. [206, 224, 225]. Microhalos are counted using a Press-Schechter mass function, and each microhalo is assumed to have concentration $c \equiv r_{\mathrm{vir}}/r_s = 2$ at some formation redshift z_f. The annihilation boost factor is thus formally a function of z_f, but as the final step, z_f is chosen such that the annihilation boost is maximized. These estimates are plotted in Fig. 7.5 as crosses. We find that this procedure overestimates annihilation rates by a factor of about 4 relative to the procedure described in this section. This discrepancy likely owes to the time it takes for a halo to stabilize its NFW (or alternative $r^{-3/2}$) profile after formation. A halo maintains $c \sim 2$ for a significant duration before its density profile (in physical coordinates) ceases to evolve, at which point c begins to grow as the background density drops. The assumption that c begins to grow at halo formation consequently leads to overestimation of the halo's central density.

7.3.3 Microhalo density profiles

The procedure of the previous section suitably treats the impact of mergers between microhalos on their aggregate annihilation signals. However, a subset of the microhalo population is further altered at late times ($z \lesssim 20$) by accretion onto much larger halos, such as those of galaxies. Chapter 5 developed a model that predicts the evolution of subhalo J factors due to a host halo's tidal forces, while Chapter 6 modeled the evolution of microhalos due to encounters with individual stars. These models require the scale parameters ρ_s and r_s of the microhalo population, and in this section we use Chapter 4's framework to estimate their distribution. As a bonus, this distribution will assist in building an intuition for the microhalo population that the framework predicts.

For each halo, we obtain ρ_s and r_s from the structural parameters $r_{\max}$ and $m_{\max}$ predicted from the Chapter 4 framework by assuming an NFW density profile. These parameters could be altered by mergers between microhalos, but Chapter 4 found that while mergers cause $r_{\max}$ and $m_{\max}$ to increase relative to their model predictions, this growth is relatively minor.[13] Thus, lacking a precise understanding of how density profiles are influenced by mergers, we assume that the predictions of ρ_s and r_s remain accurate. In this way, we obtain a distribution of microhalos in ρ_s and r_s, and in the coming sections we will apply the dynamical evolution models of Chapters 5 and 6 to this distribution in order to predict the present-day aggregate annihilation rate.

Figure 7.6 shows the microhalo distribution in ρ_s and r_s, weighted by contribution to the annihilation signal, for an EMDE scenario with $T_{\mathrm{RH}} = 2$ GeV and $k_{\mathrm{cut}}/k_{\mathrm{RH}} = 20$. The bulk of the microhalos form from density fluctuations near the free-streaming cutoff scale, and these halos comprise the dense clump in r_s-ρ_s space depicted in Fig. 7.6. However, the halo distribution also includes a tail of halos with increasingly large r_s and small ρ_s. To understand this tail, we note that as a function of comoving scale q, initial density contrasts δ that enter the horizon during an EMDE, but are much larger than the free-streaming cutoff, scale as $\delta \propto q^{-2}$. A microhalo's characteristic density is proportional to the background density at its formation time, so if a density contrast δ

---

[13]Chapter 4 found that as many as six major mergers only raised a halo's $r_{\max}$ by about 15% relative to its model prediction. $m_{\max}$ grew by as much as 50% under the same conditions, but this change compensates the change in $r_{\max}$ to leave $\rho_s \propto m_{\max}/r_{\max}^3$ almost unaltered. Note that $r_{\max}$ and $m_{\max}$ could be significantly altered by mergers even if they do not move appreciably relative to their predicted values; this would imply that the predictions already accounted for the mergers.
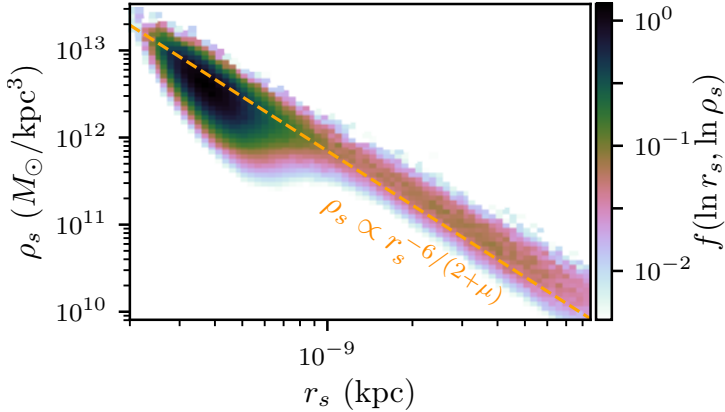
Figure 7.6: Distribution of the annihilation signal in the NFW scale parameters ρ_s and r_s of source microhalos, as predicted using the framework in Chapter 4. The EMDE scenario represented has $T_{\mathrm{RH}} = 2$ GeV and $k_{\mathrm{cut}}/k_{\mathrm{RH}} = 20$. The tail at large r_s and small ρ_s obeys $\rho_s \propto r_s^{-6/(2+\mu)}$, where $\mu = 0.901$ is the linear growth exponent, and represents the rare halos that form from fluctuations much larger than the cutoff scale (see the text). However, the dominant contribution to annihilation signals comes from the densest microhalos.

collapses to form a microhalo, then that microhalo has $\rho_s \propto \delta^{3/\mu}$, where $\mu = 0.901$ is the linear growth exponent (see Appendix F.1). Meanwhile, if q is the comoving scale of that fluctuation, then the microhalo's characteristic size is $r_s \propto q\delta^{-1/\mu}$. Consequently, for microhalos forming from density fluctuations that enter the horizon during an EMDE but are much larger than the free-streaming scale, $\rho_s \propto r_s^{-6/(2+\mu)}$. The low-density halo tail in Fig. 7.6 follows this relationship.

As another demonstration that the predicted population is sensible, we compare it to the population predicted by Press-Schechter theory [287] using ellipsoidal collapse [373]. Press-Schechter theory predicts a mass function $\mathrm{d}n/\mathrm{d}M$ describing the halo number density n distributed in halo mass M. In contrast, our halo population is distributed in the density profile parameters ρ_s and r_s. However, we can connect the two distributions by assuming $M = M_{\mathrm{vir}}$ is the mass enclosed within the virial radius r_{vir} that encloses an average density of 200 times the cosmological mean (which depends on the scale factor). Meanwhile, given ρ_s and r_s, the same virial mass M_{vir} can be estimated by assuming that the NFW profile is accurate out to r_{vir}. In Fig. 7.7, we plot, for both methods and at several different redshifts, the number density $n(< M)$ of halos with mass smaller than M in the EMDE scenario with $T_{\mathrm{RH}} = 2$ GeV and $k_{\mathrm{cut}}/k_{\mathrm{RH}} = 20$. The halo distributions predicted by the two methods are offset in mass M by up to a factor of 2, but this discrepancy is sufficiently minor and consistent that it is likely connected to the assumptions made above in order to compare the
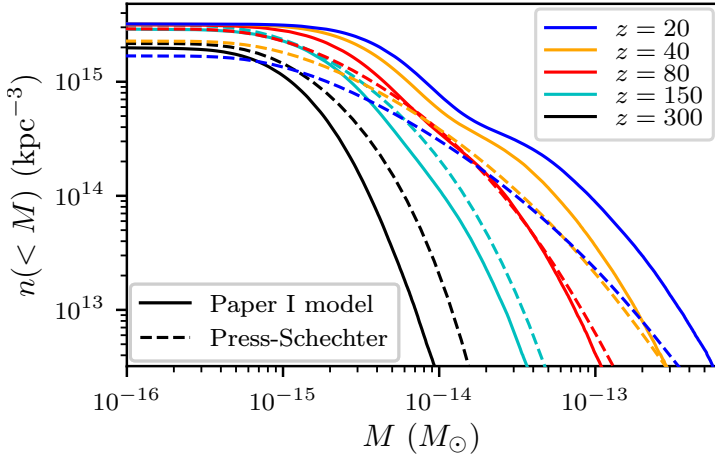
Figure 7.7: Comparison between the halo population predicted using the methods of Chapter 4 and that predicted by Press-Schechter theory. We plot the number density $n(< M)$ of halos with mass smaller than M at several redshifts as predicted by both methods for an EMDE cosmology with $T_{\mathrm{RH}} = 2$ GeV and $k_{\mathrm{cut}}/k_{\mathrm{RH}} = 20$. The halo distributions predicted by the two methods are offset in mass by a factor as large as 2, but since the two frameworks predict different quantities, certain assumptions were necessary that may not be accurate (see the text). Otherwise, the populations match reasonably well at early times. At late times, the Chapter 4 framework's neglect of halo mergers causes it to overpredict the halo count relative to the Press-Schechter calculation.

two prediction schemes. Otherwise, the two populations match reasonably well at early redshifts $z \gtrsim 50$. At late times, halo mergers start to become significant, causing the Chapter 4 framework to overpredict the number of small halos relative to Press-Schechter.

Finally, we discuss how the microhalo population is influenced by different EMDE cosmologies. In Fig. 7.8, we show the median scale density and radius values, ρ_s and r_s, associated with a variety of EMDE scenarios. As we noted in Sec. 7.3.2, the ratio $k_{\mathrm{cut}}/k_{\mathrm{RH}}$ has a large impact on ρ_s because it sets the amplitudes of the most extreme density fluctuations, while T_{RH} exerts only a minor influence by controlling the duration of the radiation-dominated epoch. In contrast, r_s is strongly sensitive to T_{RH} because later reheating means larger-scale density fluctuations are enhanced, while $k_{\mathrm{cut}}/k_{\mathrm{RH}}$ has a minor impact that owes to the fact that halos that form earlier, while the Universe was smaller, stabilize their density profiles at a smaller physical size.

7.4 Isotropic gamma-ray background

In an EMDE cosmology, dark matter annihilation within microhalos roughly traces the dark matter distribution, producing a signal similar to that of decaying dark matter. Consequently, it would contribute substantially to the IGRB. In this section, we use the Fermi Collaboration's
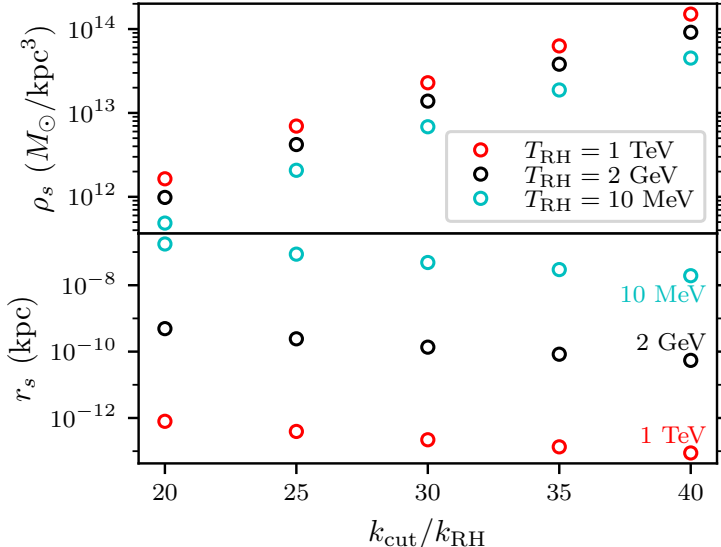
Figure 7.8: Median NFW scale density ρ_s and radius r_s of microhalos in a variety of EMDE scenarios. The ratio $k_{\rm cut}/k_{\rm RH}$ has a large impact on ρ_s and a small impact on r_s, while the reverse is true of $T_{\rm RH}$.

measurement of the IGRB [477] to constrain annihilation within microhalos.

7.4.1 Limits on annihilation

For a given annihilation channel, we can translate published bounds on the dark matter lifetime from the IGRB directly into bounds on the annihilation cross section using the procedure in Ref. [206]. This translation is possible because annihilation within (unresolved) microhalos and dark matter decay both produce a gamma-ray signal that tracks the dark matter mass distribution.[14] We equate the annihilation rate per mass, Γ/M_χ, for particles with mass m_χ and cross section $\langle \sigma v \rangle$ to the decay rate per mass of particles with mass $2m_\chi$ and effective lifetime $\tau_{\rm eff}$, obtaining

$$\frac{\Gamma}{M_\chi} = \frac{\langle \sigma v \rangle}{2m_\chi^2} \frac{\overline{\rho^2}}{\bar{\rho}} = \frac{1}{2m_\chi \tau_{\rm eff}}, \tag{7.8}$$

where $\bar{\rho}$ and $\overline{\rho^2}$ are the mean and mean squared dark matter density, respectively, as in Sec. 7.3.2. Thus, a lower bound on $\tau_{\rm eff}$ for particles of mass $2m_\chi$ leads to an upper bound on $\langle \sigma v \rangle$ for particles

---

[14]The correspondence between annihilation within microhalos and decay breaks down at sufficiently high redshifts that the microhalos have not yet formed. However, microhalos arising from the EMDE cosmologies we consider form at redshifts $z \gtrsim 200$, which lie well beyond the redshifts $z \lesssim 20$ relevant to any contribution to the IGRB from dark matter decay [478].

of mass m_χ. This procedure neglects disruption of microhalos within host halos, the impact of which we discuss soon.

We use Eq. (7.8) to derive bounds on annihilating dark matter from two classes of limits on the dark matter lifetime. Both employ the Fermi Collaboration's measurement of the IGRB [477]. The first, from Ref. [466], conservatively requires that the predicted gamma-ray flux from dark matter decay not exceed the flux reported by Fermi within any spectral bin. The second, from Ref. [467], employs models of astrophysical background gamma-ray sources, such as star-forming galaxies and active galactic nuclei, to dramatically reduce the gamma-ray flux that can be attributed to dark matter. Through Eq. (7.8), these decay bounds (for particles of mass $2m_\chi$) translate into conservative and aggressive bounds on the dark matter annihilation cross section $\langle \sigma v \rangle$ (for particles of mass m_χ), respectively.

In Fig. 7.9, we plot the resulting constraints on dark matter annihilating into $b\bar{b}$ for several EMDE cosmologies. Recall from Sec. 7.2 that dark matter with a vast range of parameters can be brought to the observed relic abundance by tuning $T_{\rm RH}$ and $T_{\rm dom}$; the main requirement is that m_χ must exceed $T_{\rm RH}$ by a sufficient margin to avoid overproducing dark matter for cross sections below the canonical 3×10^{-26} cm^{3}s^{-1}. If $k_{\rm cut}/k_{\rm RH} = 40$, the aggressive constraints can probe thermal-relic cross sections as small as $\langle \sigma v \rangle \sim 10^{-32}$ cm^{3}s^{-1}. Constraints are weaker for $k_{\rm cut}/k_{\rm RH} = 20$, but the aggressive constraints can still reach as far as $\langle \sigma v \rangle \sim 10^{-30}$ cm^{3}s^{-1}.

Equations (7.1) and (7.2) set the conditions under which the density fluctuation power spectra we employed are expected to be accurate, and we mark on Fig. 7.9 the regions that fail these conditions. Only a small region with large $\langle \sigma v \rangle$ and small m_χ fails $T_f > 2T_{\rm RH}$ (without also overproducing dark matter). On the other hand, cross sections $\langle \sigma v \rangle$ that are less than a few orders of magnitude below the canonical 3×10^{-26} cm^{3}s^{-1} tend to fail $T_{\rm dom}/T_{\rm RH} > 5(k_{\rm cut}/k_{\rm RH})^{3/2}$ if $T_{\rm dom}$ is tuned to effect the observed relic abundance. Constraints on thermal relics are tentative within these regions, and a more careful treatment is needed of the power spectra that arise therein. Using the appropriate power spectra would delay microhalo formation, weakening the bounds on $\langle \sigma v \rangle$.

7.4.2 Tidal suppression

Compared to the gamma-ray signal from decaying dark matter, the signal from annihilation within microhalos is suppressed by tidal effects within host halos. We neglected this effect when deriving the constraints shown in Fig. 7.9, and we now estimate its impact. Dark matter's contribution to
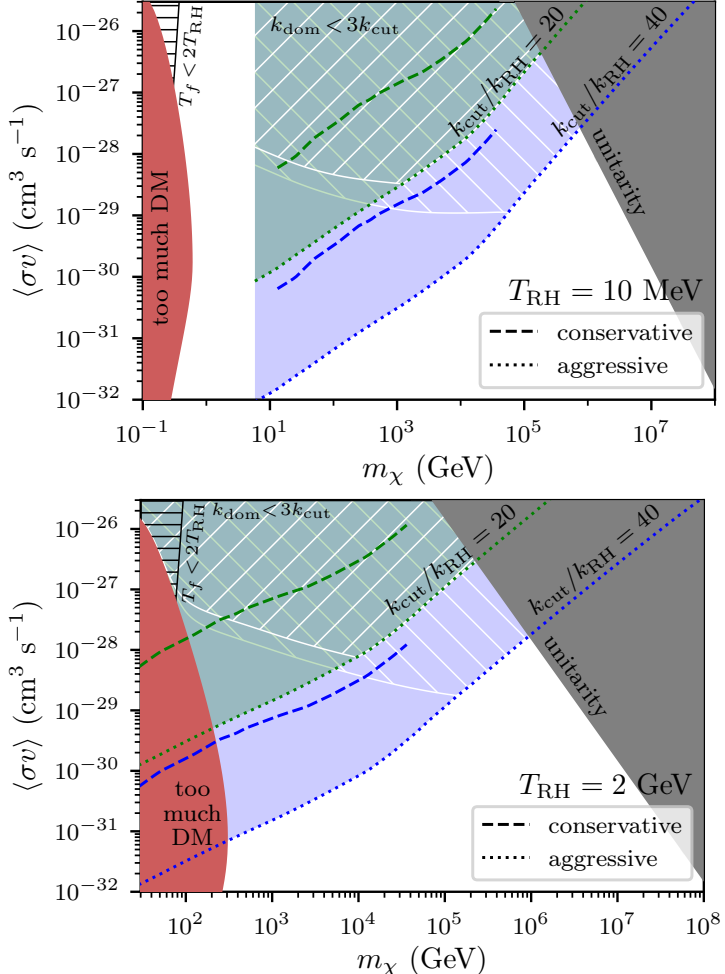
Figure 7.9: Upper bounds on the cross section for dark matter annihilating to $b\bar{b}$ for two reheat temperatures $T_{\mathrm{RH}} = 10$ MeV (top) and $T_{\mathrm{RH}} = 2$ GeV (bottom). In each case, we consider both $k_{\mathrm{cut}}/k_{\mathrm{RH}} = 20$ (green) and $k_{\mathrm{cut}}/k_{\mathrm{RH}} = 40$ (blue) and plot both the conservative and aggressive bounds derived from Fermi-LAT's measurement of the IGRB; see the text. The shaded region on the left is disallowed because it would overclose the Universe, while the shaded region on the right marks where the dark matter's coupling constant exceeds unity. The black hatched region fails Eq. (7.2) while the white hatched regions (different for each $k_{\mathrm{cut}}/k_{\mathrm{RH}}$) fail Eq. (7.1). The density fluctuation power spectra we employed do not apply within these regions, so constraints therein are tentative; further work is needed to account for the altered power spectra.

the IGRB comes from both the Galactic halo and extragalactic dark matter. To estimate the tidal influence of extragalactic host halos, we use Press-Schechter theory with ellipsoidal collapse [373] to model the host halo mass function $\mathrm{d}n/\mathrm{d}M$, where n is the number density of hosts. We exclude EMDE-boosted microhalos (as hosts) by only considering halos down to the mass scale associated with the reheating wave number k_{RH}. We associate a concentration $c = R_{\mathrm{vir}}/R_s$ to each halo mass using the median concentration-mass relation $c(M)$ from Ref. [383], and we define R_{vir} as the radius enclosing 200 times the critical density to match that work.

With the host-halo population constructed, the next step is to calculate the suppression of microhalo annihilation signals within each host. In Appendix F.2, we use the model in Chapter 5 to compute the factor S by which tidal evolution scales the aggregate annihilation rate within subhalos distributed throughout the host's phase space. A convenient fitting function for $S(\rho_s/P_s, t\sqrt{GP_s}, c)$ is presented in that appendix, where ρ_s is the scale density of the microhalos,[15] P_s is the scale density of the host, $c = R_{\mathrm{vir}}/R_s$ is the host's concentration, and t is the duration of tidal evolution. At a given redshift z, the host scale density is a function $P_s(c, M)$ of mass and concentration. If we let $\bar{S}(\rho_s, t)$ be the global factor by which the annihilation rate within microhalos is scaled due to tidal evolution for the duration t, then

$$\bar{S}(\rho_s, t) = 1 - \frac{1}{\bar{\rho}} \int \mathrm{d}M \left[1 - S\left(\frac{\rho_s}{P_s}, t\sqrt{GP_s}, c \right) \right] M \frac{\mathrm{d}n}{\mathrm{d}M} \tag{7.9}$$

(with P_s and c functions of M).

We set the tidal evolution duration to be the time elapsed since $z = 20$; this choice only marginally affects our results since any reasonable duration is essentially the age of the Universe. Figure 7.10 shows $\bar{S}$ as a function of z (solid lines) for several different ρ_s. A limitation of this calculation, however, is that at any given time, microhalos are assumed to have resided within their current host since $z = 20$. Additionally, subhalos are neglected as possible hosts. The largest host halos become less dense as time goes on, so these deficiencies explain why we improperly find that microhalo annihilation signals become less suppressed ($\bar{S}$ grows) over time even as the microhalos experience

---

[15]S can be averaged over a distribution of ρ_s, weighting by J factors, to accommodate a distribution of microhalos.
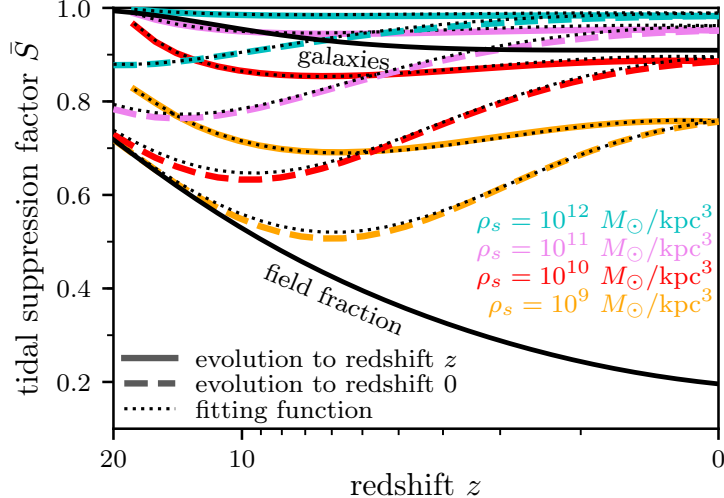
Figure 7.10: Global scaling factor $\bar{S}$ for dark matter annihilation within microhalos of scale density ρ_s due to tidal effects from host halos. The host population is characterized with a Press-Schechter mass function at each redshift z. Solid lines assume tidal evolution from redshift 20 to z, while dashed lines assume tidal evolution from $z = 20$ to $z = 0$ regardless of the redshift used to characterize the hosts. We expect that the minimal value of $\bar{S}$ under the latter calculation is a reasonable estimate for the true tidal scaling factor today; see the text. Dotted lines show the results using the fitting function in Appendix F.2 instead of integrating the individual tidal scaling factors from Chapter 5 over host halos' phase spaces as described in that appendix. The lower black line indicates the fraction of microhalos that are not subhalos. The upper black line marks the scaling of microhalo annihilation rates that results from an extreme estimate of disruption within galaxies. For values $\rho_s \geq 10^{12}\ M_\odot/\text{kpc}^3$ relevant to the EMDE scenarios we consider, all tidal suppression estimates are marginal.

uninterrupted tidal evolution.

To approximately account for this effect, we carry out the same calculation except that at each redshift z, we assume the full duration of tidal evolution (from $z = 20$ to $z = 0$) instead of only assuming tidal evolution up until the redshift z. This procedure means we can assume the microhalos continue to reside within the dense host population that existed at some redshift $z > 0$ even if those hosts later accrete onto superhosts. On the one hand, this procedure could underestimate the tidal suppression because the smaller number and size of host halos at high redshift implies that fewer microhalos are within hosts at all (see the field fraction curve in Fig. 7.10). On the other hand, it could overestimate the tidal suppression because we assume microhalos continue to reside within their dense original hosts even though many microhalos would be stripped onto a less dense superhost. In Fig. 7.10, we plot, as dashed lines, $\bar{S}$ computed using this procedure for several ρ_s. Here, the redshift z sets the host-halo population only. We expect that the minimal value of $\bar{S}$,

as a function of z, will be a reasonable estimate for the global tidal scaling factor. For $\rho_s \geq 10^{12}$ $M_\odot/\text{kpc}^3$, $\bar{S} \gtrsim 0.9$, and as Fig. 7.8 indicates, 10^{12} $M_\odot/\text{kpc}^3$ is the median ρ_s for $k_{\text{cut}}/k_{\text{RH}} = 20$ (with the effect of T_{RH} being marginal). If weighted by contribution to the annihilation signal, the average density would be even higher. Thus, we conclude that the contribution to the IGRB from annihilation within extragalactic microhalos at $z \simeq 0$ is suppressed by less than 10% due to tidal effects if $k_{\text{cut}}/k_{\text{RH}} \gtrsim 20$. Annihilation within high-redshift microhalos—which also contributes significantly to the IGRB—would be even less suppressed.

Microhalos can be also disrupted by baryonic structure within halos. As a simple estimate, we assume that galaxies span their halos' scale radii; this is roughly true of the Milky Way and of the Draco dwarf (see Sec. 7.5). We further assume that any microhalo within its host's galactic extent, defined in this way, is destroyed; this is an extreme estimate, since as we see in Sec. 7.5, annihilation from microhalos within the Draco dwarf is only slightly suppressed by encounters with stars. Finally, we assume any halo larger than $10^5 M_\odot$ forms a galaxy. The upper solid line in Fig. 7.10 shows the global scaling factor $\bar{S}$, as a function of redshift z, evaluated using these rules on the host-halo populations computed earlier. We find that even in this extreme picture, dark matter annihilation within microhalos is only suppressed by about 10% due to galactic disruption. Neither tidal forces from host halos nor disruption due to galaxies significantly reduces extragalactic microhalos' contribution to the IGRB.

Finally, we estimate the tidal suppression of the contribution to the IGRB from microhalos within the Galactic halo. To match the assumptions made in Ref. [467], we assume the Milky Way halo has an NFW density profile with scale radius 20 kpc and scale density set so that the local dark matter density at radius 8.25 kpc is 0.4 GeV/cm^3. We integrate the tidal scaling factors as in Appendix F.2, but instead of integrating over the Milky Way's volume, we integrate along the line of sight perpendicular to the Galactic plane out to the 300-kpc virial radius. The precise angle makes little difference. The resulting tidal scaling factor S_{Gal} is plotted in Fig. 7.11 as a function of microhalo scale density ρ_s. For $\rho_s \geq 10^{12}$ $M_\odot/\text{kpc}^3$, the tidal suppression is negligible.

7.5   Gamma rays from the Draco dwarf

Dwarf spheroidal galaxies represent some of the most promising targets for dark matter annihilation searches due to their high dark matter density and low astrophysical contamination [344]. Since the signal from annihilation within microhalos is similar to that from dark matter decay, we focus on
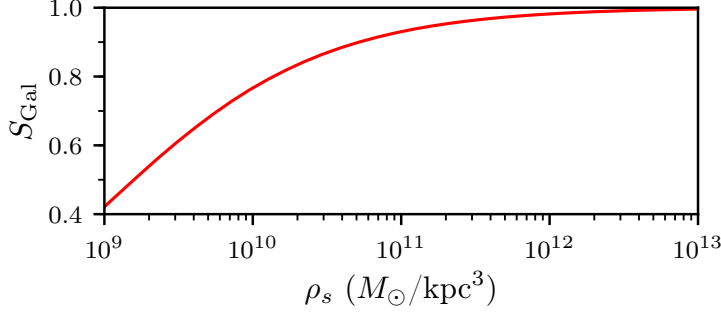
Figure 7.11: Tidal suppression of the contribution to the IGRB from microhalos within the Galactic halo. We plot, as a function of microhalo scale density ρ_s, the factor S_{Gal} by which annihilation rates along a line of sight are scaled. For values $\rho_s \geq 10^{12}\ M_\odot/\mathrm{kpc}^3$ relevant to the EMDE scenarios we consider, tidal effects reduce the annihilation rate by less than 2%.

the Draco dwarf, which among dwarf galaxies supplies the strongest constraints on the dark matter lifetime [479]. However, unlike the decaying dark matter signal, the signal from annihilation within microhalos is altered by the influence of tidal forces from the host halo and high-speed encounters with other microhalos. Due to their small size, microhalos are also susceptible to encounters with individual stars. We must account for these effects in order to characterize the microhalo-dominated annihilation signal from Draco.

To characterize Draco's dark matter halo, we assume its maximum circular velocity is $v_{\mathrm{max}} = 18.2$ km/s [480] and its density at radius 150 pc is $\rho(150\ \mathrm{pc}) = 2.4 \times 10^8\ M_\odot/\mathrm{kpc}^3$ [421]. If the halo has an NFW density profile, then these constraints imply it has scale radius $R_s = 0.435$ kpc and scale density $P_s = 1.5 \times 10^8\ M_\odot/\mathrm{kpc}^3$ (we use capital letters to distinguish these parameters from those of the microhalos). While there is evidence that many galactic halos possess uniform-density cores instead of the NFW profile's cusp (e.g., Ref. [420]), Draco's halo appears to be cuspy [421]. We assume the microhalos trace Draco's density profile with an isotropic velocity distribution.

As for its stellar content, we assume Draco has stellar luminosity $2.7 \times 10^5 L_\odot$, projected half-light radius 0.22 kpc [481], and a stellar mass-to-light ratio of 1.8 $M_\odot/L_\odot$ [482]. Additionally, we adopt a Plummer density profile [483] for its stellar mass. To model the masses of individual stars, we employ a Kroupa initial mass function with minimum mass $0.01 M_\odot$ (we include brown dwarfs) and a high-mass index of 2.7 [484]. Since Draco largely ceased star formation 10 Gyr ago [485], roughly the lifetime of a 1 $M_\odot$ star, we impose a maximum stellar mass of 1 $M_\odot$. However, we still wish to include the white dwarf remnants of dead stars, so we assume any star initially heavier than 1 $M_\odot$

173

weighs 1 $M_\odot$.[16] Finally, using the mean of the stellar mass distribution, we are able to fix the stellar number density profile $n_*(R)$.

7.5.1 Suppression of annihilation rates

Due to their small size, we expect microhalos to have essentially the same phase-space distribution as dark matter particles within Draco's halo. Thus, at each radius R within Draco, we sample 200 microhalo orbits using the isotropic distribution function given in Ref. [422]. To efficiently apply the models in Chapters 5 and 6 to full distributions of microhalos, we use these sampled orbits to construct, at each radius, an interpolation table in ρ_s for the orbit-averaged factor J/J_{init} by which annihilation within microhalos is suppressed. We consider ρ_s alone because the scale radius r_s has no impact on tidal evolution, and we verified that for relevant microhalo parameters, r_s also has no impact on the evolution by stellar encounters. Subsequently, we use this interpolation table to find J/J_{init} for the full distribution of microhalos. We then average J/J_{init} over all microhalos, weighting each halo by its initial J factor given by Eq. (7.5).

It is straightforward to apply the model in Chapter 5 to each microhalo orbit to determine the suppression of the J factor due to tidal forces from Draco's halo. In Fig. 7.12, we show, as a function of radius within Draco, this model's prediction of J/J_{init} (dashed line) averaged as described above over the microhalo distribution. Microhalo J factors also oscillate over each orbital period, becoming largest near pericenter, and the model in Chapter 5 does not account for these oscillations since they do not affect the magnitude of an annihilation signal. However, they can change the signal's morphology since they systematically bias it toward smaller radii. In Appendix F.3, we use the simulations from Chapter 5 to explore these oscillations and present a simple model for their impact. The results of this model are included in the scaling factor due to tidal forces depicted in Fig. 7.12, but we also show as dotted lines the scaling if these oscillations are neglected. Evidently, their impact is negligible for the host-subhalo parameters relevant to our scenario.

Chapters 5 and 6 describe how to account for tidal forces and stellar encounters separately.

---

[16]This treatment is approximate; white dwarf masses vary and stellar masses change over their lifetimes. However, the following scaling argument shows (and we verified) that the choice of star masses M_* has little impact on microhalo evolution. The energy injected by an encounter with impact parameter b scales as $\Delta E \propto M_*^2 b^{-4}$. Due to this scaling, the total energy injected by all encounters is dominated by the closest few encounters, which have $b \propto n_*^{-1/2}$. But at fixed stellar mass density, $n_* \propto M_*^{-1}$. Together, these relationships imply $\Delta E \propto M_*^0$.
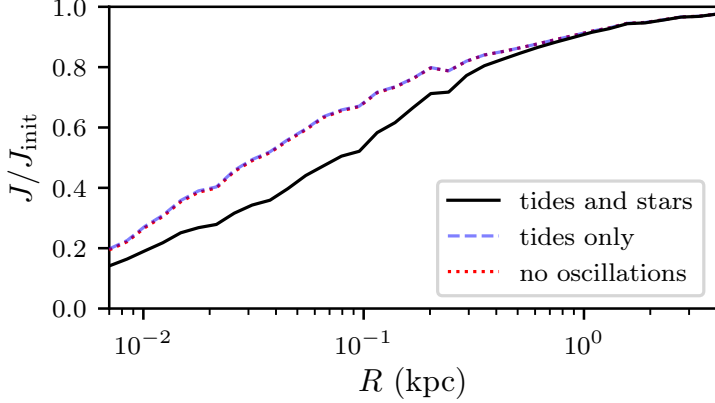
Figure 7.12: Suppression of dark matter annihilation rates in microhalos as a function of radius R within the Draco dwarf. At each radius we average over 200 randomly sampled orbits. Additionally, for each orbit, we average over 200 randomly sampled stellar encounter histories. The EMDE scenario represented has $T_{\mathrm{RH}} = 2$ GeV and $k_{\mathrm{cut}}/k_{\mathrm{RH}} = 20$.

However, it is not obvious how to combine the two effects. To determine the appropriate procedure, we carry out additional simulations using the same procedures as Chapters 5 and 6. In these simulations, a microhalo experiencing tidal forces is also subjected to stellar encounters. Appendix F.4 presents the model we build to describe this scenario. The simulations indicate that it makes little difference when the stellar encounter occurs, so our model is conceptually based on the idea of applying tidal evolution first and stellar encounters afterward.

To determine the impact of stellar encounters using the framework of Chapter 6 and Appendix F.4, we must randomly sample stellar encounter histories for each microhalo orbit. Let $f(R; V_*)$ be the stellar velocity distribution at radius R, which we assume to be Maxwell-Boltzmann with velocity dispersion equal to that of the dark halo at the same radius. As before, we take $n_*(R)$ to be Draco's stellar number density profile. We also take $V_{\mathrm{h}}(R)$ and $V_{r,\mathrm{h}}(R)$ to be the microhalo's total velocity and the radial component of its velocity, respectively, which depend on the orbit. With these definitions, the differential number of stellar encounters per radius R, impact parameter b, stellar velocity V_*, and cosine $\mu \equiv \cos\theta$ of the angle between V_{h} and V_* is

$$\frac{\mathrm{d}^4 N_{\mathrm{enc}}}{\mathrm{d}b\mathrm{d}R\mathrm{d}V_*\mathrm{d}\mu} = \pi b \frac{V_{\mathrm{rel}}[V_{\mathrm{h}}(R), V_*, \mu]}{V_{r,\mathrm{h}}(R)} n_*(R) f(R; V_*), \tag{7.10}$$

where

$$V_{\mathrm{rel}}(V_{\mathrm{h}}, V_*, \mu) \equiv \left[(V_{\mathrm{h}} - \mu V_*)^2 + (1 - \mu^2)V_*^2 \right]^{1/2} \tag{7.11}$$

175

is the relative velocity between the halo and the star. We use Eq. (7.10) to sample the stellar encounters for each orbit, evaluating the μ integral analytically and using a Markov chain Monte Carlo method [486] to sample R and V_*. For each encounter, we sample the stellar mass M_* from the modified Kroupa distribution described earlier. We assume that each orbit proceeds for 13.6 Gyr, roughly the time since $z = 20$, and for each orbit we sample 200 encounter histories. We determine the impact of stellar encounters for each history using the models in Chapter 6 and Appendix F.4, and Fig. 7.12 shows the resulting J-factor suppression averaged over orbits and encounter histories. We include the effect of the J-factor oscillations described in Appendix F.3, although, as noted above, their impact is negligible.

Finally, we explore the impact of microhalo-microhalo encounters. We will see that their influence on microhalo J factors is marginal. For concreteness, we consider a microhalo on a circular orbit at Draco's 0.22-kpc half-light radius, and for its density profile we adopt separately the median parameters ρ_s and r_s associated with the reheat temperatures $T_{\mathrm{RH}} = 10$ MeV and 2 GeV and ratios $k_{\mathrm{cut}}/k_{\mathrm{RH}} = 20$ and 40. We model the microhalos it encounters as point objects so that we can compute the energy each encounter injects similarly to stellar encounters; note that energy injections would only decrease if we were to model the microhalos as extended objects. These microhalos are distributed along the density profile $P(R)$ of Draco's halo; i.e., the number density profile of microhalos is $nP(R)/\bar{\rho}$, where n is the cosmological mean number density of microhalos. We leave n as a free parameter for now, although it is related to the known number density n_{peak} of peaks in the primordial density field. Finally, to fix the masses M of microhalos, we assume that they contain a fraction f of the dark matter, so $M = f\bar{\rho}/n$. Tidal effects likely reduce f far below 1 inside Draco by stripping microhalos' massive but weakly bound outskirts, and we generously assume $f = 0.25$.

Using a similar procedure to our treatment of stellar encounters above, we derive the fractional change $\Delta J/J$ in the subject microhalo's J factor caused by microhalo encounters over Draco's age. We seek only the relative impact of microhalo encounters, so we do not combine them with tidal evolution as in Appendix F.4, although as prescribed in that appendix we sum the encounters' energy injections instead of applying the encounters consecutively. Figure 7.13 plots $\Delta J/J$ as a function of the mean number density n of microhalos; smaller n means more massive microhalos,
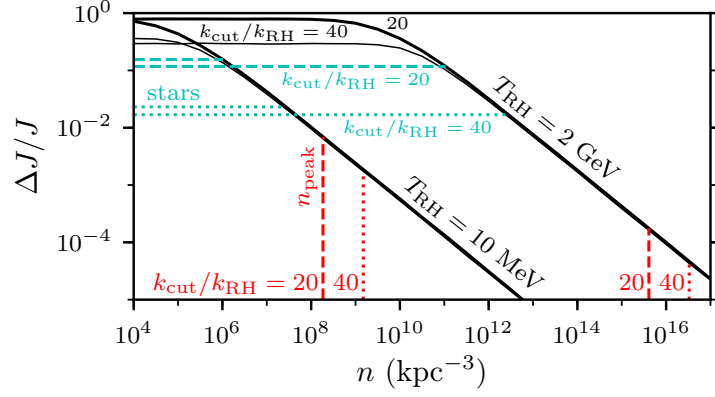
Figure 7.13: Impact of encounters with other microhalos on a microhalo with the median density profile parameters ρ_s and r_s associated with the displayed T_{RH} and $k_{\mathrm{cut}}/k_{\mathrm{RH}}$. This microhalo orbits Draco circularly with radius 0.22 kpc. Black lines show the fractional change $\Delta J/J$ in the microhalo's J factor due to all encounters over Draco's age; this ratio is averaged over 10^4 random encounter histories and plotted as a function of the cosmological mean number density n of microhalos. We assume 25% of dark matter is in microhalos. As a reference, the number density n_{peak} of peaks in the primordial density field is marked for the relevant EMDE cosmologies with vertical lines; mergers deplete n relative to n_{peak}, but likely by much less than an order of magnitude. Evidently, the impact of encounters with microhalos is negligible as long as n is not much smaller than n_{peak}. For comparison, we also mark with horizontal lines the $\Delta J/J$ induced by stellar encounters. For horizontal and vertical lines, the length indicates which T_{RH} curve it matches.

which outweighs their reduced numbers for most n.[17] For each EMDE scenario, we also indicate n_{peak}. Evidently, $\Delta J/J \ll 1$ as long as n is not smaller than n_{peak} by more than an order of magnitude. While mergers cause $n < n_{\mathrm{peak}}$, they depleted n by less than a factor of 2 by $z = 50$ in the EMDE scenario simulated by Chapter 4. For this reason, and because the assumptions made in this calculation were broadly biased toward overestimating their impact, we conclude that microhalo-microhalo encounters can be neglected. For comparison, we also mark in Fig. 7.13 the impact of stellar encounters on the same microhalo.

---

[17] The story is different for stars; increased number density there approximately compensates reduced mass (e.g., footnote 16). This contrast is a consequence of the very different regimes that stellar and microhalo encounters occupy. When the closest encounter is typically farther than the subject microhalo's scale radius r_s, as is the case with stellar encounters, the total energy injection is dominated by the closest few encounters due to the $\Delta E \propto b^{-4}$ scaling with impact parameter b. As b drops below r_s, this scaling shallows toward $\Delta E \propto b^0$ [328, 464], so when there are many encounters with $b < r_s$, the total energy injection is broadly distributed across all such encounters. The latter case applies to microhalo encounters with sufficiently large n.

7.5.2 Gamma-ray emission

We denote by $S(R)$ the orbit-averaged tidal suppression of the J factor, as a function of radius R about Draco, computed in the last section. With this quantity, we can predict the annihilation signal from microhalos within Draco. If $P(R)$ is the density profile of Draco's halo and $\bar{\rho}$ is the cosmological mean dark matter density, then

$$\frac{\mathrm{d}L}{\mathrm{d}V} = \overline{\frac{\mathrm{d}L}{\mathrm{d}V}} \frac{P(R)}{\bar{\rho}} S(R) \tag{7.12}$$

is the gamma-ray luminosity, per volume, from dark matter annihilation at radius R. Here, $\overline{\mathrm{d}L/\mathrm{d}V}$ is the cosmological mean value given by Eq. (7.7). By integrating this emission over the line of sight, we obtain the differential flux per solid angle

$$\frac{\mathrm{d}F}{\mathrm{d}\Omega} = \frac{1}{4\pi} \int_{-x_{\mathrm{max}}}^{x_{\mathrm{max}}} \mathrm{d}x \left. \frac{\mathrm{d}L}{\mathrm{d}V} \right|_{R=\sqrt{x^2 + R_{\mathrm{proj}}^2}} \tag{7.13}$$

at projected radius R_{proj} from Draco's center, where $x_{\mathrm{max}} \equiv \sqrt{R_{\mathrm{max}}^2 - R_{\mathrm{proj}}^2}$ and R_{max} is the boundary radius of Draco's halo, which we fix shortly.

The gamma-ray flux from microhalos exhibits significant sensitivity to Draco's density profile at large radii, which cannot be constrained by stellar kinematics beyond the 1.9-kpc radius of its most distant observed star [487]. The density profile at large radii would be suppressed by tidal forces from the Milky Way and its halo, and we account for this effect by assuming the density profile

$$P(R) = P_s y^{-1} (1+y)^{-2} [1 + (y/y_t)^\delta]^{-1}, \quad y \equiv R/R_s; \tag{7.14}$$

the $[1 + (y/y_t)^\delta]^{-1}$ suppression factor, with free parameters y_t and δ, is motivated by prior studies of tidal evolution in N-body simulations [340, 341, 462]. In Appendix F.5, we use the results of the tidal evolution simulations of Ref. [342], along with Draco's orbit and history, to fix $y_t = 4.3$ and $\delta = 3.9$. We then set $R_{\mathrm{max}} = 4$ kpc because this profile reaches the background density of the Galactic halo at this radius.

For illustration, Fig. 7.14 shows the flux profile $\mathrm{d}F/\mathrm{d}\Omega$ for one EMDE scenario as a function of angle $\theta = R_{\mathrm{proj}}/D$. We assume Draco lies at distance $D = 76$ kpc [488], so the emission extends out
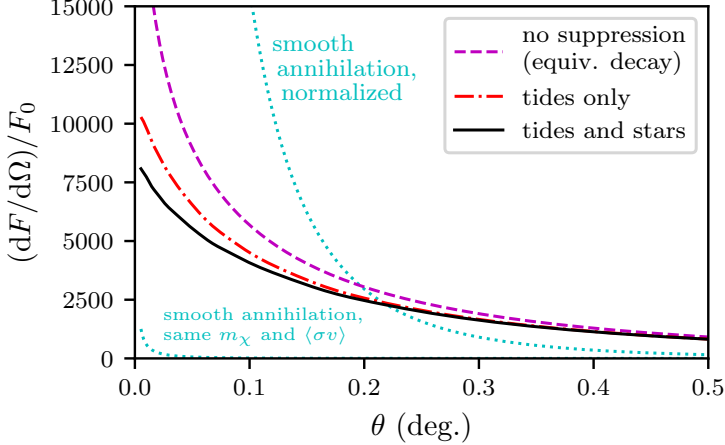
Figure 7.14: Demonstration of the influence of tidal forces and stellar encounters on the microhalo-dominated annihilation signal from Draco. We plot the projected emission profile (flux per solid angle) in the EMDE cosmology with $T_{\mathrm{RH}} = 2$ GeV and $k_{\mathrm{cut}}/k_{\mathrm{RH}} = 20$ if both, one, or neither of these effects are accounted for. Note that without suppression, the signal is morphologically equivalent to that of dark matter decay. All curves are normalized to the total flux F_0 (out to $3°$) that would be expected in the absence of tidal evolution and stellar encounters. We also show the signal from dark matter annihilation within Draco's smooth halo for comparison (dotted lines); this signal is plotted both normalized to its total flux and, in the bottom left, with the same dark matter particle as the microhalo curves. The latter curve illustrates the extent to which microhalos dominate the annihilation signal.

to $R_{\mathrm{max}}/D = 3°$ (not shown). For comparison, we also show the flux profiles if stellar encounters are neglected and if tidal evolution is also neglected. Evidently, tidal evolution and stellar encounters both influence the flux profile appreciably. Note that the unsuppressed curve is equivalent to the signal from decaying dark matter. As another comparison, we plot the flux profile from dark matter annihilation within Draco's smooth halo; it peaks much more sharply at small angles and drops off more quickly at large angles. We also show the smooth annihilation profile normalized to the same dark matter properties as the microhalo flux profiles; this profile represents the contribution from dark matter outside of microhalos.[18]

In Fig. 7.15, we plot the flux profiles $dF/d\Omega$ in a variety of EMDE cosmologies, including the contribution from annihilation outside of microhalos. Tidal evolution and stellar encounters evidently induce marked differences in signal morphology between the scenarios. This diversity arises because

---

[18]The annihilation rate outside of microhalos is scaled by the fraction $1 - f$ of dark matter not in microhalos, but we assume tidal effects cause $1 - f \simeq 1$ at the radii where smooth annihilation contributes nonnegligibly.
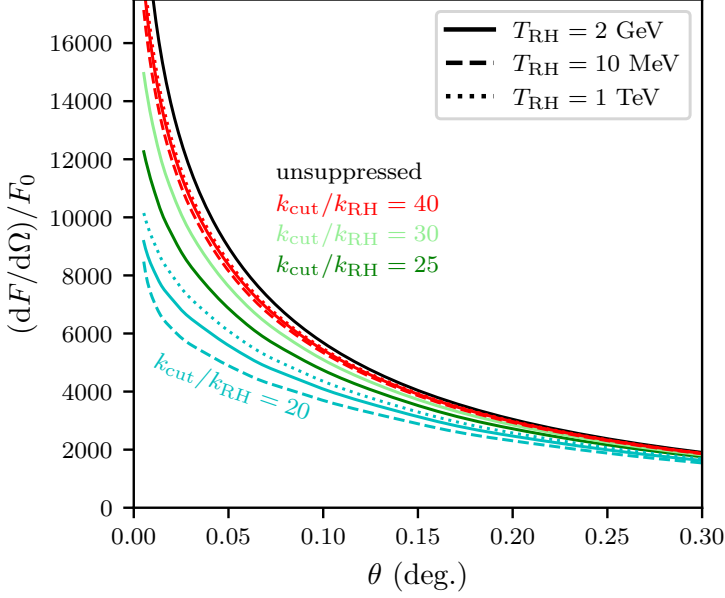
Figure 7.15: Projected emission profiles (flux per solid angle) for the Draco dwarf in a variety of EMDE scenarios. In each case, the emission profile is normalized to the total flux F_0 that would be expected in the absence of tidal evolution and stellar encounters. There are clear differences in signal morphology between the different EMDE scenarios; these differences largely arise because denser microhalos are more resistant to disruption. Thus, cosmologies that form microhalos earlier yield less-suppressed signals.

denser microhalos are more resistant to these effects. As Fig. 7.8 shows, scenarios with larger k_{cut}/k_{RH} result in denser halos, while T_{RH} mostly controls halo size and only minimally affects density. Thus, scenarios with larger k_{cut}/k_{RH} yield significantly less-suppressed annihilation signals.

7.5.3 Limits on annihilation

We calculate the best-fitting flux and spectrum of the Draco dwarf using established techniques for the detection of dim, spatially extended sources, which were first developed for dwarf galaxies by Refs. [209, 211, 489, 490]. We analyze 11 years of Fermi-LAT data taken between August 4, 2008 and September 3, 2019, extracting Pass 8 source-class photons recorded with an energy between 100 MeV and 1 TeV observed in a $30° \times 30°$ box centered on the position of Draco. We place standard cuts on the data quality and LAT configuration during events and divide the recorded events into 32 logarithmic energy bins and $0.1°$ angular bins over the region of interest.

In order to calculate the improvement to the log-likelihood generated by adding an extra degree of freedom at the position of the Draco dwarf, we first calculate the log-likelihood fit of a background model (which does not include the dwarf) to the Fermi-LAT data. We utilize the recently released

180

4FGL catalog [491], the `gll_iem_v07` diffuse model, and the `iso_P8R3_SOURCE_V2_v1` isotropic background model. We independently fit the normalization of each diffuse source, as well as every point source with a detection significance exceeding 10, independently in every energy bin, fixing the spectra of these sources to their 4FGL default values.

We then fix the parameters of all sources in the background fit and add a new degree of freedom corresponding to the Draco dSph, appropriately employing a morphological model computed using Eq. (7.13) (and depicted in Fig. 7.15). Because the likelihood profile scans over the dark matter-induced flux in each model, this stage of the analysis is sensitive only to the morphology of each emission model and not to its overall normalization. We calculate the change in the likelihood of the fit as the flux from this component increases from an initial value of 0 in each independent energy bin. Using a spectral model based on the annihilation of dark matter particles of various masses to $b\bar{b}$ final states, we calculate the 2σ combined upper limit by determining the Draco flux which worsens the log-likelihood of the fit by 2, compared to a model with no contribution from Draco. Figure 7.16 shows the resulting limits on the total gamma-ray flux from Draco for several different signal morphologies. More centrally concentrated signals are more strongly constrained, as illustrated by the strength of the flux limit for annihilation within Draco's smooth profile. Consequently, naively applying a boost factor to account for the microhalos' increased annihilation rate relative to a smooth halo would produce constraints that are too strong by a factor of about 2. However, relative to dark matter decay, the signal from microhalo-dominated annihilation in EMDE cosmologies is not sufficiently morphologically altered to significantly change the flux limits.

We translate the flux upper limit into an upper bound on the dark matter cross section by utilizing the expected net flux from Draco, which is obtained for each EMDE realization by integrating Eq. (7.12) over Draco's volume. In Fig. 7.17, we plot the resulting limits on the dark matter annihilation cross section for EMDE scenarios with $T_{\mathrm{RH}} = 10$ MeV and $T_{\mathrm{RH}} = 2$ GeV. For comparison, we also plot the constraints derived in Sec. 7.4 using the IGRB. We find that the limits from Draco are comparable to the conservative limits from the IGRB, where all of the gamma-ray flux is allowed to be attributed to dark matter, and are much weaker than the aggressive limits in which astrophysical sources are modeled and subtracted from the IGRB. Evidently, for dark matter annihilation within microhalos, Draco produces bounds that are at best comparable to those from the IGRB. We remark, however, that an advantage to searching for microhalo annihilation within
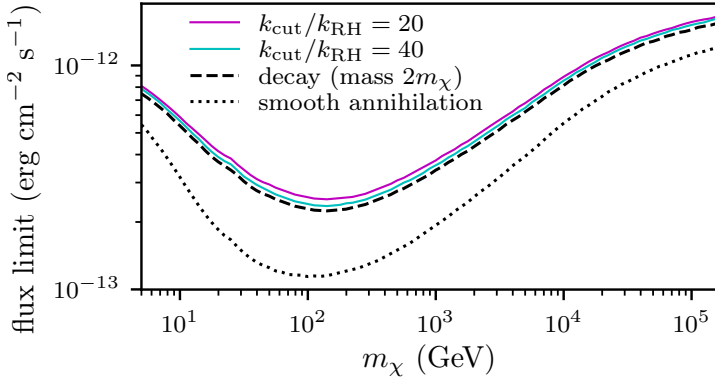
Figure 7.16: Impact of the signal morphology on the bounds derived from Fermi-LAT observations on the energy flux from Draco in gamma rays above 100 MeV. We plot 2σ upper limits assuming annihilation or decay into $b\bar{b}$; different curves assume different flux profiles as shown in Figs. 7.14 and 7.15. For the EMDE-induced signals, we assume $T_{\mathrm{RH}} = 2$ GeV. Because it is so much less centrally concentrated, the gamma-ray flux from dark matter decay is constrained less strongly than the flux from annihilation within Draco's smooth profile by roughly a factor of 2. Signals from annihilation within microhalos in EMDE cosmologies are even less centrally concentrated than decay signals due to the influence of tidal effects and stellar encounters, but this change in morphology is too small to significantly further weaken constraints.

galactic systems is the potential to distinguish it from dark matter decay through the presence of suppressive tidal effects. We leave an exploration of this possibility to future work. Another more general advantage to dark matter detection in regions with known overdensities is that any positive gamma-ray signal would be spatially correlated with that overdensity, making its attribution to dark matter more convincing.

We also note that recent analyses, such as Refs. [492–494], have considered complex statistical issues which may arise due to systematic errors in the background modeling. While more precise treatments are possible, the systematic issues become most acute in three regimes: (1) when an analysis includes a joint-likelihood treatment of many dSphs, most of which have an expected dark matter content that falls far below the brightest few dSphs; (2) when a dwarf has a significant positive (or negative) flux associated with it, which may also be due to background mismodeling; and (3) when small changes in the constraint on the dark matter annihilation rate (at the order of 10%) are highly relevant, such as in a comparison of standard annihilation constraints to dark matter models of the Galactic center gamma-ray excess [495]. Our analysis of Draco does not fall into any of these regimes, so we do not produce a detailed calculation of the expected cross section constraints from multiple blank sky locations, an analysis which is computationally costly and would

182
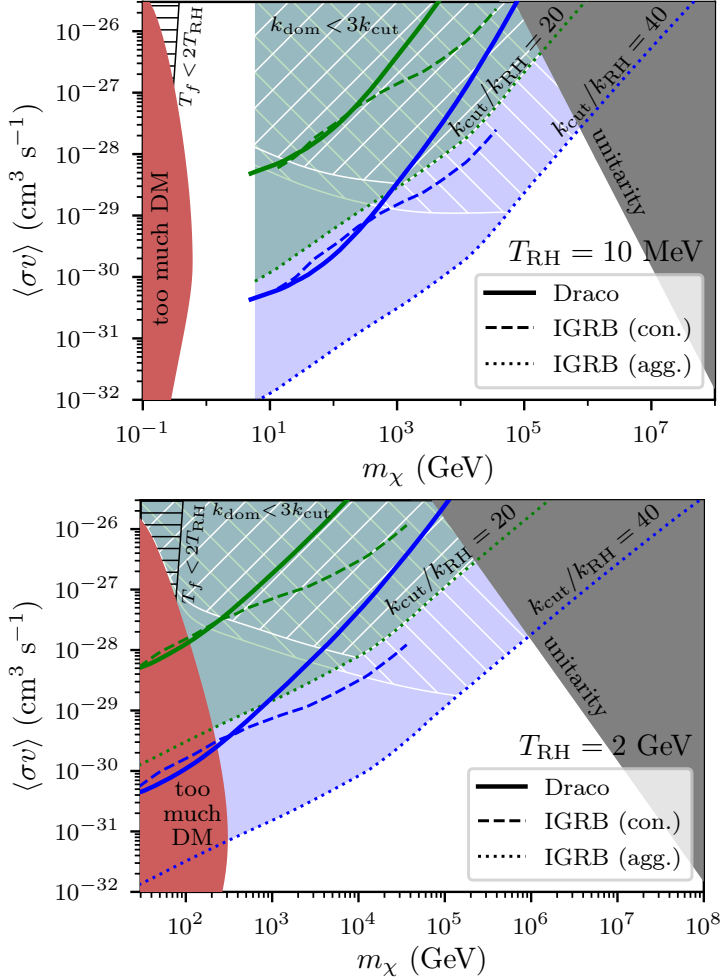
Figure 7.17: Upper bounds on the cross section for dark matter annihilating into $b\bar{b}$ for two reheat temperatures $T_{\mathrm{RH}} = 10$ MeV (top) and $T_{\mathrm{RH}} = 2$ GeV (bottom), as derived from Fermi-LAT observations of the Draco dSph. In each case, we consider both $k_{\mathrm{cut}}/k_{\mathrm{RH}} = 20$ (green) and $k_{\mathrm{cut}}/k_{\mathrm{RH}} = 40$ (blue). In addition to the bounds from Draco, we also repeat from Fig. 7.9 the conservative and aggressive bounds derived from the IGRB. We find that the Draco-derived limits are comparable to the conservative limits from the IGRB and significantly weaker than the aggressive, background-subtracted limits. The shaded region on the left is disallowed because it would overclose the Universe, while the shaded region on the right marks where the dark matter's coupling constant exceeds unity. Constraints are tentative within the hatched regions because they fail Eq. (7.1) or (7.2), which implies that the density fluctuation power spectra we employed do not apply therein.

only mildly change our calculated limits.

7.6 Conclusion

In this work, we developed a procedure to constrain thermal-relic dark matter that freezes out during or before an EMDE using existing indirect-detection probes. These scenarios reduce the annihilation cross section required for dark matter to achieve the observed relic abundance, but they also induce the formation of abundant dark matter microhalos, which can bring these smaller cross sections into view. As demonstration, we considered EMDE cosmologies with reheat temperatures $T_{\mathrm{RH}} = 10$ MeV and 2 GeV. By comparing the annihilation signals from predicted microhalo populations to Fermi-LAT gamma-ray limits, we derived new constraints, shown in Fig. 7.17, on thermal-relic dark matter in these cosmologies.

The principal challenge is to accurately model the microhalo population, and for that purpose we employed the models presented in Chapters 4–6 along with several new refinements. These models describe the formation of microhalos and their evolution within larger systems. Our refinements include accounting for the reduced growth rate of the smallest-scale dark matter density variations, modeling the combined impact of subhalo tidal evolution with stellar encounters, and accounting for transient tidal effects that trace a subhalo's orbital period. We also devised a convenient fitting function to describe the aggregate tidal suppression of subhalo annihilation rates within a host. These models allow precise tracking of the microhalo population through cosmic time with the caveat that the impact of mergers between microhalos remains unclear. We employed an approximate model based on the results of Chapter 4 and Ref. [339] to treat these mergers, and our results are subject to this approximation's accuracy. Further study is needed to precisely understand how mergers influence a microhalo population.

We separately derived limits on dark matter annihilation in EMDE cosmologies using the IGRB and the Draco dwarf, and we found that the IGRB produces stronger bounds. This result is unsurprising since the signal from microhalo annihilation roughly follows the dark matter mass distribution, so the sheer volume of the background outweighs the high density within dwarf galaxies. The same property makes IGRB-derived bounds on the dark matter lifetime (e.g., Refs. [466, 467]) stronger than those derived from dSphs (e.g., Ref. [479]). We note, however, that galactic systems can still be valuable in probing annihilation within microhalos because they can distinguish this process from dark matter decay. The two produce morphologically similar signals, but microhalos

within larger systems are subject to disruption by tidal effects and encounters with other objects, suppressing the annihilation signal near these systems' centers. We leave further investigation of this possibility to future work.

The IGRB suffers significant astrophysical contamination, so the strength of our bounds depends strongly on the degree to which astrophysical gamma-ray sources are modeled and subtracted. Using the aggressive subtraction program in Ref. [467], we are able to probe cross sections as small as 10^{-32} cm^{3}s^{-1} for dark matter annihilating into $b\bar{b}$, although the strength of constraints depends strongly on the dark matter mass, the reheat temperature, and the ratio $k_{\rm cut}/k_{\rm RH}$ between the free-streaming scale and the wave number entering the horizon at reheating. We explored only the range $20 \leq k_{\rm cut}/k_{\rm RH} \leq 40$, ratios plausible for certain supersymmetric dark matter candidates [225]. Larger values of $k_{\rm cut}/k_{\rm RH}$ are also plausible and would be much more strongly constrained, but they require accurately modeling halo formation during the radiation-dominated epoch (e.g., [206]), a problem we leave to future work. Also, thermal relics with cross sections less than a few orders of magnitude below the canonical $\langle \sigma v \rangle = 3 \times 10^{-26}$ cm^{3}s^{-1} tend to be only tentatively constrained; the EMDE cosmologies needed to effect the observed dark matter abundance for these cross sections result in density fluctuation spectra different from those we assumed. A more careful treatment is necessary to constrain thermal-relic dark matter candidates with cross sections in this regime.

This work represents an important step toward the development of robust constraints on thermal-relic dark matter that account for our ignorance of the Universe's early thermal history. The possibility of early matter domination prior to BBN vastly broadens the range of dark matter properties that can produce the observed abundance, but we exploit the dark matter annihilation boost induced by the microhalo populations that arise in these cosmologies to considerably narrow the range of viable dark matter candidates. We close by noting that while our constraints assume that dark matter is a thermal relic, the microhalo populations studied in this work could potentially be probed gravitationally through pulsar timing arrays [25, 496] and searches for lensing distortions in highly magnified stars [24]. In this way, these microhalos can prospectively be used to constrain the early thermal history without assuming that dark matter has a thermal origin.

CHAPTER 8:
CONCLUSION

The smallest dark matter halos present a promising arena in which to test three major cosmic mysteries: what drove inflation, what happened after inflation, and what is dark matter? Potential answers to these questions leave characteristic imprints in the power spectrum $\mathcal{P}(k)$ of density variations, particularly at small scales, and these dark matter minihalos represent the most powerful probe of subkiloparsec-scale density variations. However, this probe's usage is hindered by the dynamical complexity of these systems. Dark matter halos undergo deeply nonlinear dynamics, the prediction of which demands numerical simulation. However, due to their small size and high internal density, dark matter minihalos cannot be simulated in full cosmological context up to the present day. This dissertation presented an answer to this challenge.

Chapter 2 established the density profiles of the first halos. I demonstrated that the $\rho \propto r^{-9/4}$ density profile assumed by many previous works does not arise from a natural formation scenario. However, the first halos also do not develop the classic Navarro-Frenk-White profile, instead developing density profiles that asymptote to $\rho \propto r^{-3/2}$ at small radii. Chapter 2 also developed a simple model to predict minihalo density profiles based on their formation times, and I used this model to explore how the new density profile assumption altered minihalo-derived bounds on the primordial power spectrum. Surprisingly, I found that despite the reduced detectability of the new shallower density profile, constraints were tightened. Works that assumed the $\rho \propto r^{-9/4}$ density profile considered only the rare halos that form by redshift $z = 1000$, but since I found that all minihalos develop the same density profiles, I was able to relax this requirement. The inclusion of all minihalos in my analysis compensated the reduced detectability of the rare halos that form by $z = 1000$. This promising result motivated further study of dark matter minihalos.

Certain well motivated cosmological scenarios, such as those predicted by a range of hidden-sector theories, could induce even earlier halo formation. Chapter 3 explored the fate of regions so overdense that they collapse before the redshift $z = 3400$, when radiation dominated. I found that while

gravitationally bound structures cannot form where radiation dominates, localized regions can become matter dominated solely through convergent particle drift. Within these regions, bound halos can form long before radiation globally gives way to matter, and I used numerical simulations to develop a formalism that can predict when this formation occurs. These halos would be so dense that observations strongly limit their abundance, and Ref. [206] used this formalism to observationally constrain a range of hidden-sector theories.

To enable more precise characterization of minihalo populations, Chapter 4 developed a general predictive model that expanded on the specialized model presented in Chapter 2. Each minihalo can be understood to form from a peak in the primordial density field, which is directly connected to the power spectrum and hence to questions about the early Universe and the nature of dark matter. My model predicts each halo's properties from the properties of its precursor density peak. This model is formulated in a direct way using physically motivated models and scaling arguments, with a minimum of simulation-tuned parameters. Consequently, it is accurate across wildly disparate cosmological scenarios, making it a powerful tool for establishing the minihalo-cosmology connection.

The aforementioned model accurately describes the properties of first-generation halos that remain isolated. However, after formation, many minihalos merge with other objects to produce larger structures. Chapter 5 developed a model that predicts how minihalos evolve as subhalos inside the much larger halos that arose more recently. The structures of these subhalos are gradually reshaped by their host halo's tidal forces. My model predicts this evolution in terms of three physically motivated parameters of the host-subhalo system: the energy injected into subhalo particles per orbit about the host, the ratio of stretching to compressive tidal forces, and the radial distribution of tidal heating within the subhalo. Thanks to this novel parametrization, it predicts tidal evolution for subhalos on arbitrary orbits with an accuracy unparalleled by previous treatments.

Within galactic halos, sufficiently small minihalos can also be affected by encounters with individual stars. Chapter 6 developed a model that predicts how minihalos evolve in response to stellar encounters. This model is formulated solely in terms of the energy injected by the encounter into halo particles. I found that the postencounter density profile follows a universal form, making it a simple matter to treat the impact of arbitrarily many successive stellar encounters. My model accurately predicts the evolution of minihalos crossing whole fields of stars.

Finally, Chapter 7 applied these models to a problem concerning both the early Universe and

the identity of dark matter. If thermal-relic dark matter's cosmological production concluded when radiation dominated, the dark matter annihilation cross section is fixed at the canonical value $\langle \sigma v \rangle = 3 \times 10^{-26}$ cm^{3}s^{-1} by the requirement that dark matter achieve the observed abundance. Indirect-detection experiments have begun to test this cross section. However, the possibility of an early matter-dominated era vastly broadens the range of viable dark matter candidates by bringing thermal relics with smaller annihilation cross sections down to the observed abundance. Fortunately, early matter domination also boosts density variations at small scales, a change that raises the internal density of the smallest halos and thereby boosts the dark matter annihilation rate dramatically. Chapter 7 explores the extent to which this halo population brings these dark matter candidates back into the view of indirect-detection searches. I applied the models described in Chapters 4–6 to characterize the minihalo populations that arise from various EMDE scenarios and used these characterizations to predict the observational signatures from dark matter annihilation in these cosmologies. For plausible dark matter parameters, these minihalo populations allow cross sections as small as 10^{-32} cm^{3}s^{-1} to be constrained by the Fermi Gamma-ray Space Telescope's measurement of the isotropic gamma-ray background. Chapter 7 also explored the peculiar annihilation signal morphologies that arise from minihalos inside galactic systems, focusing on the Draco dSph in particular. In these environments, annihilation rates within minihalos are altered by their evolution due to tidal forces and encounters with other objects. While Draco yields weaker cross-section constraints than the isotropic background, the signal morphology from such a system could potentially distinguish the signal associated with an EMDE from that caused by dark matter decay, an otherwise unrelated prospective phenomenon.

By advancing our understanding of the formation and evolution of dark matter minihalos, this dissertation developed an observational window into dark matter and the early Universe. I developed models that treat the formation of the first halos and their evolution as they accrete onto larger structures. The principal remaining problem is to understand the impact of mergers between minihalos, the process by which larger structures are assembled. Chapter 7 presented an approximate treatment, but further work is needed to precisely understand the outcome of mergers between halos of comparable mass.

APPENDIX A:
TECHNICAL DETAILS ON SIMULATIONS OF ULTRACOMPACT MINIHALOS AND CONSTRAINING THE PRIMORDIAL POWER SPECTRUM[1]

A.1   Simulations prior to the matter-dominated era

For our numerical experiments, we employ a modified version of GADGET-2 that includes a smooth radiation component, and we begin the simulations long before matter-radiation equality. The simulation starting redshift of $z = 8 \times 10^6$ is necessary so that our enhanced fluctuations are still in the linear regime with amplitude $\delta \lesssim 0.1$. However, the assignment of initial particle velocities is more complicated in this picture than during matter domination, and we use the Zel'dovich approximation to compute them in the following way.

We begin with the density contrast field $\delta(\boldsymbol{q})$ as a function of the comoving grid coordinate $\boldsymbol{q}$. We wish to convert this description into a comoving position field $\boldsymbol{x}(\boldsymbol{q})$ and velocity field $\dot{\boldsymbol{x}}(\boldsymbol{q})$ treating $\boldsymbol{q}$ as a Lagrangian coordinate assigned to each particle. The position calculation proceeds by writing

$$\boldsymbol{x}(\boldsymbol{q}) = \boldsymbol{q} + \boldsymbol{s}(\boldsymbol{q}), \tag{A.1}$$

where the displacement vector $\boldsymbol{s}$ is related to δ at linear order by $\nabla \cdot \boldsymbol{s} = -\delta$. If we assume $\boldsymbol{s}$ is irrotational, then $\boldsymbol{s} \propto \nabla \delta$, and the Fourier-transformed quantities are related by

$$\boldsymbol{s}(\boldsymbol{k}) = \frac{i\boldsymbol{k}}{\boldsymbol{k}^2}\delta(\boldsymbol{k}). \tag{A.2}$$

Equations (A.1) and (A.2) determine the initial positions and are valid regardless of the composition of the Universe.

We next turn to the velocity field $\dot{\boldsymbol{x}}(\boldsymbol{q})$ or its Fourier transform $\dot{\boldsymbol{x}}(\boldsymbol{k}) = \dot{\boldsymbol{s}}(\boldsymbol{k})$. Let t_0 be the time at which we are generating initial conditions, and write $\boldsymbol{s}$ as a function of time, using a new function

---

$D(\mathbf{k}, t)$ to encode its time dependence:

$$\mathbf{s}(\mathbf{k}, t) = D(\mathbf{k}, t)\mathbf{s}(\mathbf{k}). \tag{A.3}$$

We define $\mathbf{s}(\mathbf{k}) \equiv \mathbf{s}(\mathbf{k}, t_0)$ so that $D(\mathbf{k}, t_0) \equiv 1$. During matter domination, $D(\mathbf{k}, t) = a(t)/a(t_0)$ independent of $\mathbf{k}$, but radiation complicates the picture. However, it is evident from Eq. (A.2) that $\mathbf{s}$ and δ evolve identically in time, implying $D(\mathbf{k}, t) = \delta(\mathbf{k}, t)/\delta(\mathbf{k}, t_0)$. The initial velocity becomes

$$\dot{\mathbf{x}}(\mathbf{k}, t_0) = \frac{\dot{\delta}(\mathbf{k}, t_0)}{\delta(\mathbf{k}, t_0)} \mathbf{s}(\mathbf{k}) = \left.\frac{\mathrm{d}\ln\delta(\mathbf{k}, t)}{\mathrm{d}t}\right|_{t=t_0} \mathbf{s}(\mathbf{k}), \tag{A.4}$$

which is evaluated using Eq. (2.3) with $\mathrm{d}/\mathrm{d}t \equiv aH(a)\mathrm{d}/\mathrm{d}a$.

To test the modified simulation code and initial conditions, we compare simulation results to linear theory. We produce a matter power spectrum at $z = 8 \times 10^6$ using the procedure described in Sec. 2.2.2, but we leave it unenhanced so that density contrasts near matter-radiation equality are well in the linear regime. We draw initial conditions from this power spectrum in a $(7.4 \text{ kpc})^3$ periodic box and then evolve this box to $z = 996$ using our modified version of GADGET-2[2]. All simulation parameters are the same as those of the reference simulation described in Appendix A.2. Figure A.1 shows the growth of the power spectrum during this simulation. It matches the linear-theory prediction of Eq. (2.3), including the scale-dependent growth. Note that without the radiation component, the power spectrum would have instead grown by a factor of about 6×10^7.

As another demonstration, we also evolve the initial density field to $z = 996$ using linear theory by applying the evolution specified by Eq. (2.3) to the Fourier-transformed density field; we may then compare the resulting density field to the one evolved using GADGET-2. In Fig. A.2, we plot a slice of the density field at $z = 996$ evolved using both methods. Our modified version of GADGET-2 with initial conditions described above successfully reproduces the results of linear theory.

---

[2]The fluctuations drawn from an unenhanced power spectrum have amplitude $\delta \sim 10^{-3}$ at $z = 8 \times 10^6$, which results in extremely small particle accelerations. To evade errors resulting from floating-point precision, we also set GADGET-2 to use double-precision arithmetic. All simulations in this work employ this setting.
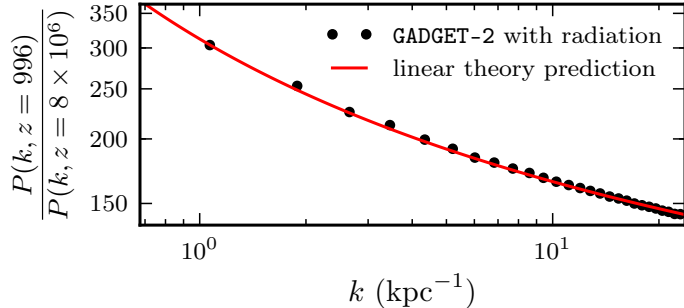
Figure A.1: The power spectrum growth from $z = 8 \times 10^6$ to $z = 996$: a comparison between GADGET-2 with an added radiation component and linear theory. In matter domination, the power spectrum would have instead grown by a factor of about 6×10^7.
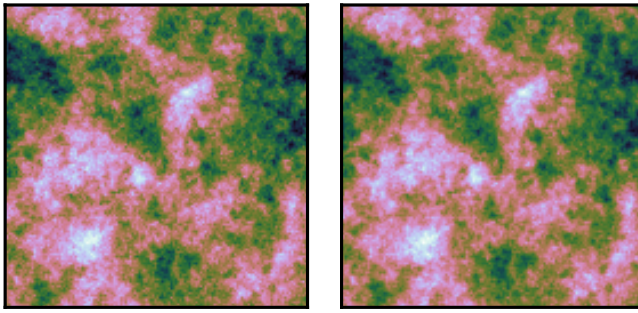
Figure A.2: Fractional overdensity fields evolved to $z = 996$ from the same initial box at $z = 8 \times 10^6$. The figure depicts a $(7.4 \text{ kpc})^2 \times 1.5\text{kpc}$ slice. The left and right panels show the results of linear theory and modified GADGET-2 respectively.

A.2 Convergence testing and simulation parameters

A.2.1 Simulation parameters

We carry out a reference simulation run and five convergence-testing runs: one with improved force accuracy, one with improved integration accuracy, two with respectively increased and reduced softening scales, and one with higher particle count. Our parameter choices for these runs are summarized in Table A.1 and described below. We refer the reader to Ref. [274] for further detail on these parameters.

Particle count N   In our reference run, we use $N = 512^3$ particles arranged in a 3-dimensional grid. In the high-particle-count run, we increase this to $N = 1024^3$. At the final redshift, the UCMH in the reference run has 2.7×10^5 particles within its virial radius r_{vir} while the UCMH in the

191

Table A.1: Simulation parameters for convergence runs. See the text for descriptions of the symbols.

label	N	$\frac{N_{\text{mesh}}}{N}$	r_s	r_{cut}	α	η	dt_{max}	$\frac{\epsilon}{\Delta r}$
reference	512^3	1	1.25	4.5	0.005	0.025	0.03	0.03
force acc.	512^3	2^3	2.5	9.0	0.002	0.025	0.03	0.03
integration	512^3	1	1.25	4.5	0.005	0.01	0.01	0.03
softening $\times 2$	512^3	1	1.25	4.5	0.005	0.025	0.03	0.06
softening $\times \frac{1}{3}$	512^3	1	1.25	4.5	0.005	0.025	0.03	0.01
N $\times 8$	1024^3	1	1.25	4.5	0.005	0.025	0.03	0.03

high-particle-count run has 2.2×10^6 particles.

Particle mesh size N_{mesh} This parameter describes the size of the particle mesh used for the long-range force calculation. In our reference run, we set $N_{\text{mesh}} = N$. In the force-accuracy run, we set $N_{\text{mesh}} = 2^3 N$ to increase the accuracy of the long-range force calculation.

Short/long-range split r_s GADGET-2 computes the long-range force using a particle mesh and the short-range force using an octree. The parameter r_s determines the splitting scale in units of mesh cells. In our reference run, we set $r_s = 1.25$ mesh cells. In the force-accuracy run, we increase this to $r_s = 2.5$ mesh cells, which effectively leaves the splitting scale unchanged since we also double the mesh frequency.

Short-range cutoff r_{cut} The short-range force calculation (using an octree) is cut off beyond r_{cut} mesh cells. In our reference run, we set $r_{\text{cut}} = 4.5$ mesh cells. In the force-accuracy run, we increase this to $r_{\text{cut}} = 9.0$ mesh cells, which similarly leaves the cutoff scale unchanged since we also double the mesh frequency.

Tree-force error parameter α GADGET-2's short-range (octree) force calculation only opens a tree node if the estimated force error from truncating it is less than α times the estimated total force. In our reference run, we set $\alpha = 0.005$. In the force-accuracy run, we set $\alpha = 0.002$ to increase the accuracy of the short-range force.

Adaptive time step parameter η GADGET-2 uses individual adaptive time steps with an accuracy parameter η. Roughly, the time step is set so that the maximum displacement due to a particle's acceleration over one time step is smaller than η times the force-softening scale. In the reference run, we set $\eta = 0.025$, while in the integration-accuracy run, we set $\eta = 0.01$ to reduce the particle time steps.

Maximum time step dt_{max} In order to avoid large integration errors at early redshifts when accelerations are small, GADGET-2 imposes a maximum particle time step dt_{max}, which is expressed in units of the Hubble time (so it is actually $d\ln a$). In the reference run, we set $dt_{\mathrm{max}} = 0.03$, while in the integration-accuracy run, we set $dt_{\mathrm{max}} = 0.01$ to improve the integration accuracy at early times.

Force softening scale ϵ GADGET-2 softens the gravitational force based on the length parameter ϵ, which we set to be a fraction $\epsilon/\Delta r$ of the initial interparticle spacing $\Delta r \equiv \mathrm{box\ size}/N^{1/3}$. Note that the force becomes fully Newtonian at 2.8ϵ; ϵ itself is defined to be the minimum radius that can appear in the point-particle potential. In the reference run, we set $\epsilon/\Delta r = 0.03$. Larger softening lengths can minimize discreteness artifacts, but they also systematically bias the forces and prevent smaller scales from being resolved. We perform two runs with altered softening: one with a larger softening scale $\epsilon/\Delta r = 0.06$ and one with a smaller softening scale $\epsilon/\Delta r = 0.01$.

A.2.2 Procedure, results, and discussion

We conduct convergence testing on the primary simulation run of Sec. 2.3. The density field is generated with 1024^3 cells but reduced to 512^3 cells for all but the high-particle-count run by averaging 8 neighboring cells. Each convergence run is carried out as in Sec. 2.3 with only the simulation accuracy parameters changed. We study here the spherically averaged density profile $\rho(r)$ of the UCMH at $z = 100$.

We find that the density profile at each radius rapidly fluctuates between closely-spaced snapshots, and that these fluctuations differ between simulation runs with different parameters. Moreover, we will see later that these fluctuations are a discreteness artifact (although they are not merely the Poisson noise in each radial bin, which is much smaller), so we wish to ignore them. To do so, we obtain density profiles in 16 snapshots between $z = 100$ and $z = 99$ and average them. We also compute the root-mean-squared variance between the snapshots as an estimate of the magnitude of this time variation. Such a small time range was chosen so that we only smooth over rapid fluctuations and not over significant global evolution (such as growth). Nevertheless, this time is short enough that it fails to average over fluctuations at large radii where the particle motion is much slower. We may estimate the upper limit of the range over which rapid fluctuations are smoothed as the radius r_{lim} where

$$\sigma_r(r_{\mathrm{lim}})\Delta t = r_{\mathrm{lim}}, \tag{A.5}$$

193
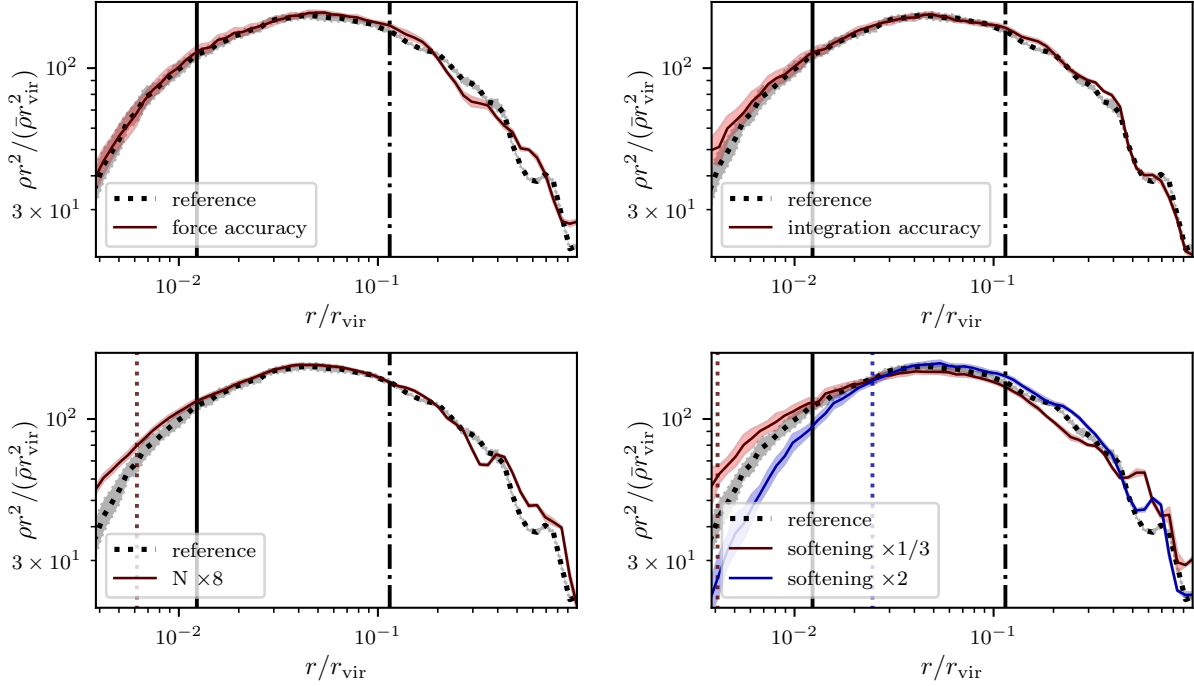
Figure A.3: Radial density profiles averaged between $z = 100$ and $z = 99$; the shading indicates the root-mean-squared variance over this interval. Clockwise from top left: force-accuracy, integration-accuracy, softening-length, and particle-resolution convergence comparisons. The vertical solid (dotted) lines indicate 2.8ϵ for the reference run (alternate runs), the range beyond which forces are exactly Newtonian. The dot-dashed line indicates $r_{\rm lim}$, the radius beyond which fluctuations are likely not averaged (see text for details). ($\bar{\rho}$ is the background matter density.)

where $\sigma_r(r_{\rm lim})$ is the radial velocity dispersion at radius $r_{\rm lim}$ and Δt is the time difference between $z = 100$ and $z = 99$. $r_{\rm lim}$ is thus the radius at which particles are moving fast enough that their radial distance traveled over the averaging period is of the same order as their radial position. For $r < r_{\rm lim}$, there can be no significant correlation between the positions of a particle at the beginning and at the end of the averaging period, so we expect to have averaged over these discreteness artifacts.

There is also an obvious lower limit to the range of radii over which we expect our results to be representative, and that is where the radius is equal to 2.8ϵ, where ϵ is the gravitational softening length. Below this radius, all forces are non-Newtonian, and the density profile will unphysically flatten out.

Our main results are shown in Fig. A.3. The dotted lines indicate the density profile of the reference simulation run, with the gray shading representing the root-mean-squared variance in snapshots between $z = 100$ and $z = 99$. The solid lines with colored shading depict alternate runs.

Force accuracy In the force-accuracy run, we reduce the tree-force error parameter α to increase the accuracy of the short-range force and simultaneously double the resolution of the particle mesh in order to increase the accuracy of the long-range force. We change the short/long range splitting parameters r_s and r_{cut} only to keep the short/long range split the same, since those parameters are expressed in mesh cells. The result is shown in Fig. A.3. We see that for $r < r_{\text{lim}}$, the density profile of the force-accuracy run matches well that of the reference run, suggesting that the reference force-accuracy parameters were sufficient.

Integration accuracy In the integration-accuracy run, we reduce the integration time step in order to reduce error from the numerical integration of particle trajectories. Specifically, we reduce the adaptive time step parameter η as well as the maximum time step $\mathrm{d}t_{\text{max}}$. The first change should improve integration accuracy at late times when particles are experiencing large accelerations, and the second should improve integration accuracy at early times when accelerations are small. The result is shown in Fig. A.3. We see that for $2.8\epsilon < r < r_{\text{lim}}$, the density profile of the integration-accuracy run matches that of the reference run, indicating that the reference integration-accuracy parameters were sufficient.

Force softening The gravitational force softening length ϵ is a more difficult parameter to tune [461, 497–501]. Forces are softened at short range to account for the way the numerical simulation uses discrete particles to represent a continuous mass distribution. Thus, a larger ϵ reduces the influence of discreteness artifacts such as two-body collisions. On the other hand, a larger ϵ also introduces a bias due to the forces being weaker than Newtonian, and a smaller ϵ can allow smaller scales to be probed. Unlike the other parameters we consider, there is no clear direction of greater accuracy in ϵ. Ref. [499] suggests a minimum softening length $\epsilon_{\text{acc}} \equiv r_{\text{vir}}/\sqrt{N_{\text{vir}}}$ (N_{vir} is the number of particles in the halo virial radius), which follows from the criterion that the maximum two-body acceleration caused by a close approach be smaller than the minimum mean-field acceleration within the system. We adopt the choice $\epsilon = 0.03\Delta r$, where Δr is the initial interparticle spacing, in our reference run, which results in $\epsilon \simeq 2.3\epsilon_{\text{acc}}$ at $z = 100$. We also execute two other simulation runs with ϵ at respectively a third and twice the reference value.

The results are shown in the bottom right of Fig. A.3. The vertical solid line represents 2.8ϵ for the reference run, while the two vertical dotted lines represent 2.8ϵ for the runs with altered softening. As one would expect, the density profile for each run flattens out for $r < 2.8\epsilon$. We hope
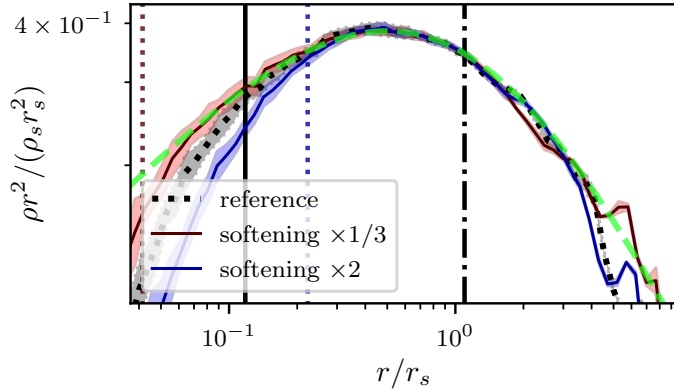
Figure A.4: The softening-length convergence test with ρ and r rescaled for each run to its Moore fitting parameters. The thick dashed line shows the fit, which is the same for all runs by construction. (Shading and vertical lines have the same meaning as in Fig. A.3.)

to find convergence for $2.8\epsilon < r < r_{\text{lim}}$ (recalling that each run has a different ϵ), but while the density profiles in these ranges are close, there is a systematic flattening as ϵ becomes larger. What has happened here may be elucidated by performing a Moore fit [Eq (2.4)] to each run and rescaling ρ and r to the fitting parameters ρ_s and r_s. The rescaled plot is shown in Fig. A.4. Evidently, each run can still be fit by the same form in the range $2.8\epsilon < r < r_{\text{lim}}$ but has a different Moore concentration parameter $c \equiv r_{\text{vir}}/r_s$: the reference run has $c = 9.6$, the reduced softening run has $c = 10.2$, and the increased softening run has $c = 9.2$. This discrepancy is likely the result of a force bias: the softening is causing a slight enlargement of the system. Fortunately, the effect is small. If we assume that either r_s or c is a linear function of ϵ, then with a purely Newtonian force, we would have $c \simeq 10.4$, corresponding to an 8% reduction in r_s relative to the reference simulation. Moreover, the softening length does not affect the major conclusion regarding the shape of the density profile: all runs fit the Moore form well for $r > 2.8\epsilon$.

Particle count We use $512^3 = 1.3 \times 10^8$ particles in the reference run, which places 2.7×10^5 particles within the virial radius of the UCMH at $z = 100$. To avoid strong discreteness effects, we must use enough particles that two-body collisions have negligible impact. To estimate this, we consider the two-body relaxation timescale t_{relax}, the timescale over which two-body encounters significantly alter a particle's energy. For a region of radius r about the halo center containing N simulation particles with total mass M, $t_{\text{relax}} = N/(8 \ln N)t_{\text{cross}}$ (e.g. [392]) with $t_{\text{cross}} \simeq r/\sqrt{GM/r}$. The relaxation timescale should be much longer than the dynamical age of the halo, which is
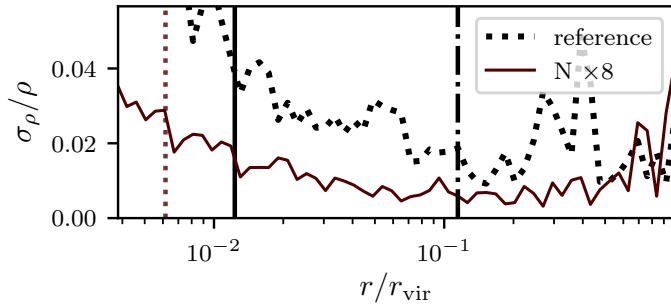
Figure A.5: Root-mean-squared variance in the density profile across 16 snapshots between $z = 100$ and $z = 99$. The reference and high-particle-count runs are compared. (Vertical lines have the same meaning as in Fig. A.3.)

essentially the age of the Universe at $z = 100$. We calculate t_{relax} for the UCMH in the reference simulation and find that even at the smallest relevant radius, $r = 2.8\epsilon$, t_{relax} is 100 times the age of the Universe at $z = 100$. This calculation suggests that the reference simulation contains enough particles that collisional artifacts are unimportant.

Nevertheless, Fig. A.3 shows a comparison between the density profiles in the reference run and in a simulation run with 8 times as many particles. As expected, the two density profiles match well in the range $2.8\epsilon < r < r_{\mathrm{lim}}$, implying that the simulation is converged with respect to particle count in these regions. Moreover, the time-fluctuations in the density profile, measured as the root-mean-squared variance across snapshots between $z = 100$ and $z = 99$, are smaller in the high-particle-count simulation than in the reference simulation, a fact that we confirm in Fig. A.5. This observation confirms our claim that the fluctuations are a discreteness artifact.

These fluctuations may be related to the artificial fragmentation of filaments that occurs in simulations with a small-scale cutoff in the power spectrum [389, 390]. We observe artificial fragmentation in our simulations using the spiked power spectrum, as evidenced in Fig. A.6, which shows one of the filaments connected to the UCMH for different simulation parameters. Like the density fluctuations, the frequency and size of these fragments is correlated with the simulation particle resolution, while their positions vary with force-accuracy parameters. The fluctuations in the density profile could be caused by the accretion of artificial fragments.
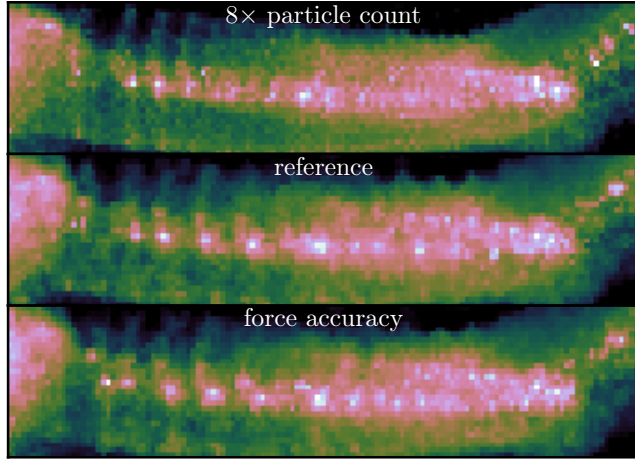
Figure A.6: The filament to the left of the UCMH (see Fig. 2.4) for different simulation parameters. This figure demonstrates the presence of artificial fragmentation: the filament fragments differently for different parameters.

A.2.3 The smallest resolved radius

We have shown that the density profile of the UCMH in the reference version of the primary simulation run is converged with respect to simulation parameters at $z = 100$ for radii r between $2.8\epsilon = 0.012 r_{\mathrm{vir}}$ and $r_{\mathrm{lim}} = 0.11 r_{\mathrm{vir}}$. This halo has $r_{\mathrm{vir}} = 1.0 \times 10^{-3}$ kpc (in physical coordinates) at $z = 100$, so the converged radius range is 1.2×10^{-5} kpc $< r < 1.1 \times 10^{-4}$ kpc. Moreover, we can regard the density profile above $r_{\mathrm{lim}} = 1.1 \times 10^{-4}$ kpc as converged in its long-range behavior, with only the small-scale fluctuations being not converged. Unfortunately, the lower limit of 1.2×10^{-5} kpc imposed by the force softening is not sufficient to capture the asymptotic behavior in $\rho(r)$ at small r (see Fig. 2.5).

We can double the resolution by employing the high-particle-count simulation run, but we would like to go still deeper into the halo. While it is computationally challenging to simulate the full box with more than 1024^3 particles, it is also unnecessary. A common practice in N-body simulations is to resample the halo progenitor at higher particle resolution and embed this high-resolution region into the same periodic box. Because the halos we consider are much more isolated than halos in a hierarchical growth picture, we need not even go this far: we can simply isolate a sphere around the halo progenitor and use vacuum boundary conditions. Figure A.7 shows the comparison between the periodic box with 1024^3 particles and an otherwise identical simulation of a vacuum-bounded
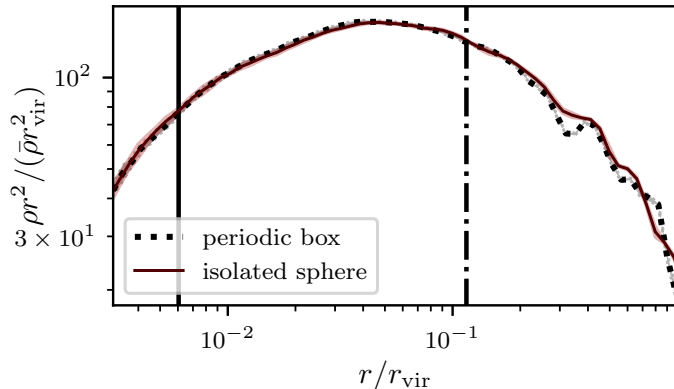
Figure A.7: A comparison between the UCMH simulated in a $(7.4 \text{ kpc})^3$ periodic box with a halo from the same initial overdense region simulated in a sphere of radius 0.92 kpc with vacuum boundary conditions. (Vertical lines have the same meaning as in Fig. A.3.)

sphere of radius 0.92 kpc around the UCMH. The spherical region is depicted in Fig. 2.2. The sphere requires only 1/122 as many particles for an identical result. We therefore exploit this method to simulate the UCMH in the primary simulation at $64\times$ particle density and the other UCMHs at $8\times$ particle density relative to the reference simulation with 512^3 particles.

However, this concordance does not hold at $z = 50$, nor is it guaranteed to hold at $z = 100$ in other boxes. The longer the simulation run, the more likely the UCMH is to be influenced by structure that originated outside of the sphere. Therefore, we restrict our use of the vacuum-bounded sphere to the primary simulation box (which we tested here) up to $z = 100$ and to other initial boxes up to $z = 400$. For the UCMH in the primary simulation box, this brings the smallest resolved radius down to 3.0×10^{-6} kpc (physical coordinates) at $z = 100$, which is sufficient to resolve the beginning of the $\rho \propto r^{-3/2}$ asymptote. This radius contains 3×10^4 particles at $z = 100$.

Due to the stability of the density profile in time, we can probe still smaller radii by viewing the density profile at earlier times, as discussed in Section 2.3. By this method, we probe radii as small as 9.0×10^{-7} kpc in Fig. 2.5 using the density profile at $z = 400$. This radius contains 4000 particles at $z = 400$ and is sufficient to demonstrate that the density profile shows no sign of leveling off toward a shallower power-law index than $3/2$.

A.2.4 Summary of simulation choices

We now summarize the simulation parameters we use to study the UCMHs in Sec. 2.3. Aside from the particle count N, all simulation runs use the reference parameters of Table A.1. We

Table A.2: The particle count N, particle mass m, simulation region size (side length or diameter), and ending redshift for each simulation used to produce the results in Sec. 2.3. The $\pi/6$ factor in the particle count comes from isolating a spherical region.

description	N	m $(M_\odot)$	size (kpc)	region	end z
primary	1024^3	1.5×10^{-5}	7.4	periodic	100
primary, $z = 50$	512^3	1.2×10^{-4}	7.4	periodic	50
primary, vacuum b.c.	$\pi/6 \times 512^3$	1.8×10^{-6}	1.85	sphere	100
secondary	512^3	1.2×10^{-4}	7.4	periodic	50
secondary, vacuum b.c.	$\pi/6 \times 256^3$	1.5×10^{-5}	1.85	sphere	400
step	512^3	1.2×10^{-4}	7.4	periodic	100

Table A.3: For each simulation used to produce the results in Sec. 2.3, this table lists the number of particles N_{vir} within the UCMH at each redshift from which results are presented. For the secondary simulations, an average figure is given.

description	$N_{\mathrm{vir}}\vert_{z=400}$	$N_{\mathrm{vir}}\vert_{z=200}$	$N_{\mathrm{vir}}\vert_{z=100}$	$N_{\mathrm{vir}}\vert_{z=50}$
primary	549 103	1 252 010	2 242 797	...
primary, $z = 50$	...	...	...	431 978
primary, vacuum b.c.	4 551 792	10 679 480	18 572 202	...
secondary	71 108.3	169 121.5	284 310.9	423 624.5
secondary, vacuum b.c.	583 019.9	...	...	...
step	...	...	11 631 568	...

employ two classes of simulation region: a comoving cube with periodic boundary conditions or an isolated comoving sphere with vacuum boundary conditions. Table A.2 shows the particle counts and simulation region sizes for all simulation runs. The mass m of the simulation particle is also shown for clarity.

The primary simulation box is the same 7.4 kpc box we used for convergence testing. The full box is simulated at 8 times the reference particle density (1024^3 particles) and a sphere around the main halo at 64 times the reference particle density up to $z = 100$, and a third run simulates the full box at reference particle density up to $z = 50$. The density profile of the UCMH shown in Fig. 2.5 comes from the isolated sphere at $64\times$ reference particle density up to $z = 100$ and from the full box at reference density at $z = 50$. Secondary simulations (Fig. 2.6) are executed at reference particle density up to $z = 50$ and at $8\times$ reference density in an isolated sphere up to $z = 400$. The N_{vir} figures for the secondary simulations in Table A.2 are average values and vary by up to 25% between simulations of different UCMHs. The density profiles of younger halos (Sec. 2.3.4) come from the full primary box at $8\times$ reference density at $z = 100$. Finally, for the stepped power spectrum, we

simulated a full box with reference parameters to $z = 100$.

All density profiles are averaged over 16 snapshots within 1/100 of a Hubble time to suppress fluctuations. Density profiles are binned logarithmically in intervals separated by a factor of 1.1 (corresponding to an interval of 0.041 in $\log_{10} r$), but we have checked that the results depend negligibly on this choice.

A.3 Constraining point-source abundance in the Milky Way

In Sec. 2.5, we defined $\mu(d) = 3M(d)/(4\pi d^3 \bar{\rho}_0)$, where $M(d)$ is the dark matter mass contained within distance d of Earth. If we are at distance r_0 from the Milky Way center, then we may write

$$\mu(d) = \frac{3}{2d^3 \bar{\rho}_0} \int_0^d s^2 ds \int_{-1}^1 dx \ \max\left\{ \rho_{\mathrm{MW}}\left(\sqrt{s^2 + r_0^2 - 2xsr_0}\right), \bar{\rho}_0 \right\}, \tag{A.6}$$

with $\rho_{\mathrm{MW}}(r)$ being the density profile of the Milky Way. This expression approximates the extragalactic density field as a uniform background. Taking the Milky Way to have an NFW profile with scale radius r_{S} and scale density ρ_{S} and the sun to be at distance r_0 from the center, the integral in Eq. (A.6) evaluates to

$$\mu(d) \simeq \frac{3r_{\mathrm{S}}^3 \rho_{\mathrm{S}}}{2r_0 \bar{\rho}_0 d^3} \begin{cases} (r_0 + r_s) \ln\left(\frac{r_0 + r_{\mathrm{S}} + d}{r_0 + r_{\mathrm{S}} - d}\right) - 2d & d < r_0 \\ 2r_{\mathrm{S}}\mathrm{arctanh}\left(\frac{r_0}{d + r_{\mathrm{S}}}\right) + r_0 \ln\left(\frac{(d+r_{\mathrm{S}})^2 - r_0^2}{\mathrm{e}^2 r_{\mathrm{S}}^2}\right) & r_0 < d < r_{\mathrm{max}} \\ 2r_0 \left[\frac{-r_{\mathrm{max}}}{r_{\mathrm{max}} + r_{\mathrm{S}}} + \ln\left(1 + \frac{r_{\mathrm{max}}}{r_{\mathrm{S}}}\right) + \frac{\bar{\rho}_0}{3r_{\mathrm{S}}^3 \rho_{\mathrm{S}}}(d^3 - r_{\mathrm{max}}^3)\right] & d > r_{\mathrm{max}} \end{cases} \tag{A.7}$$

where r_{max} is defined such that $\rho_{\mathrm{MW}}(r_{\mathrm{max}}) = \bar{\rho}_0$. The first two cases in Eq. (A.7) come from an exact evaluation of the integral in Eq. (A.6) for the Milky Way without a background, while the third case approximates $r_0 \simeq 0$ to evaluate the extragalactic contribution. Figure 2.12 shows a plot of $\mu(d)$.

A.4 Constraining the power spectrum using the statistics of peaks

In Sec. 2.5, we used the statistics of peaks as formulated in Ref. [269] (BBKS) to relate the differential halo number density by formation time, dn/da_c, to the power spectrum $\mathcal{P}(k)$. We describe that calculation in more detail here. The differential number density of peaks according to their height $\nu = \delta/\sigma$ and steepness parameter x is given in BBKS Eq. (A14), where σ is the

root-mean-squared density variance[3] and δ is the peak density contrast. For the spiked power spectrum given by Eq. (2.22), $\sigma = \mathcal{A}^{1/2}a$. Moreover, the spectral parameter γ [BBKS Eq. (4.6)] has value $\gamma = 1$, causing the x-exponential in BBKS Eq. (A14) to become a delta-function. We obtain the halo abundance by integrating this differential number density over x and ν subject to the collapse requirement $\nu\sigma > \delta_c$, with result

$$n = \frac{k_s^3}{(2\pi)^2 3^{3/2}} \int_{\delta_c/(\mathcal{A}^{1/2}a)}^{\infty} \mathrm{e}^{-\nu^2/2} f(\nu)\mathrm{d}\nu \tag{A.8}$$

where the function $f(\nu)$ is defined by BBKS Eq. (A15).

We seek $\mathrm{d}n/\mathrm{d}a$, which is obtained by differentiation as

$$\frac{\mathrm{d}n}{\mathrm{d}a} = \frac{k_s^3}{a} \, h\left(\frac{\delta_c}{\mathcal{A}^{1/2}a}\right) \tag{A.9}$$

with

$$h(\nu) \equiv \frac{\nu}{(2\pi)^2 3^{3/2}} \mathrm{e}^{-\nu^2/2} f(\nu). \tag{A.10}$$

As we noted in Sec. 2.5.3, the number density n increases monotonically due to halo formation alone. Thus, Eq. (A.9) gives us precisely $\mathrm{d}n/\mathrm{d}a_c$, which we can combine with Eq. (2.17) or (2.20) to constrain the integrated area $\mathcal{A}$ of the power spectrum.

For the general case of point sources with nonconstant $\mu(d)$, we have little choice but to numerically invert the integral in Eq. (2.17) to obtain an upper bound on $\mathcal{A}$ as a function of k_s. However, in a limiting case where μ is constant, or to derive a bound from the diffuse flux, we can fully extract the $\mathcal{A}$-dependence from the integral. In these cases, we have an integral of the form

$$\begin{aligned}
\int_0^1 \mathrm{d}a_c \frac{\mathrm{d}n}{\mathrm{d}a_c} L^p(a_c) &= k_s^3 \int_0^{\infty} \frac{\mathrm{d}\nu}{\nu} h(\nu) L^p\left(\frac{\delta_c}{\nu\mathcal{A}^{1/2}}\right) \\
&= \frac{A^p \mathcal{A}^{3p/2}}{\delta_c^{3p} k_s^{3p-3}} \int_0^{\infty} h(\nu)\nu^{3p-1}\left(\ln\frac{B\delta_c}{\nu\mathcal{A}^{1/2}}\right)^p \mathrm{d}\nu \\
&= \frac{A^p \mathcal{A}^{3p/2}}{\delta_c^{3p} k_s^{3p-3}}\left[\left(\ln\frac{B\delta_c}{\mathcal{A}^{1/2}}\right)^p I_p - \left(\ln\frac{B\delta_c}{\mathcal{A}^{1/2}}\right)^{p-1} J_p\right],
\end{aligned} \tag{A.11}$$

---

[3]There is no smoothing filter, so σ is the pointwise variance, $\sigma^2 = \int \frac{\mathrm{d}k}{k}\mathcal{P}(k)$.
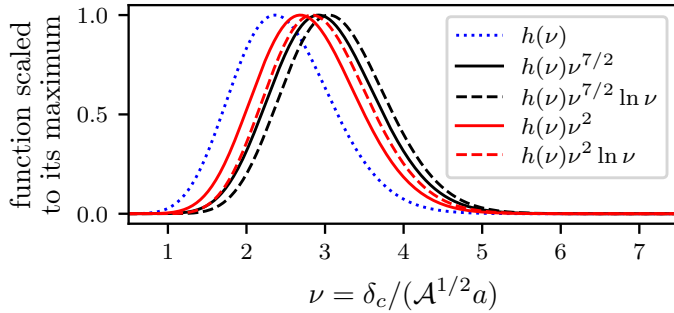
Figure A.8: Plots of the function h defined in Eq. (A.10) along with the integrands in Eq. (A.12). Each function is scaled to its maximum value to emphasize the support of these functions. The black curves are relevant to point-source constraints, while the red curves determine diffuse constraints. This figure shows that constraints are set primarily by peaks between 2σ and 4σ.

with $p = 3/2$ or $p = 1$ for point sources or the diffuse flux respectively, and where I_p and J_p are defined as

$$I_p \equiv \int_0^\infty h(\nu)\nu^{3p-1}\mathrm{d}\nu, \quad J_p \equiv p\int_0^\infty h(\nu)\nu^{3p-1}\ln\nu\ \mathrm{d}\nu. \tag{A.12}$$

In the first line, we use Eq. (A.9) with $\nu = \delta_c/(\mathcal{A}^{1/2}a)$. We saw in Sec. 2.5.4 that the integral in Eq. (A.11) is dominated by minihalos forming at $z \gtrsim 20$, so we exploit the negligible contribution to this integral of minihalos forming at $a > 1$ to extend the lower limit of the integral on the right-hand side to $\nu = 0$. In the second line, we specialize to the Moore density profile using Eq. (2.13). In the last line, we take advantage of the limited support of $h(\nu)$ to claim that $\ln\nu \ll \ln\left(B\delta_c/\mathcal{A}^{1/2}\right)$ so that we can use a binomial expansion (and this is exact for $p = 1$). Note that the integrands in Eq. (A.12) tell us the range of peaks that are relevant to constraints: as we see in Fig. A.8, most of their support lies in peaks between roughly 2σ and 4σ.

For point sources with $\mu \simeq$ const, we now have

$$\mathcal{A}\left(\ln\frac{B\delta_c}{\mathcal{A}^{1/2}}\right)^{2/9}\left[\left(\ln\frac{B\delta_c}{\mathcal{A}^{1/2}}\right)I_{3/2} - J_{3/2}\right]^{4/9} \leq \left(\frac{-3\sqrt{4\pi}\ln(1-y/x)}{\mu}\right)^{4/9}\left(\frac{\delta_c^3 k_s \mathcal{F}_{\min}}{A}\right)^{2/3}, \tag{2.25}$$

while for diffuse sources, we have

$$\mathcal{A}\left[\left(\ln\frac{B\delta_c}{\mathcal{A}^{1/2}}\right)I_1 - J_1\right]^{2/3} \leq \left(\frac{4\pi\delta_c^3}{K(\theta)A}\frac{\mathrm{d}\mathcal{F}}{\mathrm{d}\Omega}\right)^{2/3}. \tag{2.26}$$

203

These expressions follow from Eqs. (2.17), (2.20), and (A.11). The numbers $I_{3/2}$, $J_{3/2}$, I_1, and J_1 have approximate values

$$I_{3/2} = 0.228, \quad J_{3/2} = 0.370, \quad I_1 = 0.0477, \quad J_1 = 0.0478 \tag{A.13}$$

Equations (2.25) and (2.26) are now algebraic equations for the upper bounds on $\mathcal{A}$.

The constraint on $\mathcal{A}$ is not our final goal, but it is close. $\mathcal{A}a^2$ is the power associated with the spike in the (linear) matter power spectrum during matter domination. We seek instead the power $\mathcal{A}_0$ associated with the spike in the primordial curvature power spectrum. These quantities are related by a transfer function such as [502]

$$\delta(k, a) = \frac{2}{5} \frac{k^2}{\Omega_m H_0^2} \zeta(k) \, \mathcal{T}\left(\frac{\sqrt{\Omega_r} k}{H_0 \Omega_m}\right) a, \tag{A.14}$$

which relates the matter density contrast δ during matter domination to the primordial curvature fluctuation ζ. Here

$$\mathcal{T}(x) = \frac{45}{2x^2}\left(-\frac{7}{2} + \gamma_E + \ln\left(\frac{4x}{\sqrt{3}}\right)\right) \tag{A.15}$$

is a dimensionless transfer function that is valid at $x \gg 1$ or $k \gg 10^{-2}\text{Mpc}^{-1}$ ($\gamma_E \simeq 0.577$ is the Euler-Mascheroni constant). Hence, by squaring Eq. (A.14),

$$\mathcal{A}_0 = \frac{(\Omega_r/\Omega_m)^2 \, \mathcal{A}}{81\left[-\frac{7}{2} + \gamma_E + \ln\left(\frac{4\sqrt{\Omega_r} k_s}{\sqrt{3} H_0 \Omega_m}\right)\right]^2} \tag{A.16}$$

yields the desired constraint on the primordial power spectrum.

A.5 The UCMH constraint on a spiked power spectrum

Bringmann, Scott, and Akrami [234] (BSA) calculated an upper bound on the number density of UCMHs (as a function of scale wavenumber k) using the $\rho \propto r^{-9/4}$ density profile from Ref. [202]. They then converted this constraint into an upper bound on the primordial power spectrum under the assumption of local scale invariance. We followed the calculation in BSA as closely as possible in Sec. 2.5 so as to facilitate a direct comparison in constraining strength between our new minihalo model and the old UCMH model. However, because a spiked power spectrum does not exhibit local scale invariance, we must return to the UCMH abundance constraint in BSA and convert it into a

204

constraint on the delta-spiked power spectrum given by Eq. (2.22). We show that calculation here.

BSA Fig. 1 shows their constraint on the fraction f of matter contained in UCMHs. This fraction is readily converted into a number density $n = f\rho_m/M_{\text{UCMH}}$, where BSA took

$$M_{\text{UCMH}} = 4 \times 10^{13} \left(\frac{k}{\text{Mpc}^{-1}} \right)^{-3} M_\odot. \tag{A.17}$$

Here we have employed $R = 1/k$, where R is the comoving radius of the precursor overdense region; this is the same relation BSA used. The UCMHs are taken to follow the dark matter distribution, so n and ρ_m are the comoving background UCMH number density and matter density respectively.

This procedure has given us a constraint n on the comoving number density of halos of scale wavenumber k forming at $z \gtrsim 1000$. In the delta-spiked power spectrum given by Eq. (2.22), all halos form from fluctuations with wavenumber k_s, the wavenumber of the spike, so we will take $k = k_s$ in Eq. (A.17). We can then use Eq. (A.8) with $a = 10^{-3}$ to convert this upper bound on the abundance of halos that form at $z \geq 1000$ into a constraint on the primordial power spectrum, which is shown in Fig. 2.13.

APPENDIX B:
THE COLLAPSE THRESHOLD δ_c DURING RADIATION DOMINATION[1]

When radiation dominates, the linear collapse threshold δ_c is larger than its value $\delta_{c,0} \equiv 1.686$ during matter domination. In this appendix, we study the the behavior of δ_c by varying the initial conditions in the calculation of Sec. 3.2. This behavior is shown in Fig. B.1: it is a function of both the collapse scale factor a_c and the reheat temperature T_{RH}.

We now present a convenient fitting form for δ_c. To begin, we define a_{RH} as the scale factor corresponding to the temperature T_{RH} assuming radiation domination. Taking $a = 1$ today, this definition implies that

$$a_{\mathrm{RH}} = \left(\frac{3.91}{g_*(T_{\mathrm{RH}})} \right)^{1/3} \frac{T_0}{T_{\mathrm{RH}}}. \tag{B.1}$$

where $T_0 = 2.3 \times 10^{-4}$ eV is the temperature today and g_* is the effective number of relativistic degrees of freedom in the Standard Model (as a function of temperature). Note that this definition differs from other definitions of a_{RH} in the literature, and we only use it as a parameter for our fitting form. We also employ $a_{\mathrm{eq}} = \Omega_r / \Omega_m$, the scale factor of matter-radiation equality. The following fitting form for δ_c is accurate to within 0.004 for 2 MeV $< T_{\mathrm{RH}} < 1$ TeV as long as $a_c \lesssim 0.1$ (dark energy is neglected) and $a_c \gg T_0/T_{\mathrm{dom}}$ (radiation prior to the EMDE is neglected):

$$\delta_{\mathrm{c}} = \delta_{\mathrm{c},0} + f\left(\frac{a_c}{a_{\mathrm{RH}}} \right) g\left(\frac{a_c}{a_{\mathrm{eq}}}, \ln \frac{a_{\mathrm{RH}}}{a_{\mathrm{eq}}} \right) - h\left(\ln \frac{a_c}{a_{\mathrm{eq}}} \right). \tag{B.2}$$

Here, the function $f(x)$ is defined

$$f(x) = A \frac{\ln(1+x) - \frac{x + Bx^2 + Cx^3}{1 + Dx + Ex^2 + Fx^3}}{1 + G(\ln(1+x) - 2x/(2+x))},$$

$$A = 0.3549, \quad B = -0.2331, \quad C = 0.0533, \quad D = 0.4935,$$

$$E = -0.2092, \quad F = 0.09327, \quad G = 0.2683, \tag{B.3}$$
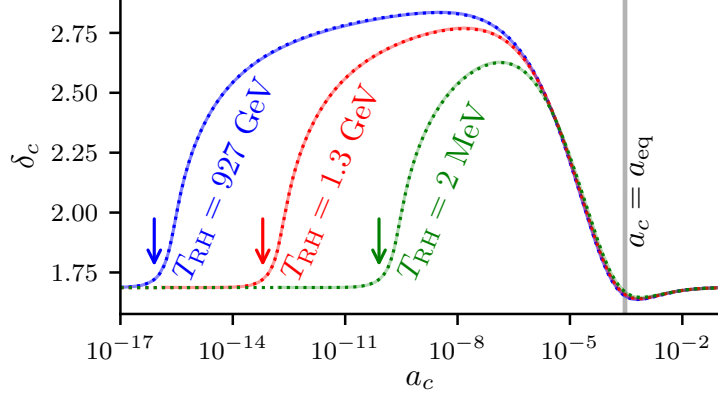
Figure B.1: The linear collapse threshold δ_c plotted against the collapse scale factor a_c for three different reheat temperatures T_{RH}. We take $a = 1$ today. The light, solid lines represent δ_c computed using the spherical collapse model as described in Section 3.2, while the dark, dotted lines employ the fitting form presented in this appendix. The arrows mark a_{RH} as defined in Eq. (B.1).

the function $g(x, y)$ is defined

$$
\begin{aligned}
g(x, y) &= \left\{ 1 + [A(y)x]^{B(y)} + [C(y)x]^{D(y)} \right\}^{-E(y)}, \\
A(y) &= 135.2 \left(1 + 0.04734y + 0.0006373y^2 \right), \\
B(y) &= 1.093 \left(1 + 0.03256y + 0.0005114y^2 \right), \\
C(y) &= 17.87 \left(1 + 0.03501y + 0.0003641y^2 \right), \\
D(y) &= 3.187 \left(1 + 0.03283y + 0.0005260y^2 \right), \\
E(y) &= 0.05388 \left(1 - 0.7380y \right),
\end{aligned}
\tag{B.4}
$$

and the function $h(x)$ is defined

$$
h(x) = A\mathrm{e}^{-B(x+C)^2},
$$
$$
A = 0.07074, \quad B = 0.1180, \quad C = 0.4258.
\tag{B.5}
$$

C.1 Collecting halo data

In Sec. 4.2, we carried out six simulations and catalogued all halos present at the final redshift of each. The models we present in Secs. 4.3 and 4.4 require data on the density profiles of these halos, and in this section, we detail our methods for collecting these data.

We first need to obtain the density profile and enclosed mass profile of each halo at the final redshift of each simulation. To reduce random noise, we use the procedure described in Chapter 2, wherein the profiles are averaged over a time interval. The profiles are binned at successive factors of 1.1 in radius, but to mitigate noise associated with the binning scheme, we use a cubic spline to smoothly interpolate them. These profiles are only valid down to the radius $r_{\rm soft}$ corresponding to the separation below which simulation forces become non-Newtonian; for GADGET-2, $r_{\rm soft}$ is 2.8 times the force softening length. At large radii, we cut off the density profile at the radius $r_{\rm vir}$ inside which the mean enclosed density is 200 times the background density. Figure C.1 shows a random sample of halo density profiles from each simulation.

The model developed in Sec. 4.3 predicts the coefficient A of the $\rho = Ar^{-3/2}$ asymptote of the density profile at small r. Thus, we wish to extract A from each density profile. Starting at $r_{\rm soft}$, we find the cumulative (logarithmic) average of $\rho r^{3/2}$ across radial bins, and we set A to be the maximum of this cumulative average. The averaging procedure is intended to minimize noise resulting from employing a narrow range of radii while at the same time minimizing the influence of any bend in the density profile at larger radii. However, we also tested the alternative procedure of simply finding the average of $\rho r^{3/2}$ within a factor of 3 in radius above $r_{\rm soft}$ and found it to yield similar results.

We also wish to accommodate deviations from $\rho \propto r^{-3/2}$ at small radii. Unlike those of Chapter 2, our simulations do not have the resolution to clearly resolve the power-law index of the small-radius

---
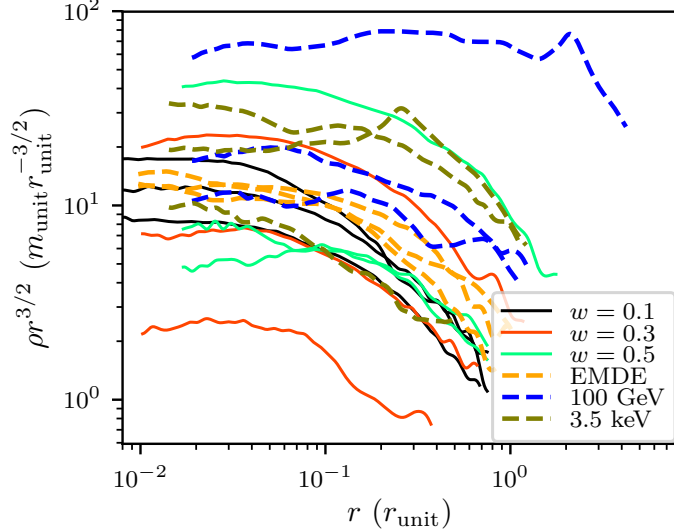
Figure C.1: The density profiles of three random halos from each simulation's final box.

asymptote, but we may still hope to see statistical correlations in our large sample. For each halo, we measure the slope γ of the small-radius asymptote $\rho \propto r^{-\gamma}$ by considering the radius range from r_{soft} to $3r_{\mathrm{soft}}$ and fitting a line in log space to the density profile within this range.

To test the models presented in Sec. 4.4, we also need to compute the radius r_{max} at which the circular velocity is maximized along with the mass $M(r_{\mathrm{max}})$. Since we already obtained the enclosed mass profile $M(r)$ for each halo, we simply find the maximum value of $M(r)/r$. The parameters r_{max} and $M(r_{\mathrm{max}})$ are then defined to be the radius and enclosed mass at which $M(r)/r$ is maximized.

C.2   Collecting peak parameters

The models we present in Secs. 4.3 and 4.4 employ data on the peaks in the linear density field $\delta(\boldsymbol{x}) \equiv \delta(\boldsymbol{x}, a)/a$ (evaluated during matter domination). We obtain these data using Fourier methods, defining

$$\delta(\boldsymbol{k}) \equiv \int \mathrm{d}^3\boldsymbol{x} \, \mathrm{e}^{-i\boldsymbol{k}\cdot\boldsymbol{x}} \delta(\boldsymbol{x}). \tag{C.1}$$

The derivatives of δ at a peak located at $\boldsymbol{x}$ immediately follow as

$$\partial_i \partial_j \delta = - \int \frac{\mathrm{d}^3\boldsymbol{k}}{(2\pi)^3} \mathrm{e}^{i\boldsymbol{k}\cdot\boldsymbol{x}} k_i k_j \delta(\boldsymbol{k}). \tag{C.2}$$

Similarly, using Poisson's equation, the derivatives of the (peculiar) gravitational potential are

$$\partial_i \partial_j \phi = 4\pi G \bar{\rho}_0 \int \frac{\mathrm{d}^3 \boldsymbol{k}}{(2\pi)^3} \mathrm{e}^{i\boldsymbol{k}\cdot\boldsymbol{x}} \frac{k_i k_j}{\boldsymbol{k}^2} \delta(\boldsymbol{k}). \tag{C.3}$$

The ellipsoidal refinement described in Sec. 4.3.2 requires the three-dimensional shape parameters e_ϕ and p_ϕ for the potential ϕ about the peak. Taking $\lambda_1 \geq \lambda_2 \geq \lambda_3$ to be the eigenvalues of $\partial_i \partial_j \phi$, these parameters are defined

$$e_\phi \equiv \frac{\lambda_1 - \lambda_3}{2(\lambda_1 + \lambda_2 + \lambda_3)} \quad \text{and} \quad p_\phi \equiv \frac{\lambda_1 + \lambda_3 - 2\lambda_2}{2(\lambda_1 + \lambda_2 + \lambda_3)}. \tag{C.4}$$

Our model in Sec. 4.4 requires the density profile $\delta(r)$ and mass profile $\Delta(r)$ about the peak. For a peak centered at $\boldsymbol{x}$, these profiles are computed as

$$\left\{ \begin{array}{c} \delta(r) \\ \Delta(r) \\ \zeta(r) \end{array} \right\} = \int \frac{\mathrm{d}^3 \boldsymbol{k}}{(2\pi)^3} \mathrm{e}^{i\boldsymbol{k}\cdot\boldsymbol{x}} \delta(\boldsymbol{k}) \left\{ \begin{array}{c} \mathrm{sinc}(kr) \\ W(kr) \\ \cos(kr) \end{array} \right\}, \tag{C.5}$$

where $\mathrm{sinc}(x) \equiv \sin(x)/x$ and W is the top-hat window function, $W(x) \equiv (3/x^3)(\sin x - x \cos x)$. The third profile $\zeta(r)$ is useful because it is related to the derivative of $\delta(r)$. In particular, to numerically integrate Eq. (4.16), we interpolate $\delta(r)$ and $\Delta(r)$ with piecewise polynomials, using the relations

$$\frac{\mathrm{d}\delta}{\mathrm{d}\ln r} = \zeta(r) - \delta(r) \quad \text{and} \quad \frac{\mathrm{d}\Delta}{\mathrm{d}\ln r} = 3\left[\delta(r) - \Delta(r)\right] \tag{C.6}$$

to fix their derivatives.

Figure C.2 shows the density profiles $\delta(r)$ of three peaks from each of the six simulations. The peaks displayed are those that later collapse into the halos depicted in Fig. C.1.

C.3 Predicting the halo population from the power spectrum

A primary goal of this work is to enable a prediction of the halo population given a power spectrum $\mathcal{P}(k)$ of density fluctuations. One option is to sample a density field from the power spectrum, use the methods described in Appendix C.2 to characterize the peaks, and then apply the models developed in this work. However, it is possible to exploit the statistics of a Gaussian random field to compute the halo distribution more directly. In this section, we outline a practical procedure
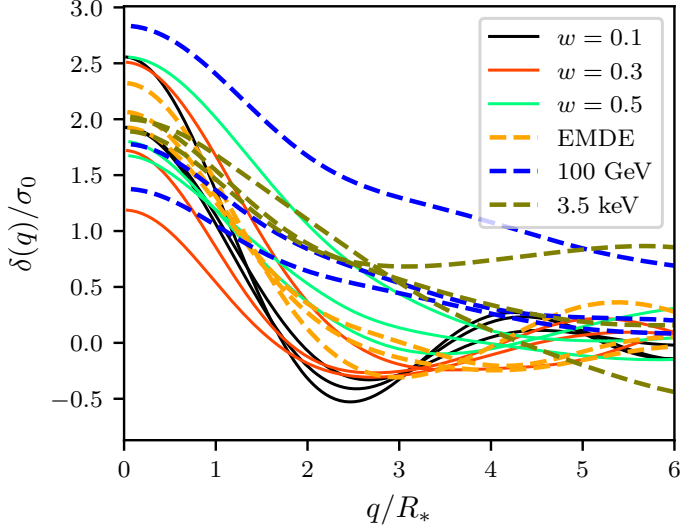
Figure C.2: The density profiles of three peaks from each simulation's initial box. These peaks are chosen to match the halos of which the density profiles are depicted in Fig. C.1.

to perform this computation by sampling from the peak distribution. Similarly to earlier sections, we define $\mathcal{P}(k) \equiv \mathcal{P}(k, a)/a^2$, where $\mathcal{P}(k, a)$ is the dimensionless matter power spectrum evaluated using linear theory during matter domination. All quantities derived therefrom, such as σ_j and $\delta(\boldsymbol{x})$, inherit similar scaling.

C.3.1 Number density of peaks

The first step is to find the total number density n of peaks. As derived in Ref. [269], the differential number density of peaks in a Gaussian random field, in terms of parameters $\nu \equiv \delta/\sigma_0 > 0$ and $x \equiv -\nabla^2\delta/\sigma_2 > 0$, is

$$\frac{\mathrm{d}^2 n}{\mathrm{d}\nu\mathrm{d}x} = \frac{e^{-\nu^2/2}}{(2\pi)^2 R_*^3} f(x) \frac{\exp\left[-\frac{1}{2}(x-\gamma\nu)^2/(1-\gamma^2)\right]}{[2\pi(1-\gamma^2)]^{1/2}}, \tag{C.7}$$

where $\gamma \equiv \sigma_1^2/(\sigma_0\sigma_2)$, σ_j and R_* are defined in Eqs. (4.2) and (4.3), and

$$f(x) \equiv \frac{x^3-3x}{2}\left[\mathrm{erf}\left(\sqrt{\frac{5}{2}}x\right)+\mathrm{erf}\left(\sqrt{\frac{5}{8}}x\right)\right]+\sqrt{\frac{2}{5\pi}}\left[\left(\frac{31}{4}x^2+\frac{8}{5}\right)e^{-\frac{5}{8}x^2}+\left(\frac{x^2}{2}-\frac{8}{5}\right)e^{-\frac{5}{2}x^2}\right]. \tag{C.8}$$

The ν integral can be carried out analytically, leading to

$$\frac{\mathrm{d}n}{\mathrm{d}x} = \frac{f(x)}{8\pi^2 R_*^3}e^{-x^2/2}\left[1+\mathrm{erf}\left(\frac{x\gamma}{\sqrt{2(1-\gamma^2)}}\right)\right], \tag{C.9}$$

and this equation can be integrated numerically over $x \geq 0$ to obtain n.

C.3.2 Asymptote A

Next, we use Monte Carlo methods to compute the distribution of coefficients A of the $\rho = Ar^{-3/2}$ small-radius asymptote. The model described in Sec. 4.3 predicts this asymptote from the amplitude δ and curvature $|\nabla^2 \delta|$ of the density peak along with the shape parameters[2] e and p associated with the potential about the peak. Equation (C.7) supplies the peak distribution in $\nu \equiv \delta/\sigma_0$ and $x \equiv -\nabla^2\delta/\sigma_2$. Meanwhile, the conditional distribution of e and p for a peak of height ν, derived in Ref. [373], is

$$f(e,p|\nu) = \frac{1125}{\sqrt{10\pi}} e(e^2 - p^2)\nu^5 \exp\left[-\frac{5}{2}\nu^2(3e^2 + p^2)\right]. \tag{C.10}$$

To compute the distribution of A, we now employ a Monte Carlo procedure. We use rejection methods to sample x from Eq. (C.9) and then sample ν from Eq. (C.7). Next, we employ the cumulative distributions of e and p,

$$F(e|\nu) = e^{-\frac{15}{2}e^2\nu^2}\left(1 - 15e^2\nu^2\right)\mathrm{erf}\left(\sqrt{5/2}e\nu\right) - 3\sqrt{10/\pi}e\nu e^{-10e^2\nu^2} + \mathrm{erf}\left(\sqrt{10}e\nu\right) \tag{C.11}$$

and

$$F(p|e,\nu) = \frac{1}{2}\frac{(5e^2\nu^2 - 1)\left[\mathrm{erf}\left(\sqrt{\frac{5}{2}}e\nu\right) + \mathrm{erf}\left(\sqrt{\frac{5}{2}}p\nu\right)\right] + \sqrt{10/\pi}\nu\left(pe^{-\frac{5}{2}p^2\nu^2} + ee^{-\frac{5}{2}e^2\nu^2}\right)}{(5e^2\nu^2 - 1)\,\mathrm{erf}\left(\sqrt{\frac{5}{2}}e\nu\right) + \sqrt{\frac{10}{\pi}}e\nu e^{-\frac{5}{2}e^2\nu^2}}, \tag{C.12}$$

numerically inverting them to inverse transform sample e and p. This procedure yields a sample of peaks with parameters ν, x, e, and p. Finally, we use Eqs. (4.6) and (4.7) to convert this sample into a halo sample distributed in the asymptote A, and we multiply the distribution by the total number density n to obtain the differential number density $\mathrm{d}n/\mathrm{d}\ln A$.

As a test, we sample 400,000 density peaks from each of our six power spectra, and for each peak, we compute its predicted asymptote A (without the proportionality constant) using the ellipsoidal collapse model of Sec. 4.3.2. We plot the resulting distributions in Fig. C.3 superposed with the distributions we find in the randomly generated simulation boxes. We find that the two distributions

---

[2]Since these parameters describe the potential, they are different from the parameters e and p in Ref. [269].
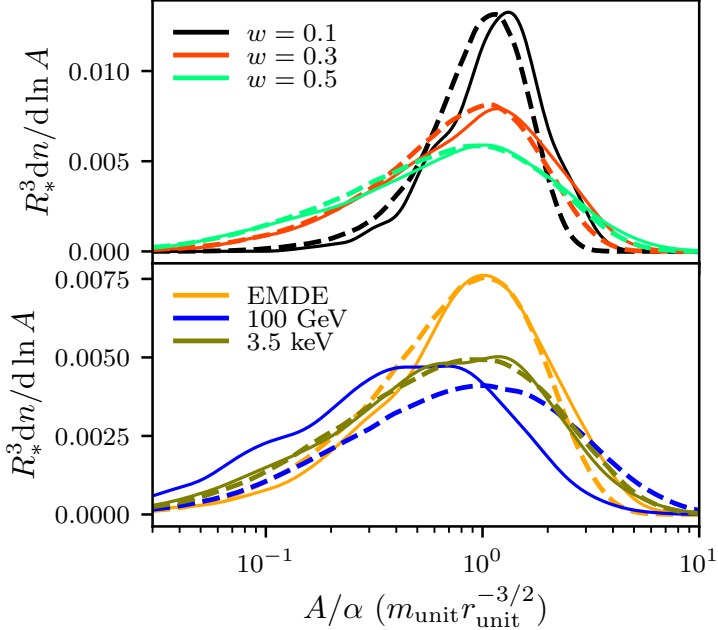
Figure C.3: A test of the Monte Carlo halo-sampling method of Appendix C.3. This figure plots the peaks drawn from our six power spectra distributed in the predictions for A from Sec. 4.3.2 (with simulation-tuned parameter α factored out). The solid lines show the distributions in the initial density field used for our simulations, while the dashed lines show the distributions computed using the Monte Carlo method.

match well for all of our power spectra except for the 100 GeV spectrum. For this power spectrum, directly sampling the power spectrum yields halos of higher predicted density that we find in the box. This discrepancy is explained by noting that the simulation box only samples fluctuation modes up to the size of the box. The 100 GeV power spectrum has sufficient power at larger scales that neglecting it significantly reduces the amplitudes of fluctuations and therefore the density of the resulting halos. In this way, sampling peaks directly from the power spectrum is more accurate than using the intermediate step of sampling a density field.

C.3.3 Outer profile: $r_{\max}$ and $M(r_{\max})$

So far, we have obtained the halo population distributed in the small-radius asymptote A. The next step is to extend this computation to find the multivariate distribution in A and the outer profile parameters $r_{\max}$ and $M(r_{\max})$ using the models discussed in Sec. 4.4. This calculation is more difficult because, instead of the finite number of Gaussian variables relevant to the neighborhood of each peak, we must now handle a Gaussian distribution in the infinitely many variables corresponding to the density profile about the peak at each radius q. Nevertheless, a numerical computation is

213
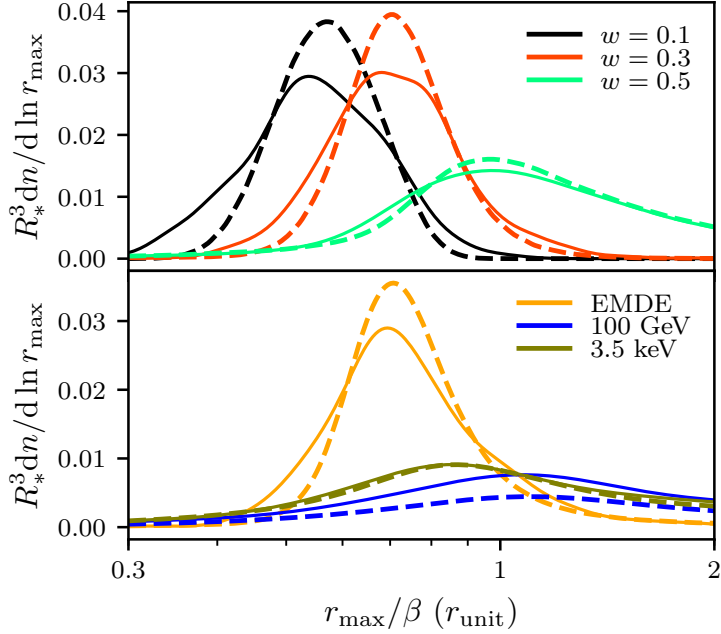
Figure C.4: Same as Fig. C.3, but distributed in the predictions for $r_{\max}$ from Sec. 4.4.2 using $s = 0$. Here, the simulation-tuned parameter β is factored out. The solid lines show the distributions in the initial density field used for our simulations, while the dashed lines show the distributions computed using the Monte Carlo method.

tractable.

The idea is to Monte Carlo sample the full density profile $\delta(q)$ about the peak. To accomplish this, we must discretize the radial coordinate such that

$$0 \leq q_1 < q_2 < ... < q_N \tag{C.13}$$

for some large N. The maximum radius may be initially set at some $q_N \gtrsim R_*$ and raised as needed. For shorthand, we will write $\delta_i = \delta(q_i)$ and use $\boldsymbol{\delta}$ to represent the full vector of δ_is. We now seek the distribution of $\boldsymbol{\delta}$ conditioned on the data we already used to find the asymptote A. In fact, $\boldsymbol{\delta}$ has vanishing covariance with the three-dimensional shape of the peak, so we need only the conditional distribution $f(\boldsymbol{\delta}|\nu, x)$. This distribution is Gaussian with mean

$$\bar{\delta}_i = \frac{\left(\langle \delta_i \nu \rangle - \gamma \langle \delta_i x \rangle \right) \nu + \left(\langle \delta_i x \rangle - \gamma \langle \delta_i \nu \rangle \right) x}{1 - \gamma^2} \tag{C.14}$$
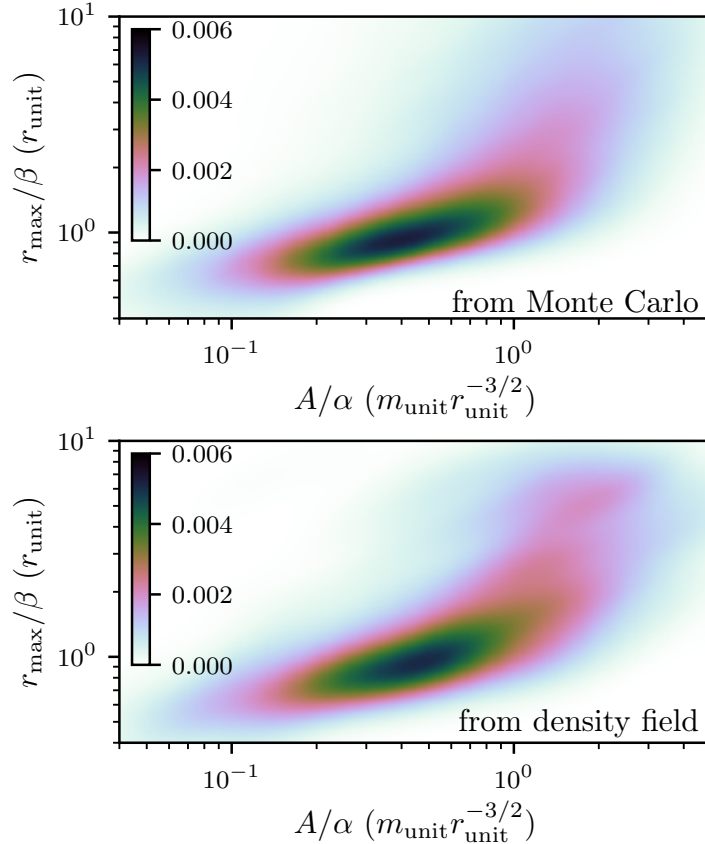
Figure C.5: The peaks drawn from the 3.5 keV power spectrum distributed in the predictions for A and r_{max} from Secs. 4.3.2 and 4.4.2, respectively (with simulation-tuned parameters α and β factored out). Top: The distribution computed using the Monte Carlo method of Appendix C.3. Bottom: The distribution in the initial density field used for our simulation. This figure shows that the Monte Carlo method accurately reproduces the correlations between A and r_{max} found in the density field. The color scale indicates the differential number density $\mathrm{d}^2 n/(\mathrm{d}\ln A\, \mathrm{d}\ln r_{\mathrm{max}})$ in units of R_*^{-3}.

(recalling $\gamma \equiv \sigma_1^2/[\sigma_0\sigma_2]$) and covariance matrix

$$C_{ij} = \langle \delta_i \delta_j \rangle - \frac{1}{1-\gamma^2} \left[\langle \delta_i \nu \rangle \langle \delta_j \nu \rangle + \langle \delta_i x \rangle \langle \delta_j x \rangle - \gamma \left(\langle \delta_i \nu \rangle \langle \delta_j x \rangle + \langle \delta_i x \rangle \langle \delta_j \nu \rangle \right) \right] \tag{C.15}$$

with the necessary covariances given by

$$\left\{ \begin{array}{c} \sigma_0 \langle \delta_i \nu \rangle \\ \sigma_2 \langle \delta_i x \rangle \\ \langle \delta_i \delta_j \rangle \end{array} \right\} = \int_0^\infty \frac{\mathrm{d}k}{k} \mathcal{P}(k) \left\{ \begin{array}{c} \mathrm{sinc}(k q_i) \\ k^2 \,\mathrm{sinc}(k q_i) \\ \mathrm{sinc}(k q_i)\,\mathrm{sinc}(k q_j) \end{array} \right\}. \tag{C.16}$$

It is helpful to diagonalize $C = PDP^T$ so that P is an orthogonal matrix and $D = \text{diag}(\lambda_1, ..., \lambda_N)$ is diagonal. If we define a new vector $\boldsymbol{\kappa} \equiv P^T(\boldsymbol{\delta} - \bar{\boldsymbol{\delta}})$, then $\boldsymbol{\kappa}$ is distributed as

$$f(\boldsymbol{\kappa}|\nu, x) = \prod_{i=1}^{N} \frac{1}{(2\pi\lambda_i)^{1/2}} \exp\left(-\frac{\kappa_i^2}{2\lambda_i}\right). \tag{C.17}$$

We then sample each κ_i from its respective univariate Gaussian distribution, and the density profile $\boldsymbol{\delta}$ immediately follows using $\boldsymbol{\delta} = \bar{\boldsymbol{\delta}} + P\boldsymbol{\kappa}$. From the density profile $\boldsymbol{\delta} \to \delta(q)$, we can find the mass profile $\Delta(q)$ using Eq. (4.8). With these profiles in hand, it is now a simple matter to apply any of the models detailed in Sec. 4.4.

To test this procedure, we sample density profiles for the same 400,000 peaks from each power spectrum for which we already sampled the peak parameters. Using the $s = 0$ contraction model in Sec. 4.4.2, Fig. C.4 compares the r_{max} distributions binned from our initial density fields to those computed using the Monte Carlo method. As before, the distributions from the 100 GeV power spectrum are discrepant, likely owing again to the finite size of the random density fields. Also, there is a tendency for the random density fields to produce less sharply peaked distributions than the Monte Carlo method, especially for the $w = 0.1$, $w = 0.3$, and EMDE power spectra. It is unclear where this discrepancy arises, but it could be connected to the finite grid resolution of the random density fields. For a second test, we also plot the combined A-r_{max} distribution for the 3.5 keV power spectrum in Fig. C.5. The Monte Carlo method proposed in this section accurately reproduces the correlations between A and r_{max} found in the density field.

APPENDIX D:
TECHNICAL DETAILS ON SIMULATING AND MODELING THE TIDAL EVOLUTION OF SUBHALOS[1]

D.1   Simulation details

D.1.1   High- and low-resolution particles

As Sec. 5.2 notes, we sample the subhalo's central region at increased resolution such that particles whose orbital pericenters are below $r_s/3$ have 1/64 the mass and 64 times the number density of the other particles. When simulation particles have different masses, it is possible for two-body interactions to artificially transfer energy from the heavy to the light particles. To verify that this effect is not significant in our simulations, we show in Fig. D.1 the density profiles of light and heavy particles in a subhalo not exposed to tidal forces. Even after duration $t = 318(G\rho_s)^{-1/2}$, where ρ_s is the subhalo's scale density, there is no visible tendency for the heavy particles to sink to smaller radii.

D.1.2   Density profiles and J factors

We obtain each subhalo's density profile by binning it in factors of 1.1 in the radius. At small radii, there is a resolution limit driven by three effects: force softening, Poisson noise, and artificial relaxation. Each effect is associated with a minimum resolved radius below which the density profile artificially flattens. For force softening, that radius is the distance $r_{\text{soft}} = 2.8\epsilon$, where ϵ is GADGET-2's force-softening parameter, at which forces become non-Newtonian. For Poisson noise, we take it to be the radius r_{100} enclosing 100 particles. To estimate the radius r_{rel} at which artificial relaxation becomes significant, we compute the relaxation time [392]

$$t_{\text{relax}} = \frac{N}{8 \ln \Lambda} \frac{r}{\sqrt{GM/r}} \tag{D.1}$$

at each radius r, where M and N are the mass and particle count interior to r, and $\Lambda = \max\{N, r/\epsilon\}$. If αt_{relax} at radius r, with an appropriate proportionality constant α, is shorter than the system age,

---
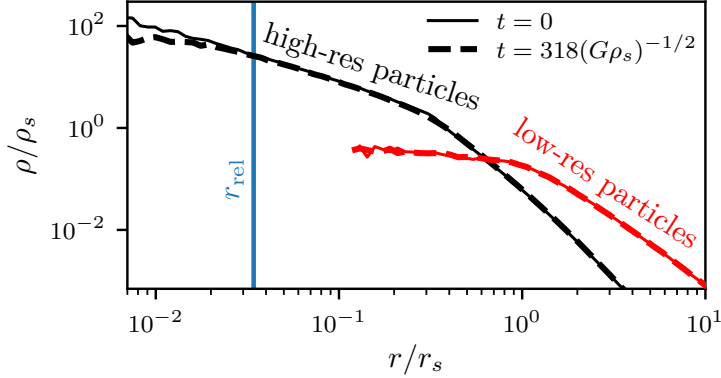
Figure D.1: Absence of relaxation effects associated with the use of different particle masses. This figure shows separately the density profiles of light (high-resolution) and heavy (low-resolution) particles inside the same halo; this halo is not exposed to tidal forces. There is no visible tendency for the heavy particles to sink to lower radii even after duration $t = 318(G\rho_s)^{-1/2}$ (dashed lines). The profile of low-resolution particles is plotted down to the radius containing 100 such particles. As a separate effect, the density profile of light particles shallows at small radii due to two-body relaxation (between light particles alone); the resolution limit r_{rel} imposed by this effect, described in Appendix D.1.2, is shown (vertical line).

then $r < r_{\mathrm{rel}}$. The proportionality constant α is tuned to predict the correct r_{rel} in a simulation of the subhalo without a host; in that case, any change to the density profile is artificial since the halo was built from an equilibrium distribution. From this calibration we use $\alpha = 5$. Figure D.1 shows how r_{rel} marks where the density profile begins to shallow due to relaxation effects.

The minimum resolved radius of the density profile is $r_{\mathrm{min}} = \max\{r_{\mathrm{soft}}, r_{100}, r_{\mathrm{rel}}\}$. For the purpose of accurately computing J factors we extrapolate the density profile below r_{min} as $\rho = Ar^{-1}$, where A is the average of ρr in the three smallest radial bins above r_{min}, so that

$$J = 4\pi A^2 r_{\mathrm{min}} + \int_{r_{\mathrm{min}}}^{\infty} \rho(r)^2 4\pi r^2 \mathrm{d}r. \tag{D.2}$$

Effectively, this procedure produces a lower bound on J under the assumption that larger radii are always stripped more than smaller radii. Below r_{min}, we simply assume all radii are stripped equally. We can also compute an upper bound on J by assuming that radii below r_{min} are completely unaffected (so $A = \rho_s r_s$), and this allows us to estimate the uncertainty in our J factors. We find that by the termination time of each subhalo's J-factor trajectory (as defined in Sec. 5.4), the uncertainty in the J factor, taken as $J_{\mathrm{upper}}/J_{\mathrm{lower}} - 1$, is 31% for one simulation (parameters $x = 31$, $y = 11$, $z = 0.07$; see Sec. 5.4), smaller than 17% for the remaining 51 simulations, and smaller than

10% for 44 of them.

To understand the J factors in the cases where $|\mathrm{d}\ln J/\mathrm{d}\ln t| \gtrsim 1$, another step is necessary. In this regime, the elongated tidal stream can contribute significantly to the J factor, making the spherical integral Eq. (D.2) inaccurate. Thus, we also compute the J factor as the sum over simulation particles

$$J = \sum_i \rho_i m_i, \tag{D.3}$$

where m_i is the mass of particle i and ρ_i is its local density. The density ρ_i is estimated as

$$\rho_i = \sum_{j=1}^{N} m_j W(r_{ij}, h_i) \tag{D.4}$$

over the $N = 50$ nearest particles j, where r_{ij} is the distance to particle j, h_i is the distance to the Nth particle, and $W(r, h)$ is the cubic spline kernel defined as in Ref. [274].

Equation (D.3) underestimates the J-factor contribution at $r < r_{\min}$ due to artificial flattening of the density profile. To accommodate the extrapolation procedure in Eq. (D.2) that addresses this problem, an additional step is required. We find the bound remnant of the subhalo using a procedure similar to that in Ref. [328]. Beginning with the assumption that all particles are bound, we iteratively compute the gravitational potential of each particle due to all other bound particles using a Barnes-Hut octree [503] with $\theta = 0.7$ and the same softening length as the simulation. Subsequently, we mark each particle as unbound if its total energy is positive and bound if its total energy is negative. At each step, we find the center-of-mass position and velocity of the 100 most bound particles and recenter the full system to be relative to this center of mass. All particles are initially marked as bound, and the procedure terminates when the count of bound particles converges.[2]

By assuming that the bound remnant is spherically symmetric, we can estimate the J factor both including spherical asymmetry and compensating for the flattening of the density profile below $r_{\min}$. If J_{full} is the J factor of the full system computed using Eq. (D.3) and $J_{\mathrm{bd,rad}}$ and J_{bd} are the

---

[2]This halting condition is stricter than the one in Ref. [328].
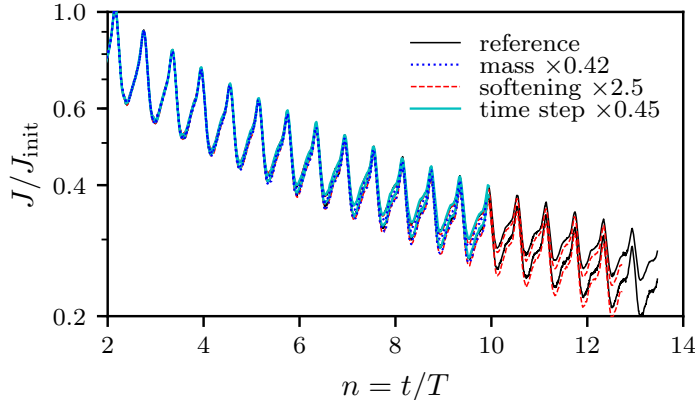
Figure D.2: Simulations of the same tidal evolution scenario carried out with different simulation parameters. For each simulation, two J-factor trajectories are plotted corresponding to the lower and upper limits discussed in Appendix D.1 (the lower limit is the value we use throughout this work). The upper and lower limits of each simulation overlap, implying numerical convergence.

J factors of the bound remnant computed using Eqs. (D.2) and (D.3), respectively, then

$$J = J_{\text{full}} - J_{\text{bd}} + J_{\text{bd,rad}}. \tag{D.5}$$

D.1.3 Numerical convergence

In our simulations, we set GADGET-2's force-softening length to be $\epsilon = 0.003 r_s$. This small value is intended to evade the artificial subhalo disruption observed by Ref. [409]. Meanwhile, the subhalo's high-resolution particles (see Sec. 5.2) have mass $4.3 \times 10^{-7} \rho_s r_s^3$. To check that numerical artifacts in our simulations are under control, we test the impact of changing the softening length and the particle resolution. Additionally, we test the impact of altering the (adaptive) integration time steps in order to ensure there are no artifacts arising from the application of the host's tidal field over these discrete intervals. In Fig. D.2, we plot the J-factor trajectory in a reference simulation (with system parameters $x = 34$, $y = 0.018$, and $z = 0.15$; see Sec. 5.4) along with three simulations of the same system with different particle resolution, force softening, and integration time steps. We plot the upper and lower limits of the J-factor trajectory as discussed above. These limits overlap for all simulation parameters, suggesting that the simulation is converged.

D.2 Subhalo size

In our simulations we applied the host halo's tidal forces using the linearized expression given by Eq. (5.3), which is valid in the limit that the subhalo is much smaller than its orbital radius. Thus,
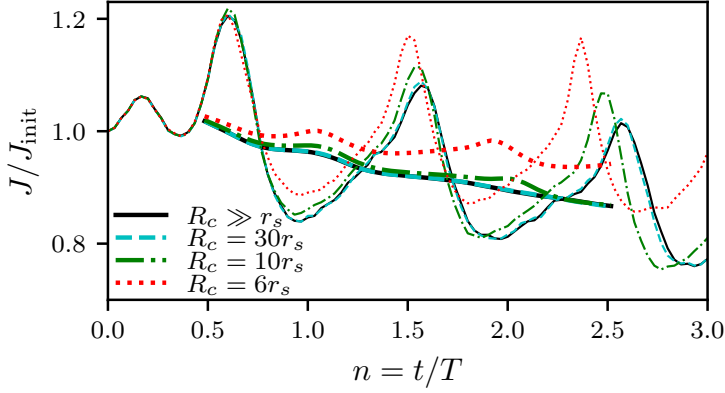
Figure D.3: Influence of a subhalo's size on its tidal evolution. This figure shows the trajectory of a subhalo's J factor for several different values of the ratio r_s/R_c between the subhalo's scale radius and the radius of its orbit about the host; the relative orbital radius R_c/R_s is held fixed along with all other parameters. Thin lines show full trajectories while thick lines show averages over each orbital period. When $r_s \gtrsim 0.1 R_c$, the tidal evolution begins to diverge from the evolution in the $r_s \ll R_c$ limit (solid curve). The double peak in the first orbit arises because of the subhalo's truncation radius in these simulations and is not relevant to the comparison.

our results are applicable in the $r_s \ll R_c$ limit. In this appendix, we explore precisely how far the applicability of our results can be taken. For this purpose we executed several simulations using the exact tidal force $\boldsymbol{F}_{\text{tidal}}(\boldsymbol{r}) = \boldsymbol{F}(\boldsymbol{R} + \boldsymbol{r}) - \boldsymbol{F}(\boldsymbol{R})$ instead of the linearized version, and we compare the results of these simulations to those of a simulation that employed the linearized force. The subhalos in all of these simulations are cut off at radius $5r_s$ to avoid excessive overlap with the host's center; this change does not affect the comparison since it applies equally to every simulation.

We subjected subhalos of different sizes to the same tidal evolution scenario with parameters $x = 21$, $y = 0.056$, and $z = 0.18$ in the parametrization given in Sec. 5.4. Figure D.3 shows the tidal evolution of the subhalo's J factor for different values of the ratio r_s/R_c between the subhalo's scale radius and the radius of its orbit about the host. We find that the tidal evolution begins to diverge markedly from that induced by the linearized tidal force when $r_s \gtrsim 0.1 R_c$. Note that this analysis still neglects dynamical friction (including self-friction, due to the limited duration of these simulations); the influence of this effect is also sensitive to the subhalo's size. Thus, our results are applicable if both $r_s \lesssim 0.1 R_c$ and dynamical friction can be neglected (see Sec. 5.2).

D.3 Computational details

In this appendix, we present practical ways to compute the reduced variables x, y, and z along with the orbital period T. For convenience, we include fitting formulas to approximate the necessary

integrals. In what follows, the host is assumed to possess an NFW profile with scale radius R_s and scale density P_s; its mass profile is

$$M(R) = 4\pi P_s R_s^3 \left[\ln\left(1 + \frac{R}{R_s}\right) - \frac{R/R_s}{1 + R/R_s} \right],$$ (D.6)

its force profile is $F(R) = GM(R)/R^2$, and its potential profile is

$$\Phi(R) = -4\pi G P_s R_s^2 \frac{\ln(1 + R/R_s)}{R/R_s}.$$ (D.7)

Meanwhile, the subhalo's orbit about the host is parametrized by the circular orbit radius R_c and circularity η, and as shorthand, we define $y_c \equiv R_c/R_s$.

D.3.1 Computing $x = |E_b|/\Delta E_{\mathrm{imp}}$

The binding energy E_b of a particle at the subhalo's scale radius r_s is given by Eq. (5.15). Meanwhile, the total energy ΔE_{imp} injected into a particle at radius r by tidal forces over the course of a subhalo orbit is computed using the impulse approximation, as described in Ref. [425]. This energy depends on the particle's full three-dimensional position within the subhalo, but we simplify the picture by averaging this energy over the sphere at radius r. Dimensionally, $\Delta E_{\mathrm{imp}}/r^2 \sim F(R_c)/R_c$, and we can approximate

$$\frac{\Delta E_{\mathrm{imp}}}{r^2} = P_1(y_c) \exp\left\{ P_2(y_c) \left[1 - \eta^{P_3(y_c)} \right] \right\} \frac{F(R_c)}{R_c},$$ (D.8)

where $P_1(y_c)$ is defined

$$P_1(y_c) = \frac{A(1 + B\ln(1 + y_c) - Cy_c/(D + y_c))}{1 + E(\ln(1 + y_c) - 2y_c/(2 + y_c))},$$
$$A = 3.327, \ B = 0.6463, \ C = 0.8837, \ D = 0.8809, \ E = 0.2156,$$ (D.9)

$P_2(y_c)$ is defined

$$P_2(y_c) = A(1 + (y_c/c)^a)^b,$$
$$A = 3.005, \ a = 3.641, \ b = 0.08513, \ c = 0.5703,$$ (D.10)
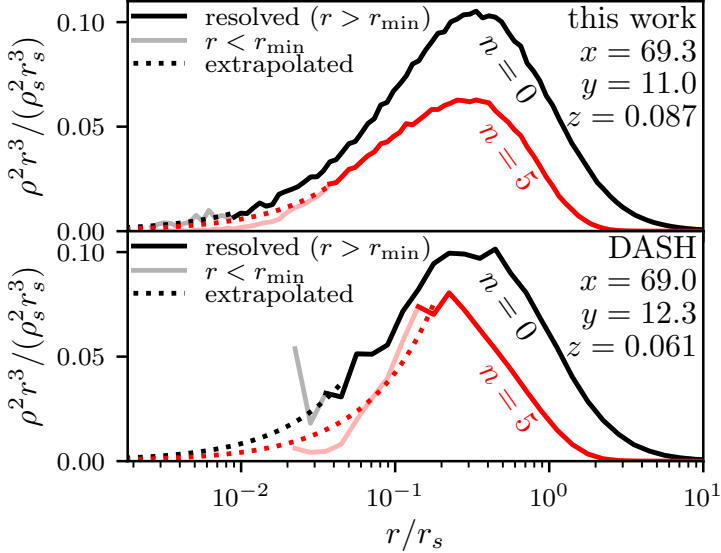
Figure D.4: A resolution comparison between our simulations (top) and those of the DASH library (bottom). The (log-space) integrand for the J factor, $\rho^2 r^3$, is plotted for an example subhalo from each catalogue with similar system parameters (x, y, and z; see Sec. 5.4) at $n = 0$ and $n = 5$ orbits. The J factor is the area under the curve. Below the resolution limit $r_{\min}$, we plot a pessimistic extrapolation of the density profile; see Appendix D.1.

and $P_3(y_c)$ is defined

$$P_3(y_c) = \frac{A(1 + (y_c/c_1)^{a_1})^{b_1}}{(1 + (y_c/c_2)^{a_2})^{b_2}(1 + (y_c/c_3)^{a_3})^{b_3}},$$

$$A = 0.2150, \ a_1 = 1.017, \ b_1 = 0.8650, \ c_1 = 0.5057, \ a_2 = 2.774,$$

$$b_2 = 0.2426, \ c_2 = 0.6415, \ a_3 = 0.7663, \ b_3 = 0.6508, \ c_3 = 18.84.$$

(D.11)

For $\eta > 0.04$, this expression is accurate to within 3% for $y_c < 10$ and within 14% for $y_c < 10^3$.

D.3.2 Computing $y = \bar{R}/R_s$

The time-averaged radius $\bar{R}$ of the orbit is approximately R_c, and, in fact, $\bar{R}/R_c \to 1$ as $R_c/R_s \to 0$. More broadly, the expression

$$\frac{\bar{R}}{R_c} = \frac{1 + B(1 - F\eta^G)\ln(1 + y_c) - Cy_c/[D(1 - H\eta^I) + y_c]}{1 + E(\ln(1 + y_c) - 2y_c/(2 + y_c))},$$

$$B = 0.3777, \ C = 0.4892, \ D = 2.412, \ E = 0.2426, \ F = 0.3556, \ G = 1.860, \ H = 0.1665,$$

(D.12)

is accurate to within 0.3% for $\eta > 0.04$ and $y_c < 10^3$.

223
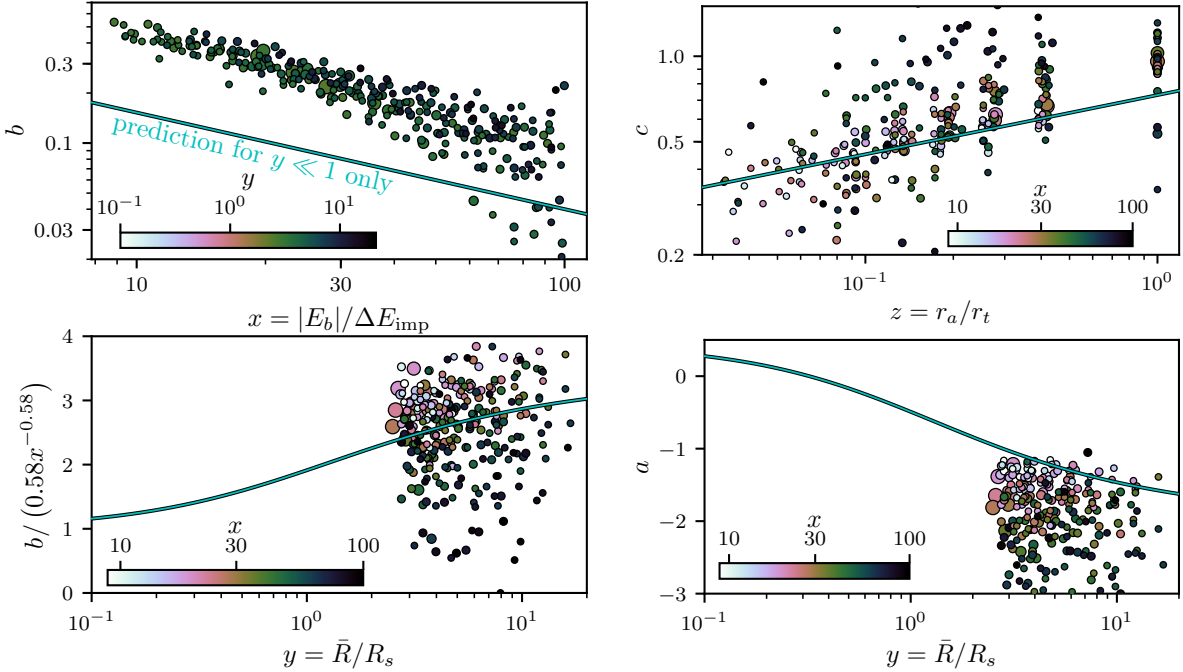
Figure D.5: A test of our model against the DASH simulations. This figure plots the J-factor trajectory parameters a, b, and c for the DASH simulations against the system parameters x, y, and z. The solid curves are our model predictions; they are the same curves shown in Figs. 5.10, 5.11, and 5.13. Note that the offset between the solid line and the simulations in the upper-left panel is not a discrepancy, for the solid line is only valid for $y \ll 1$. The DASH simulations exhibit significant scatter but broadly support our model with some systematic discrepancies discussed in Appendix D.4. The radius of each marker is proportional to the number of orbital periods, which ranges from 5 to 11.

D.3.3 Computing $z = r_a/r_t$

We define the adiabatic shielding radius r_a and the tidal radius r_t as the solutions to $m(r_a)/r_a^3 = \rho_a$ and $m(r_t)/r_t^3 = \rho_t$, respectively, where $m(r)$ is the subhalo's initial NFW mass profile [see Eq. (D.6)]. Here, ρ_a and ρ_t are functions of the subhalo's orbit; in particular,

$$\rho_a \equiv \frac{V_p^2}{GR_p^2} = \eta^2 \frac{M(R_c)R_c}{R_p^4} \quad \text{and} \quad \rho_t \equiv \frac{M(R_a)}{R_a^3}, \tag{D.13}$$

where R_p and R_a are the orbital pericenter and apocenter radii, which may be obtained as the two solutions R to

$$\Phi(R_c) - \Phi(R) + \left(1 - \eta^2 \frac{R_c^2}{R^2}\right) \frac{GM(R_c)}{2R_c} = 0. \tag{D.14}$$

224

D.3.4 Computing T

Dimensionally, the radial orbit period $T \sim t_0$, where $t_0 \equiv \sqrt{R_c/F(R_c)}$. More precisely, the expression

$$\frac{T}{t_0} = \frac{A(1 + F\eta^G)[1 + B\ln(1 + y_c) - Cy_c/(D + y_c)]}{1 + E(1 + H\eta^I)(\ln(1 + y_c) - 2y_c/(2 + y_c))},$$

$$A = 3.460, \ B = 0.6076, \ C = 0.8831, \ D = 2.312, \ E = 0.3325, \tag{D.15}$$

$$F = 0.04827, \ G = 1.261, \ H = 0.03606, \ I = 1.288,$$

is accurate to within 0.2% for $\eta > 0.04$ and $y_c < 10^3$.

D.4 Comparison to the DASH library

Reference [342] published a library called Dynamical Aspects of SubHaloes (DASH) of idealized subhalo simulations. This library includes the results of 2177 simulations, with different system parameters, of an N-body subhalo orbiting an analytic host potential. These simulations resolve significantly less of the subhalo density profile than do ours; as shown in Fig. D.4, they can leave large fractions of the J factor unresolved. Also, the DASH library covers a smaller parameter range in x, y, and z. Nevertheless, because of the extraordinary volume of this library, it can serve as a test for our model.

We use the procedure in Appendix D.1 to find the J-factor trajectory of each DASH simulation,[3] imposing an additional constraint that the trajectory halt when the maximum uncertainty in the J factor is larger than a factor of 3. Next, we fit the parameters a, b, and c to this trajectory as in Sec. 5.4. For the DASH simulations, Fig. D.5 plots (in the same way as Figs. 5.10, 5.11, and 5.13) the trajectory parameters a, b, and c against the system parameters x, y, and z. Superposed are our model predictions, as solid lines, using the parameters obtained in Sec. 5.4.

We first remark that all DASH simulations have $y > 2$, so we cannot directly test Eq. (5.18) describing the behavior of b in the $y \ll 1$ self-similar regime. Nevertheless, the upper-left panel of Fig. D.5 shows that the DASH simulations exhibit roughly the same power-law behavior $b \propto x^{-0.58}$ predicted by Eq. (5.19) (the offset between our curve and the simulations here is not a discrepancy). The lower panels show the sensitivity of a and b to y. Because the DASH simulations only cover

---

[3]We use a larger $\alpha = 20$ to find $r_{\rm rel}$ for the DASH simulations, obtained by recalibrating for these simulations. Note that larger α implies more optimism about simulation resolution.

a small range of y, we cannot verify the functional form of each parameter in y. Also, there is substantial scatter, especially at large x. Nevertheless, our model predicts roughly the correct values of a and b for these simulations, although there is a tendency for the simulations to have smaller values of a and larger values of b. Finally, although the scatter in c is quite large, the relationship between c and z is approximately borne out in the DASH simulations.

The tendency for the DASH simulations to yield small a and large b can be understood as a resolution artifact. Below the resolution limit, we extrapolate the density profile in a way that always underestimates the J factor (see Appendix D.1). This underestimation both increases the immediate loss of the J factor, reducing a, and increases the rate at which J decays (since artificial relaxation worsens the resolution over time), raising b.

Also, there is a tendency for systems at the large-x end to exhibit large scatter in a, b, and c as well as a precipitous drop in b (sometimes even to $b < 0$). This trend is also an unphysical artifact. In our simulations, we observed the same trend when $x \gtrsim 200$, which is why our simulation sample in Sec. 5.4 only includes $x < 200$. For the lower-resolution DASH simulations, the trend begins at $x \gtrsim 50$. The numerical difficulty with large x is unclear, but it is likely connected to the fact that large x implies the subhalo's internal forces are much stronger than the external tides. The vast difference in the scales of these forces could lead to issues in numerical precision when the tiny tidal forces are added to the large internal forces.

D.5 The broader density profile

References [340] (hereafter H03) and [341] (hereafter P10) studied the tidal evolution of a subhalo's density profile, focusing on the structural parameters v_{max}, the maximum circular velocity within the subhalo, and r_{max}, the radius at which this velocity is attained. Prior treatments of the annihilation rate in subhalos (e.g., Refs. [347, 407]) have employed these works' predictions of r_{max} and v_{max}, along with the assumption that subhalos retain NFW profiles, to predict subhalo J factors. To understand the connection between our work and these prior works, this appendix investigates the evolution of r_{max} and v_{max} in our simulations.

At each snapshot of our simulations, we find r_{max} as the radius $r < r_t$ that maximizes $v_{\mathrm{circ}} = \sqrt{Gm(r)/r}$, and v_{max} is the corresponding maximum. We only consider snapshots up to the point where $|\mathrm{d}\ln J/\mathrm{d}\ln t| = 1$, as discussed in Sec. 5.4. Additionally, we halt the r_{max} and v_{max} trajectory when r_{max} becomes smaller than the resolution limit (see Appendix D.1), and we only include
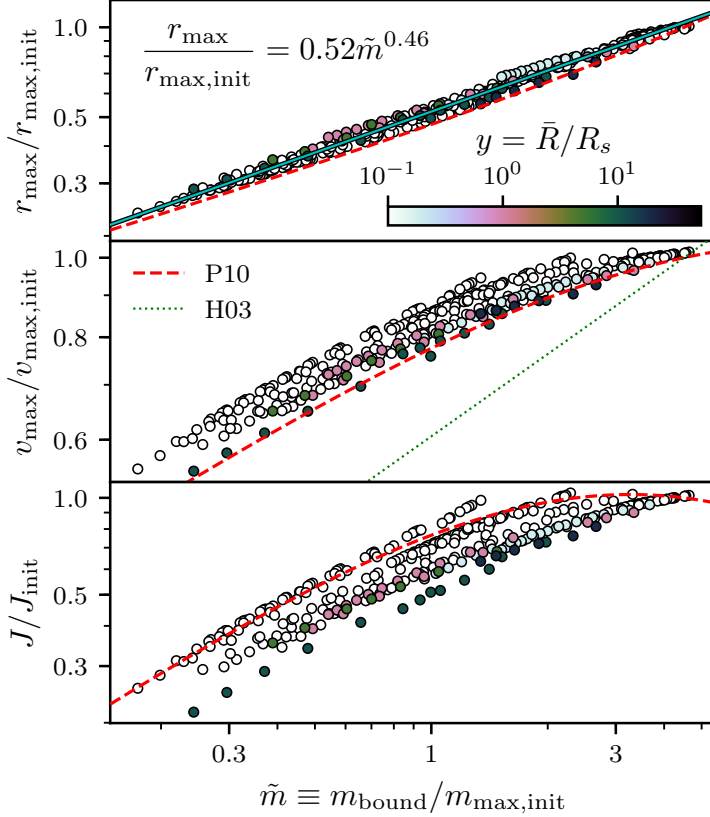
Figure D.6: The relationship of the subhalo properties r_{max} (top), v_{max} (middle), and J (bottom) to its bound mass m_{bound} after tidal stripping. r_{max} is cleanly related to m_{bound}, but the scatter is larger for v_{max} and still larger for J. Each point represents the average over a single orbit in our simulations, and the solid lines represent the displayed fitting functions. The dashed and dotted lines correspond to the predictions of P10 and H03, respectively, assuming that the initial mass is $4.5 m_{\mathrm{max,init}}$. The P10 prediction in the last panel additionally assumes an NFW profile.

simulations whose trajectories cover at least five orbits about the host. This restriction reduces our simulation count to 41, 33 of which are in the self-similar regime ($R_c/R_s < 0.3$).

D.5.1 Relations between structural parameters

Following H03 and P10, we first explore the relationship between a subhalo's structural parameters and its total mass loss. These prior works parametrize the mass loss using the ratio $m_{\mathrm{bound}}/m_{\mathrm{acc}}$, where m_{bound} is the mass that remains bound to the subhalo and m_{acc} is its virial mass at accretion. However, this parametrization implies that the impact of tides is strongly sensitive to the subhalo's initial concentration, and we propose that this sensitivity is unphysical since the outer layers may be stripped almost immediately upon accretion onto the host. To evade this problem, we instead parametrize the mass loss using the ratio $\tilde{m} \equiv m_{\mathrm{bound}}/m_{\mathrm{max,init}}$ of m_{bound} to the mass initially
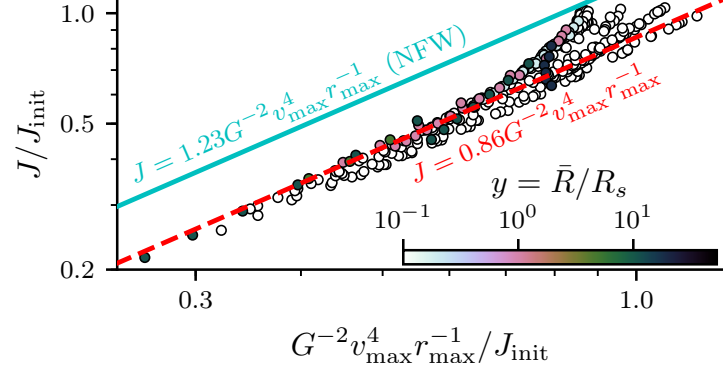
Figure D.7: The relationship between a subhalo's J factor and its structural parameters r_{max} and v_{max}; for an NFW profile, $J = 1.23 G^{-2} v_{\mathrm{max}}^4 r_{\mathrm{max}}^{-1}$ (solid line). In our simulations, the J factor lies consistently about 30% below the value that would be expected assuming an NFW profile, as illustrated by the dashed line. Each point represents the average over a single orbit in our simulations.

enclosed within r_{max}; this ratio is initially larger than unity. We compute m_{bound} using the procedure in Appendix D.1, and Fig. D.6 shows these relationships. For comparison we also plot the predictions of H03 and P10 assuming $m_{\mathrm{acc}} = 4.5 m_{\mathrm{max,init}}$, which corresponds to subhalo concentration $c_{\mathrm{sub}} \simeq 20$ at accretion.

We find that r_{max} is cleanly related to m_{bound} by a power law. Additionally, for both r_{max} and v_{max}, the predictions of P10 (with $c_{\mathrm{sub}} \simeq 20$) work reasonably well as long as $\bar{R} > R_s$. However, the bottom panel of Fig. D.6 shows that there is substantial scatter in the relationship between J and m_{bound}, and P10 does not accurately predict the J factor if an NFW profile is assumed. The scatter partially results from the modest scatter in v_{max}, since $J \propto v_{\mathrm{max}}^4$, but it also reflects that tidally altered density profiles differ significantly from NFW. Figure D.7 investigates this effect further and shows that a subhalo's J factor is roughly 30% smaller than what would be predicted from r_{max} and v_{max} assuming an NFW profile.

D.5.2   Time evolution of structural parameters

We can also predict the evolution of the subhalo's structural parameters more explicitly. Subjected to tidal forces, r_{max} and v_{max} follow qualitatively similar trajectories to the J factor:

$$\ln \frac{r_{\mathrm{max}}}{r_{\mathrm{max,init}}} = b_r \left[a_r - \frac{1}{1 - c_r} \left(n^{1-c_r} - 1 \right) \right], \tag{D.16}$$

$$\ln \frac{v_{\mathrm{max}}}{v_{\mathrm{max,init}}} = b_v \left[a_v - \frac{1}{1 - c_v} \left(n^{1-c_v} - 1 \right) \right], \tag{D.17}$$

Figure D.8: The r_{max} and v_{max} trajectory parameters b_r and b_v plotted against the system parameters x and y (cf. Fig. 5.10); see Eqs. (D.16) and (D.17). The radius of each marker is proportional to the number of orbital periods, which ranges from 5 to 15 for this sample.

where $n = t/T$ is the number of orbits [compare Eq. (5.14)]. Note that the total bound mass, m_{bd}, behaves similarly; its trajectory follows from Eq. (D.16) by inverting the equation in the top panel of Fig. D.6. As shown in Figs. D.8, D.9, and D.10, b_r, c_r, b_v, and c_v appear to depend on the system parameters x, y, and z in the same way that b and c did:

$$b_r = 0.48x^{-0.38}\left[1 + 0.70f(y)\right], \tag{D.18}$$

$$c_r = 0.91z^{0.13}, \tag{D.19}$$

$$b_v = 0.28x^{-0.58}\left[1 + 1.36f(y)\right], \tag{D.20}$$

$$c_v = 0.78z^{0.22}. \tag{D.21}$$

However, Fig. D.9 shows that unlike a, the parameters a_r and a_v depend not only on y but also on x. Moreover, they are only sensitive to x in the self-similar regime ($R_c/R_s < 0.3$). We fit the equation $a_r = a_{r0}\ln(x/a_{r1})$, and likewise for a_v, in the self-similar regime. Next, we fit $a_r - a_{r0}\ln(x/a_{r1})[1 - f(y)/2] = -a_{r2}f(y)$, and likewise for a_v, using all simulations. The function $f(y)$ asymptotes at 2 for large y, so the combination $[1 - f(y)/2]$ suppresses the x-dependent part of

Figure D.9: The $r_{\max}$ and $v_{\max}$ trajectory parameters a_r and a_v plotted against the system parameters x and y (cf. Fig. 5.11); see Eqs. (D.16) and (D.17). The radius of each marker is proportional to the number of orbital periods, which ranges from 5 to 15 for this sample.

a_r and a_v at large r. Hence, we obtain

$$a_r = 0.53\ln(x/84)\left[1 - f(y)/2\right] - 1.26f(y) \tag{D.22}$$

$$a_v = 0.37\ln(x/12)\left[1 - f(y)/2\right] - 1.21f(y), \tag{D.23}$$

as depicted in Fig. D.9.

Broadly, there is more scatter in the trajectory parameters a_r, b_r, c_r, a_v, b_v, and c_v of $r_{\max}$ and $v_{\max}$ than in the parameters a, b, and c of the J factor, when plotted against the system parameters x, y, and z (cf. Figs. 5.10, 5.11, and 5.13). The source of this scatter is unclear, but it is likely that $r_{\max}$ and $v_{\max}$ are more sensitive than J to additional effects beyond those accounted for by the parameters x, y, and z. Such heightened sensitivity is plausible for two reasons. First, $r_{\max}$ and $v_{\max}$ are more sensitive than J to the density profile at large radii, which could depend on details of the tidal forces to which the inner profile is insensitive. Second, $r_{\max}$ and $v_{\max}$, being defined using the condition $\mathrm{d}(m(r)/r)/\mathrm{d}r = 4\pi r\rho(r) - m(r)/r^2 = 0$, can be sensitive to fine details in the density profile $\rho(r)$. As an integrated quantity, the J factor does not exhibit this sensitivity.
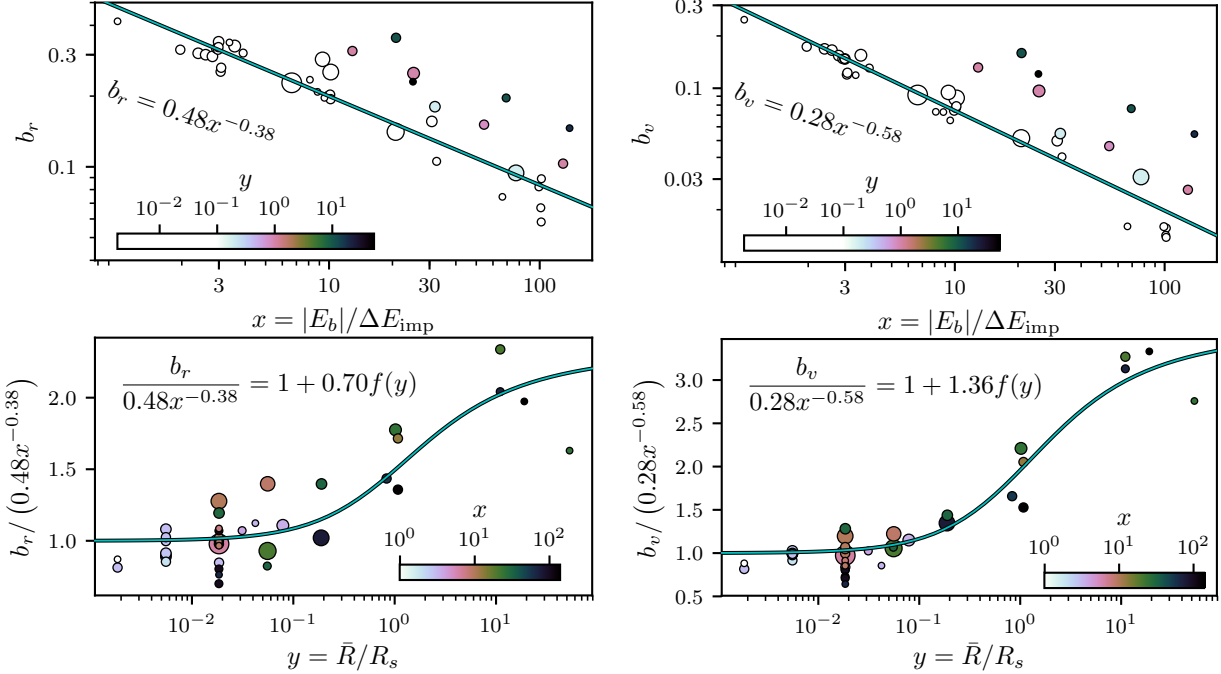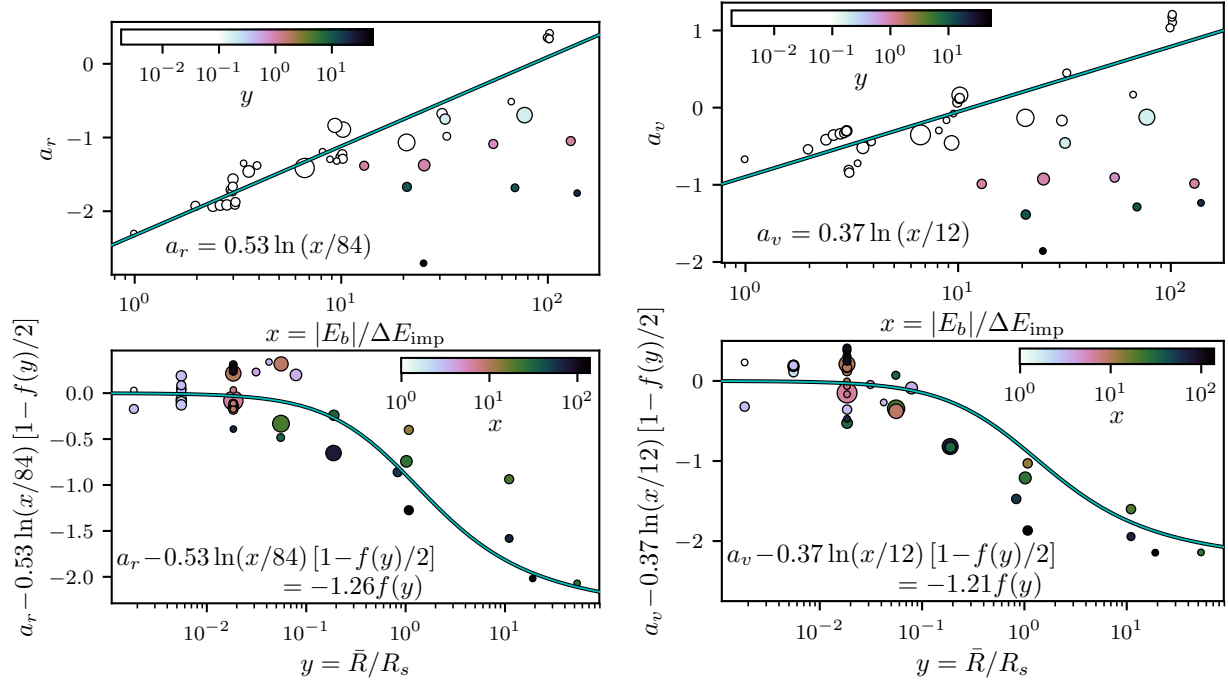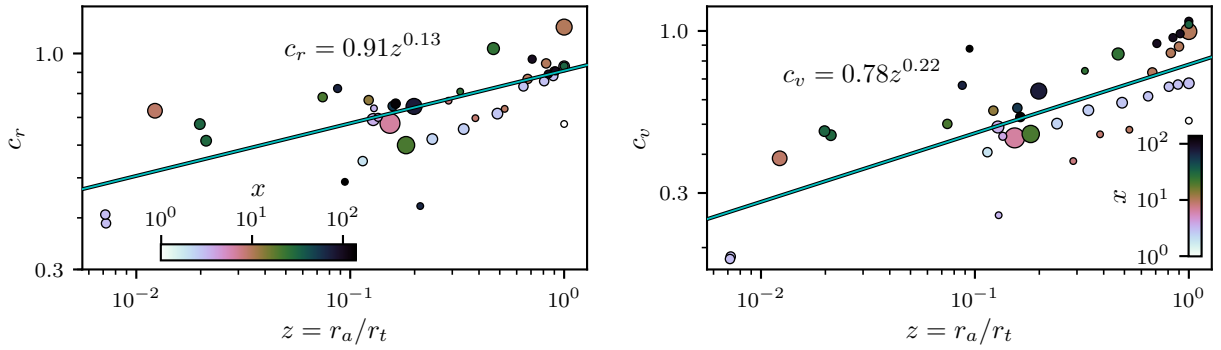
Figure D.10: The $r_{\max}$ and $v_{\max}$ trajectory parameters c_r and c_v plotted against the system parameter z (cf. Fig. 5.13); see Eqs. (D.16) and (D.17). The radius of each marker is proportional to the number of orbital periods, which ranges from 5 to 15 for this sample.

APPENDIX E:
TECHNICAL DETAILS ON MODELING THE IMPACT OF STELLAR ENCOUNTERS ON MICROHALO DENSITY PROFILES[1]

E.1   Accuracy of the impulse approximation

In this appendix, we explicitly simulate microhalo-stellar encounters in order to test the validity of the impulse approximation employed in Sec. 6.2. Reference [322] used such simulations to demonstrate that the impulse approximation is accurate in the case where the stellar encounter timescale is of order 10^{-3} the microhalo dynamical timescale. However, we aim to explore how far the impulse approximation can be taken.

For these simulations, we set the encounter parameters $b = 16r_s$ and $M_*/(Vb^2) = 0.76\sqrt{\rho_s/G}$. As discussed in Sec. 6.3, these parameters suffice to fully describe the encounter, at least in the impulsive regime, and they correspond to the parameters $q = 0.093$ and $p = 16$ as defined in that section. With these parameters, we prepare an N-body microhalo as in Sec. 6.2, but instead of perturbing the particle velocities using the impulse approximation, we insert the star as a point mass in the simulation. The star is placed at position $(800r_s, b, 0)$ with velocity $(-V, 0, 0)$, and the simulation is carried out for a duration of $1600r_s/V$, so that since its trajectory is essentially unperturbed, the star's final position is $(-800r_s, b, 0)$. The maximum time step of simulation particles is enforced to be $0.2b/V$ so that there are at least 500 time steps, and we verified that a naive numerical integral with this time stepping scheme accurately reproduces the analytic impulse approximation.

At the end of this simulation, we remove the star and subsequently continue the simulation for the duration $10t_{\mathrm{dyn}}$ with the same parameters as in Sec. 6.2. The time step is no longer artificially small. We executed this procedure for several different encounter velocities V, and the resulting microhalo density profiles are shown in Fig. E.1. The validity of the impulse approximation can be conditioned on the comparison between the encounter timescale b/V and the microhalo's internal dynamical timescale t_{dyn} given by Eq. (6.4), and we find that deviations from the impulse approximation become significant only when $t_{\mathrm{dyn}} \lesssim 5b/V$. The heightened efficacy of slow encounters

---
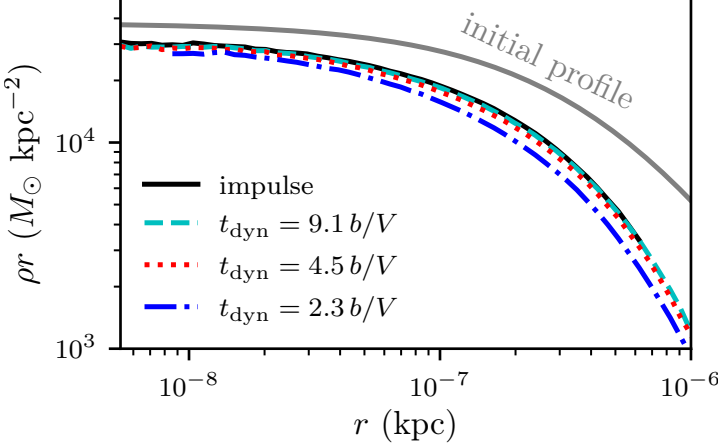
Figure E.1: A test of the impulse approximation. This figure shows the microhalo density profile resulting from several different stellar encounters; b and M_*/V are held fixed, but we vary the velocity V. The impulse approximation (solid line) corresponds to $V \to \infty$, and we find that as long as the microhalo's internal dynamical timescale $t_{\mathrm{dyn}} \gtrsim 5b/V$, the final density profile is identical to that resulting from the impulse approximation.

at altering a microhalo's structure, apparent in Fig. E.1, can be understood in light of the tendency for postencounter relaxation to make a halo more susceptible to future encounters (see Sec. 6.4.1). If $t_{\mathrm{dyn}} \lesssim b/V$, the halo begins to relax even as the encounter progresses, increasing its susceptibility to that same encounter.

E.2 Encounters in close succession

In this appendix, we test a microhalo's response to multiple encounters occurring within its dynamical timescale. Recall that on average, encounters separated by a time interval $t \gg t_{\mathrm{dyn}}$ are more efficient than simultaneous encounters at altering the microhalo's structure. To test the intermediate $t \lesssim t_{\mathrm{dyn}}$ regime, we carry out a series of simulations of two identical encounters separated by varying time t. The impact of two closely spaced encounters is highly sensitive to the geometry between them, so we consider two extreme cases. In the first case, the encounters are collinear, so their velocity injections add constructively. In the second case, the velocity injections add destructively; this is attained by making them parallel but in perpendicular directions from the halo [e.g., swapping the y and z coordinates in the scenario of Eq. (6.2)].

The encounters we study here have relative energy injection parameter $q = 1/120$, and we plot in Fig. E.2 the changes in the microhalo's scale radius r_s that result from these scenarios. At each time separation t, we also compute the average between the constructive and destructive scenarios
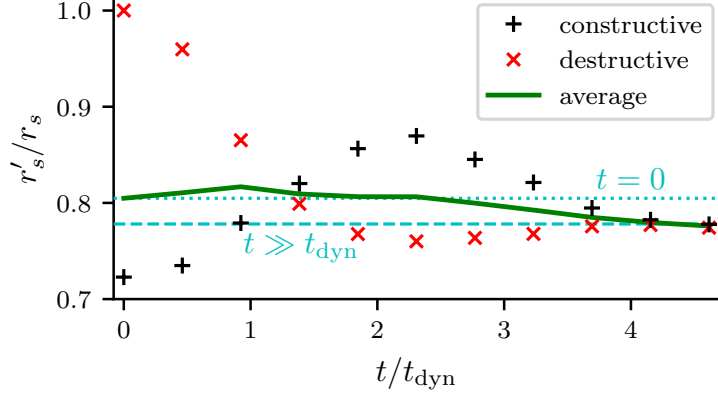
Figure E.2: The impact of two encounters separated by a short time t. We plot the change in r_s for two encounter geometries, one in which the velocity injections add constructively and one in which they add destructively. The solid line indicates the average between the two cases, computed as described in the text. The dashed line marks the change in r_s in the $t \gg t_{\text{dyn}}$ scenario while the dotted line represents the expected impact of simultaneous encounters. Evidently, encounters should be treated as simultaneous if they are separated by less than a few dynamical time intervals.

in the following way. We compute an effective parameter q_{eff} for each double-encounter scenario by inverting Eq. (6.13). Next, we average the effective energy injections q_{eff} for the constructive and destructive scenarios, and we use Eq. (6.13) to convert the resulting average q_{eff} into a change in r_s. This procedure automatically yields the correct expected impact of two encounters of arbitrary geometry in the $t = 0$ case, but for $t > 0$ it can be considered only a guide. The result is also plotted in Fig. E.2, and we find that, roughly speaking, two encounters can be treated as simultaneous if they are separated by less than a few dynamical time intervals.

E.3 Impact of encounters on the phase-space distribution

Figures 6.5 and 6.6 depict a remarkably precise relationship between the relative energy injection parameter q and the change in a microhalo's density profile. This precision suggests that it should be possible to derive from first principles the parameters $\zeta = 0.63$ and $\eta = 0.72$ that set these relationships. However, the change in the density profile is determined in a complicated way by both the initial heating of halo material and the subsequent relaxation of the halo, making such a derivation challenging. As a demonstration, we plot in Fig. E.3 the phase-space density $f(E)$ of a microhalo before and after various stellar encounters. The function $f(E)$ after a stellar encounter is not related in an obvious way to $f(E)$ beforehand; for instance, it is not related, even approximately, by either truncation beyond some energy E_t or a combination of that truncation with the lowering of $f(E)$ to maintain continuity at E_t, procedures suggested by Ref. [504].
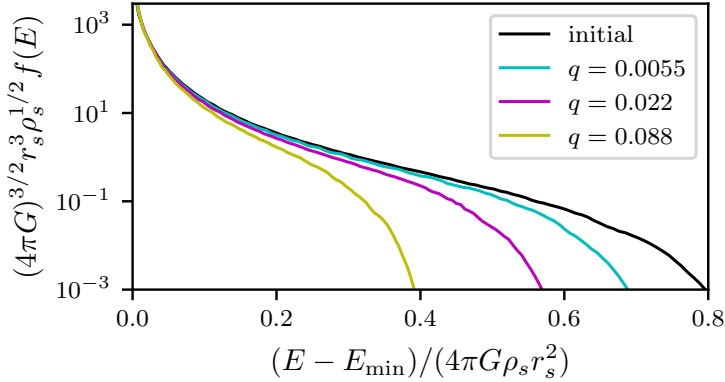
Figure E.3: Phase-space density $f(E) = \mathrm{d}^6 m/(\mathrm{d}^3 \boldsymbol{x} \mathrm{d}^3 \boldsymbol{v})$, as a function of energy E of halo particles, for a microhalo before and after different stellar encounters; the relative energy parameter q associated with each encounter is listed. E and f are normalized to properties of the initial density profile, and E is additionally specified relative to the floor $E_{\min}$ of the potential well. We choose an initial halo that has already experienced a stellar encounter, so it has a density profile described by Eq. (6.5) with $\alpha = 0.78$ instead of an NFW profile. As discussed in Appendix E.3, simple interpretations fail to accurately describe how $f(E)$ changes in response to an encounter.

The key challenge to such a simple interpretation is that particles throughout the halo are heated by the stellar encounter, even those that remain tightly bound. The resulting elevation of halo particles alters the gravitational potential even at small radii, which in turn further changes the energies E of halo particles. For this reason, Fig. E.3 shows that $f(E)$ decreases significantly in response to an encounter even at small E, an effect these simple interpretations do not capture. Due to these challenges, we leave to future work a first-principles derivation of Eqs. (6.13) and (6.14) and their parameters ζ and η.

APPENDIX F:
TECHNICAL DETAILS AND FURTHER MODEL DEVELOPMENT FOR PREDICTING THE GAMMA-RAY SIGNATURE OF EARLY MATTER DOMINATION[1]

F.1 Baryonic suppression of small-scale dark matter density fluctuations

Before recombination, baryons do not accrete into overdense regions because they are coupled to the photons. Afterward, they still resist gravitational infall on small scales because a residual ionization fraction maintains the baryons at a temperature close to that of the cosmic microwave background [471]. In particular, dark matter structures of mass smaller than about $10^5 M_\odot$ are not expected to accrete baryons. Consequently, dark matter density fluctuations at the microhalo scales we are concerned with grow more slowly than would otherwise be expected, and in this appendix we discuss how this effect influences the population of microhalos determined by the framework in Chapter 4.

During matter domination, matter density contrasts $\delta \equiv \delta\rho/\bar\rho$ grow as $\delta(a) \propto a$ in the linear regime ($\delta \ll 1$) if both baryons and dark matter contribute (or if baryons are absent). However, if baryons do not accrete into dark matter overdensities, then the dark matter density contrasts instead grow as $\delta(a) \propto a^\mu$ with [273]

$$\mu = \frac{5}{4}\left(1 - \frac{24}{25}\frac{\Omega_b}{\Omega_m}\right)^{1/2} - \frac{1}{4}.$$ (F.1)

Here, Ω_b and Ω_m are the ratios of baryon and matter density today, respectively, to the critical density; if $\Omega_m = 0.31$ and $\Omega_b = 0.049$ [476], then $\mu = 0.901$. This difference in growth rate is significant. As an approximate example, a density contrast $\delta = 0.17$ at $z = 3000$ would reach the critical linear threshold $\delta_c = 1.686$ and collapse at $z_c \simeq 300$ if $\delta \propto a$ or at $z_c \simeq 230$ if $\delta \propto a^\mu$. Since the characteristic density of the resulting halo is proportional to $(1 + z_c)^3$, incorrectly adopting $\delta \propto a$ would lead to overestimation of this halo's density, and hence annihilation rate, by a factor of 2.

---

[1]This appendix accompanied an article that was previously published in Physical Review D, and it is copyright © 2019 American Physical Society. The original reference is as follows: M. S. Delos, T. Linden, and A. L. Erickcek, *Breaking a dark degeneracy: The gamma-ray signature of early matter domination*, Physical Review D **100**, 123546 (2019).

By numerically integrating the spherical collapse model with baryons treated as a smooth background, we verified that the critical linear density contrast for collapse remains $\delta_c = 1.686$. That is, an initial spherical overdensity $\delta_i \ll 1$ at scale factor a_i collapses at scale factor $(1.686/\delta_i)^{1/\mu} a_i$. Additionally, the turnaround radius—the apocenter of the trajectory of the spherical shell enclosing the overdensity—is $r_{\text{ta}} = (3/5) r_i / \delta_i^{1/\mu}$; the coefficient 3/5 is unaltered from its standard value.

To account for the slower growth rate of δ, we alter the definition in Chapter 4 of the scaled density field to become

$$\delta(\boldsymbol{x}) \equiv \delta(\boldsymbol{x}, a)/a^{\mu}. \tag{F.2}$$

Applying this definition and the spherical collapse solution above, we find that Chapter 4's prediction of the coefficient A of a halo's $\rho = A r^{-3/2}$ inner asymptote becomes

$$A = \alpha \delta_c^{\frac{3}{2}\left(1 - \frac{1}{\mu}\right)} \bar{\rho} \delta^{\frac{3}{4}\left(\frac{2}{\mu}+1\right)} |\nabla^2 \delta|^{-3/4} f_{\text{ec}}^{-\frac{3}{2\mu}}(e, p), \tag{F.3}$$

where $\alpha = 12.1$ is the same proportionality constant as in Chapter 4. Here, $\bar{\rho} \simeq 33.1 \ M_{\odot}/\text{kpc}^3$ is the comoving mean dark matter density [476] and $f_{\text{ec}}(e, p) \equiv \delta_{\text{ec}}/\delta_{\text{c}}$ is an ellipsoidal collapse correction [373]. Meanwhile, in the turnaround model, the final radius of a mass shell at initial comoving radius q is

$$r = \beta q / \Delta(q)^{1/\mu}, \tag{F.4}$$

where $\Delta(q) = \Delta(q, a)/a^{\mu}$ is the fractional mass excess enclosed, in linear theory, and $\beta = 0.131$ is the same proportionality constant as in Chapter 4. The enclosed mass

$$M(q) = \beta_M (4\pi/3) q^3 \bar{\rho} \tag{F.5}$$

($\beta_M = 0.273$) is unaltered from its expression in Chapter 4, leading to

$$\frac{\mathrm{d} \ln M}{\mathrm{d} \ln r} = \frac{3}{1 + 3\epsilon(q)/\mu} \tag{F.6}$$

with $\epsilon(q) \equiv (-1/3) \mathrm{d} \ln \Delta / \mathrm{d} \ln q = 1 - \delta(q)/\Delta(q)$. The radius r_{max} of maximum circular velocity and mass m_{max} enclosed are obtained by solving $\mathrm{d} \ln M/\mathrm{d} \ln r = 1$ (or $\epsilon(q) = 2\mu/3$); this computation yields an initial comoving radius q_{max} from which Eqs. (F.4) and (F.5) yield the desired quantities.

F.2 Aggregate tidal suppression of subhalo annihilation rates

In this appendix, we use the model in Chapter 5 to derive, and find a fitting function for, the overall factor by which annihilation rates from subhalos are scaled within a host due to tidal evolution. For an individual subhalo with scale density ρ_s orbiting with circular orbit radius R_c and circularity η,[2] the Chapter 5 model predicts the factor

$$s(\rho_s/P_s, R_c/R_s, \eta, t/T) \equiv J/J_{\text{init}} \tag{F.7}$$

by which the subhalo's J factor is scaled by tidal evolution. Here, R_s and P_s are the scale radius and density of the host, t is the duration of the tidal evolution, and T is the subhalo's radial (apocenter-to-apocenter) orbit period. To characterize the aggregate tidal suppression of all subhalos within the host, we seek the quantity

$$S(\rho_s/P_s, t\sqrt{GP_s}, c) \equiv \frac{\sum J}{\sum J_{\text{init}}}, \tag{F.8}$$

where the sums proceed over subhalos distributed throughout the host's phase space. Here, $c = R_{\text{host}}/R_s$ is the radius of the host in units of R_s, which can be interpreted as its concentration R_{vir}/R_s. As Eq. (F.8) expresses, and we verified, S only depends on system parameters in the combinations ρ_s/P_s, $t\sqrt{GP_s}$, and R_{host}/R_s. This property follows from the dependencies of s in Eq. (F.7), noting that subhalo orbital periods are proportional to the host's dynamical timescale $(GP_s)^{-1/2}$.

We let $f(E, L, R)$ be the host halo's distribution function, where E is energy (per mass), L is angular momentum (per mass), and R is radius. The host's density profile $P(R)$ can be decomposed in the orbital parameters as

$$P(R) = \int_{R_{c,\text{min}}(R)}^{\infty} \mathrm{d}R_c \int_{0}^{\eta_{\text{max}}(R, R_c)} \mathrm{d}\eta \; g(R, R_c, \eta), \tag{F.9}$$

---

[2]As defined in Chapter 5 and elsewhere, for an orbit with energy E the circular orbit radius is the radius of the circular orbit with that energy. Meanwhile, the circularity is the ratio $\eta = L/L_c$ between the orbit's angular momentum and that of the circular orbit with energy E.

where

$$g(R, R_c, \eta) \equiv 4\sqrt{2}\pi f\left(K(R_c) + \Phi(R_c), \eta R_c\sqrt{2K(R_c)}, R\right)$$
$$\times \frac{[K(R_c)/R_c + 2\pi G P(R_c)R_c]\, K(R_c)\eta R_c^2/R^2}{\sqrt{K(R_c)(1 - \eta^2 R_c^2/R^2) + \Phi(R_c) - \Phi(R)}} \qquad \text{(F.10)}$$

follows from the definitions of R_c and η. Here, $K(R_c) \equiv GM(R_c)/(2R_c)$ is the circular orbit kinetic energy (per mass), $\Phi(R)$ is the host's potential profile, and $M(R)$ is its enclosed mass profile. The integration limits in Eq. (F.9) are defined such that

$$K(R_{c,\mathrm{min}}) + \Phi(R_{c,\mathrm{min}}) = \Phi(R), \qquad \text{(F.11)}$$

$$\eta_{\mathrm{max}} \equiv (R/R_c)\sqrt{1 + [\Phi(R_c) - \Phi(R)]/K(R_c)}. \qquad \text{(F.12)}$$

The decomposition in Eq. (F.9) is valuable because we can insert the individual tidal scaling factor s into the integrand. The aggregate tidal scaling factor is thus

$$S = \frac{1}{M_{\mathrm{host}}} \int_0^{R_{\mathrm{host}}} 4\pi R^2 \mathrm{d}R \int_{R_{c,\mathrm{min}}(R)}^{\infty} \mathrm{d}R_c \int_0^{\eta_{\mathrm{max}}(R,R_c)} \mathrm{d}\eta\, g(R, R_c, \eta)s(\rho_s/P_s, R_c/R_s, \eta, t/T), \qquad \text{(F.13)}$$

where $T = T(P_s, R_c/R_s, \eta)$ and M_{host} is the host's mass (within R_{host}).

For convenience, we supply the following fitting function for S. We assume the host halo has an isotropic distribution function $f(E)$ and employ the fitting form for f given in Ref. [422] to evaluate S. Let $p \equiv \rho_s/P_s$ and $\tau \equiv t\sqrt{GP_s}$. For $1 < c < 10^2$, $1 < p < 10^8$, and $1 < \tau < 10^4$, the expression

$$S(p, \tau, c) = \exp\left[-(c/\alpha)^{-\beta}\right],$$
$$\alpha = 2.84 p^{-0.698}\tau^{0.557}\exp(-6.67/\tau), \quad \beta = 0.577 p^{0.0476}\tau^{-0.0526}\exp(-0.563/\tau) \qquad \text{(F.14)}$$

is accurate to within 0.08, with better accuracy when $p > 10$. When predicting in Fig. 7.10 the suppression of annihilation signals from subhalos within the whole population of hosts, Eq. (F.14) produces results that are accurate to within 2%. The predictions that use this fitting function are shown as thin dotted lines.
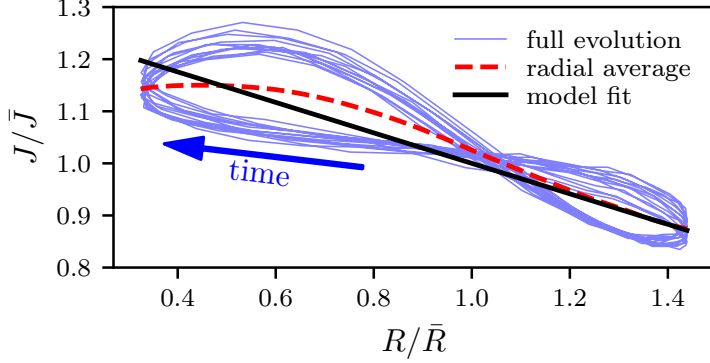
Figure F.1: The trajectory of the J-factor oscillations, $J/\bar{J}$ (where $\bar{J}$ is the orbital period-averaged trajectory), in radius $R/\bar{R}$, where $\bar{R}$ is the time-averaged orbital radius. The J factor is larger at smaller radii due to compressive tides. The red dashed line shows the average value of $J/\bar{J}$ at each radius, and the solid line shows our fit using Eq. (F.15).

F.3 J-factor oscillations during subhalo orbits

It is useful to model the periodic oscillations in the J factor observed in Chapter 5. While these oscillations do not alter the overall annihilation rate in subhalos, they still introduce a systematic biasing effect because subhalos at smaller radii have larger J, and this effect can alter the morphology of an annihilation signal. In this appendix, we reanalyze the tidal evolution simulations in Chapter 5 to develop a simple model for the impact of these oscillations. In particular, we model $J/\bar{J}$, where $\bar{J}$ is the orbital period-averaged J factor, as a function of the ratio $R/\bar{R}$ of the instantaneous to the orbital period-averaged radius. Figure F.1 plots $J/\bar{J}$ against $R/\bar{R}$ for one simulation. We will also employ the relative energy parameter $x = |E_b|/\Delta E_{\rm imp}$ and the relative orbital radius parameter $y = \bar{R}/R_s$ defined in Chapter 5 that describe the host-subhalo system.

For each simulation, we obtain the average value of $J/\bar{J}$ at each radius starting at the pericenter of the fifth orbit about the host and ending at the final pericenter. We also consider several additional simulations with $x < 3$ in order to understand the small-x behavior. Next, we fit

$$J/\bar{J} = 1 - d(R/\bar{R} - 1), \tag{F.15}$$

the simplest possible relationship, to this average value. Here, d is the fitting parameter, and it is easy to see that this equation manifestly preserves the time-averaged J factor. Both the radial average and the fit are also depicted in Fig. F.1. One may worry that Eq. (F.15) unphysically allows $J < 0$. However, we will see shortly that $0 \leq d \lesssim 0.5$, implying that $J > 0$ as long as $R_a/\bar{R} < 3$,
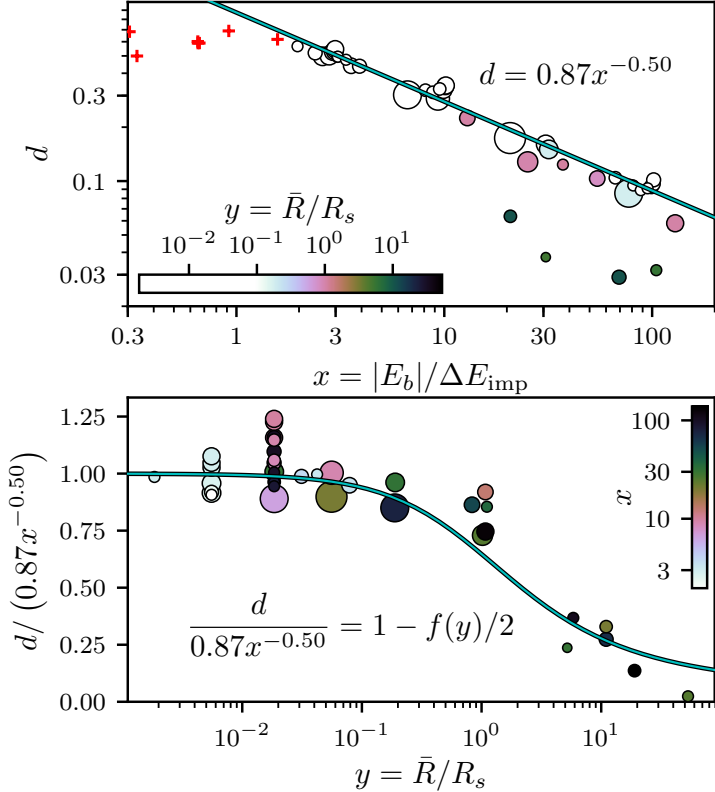
Figure F.2: The dependence of the parameter d that describes the J-factor oscillations on the host-subhalo system parameters x and y defined in Chapter 5. Top: in the $\bar{R} \ll R_s$ regime, d follows a power law in x, the best fit of which is shown as a solid line. At the small-x end, we see that x caps at roughly 0.5; the "+" markers are additional simulations at small x not used in the fit. Bottom: scaling of the normalization of d with $y = \bar{R}/R_s$. The solid line depicts the anticipated relationship (see the text) and is not a fit. Each marker is a simulation, and the marker radius is proportional to the number of orbital periods, which ranges from 6 to 20.

where R_a is the radius of the subhalo's orbital apocenter. If the host has an NFW profile, then $R_a/\bar{R} \le 1.5$.

Next, we relate d to the system parameters x and y. As shown in the top panel of Fig. F.2, d follows a power law in x in the $\bar{R} \ll R_s$ regime, but additionally, d does not exceed roughly 0.5. We find that

$$d \simeq \min\{d_0 x^{-d_1}, 0.5\}, \text{ if } \bar{R} \ll R_s \tag{F.16}$$

with $d_0 = 0.87$ and $d_1 = 0.50$. Beyond the $\bar{R} \ll R_s$ regime, d is also sensitive to $y = \bar{R}/R_s$. To understand this sensitivity, note that as discussed in Chapter 5, the subhalo experiences compressive tidal forces proportional to F/R along the axes perpendicular to the host-subhalo axis and stretching

Figure F.3: Impact of the time of a stellar encounter for a subhalo undergoing tidal evolution. This figure plots the J-factor trajectories of simulations of the same tidal evolution scenario where the subhalo is subjected to the same stellar encounter at different times; the labels indicate the time n of the encounter. The stellar encounter's impact is sensitive to the subhalo's position within its orbit during the encounter, but otherwise, the time of the encounter has minimal impact.

forces proportional to $f(R/R_s)F/R$ along the host-subhalo axis, where

$$f(y) \equiv \frac{2\ln(1+y) - y(2+3y)/(1+y)^2}{\ln(1+y) - y/(1+y)} \tag{F.17}$$

and F is the host halo's gravitational force at radius R. These forces cause the subhalo's size to scale as $1 - A$ along two axes and $1 + Af(R/R_s)$ along the other, where A is a factor that is common to all axes. Hence, the volume scales as $V \propto (1-A)^2(1+fA)$, where $f = f(R/R_s)$, so taking $J \propto 1/V$ and expanding to linear order in A, we obtain $J \propto 1 + 2A(1 - f/2)$. Combined with Eq. (F.16), this argument predicts the expression

$$d = \min\{d_0 x^{-d_1}, 0.5\}\left[1 - f(y)/2\right], \tag{F.18}$$

where $y = \bar{R}/R_s$ as before. The bottom panel of Fig. F.2 shows that this y-scaling works reasonably well.

F.4 Combined impact of tidal forces and stellar encounters

Chapter 5 explored the evolution of dark matter annihilation rates in subhalos due to the host halo's tidal forces, while Chapter 6 explored the evolution of microhalos subjected to encounters with individual stars. In this appendix, we explore how to combine the two effects. For this purpose, we simulated a variety of scenarios in which tidal evolution is combined with one or more stellar
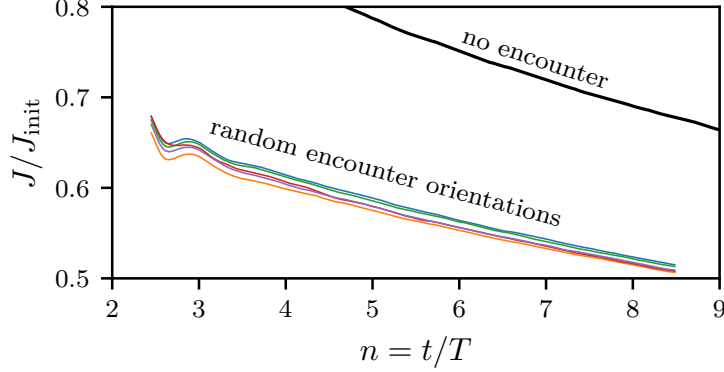
Figure F.4: Impact of the orientation of a stellar encounter for a subhalo undergoing tidal evolution. This figure plots the J-factor trajectories of simulations of the same tidal evolution scenario where the subhalo is subjected to the same stellar encounter with five random orientations. Evidently, the impact of encounter orientation is marginal.

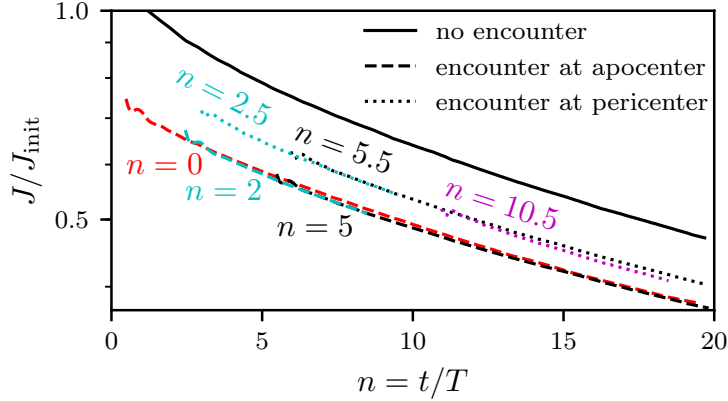encounters. These simulations were carried out using the methods of Chapters 5 and 6; in particular, velocity changes due to the passing star are applied directly and the star is not explicitly simulated. We track the evolution of the subhalo's J factor in each simulation as in Chapter 5. In all of these scenarios, the orbital radius is within the host's scale radius. This region is most relevant for stellar encounters; for instance, Draco's stellar half-light radius of 0.22 kpc is within its 0.44-kpc scale radius (see Sec. 7.5).

We first consider a tidal evolution scenario with ratio $\rho_s/P_s = 1285$ between the subhalo and host scale density and ratio $R_c/R_s = 0.055$ between the subhalo's circular orbit radius and the host's scale radius. We take the subhalo's orbital circularity to be $\eta = 0.5$.[3] In separate simulations, we applied the same stellar encounter at the beginning of the simulation, which is an apocenter passage, and also at the second and fifth subsequent apocenter passages. For the subhalo's initial density profile, this encounter has relative energy injection $q \equiv \Delta E/|E_b| = 1/50$, with q as defined in Chapter 6, and its impact parameter is much larger than the subhalo's scale radius. Figure F.3 shows the J-factor evolution (averaged over an orbital period as in Chapter 5) that results from these scenarios. Notably, the trajectory is essentially independent of the time of the encounter as long as it occurs at an apocenter. We also show the trajectory if the encounter occurs during a pericenter passage. As discussed in Appendix F.3, the subhalo is most compact near pericenter,

---

[3]See footnote 2 for definitions of R_c and η.
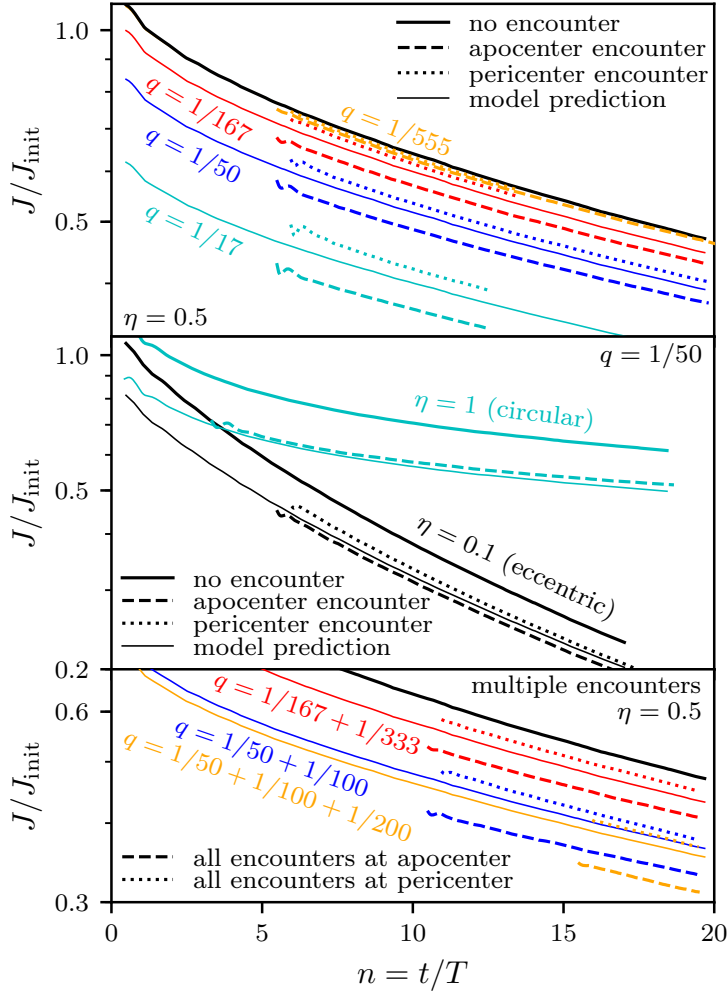
Figure F.5: Validation and tuning of the model developed in Appendix F.4 for combining the impact of a host halo's tidal forces with those of stellar encounters. We plot J-factor trajectories extracted from a variety of simulations (thick dashed and dotted lines) that include both tidal evolution and a stellar encounter; in the upper panel we vary the stellar encounter (labeling the relative energy parameter q), while in the middle panel we vary the subhalo orbit (labeling the orbit circularity η). We also show simulations involving multiple stellar encounters in the lower panel. Appropriately tuned, the model predictions (thin lines) match the simulations reasonably well. Note that for the $q = 1/555$ encounter in the upper panel, the model predicts no change in the J factor.
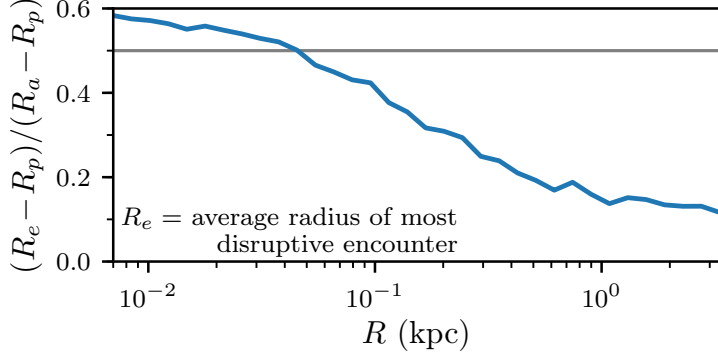
Figure F.6: Average radius R_e of the stellar encounter injecting the most energy for microhalos orbiting Draco. We plot R_e as a function of radius R about Draco; it is averaged at each radius over microhalo orbits and stellar encounter histories. R_e is plotted relative to the subhalo's pericenter and apocenter, so because the curve mostly lies below 0.5 (horizontal line), disruption tends to occur closer to pericenter.

and this compactness makes it more resistant to the stellar encounter. However, the same time independence holds.

Tidal forces break the spherical symmetry that a subhalo would otherwise be expected to possess, so we also verify explicitly that the orientation of the stellar encounter is inconsequential. We simulated the above tidal evolution scenario subjected to the same stellar encounter at a fixed time but with five random orientations. We plot the resulting J-factor trajectories in Fig. F.4. The scatter between these trajectories is only about 5% of the change in J caused by the encounters, which confirms that the encounter orientation does not have a significant impact.

Since the time of a stellar encounter has little impact on the resulting J-factor evolution, we can build a model for the impact of stellar encounters based on the idea of inserting the encounters after the tidal evolution. Let s be the orbital period-averaged tidal scaling factor for the subhalo's J factor due to the host's tidal forces; that is, $s = J/J_{\text{init}}$ is the quantity predicted by the model in Chapter 5. To build our model, we make the ansatz that for the purpose of stellar encounters, the subhalo's scale parameters are related to their initial NFW values by

$$r_s/r_s^{\text{init}} = fs^\zeta \quad \text{and} \quad \rho_s/\rho_s^{\text{init}} = gs^{-\xi}. \tag{F.19}$$

We will tune the parameters f, g, ζ, and ξ to simulations, but we enforce $3\zeta - 2\xi = 1$ to ensure $J \propto \rho_s^2 r_s^3$. For the purpose of our model, we assume that ρ_s and r_s are the parameters of the density

245

profile

$$\rho(r) = \rho_s \frac{r_s}{r} \exp\left[-\frac{1}{\alpha}\left(\frac{r}{r_s}\right)^{\alpha}\right], \quad \alpha = 0.78, \tag{F.20}$$

which Chapter 6 found to be a universal outcome of stellar encounters. We can now apply the model of Chapter 6 to find the scale parameters ρ_s' and r_s' after stellar encounters have taken place, and by integrating the density profile we find that the subhalo's final J factor is

$$J = 4.34\rho_s'^2 r_s'^3. \tag{F.21}$$

Finally, if stellar encounters would be predicted to increase J, we instead assume they have no effect.

To validate and tune our model, we carried out simulations with different stellar encounters and different subhalo orbits. The upper panel of Fig. F.5 shows the impact of different stellar encounters, while the middle panel shows different orbits. We also plot the predictions of the above model using the parameters $f = 0.875$, $g = 1.245$, $\zeta = 0.71$, and $\xi = 0.57$, and we find that it matches the simulation results reasonably well. In tuning these parameters, we aim for a trajectory closer to the simulation results for encounters at pericenter than to the results for encounters at apocenter. This preference is justified by Fig. F.6, which plots the average radius of the most disruptive stellar encounter, relative to apocenter and pericenter, for microhalos orbiting Draco in one of the EMDE scenarios studied in Sec. 7.5. This quantity is plotted as a function of radius about Draco and is averaged over microhalo orbits at that radius and over stellar encounter histories. We see that the most disruptive encounter generally occurs closer to pericenter than to apocenter.

We also simulated scenarios involving two to three stellar encounters, the results of which are shown in the lower panel of Fig. F.5. These encounters occur at intervals of five orbital periods, and each encounter injects half the energy of the previous one.[4] In order to match the predictions from the model to these results, we find it necessary to add encounter energy injections directly rather than apply the encounters consecutively. In the language of Chapter 6, we set $\lambda = \infty$; the conceptual interpretation is that a tidally evolving halo does not relax after an encounter.

---

[4]The b^{-4} scaling of energy injection with impact parameter implies that the three most disruptive encounters typically inject roughly 62%, 14%, and 6%, respectively, of the total energy injected by all encounters.
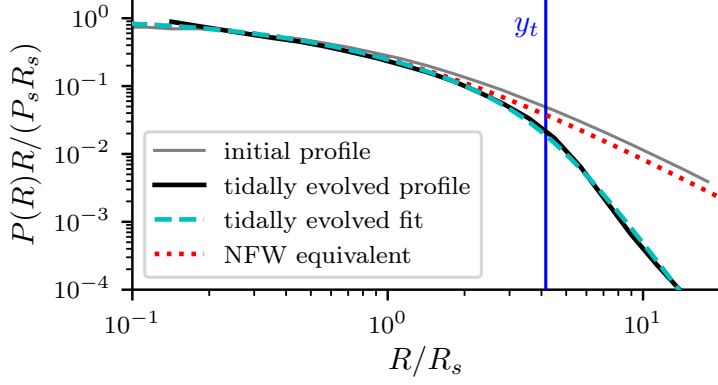
Figure F.7: Density profile $P(R)$ of a subhalo simulated by Ref. [342] after 7 Gyr of tidal evolution; the host, subhalo, and orbital properties are similar to those of the Milky Way-Draco system. The initial and final profiles in the simulation are shown as solid lines, while the dashed lines show the fit to the tidally evolved profile using Eq. (7.14). The dotted line shows the NFW profile with the same scale parameters R_s and P_s as obtained in the fit to the evolved profile; it is not a fit to the initial profile.

F.5 Draco's outer density profile

We assume Draco's density profile asymptotes to $\rho \propto r^{-1}$ at small radii as observed in halos that form in cosmological dark matter simulations [205, 260]. However, as a subhalo of the Milky Way, Draco's profile at large radii is altered by tidal forces. We assume Draco's tidally evolved density profile follows the form

$$P(R) = P_s y^{-1} (1+y)^{-2} [1 + (y/y_t)^\delta]^{-1}, \quad y \equiv R/R_s, \tag{7.14}$$

which begins to diverge from the NFW profile near the radius $y_t R_s$. To determine the parameters y_t and δ, we analyze the Dynamical Aspects of SubHaloes (DASH) library of tidal evolution simulations published by Ref. [342].

In this library, a host-subhalo system is parametrized by the host and subhalo concentration parameters c_{host} and c_{sub}, where a halo's concentration $c \equiv r_{\text{vir}}/r_s$ is the ratio between virial and scale radii, and the subhalo's relative circular orbit radius $x_c \equiv r_c/r_{\text{vir,host}}$ and circularity η.[5] These properties are determined at the time of subhalo accretion, which we assume to be roughly 10 Gyr

---

[5]See footnote 2 for definitions of r_c and η.
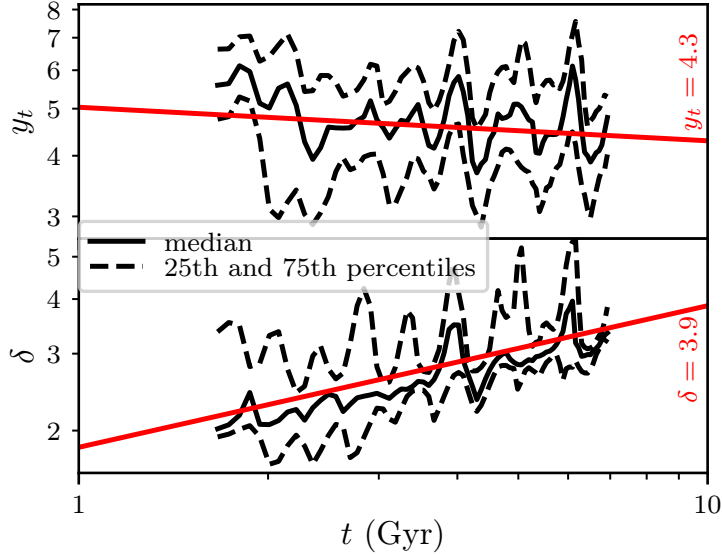
Figure F.8: Evolution of the parameters y_t (top) and δ (bottom) of the subhalo density profile given by Eq. (7.14) for tidal evolution simulations with host-subhalo parameters similar to those of the Draco-Milky Way system. The median (solid curve) and 25th and 75th percentiles (dashed curves) are plotted at each time. We extrapolate each parameter's evolution to 10 Gyr by fitting a power law (red line) to the full dataset; the extrapolated parameters at 10 Gyr are shown.

ago at redshift $z \simeq 2$.[6] Draco's scale radius $R_s = 0.435$ kpc and scale density $P_s = 1.5 \times 10^8$ $M_\odot/\text{kpc}^3$ imply that $c_{\text{sub}} \simeq 15$ at $z = 2$. Meanwhile, various Milky Way mass models place its concentration c_{host} in the range 3–7 at redshift 2 [286, 505–508]. For the same mass models, kinematic data [509, 510] put Draco on an orbit with x_c ranging from 0.7 to 1.1 at accretion and $\eta \simeq 0.8$.

To match the Milky Way-Draco system, we consider 27 DASH simulations spanning the parameter range $3.2 \leq c_{\text{host}} \leq 6.3$, $12.6 \leq c_{\text{sub}} \leq 20.0$, $0.87 \leq x_c \leq 1.15$,[7] and $\eta = 0.8$. With time units rescaled to $z = 2$, these simulations run for 7 Gyr, and in Fig. F.7 we plot the density profile of the subhalo after 7 Gyr of tidal evolution for an example set of parameters. We fit Eq. (7.14) to the evolved density profile in each simulation, generally obtaining $y_t \simeq 5$ and $\delta \simeq 3$. This fit is plotted in Fig. F.7, and to illustrate the effect of y_t and δ, we also show the NFW profile with the same R_s and P_s. Since the DASH simulations only extend to 7 Gyr, we must extrapolate the evolution of y_t and

---

[6]While c_{sub}, c_{host}, and x_c exhibit significant sensitivity to redshift z through the host and subhalo virial radii, they vary together in a way that does not alter the tidal evolution. This property is a consequence of the insensitivity of tidal evolution to the virial radii (e.g., Chapter 5). Thus, it is not necessary to precisely tune the accretion time or redshift; it only controls the duration of tidal evolution, which varies marginally for large changes in redshift.
[7]$x_c \lesssim 0.8$ at accretion is atypical [342] and is consequently not included in the DASH simulations.

δ, and we do so by fitting power laws to the evolution of these parameters over all 27 simulations. Figure F.8 shows this evolution and the power-law fits; we obtain $\delta \simeq 3.9$ and $y_t \simeq 4.3$ at 10 Gyr.

We use the tidally altered density profile determined in this section to calculate the gamma-ray flux profile from microhalos in Sec. 7.5.2. Note that with the chosen y_t and δ, the modified profile alters the determination of R_s and P_s described in Sec. 7.5 by less than 0.1%. Also, for simplicity, we do not account for tidal alteration of the profile when computing the suppression of microhalo J factors in Sec. 7.5.1. Properly accounting for the tidally evolved profile in this calculation would be complicated because the profile changes over the course of tidal evolution. Fortunately, the suppression of the annihilation rates within microhalos is already minimal at the radii at which Draco's density profile is tidally altered. Since using the modified density profile would further reduce this suppression, using the original profile is a simplification that does not significantly impact our results.

REFERENCES

[1] A. H. Guth, *Inflationary universe: A possible solution to the horizon and flatness problems*, Physical Review D **23**, 347 (1981).

[2] A. Albrecht and P. J. Steinhardt, *Cosmology for grand unified theories with radiatively induced symmetry breaking*, Physical Review Letters **48**, 1220 (1982).

[3] A. D. Linde, *A new inflationary universe scenario: a possible solution of the horizon, flatness, homogeneity, isotropy and primordial monopole problems*, Physics Letters B **108**, 389 (1982).

[4] J. E. Lidsey, A. R. Liddle, E. W. Kolb, E. J. Copeland, T. Barreiro, and M. Abney, *Reconstructing the inflaton potential—an overview*, Reviews of Modern Physics **69**, 373 (1997), arXiv:`astro-ph/9508078`.

[5] N. Aghanim, Y. Akrami, M. Ashdown, J. Aumont, C. Baccigalupi, M. Ballardini, A. Banday, R. Barreiro, N. Bartolo, S. Basak, et al. (Planck Collaboration), *Planck 2018 results. VI. Cosmological parameters*, arXiv preprint (2018), arXiv:`1807.06209`.

[6] M. Kawasaki, K. Kohri, and N. Sugiyama, *Cosmological constraints on late-time entropy production*, Physical Review Letters **82**, 4168 (1999), arXiv:`astro-ph/9811437`.

[7] M. Kawasaki, K. Kohri, and N. Sugiyama, *MeV-scale reheating temperature and thermalization of the neutrino background*, Physical Review D **62**, 023506 (2000), arXiv:`astro-ph/0002127`.

[8] S. Hannestad, *What is the lowest possible reheating temperature?*, Physical Review D **70**, 043506 (2004), arXiv:`astro-ph/0403291`.

[9] K. Ichikawa, M. Kawasaki, and F. Takahashi, *Oscillation effects on thermalization of the neutrinos in the universe with low reheating temperature*, Physical Review D **72**, 043522 (2005), arXiv:`astro-ph/0505395`.

[10] K. Ichikawa, M. Kawasaki, and F. Takahashi, *Constraint on the effective number of neutrino species from the WMAP and SDSS LRG power spectra*, Journal of Cosmology and Astroparticle Physics **05**, 007 (2007), arXiv:`astro-ph/0611784`.

[11] F. De Bernardis, L. Pagano, and A. Melchiorri, *New constraints on the reheating temperature of the universe after WMAP-5*, Astroparticle Physics **30**, 192 (2008).

[12] A. Lewis et al. (Planck Collaboration), *Planck 2015 results. XVII. Constraints on primordial non-gaussianity*, Astronomy and Astrophysics **594**, A17 (2016), arXiv:`1502.01592`.

[13] *Planck 2018 results. X. Constraints on inflation*, Astronomy and Astrophysics p. A20 (2019), arXiv:`1807.06211`.

[14] T. Abbott, F. Abdalla, A. Alarcon, J. Aleksić, S. Allam, S. Allen, A. Amara, J. Annis, J. Asorey, S. Avila, et al., *Dark Energy Survey year 1 results: Cosmological constraints from galaxy clustering and weak lensing*, Physical Review D **98**, 043526 (2018), arXiv:`1708.01530`.

[15] S. Bird, H. V. Peiris, M. Viel, and L. Verde, *Minimally parametric power spectrum reconstruction from the Lyman α forest*, Monthly Notices of the Royal Astronomical Society **413**, 1717 (2011), arXiv:`1010.1519`.

[16] P. A. R. Ade et al. (Planck Collaboration), *Planck 2015 results-XIII. Cosmological parameters*, Astronomy and Astrophysics **594**, A13 (2016), arXiv:`1502.01589`.

[17] S. Yoshiura, K. Takahashi, and T. Takahashi, *Probing small scale primordial power spectrum with 21cm line global signal* (2019), arXiv:`1911.07442`.

[18] J. B. M. noz, C. Dvorkin, and F.-Y. Cyr-Racine, *Probing the small-scale matter power spectrum with large-scale 21-cm data* (2019), arXiv:`1911.11144`.

[19] J. Chluba, A. L. Erickcek, and I. Ben-Dayan, *Probing the inflaton: Small-scale power spectrum constraints from measurements of the cosmic microwave background energy spectrum*, Astrophysical Journal **758**, 76 (2012), arXiv:`1203.2681`.

[20] C. T. Byrnes, P. S. Cole, and S. P. Patil, *Steepest growth of the power spectrum and primordial black holes*, Journal of Cosmology and Astroparticle Physics **06**, 028 (2019), arXiv:`1811.11158`.

[21] A. Kalaja, N. Bellomo, N. Bartolo, D. Bertacca, S. Matarrese, I. Musco, A. Raccanelli, and L. Verde, *From primordial black holes abundance to primordial curvature power spectrum (and back)*, Journal of Cosmology and Astroparticle Physics **10**, 031 (2019), arXiv:`1908.03596`.

[22] D. Jeong, J. Pradler, J. Chluba, and M. Kamionkowski, *Silk damping at a redshift of a billion: New limit on small-scale adiabatic perturbations*, Physical Review Letters **113**, 061301 (2014), arXiv:`1403.3697`.

[23] M. Karami, N. Afshordi, and J. Zavala, *Forward modelling of quasar light curves and the cosmological matter power spectrum on milliparsec scales* (2018), arXiv:`1805.06984`.

[24] L. Dai and J. Miralda-Escudé, *Gravitational lensing signatures of axion dark matter minihalos in highly magnified stars*, The Astronomical Journal **159**, 49 (2020), arXiv:`1908.01773`.

[25] J. A. Dror, H. Ramani, T. Trickle, and K. M. Zurek, *Pulsar timing probes of primordial black holes and subhalos*, Physical Review D **100**, 023003 (2019), arXiv:`1901.04490`.

[26] M. S. Delos, A. L. Erickcek, A. P. Bailey, and M. A. Alvarez, *Density profiles of ultracompact minihalos: Implications for constraining the primordial power spectrum*, Physical Review D **98**, 063527 (2018), arXiv:`1806.07389`.

[27] D. S. Salopek, J. R. Bond, and J. M. Bardeen, *Designing density fluctuation spectra in inflation*, Physical Review D **40**, 1753 (1989).

[28] A. A. Starobinsky, *Spectrum of adiabatic perturbations in the universe when there are singularities in the inflaton potential*, JETP lett **55**, 489 (1992).

[29] P. Ivanov, P. Naselsky, and I. Novikov, *Inflation and primordial black holes as dark matter*, Physical Review D **50**, 7173 (1994).

[30] A. A. Starobinsky, *Beyond the simplest inflationary cosmological models*, Gravitation and Cosmology **4**, 489 (1998), arXiv:`astro-ph/9811360`.

[31] M. Joy, V. Sahni, and A. A. Starobinsky, *New universal local feature in the inflationary perturbation spectrum*, Physical Review D **77**, 023514 (2008), arXiv:`0711.1585`.

[32] G. A. Palma, *Untangling features in the primordial spectra*, Journal of Cosmology and Astroparticle Physics **04**, 035 (2015), arXiv:`1412.5615`.

[33] Y.-F. Cai, E. G. M. Ferreira, B. Hu, and J. Quintin, *Searching for features of a string-inspired inflationary model with cosmological observations*, Physical Review D **92**, 121303 (2015), arXiv:`1507.05619`.

[34] A. G. Cadavid, A. E. Romano, and S. Gariazzo, *Effects of local features of the inflaton potential on the spectrum and bispectrum of primordial perturbations*, European Physical Journal C **76**, 385 (2016), arXiv:`1508.05687`.

[35] A. G. Cadavid, A. E. Romano, and S. Gariazzo, *CMB anomalies and the effects of local features of the inflaton potential*, European Physical Journal C **77**, 242 (2017), arXiv:`1612.03490`.

[36] A. Gallego Cadavid, *Features in single field slow-roll inflation*, Journal of Physics: Conference Series **831**, 012003 (2017), arXiv:`1703.04375`.

[37] G. Domènech and M. Kamionkowski, *Lensing anomaly and oscillations in the primordial power spectrum*, Journal of Cosmology and Astroparticle Physics **11**, 040 (2019), arXiv:`1905.04323`.

[38] J. Silk and M. S. Turner, *Double inflation*, Physical Review D **35**, 419 (1987).

[39] D. Polarski and A. A. Starobinsky, *Spectra of perturbations produced by double inflation with an intermediate matter-dominated stage*, Nuclear Physics **B385**, 623 (1992).

[40] J. A. Adams, G. G. Ross, and S. Sarkar, *Multiple inflation*, Nuclear Physics **B503**, 405 (1997), arXiv:`hep-ph/9704286`.

[41] L. A. Kofman and D. Y. Pogosyan, *Nonflat perturbations in inflationary cosmology*, Physics Letters B **214**, 508 (1988).

[42] X. Chen and Y. Wang, *Quasi-single field inflation with large mass*, Journal of Cosmology and Astroparticle Physics **09**, 021 (2012), arXiv:`1205.0160`.

[43] X. Chen and Y. Wang, *Anomalous high energy dependence in inflationary density perturbations* (2012), arXiv:`1207.0100`.

[44] A. Achúcarro, J.-O. Gong, S. Hardeman, G. A. Palma, and S. P. Patil, *Effective theories of single field inflation when heavy fields matter*, Journal of High Energy Physics **5**, 66 (2012), arXiv:`1201.6342`.

[45] R. Saito, M. Nakashima, Y.-i. Takamizu, and J. Yokoyama, *Resonant signatures of heavy scalar fields in the cosmic microwave background*, Journal of Cosmology and Astroparticle Physics **11**, 036 (2012), arXiv:`1206.2164`.

[46] G. A. Palma and A. Soto, *B modes and the sound speed of primordial fluctuations*, Physical Review D **91**, 063525 (2015), arXiv:`1412.0033`.

[47] Q.-G. Huang and S. Pi, *Power-law modulation of the scalar power spectrum from a heavy field with a monomial potential*, Journal of Cosmology and Astroparticle Physics **04**, 001 (2018), arXiv:`1610.00115`.

[48] N. Bolis, T. Fujita, S. Mizuno, and S. Mukohyama, *Quantum entanglement in multi-field inflation*, Journal of Cosmology and Astroparticle Physics **09**, 004 (2018), arXiv:`1805.09448`.

[49] D. J. H. Chung, E. W. Kolb, A. Riotto, and I. I. Tkachev, *Probing Planckian physics: Resonant production of particles during inflation and features in the primordial power spectrum*, Physical Review D **62**, 043508 (2000), arXiv:`hep-ph/9910437`.

[50] A. Ashoorioon, A. Krause, and K. Turzynski, *Energy transfer in multi field inflation and cosmological perturbations*, Journal of Cosmology and Astroparticle Physics **02**, 014 (2009), arXiv:`0810.4660`.

[51] N. Barnaby and Z. Huang, *Particle production during inflation: observational constraints and signatures*, Physical Review D **80**, 126018 (2009), arXiv:0909.0751.

[52] N. Barnaby, *Features and non-gaussianity from inflationary particle production*, Physical Review D **82**, 106009 (2010), arXiv:1006.4615.

[53] A. Achúcarro, J.-O. Gong, S. Hardeman, G. A. Palma, and S. P. Patil, *Features of heavy physics in the CMB power spectrum*, Journal of Cosmology and Astroparticle Physics **01**, 030 (2011), arXiv:1010.3693.

[54] G. Shiu and J. Xu, *Effective field theory and decoupling in multi-field inflation: An illustrative case study*, Physical Review D **84**, 103509 (2011), arXiv:1108.0981.

[55] A. Avgoustidis, S. Cremonini, A.-C. Davis, R. H. Ribeiro, K. Turzyński, and S. Watson, *The importance of slow-roll corrections during multi-field inflation*, Journal of Cosmology and Astroparticle Physics **02**, 038 (2012), arXiv:1110.4081.

[56] S. Cespedes, V. Atal, and G. A. Palma, *On the importance of heavy fields during inflation*, Journal of Cosmology and Astroparticle Physics **05**, 008 (2012), arXiv:1201.4848.

[57] X. Gao, D. Langlois, and S. Mizuno, *Influence of heavy modes on perturbations in multiple field inflation*, Journal of Cosmology and Astroparticle Physics **10**, 040 (2012), arXiv:1205.5275.

[58] L. McAllister, S. Renaux-Petel, and G. Xu, *A statistical approach to multifield inflation: many-field perturbations beyond slow roll*, Journal of Cosmology and Astroparticle Physics **10**, 046 (2012), arXiv:1207.0317.

[59] S. Pi and M. Sasaki, *Curvature perturbation spectrum in two-field inflation with a turning trajectory*, Journal of Cosmology and Astroparticle Physics **10**, 051 (2012), arXiv:1205.0161.

[60] X. Gao, D. Langlois, and S. Mizuno, *Oscillatory features in the curvature power spectrum after a sudden turn of the inflationary trajectory*, Journal of Cosmology and Astroparticle Physics **10**, 023 (2013), arXiv:1306.5680.

[61] T. Noumi, M. Yamaguchi, and D. Yokoyama, *Effective field theory approach to quasi-single field inflation and effects of heavy fields*, Journal of High Energy Physics **6**, 51 (2013), arXiv:1211.1624.

[62] T. Noumi and M. Yamaguchi, *Primordial spectra from sudden turning trajectory*, Journal of Cosmology and Astroparticle Physics **12**, 038 (2013), arXiv:1307.7110.

[63] M. Konieczka, R. H. Ribeiro, and K. Turzyński, *The effects of a fast-turning trajectory in multiple-field inflation*, Journal of Cosmology and Astroparticle Physics **07**, 030 (2014), arXiv:1401.6163.

[64] S. Mizuno, R. Saito, and D. Langlois, *Combined features in the primordial spectra induced by a sudden turn in two-field dbi inflation*, Journal of Cosmology and Astroparticle Physics **11**, 032 (2014), arXiv:1405.4257.

[65] X. Gao and J.-O. Gong, *Towards general patterns of features in multi-field inflation*, Journal of High Energy Physics **8**, 115 (2015), arXiv:1506.08894.

[66] K.-i. Maeda, S. Mizuno, and R. Tozuka, *α-attractor-type double inflation*, Physical Review D **98**, 123530 (2018), arXiv:1810.06914.

[67] S. Pi, Y.-l. Zhang, Q.-G. Huang, and M. Sasaki, *Scalaron from R^2-gravity as a heavy field*, Journal of Cosmology and Astroparticle Physics **05**, 042 (2018), arXiv:`1712.09896`.

[68] S. Garcia-Saenz, S. Renaux-Petel, and J. Ronayne, *Primordial fluctuations and non-gaussianities in sidetracked inflation*, Journal of Cosmology and Astroparticle Physics **07**, 057 (2018), arXiv:`1804.11279`.

[69] N. Barnaby and M. Peloso, *Large non-gaussianity in axion inflation*, Physical Review Letters **106**, 181301 (2011), arXiv:`1011.1500`.

[70] N. Barnaby, E. Pajer, and M. Peloso, *Gauge field production in axion inflation: Consequences for monodromy, non-gaussianity in the CMB, and gravitational waves at interferometers*, Physical Review D **85**, 023525 (2012), arXiv:`1110.3327`.

[71] L. Covi and D. H. Lyth, *Running-mass models of inflation and their observational constraints*, Physical Review D **59**, 063515 (1999), arXiv:`hep-ph/9809562`.

[72] L. Covi, D. H. Lyth, and L. Roszkowski, *Observational constraints on an inflation model with a running mass*, Physical Review D **60**, 023509 (1999), arXiv:`hep-ph/9809310`.

[73] L. Randall, M. Soljačić, and A. H. Guth, *Supernatural inflation: inflation from supersymmetry with no (very) small parameters*, Nuclear Physics **B472**, 377 (1996), arXiv:`hep-ph/9512439`.

[74] J.-O. Gong and M. Sasaki, *Waterfall field in hybrid inflation and curvature perturbation*, Journal of Cosmology and Astroparticle Physics **03**, 028 (2011), arXiv:`1010.3405`.

[75] D. H. Lyth, *Contribution of the hybrid inflation waterfall to the primordial curvature perturbation1*, Journal of Cosmology and Astroparticle Physics **07**, 035 (2011), arXiv:`1012.4617`.

[76] E. Bugaev and P. Klimai, *Curvature perturbation spectra from waterfall transition, black hole constraints and non-gaussianity*, Journal of Cosmology and Astroparticle Physics **11**, 028 (2011), arXiv:`1107.3754`.

[77] E. J. Copeland, A. R. Liddle, J. E. Lidsey, and D. Wands, *Black holes and gravitational waves in string cosmology*, Physical Review D **58**, 063508 (1998), arXiv:`gr-qc/9803070`.

[78] J. Martin, A. Riazuelo, and M. Sakellariadou, *Nonvacuum initial states for cosmological perturbations of quantum-mechanical origin*, Physical Review D **61**, 083518 (2000), arXiv:`astro-ph/9904167`.

[79] J. Martin and R. H. Brandenberger, *Trans-Planckian problem of inflationary cosmology*, Physical Review D **63**, 123501 (2001), arXiv:`hep-th/0005209`.

[80] E. D. Stewart, *Flattening the inflaton's potential with quantum corrections. II*, Physical Review D **56**, 2019 (1997), arXiv:`hep-ph/9703232`.

[81] I. Ben-Dayan and R. Brustein, *Cosmic microwave background observables of small field models of inflation*, Journal of Cosmology and Astroparticle Physics **09**, 007 (2010), arXiv:`0907.2384`.

[82] C. van de Bruck and M. Robinson, *Power spectra beyond the slow roll approximation in theories with non-canonical kinetic terms*, Journal of Cosmology and Astroparticle Physics **08**, 024 (2014), arXiv:`1404.7806`.

[83] S. Gariazzo, O. Mena, H. Ramirez, and L. Boubekeur, *Primordial power spectrum features in phenomenological descriptions of inflation* (2016), arXiv:`1606.00842`.

[84] Y.-S. Piao and E. Zhou, *Nearly scale-invariant spectrum of adiabatic fluctuations may be from a very slowly expanding phase of the universe*, Physical Review D **68**, 083515 (2003), arXiv:`hep-th/0308080`.

[85] S. Gratton, J. Khoury, P. J. Steinhardt, and N. Turok, *Conditions for generating scale-invariant density perturbations*, Physical Review D **69**, 103505 (2004), arXiv:`astro-ph/0301395`.

[86] L. E. Allen and D. Wands, *Cosmological perturbations through a simple bounce*, Physical Review D **70**, 063515 (2004), arXiv:`astro-ph/0404441`.

[87] Y.-S. Piao and Y.-Z. Zhang, *Primordial perturbation spectra from various expanding and contracting phases before the "bounce"*, Physical Review D **70**, 043516 (2004), arXiv:`astro-ph/0403671`.

[88] Y.-S. Piao, *Scalar perturbation spectra in an emergent cosmological island*, Physical Review D **74**, 043509 (2006), arXiv:`gr-qc/0512161`.

[89] Y.-S. Piao, *Primordial perturbations during a slow expansion*, Physical Review D **76**, 083505 (2007), arXiv:`0706.0981`.

[90] D. Wands, *Cosmological perturbations through the big bang* (2008), arXiv:`0809.4556`.

[91] J. Magueijo and J. Noller, *Primordial fluctuations without scalar fields*, Physical Review D **81**, 043509 (2010), arXiv:`0907.1772`.

[92] J.-L. Lehners and P. J. Steinhardt, *Dynamical selection of the primordial density fluctuation amplitude*, Physical Review Letters **106**, 081301 (2011), arXiv:`1008.4567`.

[93] J. Khoury and P. J. Steinhardt, *Generating scale-invariant perturbations from rapidly-evolving equation of state*, Physical Review D **83**, 123502 (2011), arXiv:`1101.3548`.

[94] A. Joyce and J. Khoury, *Scale invariance via a phase of slow expansion*, Physical Review D **84**, 023508 (2011), arXiv:`1104.4347`.

[95] T. Qiu, *Reconstruction of a nonminimal coupling theory with scale-invariant power spectrum*, Journal of Cosmology and Astroparticle Physics **06**, 041 (2012), arXiv:`1204.0189`.

[96] D. Bessada and W. H. Kinney, *Attractor solutions in tachyacoustic cosmology*, Physical Review D **86**, 083502 (2012), arXiv:`1206.2711`.

[97] R. H. Brandenberger, *The matter bounce alternative to inflationary cosmology* (2012), arXiv:`1206.4196`.

[98] O. Dreyer, *The world is discrete* (2013), arXiv:`1307.6169`.

[99] Y.-F. Cai, E. McDonough, F. Duplessis, and R. H. Brandenberger, *Two field matter bounce cosmology*, Journal of Cosmology and Astroparticle Physics **10**, 024 (2013), arXiv:`1305.5259`.

[100] C. Li and Y.-K. E. Cheung, *The scale invariant power spectrum of the primordial curvature perturbations from the coupled scalar tachyon bounce cosmos*, Journal of Cosmology and Astroparticle Physics **07**, 008 (2014), arXiv:`1401.0094`.

[101] S. Alexander, C. Bambi, A. Marcianò, and L. Modesto, *Fermi-bounce cosmology and scale-invariant power spectrum*, Physical Review D **90**, 123510 (2014), arXiv:`1402.5880`.

255

[102] M. Libanov, V. Rubakov, and G. Rubtsov, *Towards conformal cosmology*, JETP Letters **102**, 561 (2015), arXiv:`1508.07728`.

[103] A. Ijjas and P. J. Steinhardt, *The anamorphic universe*, Journal of Cosmology and Astroparticle Physics **10**, 001 (2015), arXiv:`1507.03875`.

[104] B. Vlahovic, M. Eingorn, and C. Ilie, *Uniformity of cosmic microwave background as a non-inflationary geometrical effect*, Modern Physics Letters A **30**, 1530026 (2015), arXiv:`1511.00369`.

[105] R. H. Brandenberger, *String gas cosmology after Planck*, Classical and Quantum Gravity **32**, 234002 (2015), arXiv:`1505.02381`.

[106] D. Battefeld and P. Peter, *A critical review of classical bouncing cosmologies*, Physics Reports **571**, 1 (2015), arXiv:`1406.2790`.

[107] F. Melia, *Cosmological perturbations without inflation*, Classical and Quantum Gravity **34**, 015011 (2016), arXiv:`1606.09565`.

[108] A. Ijjas and P. J. Steinhardt, *Bouncing cosmology made simple*, Classical and Quantum Gravity **35**, 135004 (2018), arXiv:`1803.01961`.

[109] Y.-K. E. Cheung, X. Song, S. Li, Y. Li, and Y. Zhu, *The CST bounce universe model — a parametric study*, Science China Physics, Mechanics & Astronomy **62**, 10011 (2018), arXiv:`1601.03807`.

[110] H. Hamber, *Gravitational fluctuations as an alternative to inflation*, Universe **5**, 31 (2019), arXiv:`1807.10704`.

[111] H. W. Hamber and L. H. S. Yu, *Gravitational fluctuations as an alternative to inflation II. CMB angular power spectrum*, Universe **5**, 216 (2019), arXiv:`1910.02990`.

[112] Y. Wang and M. Zhu, *Quantum creation of a toy universe without inflation* (2019), arXiv:`1908.10517`.

[113] J. Khoury, B. A. Ovrut, P. J. Steinhardt, and N. Turok, *Ekpyrotic universe: Colliding branes and the origin of the hot big bang*, Physical Review D **64**, 123522 (2001), arXiv:`hep-th/0103239`.

[114] P. J. Steinhardt, *A cyclic model of the universe*, Science **296**, 1436 (2002), arXiv:`hep-th/0111030`.

[115] P. J. Steinhardt and N. Turok, *The cyclic universe: An informal introduction*, Nuclear Physics B Proceedings Supplements **124**, 38 (2003), arXiv:`astro-ph/0204479`.

[116] J. Khoury, P. J. Steinhardt, and N. Turok, *Inflation versus cyclic predictions for spectral tilt*, Physical Review Letters **91**, 161301 (2003), arXiv:`astro-ph/0302012`.

[117] P. J. Steinhardt and N. Turok, *The cyclic model simplified*, New Astronomy Reviews **49**, 43 (2005), arXiv:`astro-ph/0404480`.

[118] J. K. Erickson, S. Gratton, P. J. Steinhardt, and N. Turok, *Cosmic perturbations through the cyclic ages*, Physical Review D **75**, 123507 (2007), arXiv:`hep-th/0607164`.

[119] J.-L. Lehners, P. McFadden, N. Turok, and P. J. Steinhardt, *Generating ekpyrotic curvature perturbations before the big bang*, Physical Review D **76**, 103501 (2007), arXiv:`hep-th/0702153`.

[120] E. I. Buchbinder, J. Khoury, and B. A. Ovrut, *New ekpyrotic cosmology*, Physical Review D **76**, 123503 (2007), arXiv:`hep-th/0702154`.

[121] J.-L. Lehners, *Ekpyrotic and cyclic cosmology*, Physics Reports **465**, 223 (2008), arXiv:`0806.1245`.

[122] J.-L. Lehners, P. J. Steinhardt, and N. Turok, *The return of the phoenix universe*, International Journal of Modern Physics D **18**, 2231 (2009), arXiv:`0910.0834`.

[123] J. Khoury and P. J. Steinhardt, *Adiabatic ekpyrosis: Scale-invariant curvature perturbations from a single scalar field in a contracting universe*, Physical Review Letters **104**, 091301 (2010), arXiv:`0910.2230`.

[124] Y.-S. Piao, *Design of a cyclic multiverse*, Physics Letters B **691**, 225 (2010), arXiv:`1001.0631`.

[125] J.-L. Lehners and P. J. Steinhardt, *Planck 2013 results support the cyclic universe*, Physical Review D **87**, 123533 (2013), arXiv:`1304.3122`.

[126] A. Ijjas, P. J. Steinhardt, and A. Loeb, *Inflationary paradigm in trouble after Planck2013*, Physics Letters B **723**, 261 (2013), arXiv:`1304.2785`.

[127] E. Wilson-Ewing, *Ekpyrotic loop quantum cosmology*, Journal of Cosmology and Astroparticle Physics **08**, 015 (2013), arXiv:`1306.6582`.

[128] C. Gao, Y. Lu, and Y.-G. Shen, *Cyclic universe due to phantom and quintessence*, General Relativity and Gravitation **46**, 1791 (2014), arXiv:`1402.3863`.

[129] A. Ijjas, P. J. Steinhardt, and A. Loeb, *Scale-free primordial cosmology*, Physical Review D **89**, 023525 (2014), arXiv:`1309.4480`.

[130] A. Ijjas, J.-L. Lehners, and P. J. Steinhardt, *General mechanism for producing scale-invariant perturbations and small non-gaussianity in ekpyrotic models*, Physical Review D **89**, 123520 (2014), arXiv:`1404.1265`.

[131] A. Fertig, J.-L. Lehners, and E. Mallwitz, *Ekpyrotic perturbations with small non-gaussian corrections*, Physical Review D **89**, 103537 (2014), arXiv:`1310.8133`.

[132] A. M. Levy, A. Ijjas, and P. J. Steinhardt, *Scale-invariant perturbations in ekpyrotic cosmologies without fine-tuning of initial conditions*, Physical Review D **92**, 063524 (2015), arXiv:`1506.01011`.

[133] E. Gould and N. Afshordi, *Does history repeat itself? Periodic time cosmology*, Journal of Cosmology and Astroparticle Physics **09**, 058 (2019), arXiv:`1903.09694`.

[134] A. Ijjas and P. J. Steinhardt, *A new kind of cyclic universe*, Physics Letters B **795**, 666 (2019), arXiv:`1904.08022`.

[135] R. Brandenberger and Z. Wang, *Nonsingular ekpyrotic cosmology with a nearly scale-invariant spectrum of cosmological perturbations and gravitational waves* (2020), arXiv:`2001.00638`.

[136] A. R. Liddle, *The inflationary energy scale*, Physical Review D **49**, 739 (1994), arXiv:`astro-ph/9307020`.

[137] Z.-K. Guo, D. J. Schwarz, and Y.-Z. Zhang, *Observational constraints on the energy scale of inflation*, Physical Review D **83**, 083522 (2011), arXiv:`1008.5258`.

[138] A. M. Sirunyan, A. Tumasyan, W. Adam, F. Ambrogi, E. Asilar, T. Bergauer, J. Brandstetter, M. Dragicevic, J. Erö, A. Escalante Del Valle, et al. (CMS Collaboration), *Search for dark matter particles produced in association with a top quark pair at $\sqrt{s} = 13$ TeV*, Physical Review Letters **122**, 011803 (2019), arXiv:1807.06522.

[139] A. M. Sirunyan, A. Tumasyan, W. Adam, F. Ambrogi, E. Asilar, T. Bergauer, J. Brandstetter, E. Brondolin, M. Dragicevic, et al. (CMS Collaboration), *Search for narrow and broad dijet resonances in proton-proton collisions at $\sqrt{s} = 13$ TeV and constraints on dark matter mediators and other new particles*, Journal of High Energy Physics **8**, 130 (2018), arXiv:1806.00843.

[140] A. M. Sirunyan, A. Tumasyan, W. Adam, F. Ambrogi, E. Asilar, T. Bergauer, J. Brandstetter, M. Dragicevic, J. Erö, et al. (CMS Collaboration), *Search for dark matter produced in association with a Higgs boson decaying to $\gamma\gamma$ or $\tau^+\tau^-$ at $\sqrt{s} = 13$ TeV*, Journal of High Energy Physics **9**, 46 (2018), arXiv:1806.04771.

[141] A. M. Sirunyan, A. Tumasyan, W. Adam, F. Ambrogi, E. Asilar, T. Bergauer, J. Brandstetter, E. Brondolin, M. Dragicevic, et al. (CMS Collaboration), *Search for new physics in dijet angular distributions using proton-proton collisions at $\sqrt{s} = 13$ TeV and constraints on dark matter and other models*, The European Physical Journal C **78**, 789 (2018), arXiv:1803.08030.

[142] A. M. Sirunyan, A. Tumasyan, W. Adam, F. Ambrogi, E. Asilar, T. Bergauer, J. Brandstetter, E. Brondolin, M. Dragicevic, et al. (CMS Collaboration), *Search for dark matter in events with energetic, hadronically decaying top quarks and missing transverse momentum at $\sqrt{s} = 13$ TeV*, Journal of High Energy Physics **6**, 27 (2018), arXiv:1801.08427.

[143] A. M. Sirunyan, A. Tumasyan, W. Adam, F. Ambrogi, E. Asilar, T. Bergauer, J. Brandstetter, E. Brondolin, M. Dragicevic, J. Erö, et al. (CMS Collaboration), *Search for top squarks and dark matter particles in opposite-charge dilepton final states at $\sqrt{s} = 13$ TeV*, Physical Review D **97**, 032009 (2018), arXiv:1711.00752.

[144] M. Aaboud, G. Aad, B. Abbott, O. Abdinov, B. Abeloos, S. Abidi, O. AbouZeid, N. Abraham, H. Abramowicz, H. Abreu, et al. (ATLAS Collaboration), *Search for an invisibly decaying Higgs boson or dark matter candidates produced in association with a Z boson in pp collisions at $\sqrt{s} = 13$ TeV with the ATLAS detector*, Physics Letters B **776**, 318–337 (2018), arXiv:1708.09624.

[145] M. A. Amin, M. P. Hertzberg, D. I. Kaiser, and J. Karouby, *Nonperturbative dynamics of reheating after inflation: A review*, International Journal of Modern Physics D **24**, 1530003 (2015), arXiv:1410.3808.

[146] M. Pospelov, A. Ritz, and M. Voloshin, *Secluded WIMP dark matter*, Physics Letters B **662**, 53 (2008), arXiv:0711.4866.

[147] N. Arkani-Hamed, D. P. Finkbeiner, T. R. Slatyer, and N. Weiner, *A theory of dark matter*, Physical Review D **79**, 015014 (2009), arXiv:0810.0713.

[148] D. Hooper, N. Weiner, and W. Xue, *Dark forces and light dark matter*, Physical Review D **86**, 056009 (2012), arXiv:1206.2929.

[149] M. Abdullah, A. DiFranzo, A. Rajaraman, T. M. P. Tait, P. Tanedo, and A. M. Wijangco, *Hidden on-shell mediators for the Galactic Center γ-ray excess*, Physical Review D **90**, 035004 (2014), arXiv:1404.6528.

[150] A. Berlin, P. Gratia, D. Hooper, and S. D. McDermott, *Hidden sector dark matter models for the Galactic Center gamma-ray excess*, Physical Review D **90**, 015032 (2014), arXiv:1405.5204.

[151] A. Martin, J. Shelton, and J. Unwin, *Fitting the Galactic Center gamma-ray excess with cascade annihilations*, Physical Review D **90**, 103513 (2014), arXiv:1405.0272.

[152] Y. Zhang, *Long-lived light mediator to dark matter and primordial small scale spectrum*, Journal of Cosmology and Astroparticle Physics **05**, 008 (2015), arXiv:1502.06983.

[153] A. Berlin, D. Hooper, and G. Krnjaic, *PeV-scale dark matter as a thermal relic of a decoupled sector*, Physics Letters B **760**, 106 (2016), arXiv:1602.08490.

[154] A. Berlin, D. Hooper, and G. Krnjaic, *Thermal dark matter from a highly decoupled sector*, Physical Review D **94**, 095019 (2016), arXiv:1609.02555.

[155] J. A. Dror, E. Kuflik, and W. H. Ng, *Codecaying dark matter*, Physical Review Letters **117**, 211801 (2016), arXiv:1607.03110.

[156] T. Tenkanen and V. Vaskonen, *Reheating the Standard Model from a hidden sector*, Physical Review D **94**, 083516 (2016), arXiv:1606.00192.

[157] J. A. Dror, E. Kuflik, B. Melcher, and S. Watson, *Concentrated dark matter: Enhanced small-scale structure from codecaying dark matter*, Physical Review D **97**, 063524 (2018), arXiv:1711.04773.

[158] T. Tenkanen, *Standard model higgs field and hidden sector cosmology*, Physical Review D **100**, 083515 (2019), arXiv:1905.11737.

[159] G. D. Coughlan, W. Fischler, E. W. Kolb, S. Raby, and G. G. Ross, *Cosmological problems for the polonyi potential*, Physics Letters B **131**, 59 (1983).

[160] B. De Carlos, J. A. Casas, F. Quevedo, and E. Roulet, *Model-independent properties and cosmological implications of the dilaton and moduli sectors of 4D strings*, Physics Letters B **318**, 447 (1993), arXiv:hep-ph/9308325.

[161] T. Banks, D. B. Kaplan, and A. E. Nelson, *Cosmological implications of dynamical supersymmetry breaking*, Physical Review D **49**, 779 (1994), arXiv:hep-ph/9308292.

[162] T. Banks, M. Berkooz, and P. J. Steinhardt, *Cosmological moduli problem, supersymmetry breaking, and stability in postinflationary cosmology*, Physical Review D **52**, 705 (1995), arXiv:hep-th/9501053.

[163] T. Banks, M. Berkooz, S. H. Shenker, G. Moore, and P. J. Steinhardt, *Modular cosmology*, Physical Review D **52**, 3548 (1995), arXiv:hep-th/9503114.

[164] B. S. Acharya, G. Kane, and E. Kuflik, *Bounds on scalar masses in theories of moduli stabilization*, International Journal of Modern Physics A **29**, 1450073 (2014), arXiv:1006.3272.

[165] G. Kane, K. Sinha, and S. Watson, *Cosmological moduli and the post-inflationary universe: A critical review*, International Journal of Modern Physics D **24**, 1530022 (2015), arXiv:1502.07746.

[166] J. T. Giblin, G. Kane, E. Nesbit, S. Watson, and Y. Zhao, *Was the universe actually radiation dominated prior to nucleosynthesis?*, Physical Review D **96**, 043525 (2017), arXiv:1706.08536.

[167] S. Mollerach, *Isocurvature baryon perturbations and inflation*, Physical Review D **42**, 313 (1990).

[168] A. Linde and V. Mukhanov, *Non-gaussian isocurvature perturbations from inflation*, Physical Review D **56**, 535(R) (1997), arXiv:`astro-ph/9610219`.

[169] D. H. Lyth and D. Wands, *Generating the curvature perturbation without an inflaton*, Physics Letters B **524**, 5 (2002), arXiv:`hep-ph/0110002`.

[170] T. Moroi and T. Takahashi, *Effects of cosmological moduli fields on cosmic microwave background*, Physics Letters B **522**, 215 (2001), erratum: 539, 303 (2002), arXiv:`hep-ph/0110096`.

[171] A. Albrecht, P. J. Steinhardt, M. S. Turner, and F. Wilczek, *Reheating an inflationary universe*, Physical Review Letters **48**, 1437 (1982).

[172] M. S. Turner, *Coherent scalar-field oscillations in an expanding universe*, Physical Review D **28**, 1243 (1983).

[173] J. H. Traschen and R. H. Brandenberger, *Particle production during out-of-equilibrium phase transitions*, Physical Review D **42**, 2491 (1990).

[174] L. Kofman, A. Linde, and A. A. Starobinsky, *Reheating after inflation*, Physical Review Letters **73**, 3195 (1994), arXiv:`hep-th/9405187`.

[175] L. Kofman, A. Linde, and A. A. Starobinsky, *Towards the theory of reheating after inflation*, Physical Review D **56**, 3258 (1997), arXiv:`hep-ph/9704452`.

[176] J. F. Dufaux, G. N. Felder, L. Kofman, M. Peloso, and D. Podolsky, *Preheating with trilinear interactions: Tachyonic resonance*, Journal of Cosmology and Astroparticle Physics **07**, 006 (2006), arXiv:`hep-ph/0602144`.

[177] R. Allahverdi, R. Brandenberger, F.-Y. Cyr-Racine, and A. Mazumdar, *Reheating in inflationary cosmology: theory and applications*, Annual Review of Nuclear and Particle Science **60**, 27 (2010), arXiv:`1001.2600`.

[178] K. Jedamzik, M. Lemoine, and J. Martin, *Collapse of small-scale density perturbations during preheating in single field inflation*, Journal of Cosmology and Astroparticle Physics **09**, 034 (2010), arXiv:`1002.3039`.

[179] R. Easther, R. Flauger, and J. B. Gilmore, *Delayed reheating and the breakdown of coherent oscillations*, Journal of Cosmology and Astroparticle Physics **04**, 027 (2011), arXiv:`1003.3011`.

[180] N. Musoke, S. Hotchkiss, and R. Easther, *Lighting the dark: The evolution of the post-inflationary universe* (2019), arXiv:`1909.11678`.

[181] A. L. Erickcek and K. Sigurdson, *Reheating effects in the matter power spectrum and implications for substructure*, Physical Review D **84**, 083503 (2011), arXiv:`1106.0536`.

[182] G. Barenboim and J. Rasero, *Structure formation during an early period of matter domination*, Journal of High Energy Physics **04**, 138 (2014), arXiv:`1311.4034`.

[183] J. J. Fan, O. Ö.zsoy, and S. Watson, *Nonthermal histories and implications for structure formation*, Physical Review D **90**, 043536 (2014), arXiv:`1405.7373`.

[184] B. Spokoiny, *Deflationary universe scenario*, Physics Letters B **315**, 40 (1993), arXiv:`gr-qc/9306008`.

[185] M. Joyce, *Electroweak baryogenesis and the expansion rate of the universe*, Physical Review D **55**, 1875 (1997), arXiv:`hep-ph/9606223`.

[186] P. G. Ferreira and M. Joyce, *Cosmology with a primordial scaling field*, Physical Review D **58**, 023503 (1998), arXiv:`astro-ph/9711102`.

[187] P. J. E. Peebles and A. Vilenkin, *Quintessential inflation*, Physical Review D **59**, 063505 (1999), arXiv:`astro-ph/9810509`.

[188] K. Dimopoulos and J. Valle, *Modeling quintessential inflation*, Astroparticle Physics **18**, 287 (2002), arXiv:`astro-ph/0111417`.

[189] K. Dimopoulos, *Curvaton hypothesis and the η problem of quintessential inflation, with and without branes*, Physical Review D **68**, 123506 (2003), arXiv:`astro-ph/0212264`.

[190] D. J. Chung, L. L. Everett, K. Kong, and K. T. Matchev, *Connecting LHC, ILC, and quintessence*, Journal of High Energy Physics **10**, 016 (2007), arXiv:`0706.2375`.

[191] K. Redmond, A. Trezza, and A. L. Erickcek, *Growth of dark matter perturbations during kination*, Physical Review D **98**, 063504 (2018), arXiv:`1807.01327`.

[192] F. Zwicky, *Die rotverschiebung von extragalaktischen nebeln*, Helvetica physica acta **6**, 110 (1933).

[193] D. Clowe, A. Gonzalez, and M. Markevitch, *Weak-lensing mass reconstruction of the interacting cluster 1e 0657–558: Direct evidence for the existence of dark matter*, Astrophysical Journal **604**, 596 (2004), arXiv:`astro-ph/0312273`.

[194] C. S. Frenk and S. D. M. White, *Dark matter and cosmic structure*, Annalen der Physik **524**, 507 (2012), arXiv:`1210.0544`.

[195] G. Bertone and T. M. P. Tait, *A new era in the search for dark matter*, Nature **562**, 51 (2018), arXiv:`1810.01668`.

[196] J. L. Feng, *Dark matter candidates from particle physics and methods of detection*, Annual Review of Astronomy and Astrophysics **48**, 495 (2010), arXiv:`1003.0904`.

[197] G. Bertone, *Particle Dark Matter: Observations, Models and Searches* (Cambridge University Press, Cambridge, England, 2010).

[198] G. Bertone, D. Hooper, and J. Silk, *Particle dark matter: Evidence, candidates and constraints*, Physics Reports **405**, 279 (2005), arXiv:`hep-ph/0404175`.

[199] L. Bergström, *Non-baryonic dark matter: observational evidence and detection methods*, Reports on Progress in Physics **63**, 793 (2000), arXiv:`hep-ph/0002126`.

[200] D. Erkal and V. Belokurov, *Forensics of subhalo–stream encounters: the three phases of gap growth*, Monthly Notices of the Royal Astronomical Society **450**, 1136 (2015), arXiv:`1412.6035`.

[201] D. Erkal, V. Belokurov, J. Bovy, and J. L. Sanders, *The number and size of subhalo-induced gaps in stellar streams*, Monthly Notices of the Royal Astronomical Society **463**, 102 (2016), arXiv:`1606.04946`.

[202] M. Ricotti and A. Gould, *A new probe of dark matter and high-energy universe using microlensing*, Astrophysical Journal **707**, 979 (2009), arXiv:`0908.0735`.

[203] E. Bertschinger, *Self-similar secondary infall and accretion in an einstein-de sitter universe*, Astrophysical Journal Supplement Series **58**, 39 (1985).

[204] G. Aslanyan, L. C. Price, J. Adams, T. Bringmann, H. A. Clark, R. Easther, G. F. Lewis, and P. Scott, *Ultracompact minihalos as probes of inflationary cosmology*, Physical Review Letters **117**, 141102 (2016), arXiv:`1512.04597`.

[205] J. F. Navarro, C. S. Frenk, and S. D. M. White, *A universal density profile from hierarchical clustering*, Astrophysical Journal **490**, 493 (1997), arXiv:`astro-ph/9611107`.

[206] C. Blanco, M. S. Delos, A. L. Erickcek, and D. Hooper, *Annihilation signatures of hidden sector dark matter within early-forming microhalos*, Physical Review D **100**, 103010 (2019), arXiv:`1906.00010`.

[207] J. Wang, S. Bose, C. S. Frenk, L. Gao, A. Jenkins, V. Springel, and S. D. M. White, *Universality in the structure of dark matter haloes over twenty orders of magnitude in halo mass* (2019), arXiv:`1911.09720`.

[208] G. Steigman, B. Dasgupta, and J. F. Beacom, *Precise relic WIMP abundance and its impact on searches for dark matter annihilation*, Physical Review D **86**, 023506 (2012), arXiv:`1204.3622`.

[209] M. Ackermann et al. (Fermi-LAT Collaboration), *Searching for dark matter annihilation from Milky Way dwarf spheroidal galaxies with six years of Fermi Large Area Telescope data*, Physical Review Letters **115**, 231301 (2015), arXiv:`1503.02641`.

[210] M. L. Ahnen et al. (MAGIC Collaboration), *Limits to dark matter annihilation cross-section from a combined analysis of MAGIC and Fermi-LAT observations of dwarf satellite galaxies*, Journal of Cosmology and Astroparticle Physics **02**, 039 (2016), arXiv:`1601.06590`.

[211] A. Albert et al. (Fermi-LAT and DES Collaborations), *Searching for dark matter annihilation in recently discovered Milky Way satellites with Fermi-LAT*, Astrophysical Journal **834**, 110 (2017), arXiv:`1611.03184`.

[212] H. Abdallah et al. (H.E.S.S. Collaboration), *Search for dark matter annihilations towards the inner Galactic halo from 10 years of observations with H.E.S.S.*, Physical Review Letters **117**, 111301 (2016).

[213] M. Kamionkowski and M. S. Turner, *Thermal relics: Do we know their abundances?*, Physical Review D **42**, 3310 (1990).

[214] G. F. Giudice, E. W. Kolb, and A. Riotto, *Largest temperature of the radiation era and its cosmological implications*, Physical Review D **64**, 023508 (2001), arXiv:`hep-ph/0005123`.

[215] G. Gelmini and P. Gondolo, *Neutralino with the right cold dark matter abundance in (almost) any supersymmetric model*, Physical Review D **74**, 023510 (2006), arXiv:`hep-ph/0602230`.

[216] G. L. Kane, P. Kumar, B. D. Nelson, and B. Zheng, *Dark matter production mechanisms with a nonthermal cosmological history: A classification*, Physical Review D **93**, 063527 (2016), arXiv:`1502.05406`.

[217] M. Drees and F. Hajkarim, *Dark matter production in an early matter dominated era*, Journal of Cosmology and Astroparticle Physics **02**, 057 (2018), arXiv:`1711.05007`.

[218] M. Drees and F. Hajkarim, *Neutralino dark matter in scenarios with early matter domination*, Journal of High Energy Physics **12**, 042 (2018), arXiv:`1808.05706`.

[219] N. Bernal, C. Cosme, and T. Tenkanen, *Phenomenology of self-interacting dark matter in a matter-dominated universe*, European Physical Journal C **79**, 99 (2019), arXiv:`1803.08064`.

[220] N. Bernal, C. Cosme, T. Tenkanen, and V. Vaskonen, *Scalar singlet dark matter in non-standard cosmologies*, European Physical Journal C **79**, 30 (2019), arXiv:`1806.11122`.

[221] M. Cirelli, Y. Gouttenoire, K. Petraki, and F. Sala, *Homeopathic dark matter, or how diluted heavy substances produce high energy cosmic rays*, Journal of Cosmology and Astroparticle Physics **02**, 014 (2019), arXiv:`1811.03608`.

[222] R. Allahverdi and J. K. Osiński, *Nonthermal production of dark matter prior to early matter domination* (2019), arXiv:`1909.01457`.

[223] J. A. Evans, A. Ghalsasi, S. Gori, M. Tammaro, and J. Zupan, *Light dark matter from entropy dilution* (2019), arXiv:`1910.06319`.

[224] A. L. Erickcek, *The dark matter annihilation boost from low-temperature reheating*, Physical Review D **92**, 103505 (2015), arXiv:`1504.03335`.

[225] A. L. Erickcek, K. Sinha, and S. Watson, *Bringing isolated dark matter out of isolation: late-time reheating and indirect detection*, Physical Review D **94**, 063502 (2016), arXiv:`1510.04291`.

[226] M. S. Delos, A. L. Erickcek, A. P. Bailey, and M. A. Alvarez, *Are ultracompact minihalos really ultracompact?*, Physical Review D **97**, 041303(R) (2018), arXiv:`1712.05421`.

[227] P. Scott and S. Sivertsson, *Gamma rays from ultracompact primordial dark matter minihalos*, Physical Review Letters **103**, 211301 (2009), arXiv:`0908.4082`.

[228] R. Saito and S. Shirai, *Primordial black hole as a source of the boost factor*, Physics Letters B **697**, 95 (2011), arXiv:`1009.1947`.

[229] Y. Yang, L. Feng, X. Huang, X. Chen, T. Lu, and H. Zong, *Constraints on ultracompact minihalos from extragalactic γ-ray background*, Journal of Cosmology and Astroparticle Physics **12**, 020 (2011), arXiv:`1112.6229`.

[230] V. S. Berezinsky, V. I. Dokuchaev, and Y. N. Eroshenko, *Formation and internal structure of superdense dark matter clumps and ultracompact minihaloes*, Journal of Cosmology and Astroparticle Physics **11**, 059 (2013), arXiv:`1308.6742`.

[231] F. Yang and M. Su, *Dark matter annihilation from nearby ultra-compact micro halos to explain the tentative excess at 1.4 TeV in DAMPE data*, arXiv preprint (2017), arXiv:`1712.01724`.

[232] T. Nakama, T. Suyama, K. Kohri, and N. Hiroshima, *Constraints on small-scale primordial power by annihilation signals from extragalactic dark matter minihalos*, Physical Review D **97**, 023539 (2018), arXiv:`1712.08820`.

[233] A. S. Josan and A. M. Green, *Gamma rays from ultracompact minihalos: Potential constraints on the primordial curvature perturbation*, Physical Review D **82**, 083527 (2010), arXiv:`1006.4970`.

[234] T. Bringmann, P. Scott, and Y. Akrami, *Improved constraints on the primordial power spectrum at small scales from ultracompact minihalos*, Physical Review D **85**, 125027 (2012), arXiv:`1110.2484`.

[235] Y. Yang, G. Yang, and H. Zong, *Neutrino signals from ultracompact minihalos and constraints on the primordial curvature perturbation*, Physical Review D **87**, 103525 (2013), arXiv:1305.4213.

[236] Y. Yang and Y. Qin, *Tau neutrinos from ultracompact dark matter minihalos and constraints on the primordial curvature perturbations*, Physical Review D **96**, 103509 (2017), arXiv:1711.00993.

[237] Y. Yang, X. Chen, T. Lu, and H. Zong, *The abundance of new kind of dark-matter structures*, European Physical Journal Plus **126**, 123 (2011), arXiv:1112.6228.

[238] D. Zhang, *Impact of primordial ultracompact minihaloes on the intergalactic medium and first structure formation*, Monthly Notices of the Royal Astronomical Society **418**, 1850 (2011), arXiv:1011.1935.

[239] Y. Yang, *Contributions of dark matter annihilation within ultracompact minihalos to the 21 cm background signal*, European Physical Journal Plus **131**, 432 (2016), arXiv:1612.06559.

[240] H. A. Clark, N. Iwanus, P. J. Elahi, G. F. Lewis, and P. Scott, *Heating of galactic gas by dark matter annihilation in ultracompact minihalos*, Journal of Cosmology and Astroparticle Physics **05**, 048 (2017), arXiv:1611.08619.

[241] Y. Yang, X. Huang, X. Chen, and H. Zong, *New constraints on primordial minihalo abundance using cosmic microwave background observations*, Physical Review D **84**, 043506 (2011), arXiv:1109.0156.

[242] Y. Yang, G. Yang, X. Huang, X. Chen, T. Lu, and H. Zong, *Contribution of ultracompact dark matter minihalos to the isotropic radio background*, Physical Review D **87**, 083519 (2013), arXiv:1206.3750.

[243] G. Beck and S. Colafrancesco, *Through a mini halo, darkly* (2018), arXiv:1804.06624.

[244] E. Zackrisson et al., *Hunting for dark halo substructure using submilliarcsecond-scale observations of macrolensed radio jets*, Monthly Notices of the Royal Astronomical Society **431**, 2172 (2013), arXiv:1208.5482.

[245] H. A. Clark, G. F. Lewis, and P. Scott, *Investigating dark matter substructure with pulsar timing–I. Constraints on ultracompact minihaloes*, Monthly Notices of the Royal Astronomical Society **456**, 1394 (2016), erratum: 464, 2468 (2017), arXiv:1509.02938.

[246] F. Li, A. L. Erickcek, and N. M. Law, *A new probe of the small-scale primordial power spectrum: astrometric microlensing by ultracompact minihalos*, Physical Review D **86**, 043519 (2012), arXiv:1202.1284.

[247] Y.-P. Yang, G.-L. Yang, and H.-S. Zong, *Dark-matter decay and the abundance of ultracompact minihalos*, Europhysics Letters **101**, 69001 (2013), arXiv:1210.1409.

[248] Y. Yang, *Constraints on the primordial power spectrum of small scales using the neutrino signals from the dark matter decay*, International Journal of Modern Physics A **29**, 1450194 (2014), arXiv:1501.00789.

[249] H. A. Clark, G. F. Lewis, and P. Scott, *Investigating dark matter substructure with pulsar timing–II. Improved limits on small-scale cosmology*, Monthly Notices of the Royal Astronomical Society **456**, 1402 (2016), erratum: 464, 955 (2017), arXiv:1509.02941.

[250] K.-Y. Choi and T. Takahashi, *New bound on low reheating temperature for dark matter in models with early matter domination*, Physical Review D **96**, 041301 (2017), arXiv:1705.01200.

[251] R. Hlozek et al., *The Atacama Cosmology Telescope: a measurement of the primordial power spectrum*, Astrophysical Journal **749**, 90 (2012), arXiv:1105.4887.

[252] A. S. Josan, A. M. Green, and K. A. Malik, *Generalized constraints on the curvature perturbation from primordial black holes*, Physical Review D **79**, 103520 (2009), arXiv:0903.3184.

[253] J. A. Fillmore and P. Goldreich, *Self-similar gravitational collapse in an expanding universe*, Astrophysical Journal **281**, 1 (1984).

[254] M. Vogelsberger, S. D. M. White, R. Mohayaee, and V. Springel, *Caustics in growing cold dark matter haloes*, Monthly Notices of the Royal Astronomical Society **400**, 2174 (2009), arXiv:0906.4341.

[255] M. Vogelsberger, R. Mohayaee, and S. D. M. White, *Non-spherical similarity solutions for dark halo formation*, Monthly Notices of the Royal Astronomical Society **414**, 3044 (2011), arXiv:1007.4195.

[256] A. Huss, B. Jain, and M. Steinmetz, *How universal are the density profiles of dark halos?*, Astrophysical Journal **517**, 64 (1999), arXiv:astro-ph/9803117.

[257] J. D. MacMillan, L. M. Widrow, and R. N. Henriksen, *On universal halos and the radial orbit instability*, Astrophysical Journal **653**, 43 (2006), arXiv:astro-ph/0604418.

[258] J. M. Bellovary, J. J. Dalcanton, A. Babul, T. R. Quinn, R. W. Maas, C. G. Austin, L. L. R. Williams, and E. I. Barnes, *The role of the radial orbit instability in dark matter halo formation and structure*, Astrophysical Journal **685**, 739 (2008), arXiv:0806.3434.

[259] J. F. Navarro, C. S. Frenk, and S. D. M. White, *Simulations of X-ray clusters*, Monthly Notices of the Royal Astronomical Society **275**, 720 (1995), arXiv:astro-ph/9408069.

[260] J. F. Navarro, C. S. Frenk, and S. D. M. White, *The structure of cold dark matter halos*, Astrophysical Journal **462**, 563 (1996), arXiv:astro-ph/9508025.

[261] G. Ogiya and O. Hahn, *What sets the central structure of dark matter haloes?*, Monthly Notices of the Royal Astronomical Society **473**, 4339 (2018), arXiv:1707.07693.

[262] R. E. Angulo, O. Hahn, A. D. Ludlow, and S. Bonoli, *Earth-mass haloes and the emergence of NFW density profiles*, Monthly Notices of the Royal Astronomical Society **471**, 4687 (2017), arXiv:1604.03131.

[263] D. Anderhalden and J. Diemand, *Density profiles of CDM microhalos and their implications for annihilation boost factors*, Journal of Cosmology and Astroparticle Physics **04**, 009 (2013), erratum: 08, E02 (2013), arXiv:1302.0003.

[264] T. Ishiyama, J. Makino, and T. Ebisuzaki, *Gamma-ray signal from Earth-mass dark matter microhalos*, Astrophysical Journal Letters **723**, L195 (2010), arXiv:1006.3392.

[265] T. Ishiyama, *Hierarchical formation of dark matter halos and the free streaming scale*, Astrophysical Journal **788**, 27 (2014), arXiv:1404.1650.

[266] E. Polisensky and M. Ricotti, *Fingerprints of the initial conditions on the density profiles of cold and warm dark matter haloes*, Monthly Notices of the Royal Astronomical Society **450**, 2172 (2015), arXiv:1504.02126.

[267] M. Gosenca, J. Adamek, C. T. Byrnes, and S. Hotchkiss, *3D simulations with boosted primordial power spectra and ultracompact minihalos*, Physical Review D **96**, 123519 (2017), arXiv:1710.02055.

[268] W. B. Atwood et al. (Fermi-LAT Collaboration), *The large area telescope on the Fermi gamma-ray space telescope mission*, Astrophysical Journal **697**, 1071 (2009), arXiv:0902.1089.

[269] J. M. Bardeen, J. R. Bond, N. Kaiser, and A. S. Szalay, *The statistics of peaks of gaussian random fields*, Astrophysical Journal **304**, 15 (1986).

[270] A. Challinor and A. Lewis, *Linear power spectrum of observed source number counts*, Physical Review D **84**, 043516 (2011), arXiv:1105.5292.

[271] A. Lewis and A. Challinor, *21 cm angular-power spectrum from the dark ages*, Physical Review D **76**, 083005 (2007), arXiv:astro-ph/0702600.

[272] P. Meszaros, *The behaviour of point masses in an expanding cosmological substratum*, Astronomy and Astrophysics **37**, 225 (1974).

[273] W. Hu and N. Sugiyama, *Small-scale cosmological perturbations: an analytic approach*, Astrophysical Journal **471**, 542 (1996), arXiv:astro-ph/9510117.

[274] V. Springel, *The cosmological simulation code GADGET-2*, Monthly Notices of the Royal Astronomical Society **364**, 1105 (2005), arXiv:astro-ph/0505010.

[275] V. Springel, N. Yoshida, and S. D. M. White, *GADGET: a code for collisionless and gasdynamical cosmological simulations*, New Astronomy **6**, 79 (2001), arXiv:astro-ph/0003162.

[276] S. Dodelson, *Modern Cosmology* (Academic Press, New York, 2003).

[277] P. S. Behroozi, R. H. Wechsler, and H.-Y. Wu, *The rockstar phase-space temporal halo finder and the velocity offsets of cluster cores*, Astrophysical Journal **762**, 109 (2013), arXiv:1110.4372.

[278] B. Moore, T. Quinn, F. Governato, J. Stadel, and G. Lake, *Cold collapse and the core catastrophe*, Monthly Notices of the Royal Astronomical Society **310**, 1147 (1999), arXiv:astro-ph/9903164.

[279] R. H. Wechsler, J. S. Bullock, J. R. Primack, A. V. Kravtsov, and A. Dekel, *Concentrations of dark halos from their assembly histories*, Astrophysical Journal **568**, 52 (2002), arXiv:astro-ph/0108151.

[280] G. Ogiya, D. Nagai, and T. Ishiyama, *Dynamical evolution of primordial dark matter haloes through mergers*, Monthly Notices of the Royal Astronomical Society **461**, 3385 (2016), arXiv:1604.02866.

[281] Y. Li, H. J. Mo, F. C. van den Bosch, and W. P. Lin, *On the assembly history of dark matter haloes*, Monthly Notices of the Royal Astronomical Society **379**, 689 (2007), arXiv:astro-ph/0510372.

[282] Y. Lu, H. J. Mo, N. Katz, and M. D. Weinberg, *On the origin of cold dark matter halo density profiles*, Monthly Notices of the Royal Astronomical Society **368**, 1931 (2006), arXiv:`astro-ph/0508624`.

[283] G. Jungman, M. Kamionkowski, and K. Griest, *Supersymmetric dark matter*, Physics Reports **267**, 195 (1996), arXiv:`hep-ph/9506380`.

[284] V. Berezinsky, V. Dokuchaev, and Y. Eroshenko, *Remnants of dark matter clumps*, Physical Review D **77**, 083519 (2008), arXiv:`0712.3499`.

[285] V. S. Berezinsky, A. V. Gurevich, and K. P. Zybin, *Distribution of dark matter in the galaxy and the lower limits for the masses of supersymmetric particles*, Physics Letters B **294**, 221 (1992).

[286] G. Battaglia, A. Helmi, H. Morrison, P. Harding, E. W. Olszewski, M. Mateo, K. C. Freeman, J. Norris, and S. A. Shectman, *The radial velocity dispersion profile of the Galactic halo: constraining the density profile of the dark halo of the Milky Way*, Monthly Notices of the Royal Astronomical Society **364**, 433 (2005), arXiv:`astro-ph/0506102`.

[287] W. H. Press and P. Schechter, *Formation of galaxies and clusters of galaxies by self-similar gravitational condensation*, Astrophysical Journal **187**, 425 (1974).

[288] R. Barkana, Z. Haiman, and J. P. Ostriker, *Constraints on warm dark matter from cosmological reionization*, Astrophysical Journal **558**, 482 (2001), arXiv:`astro-ph/0102304`.

[289] A. J. Benson, A. Farahi, S. Cole, L. A. Moustakas, A. Jenkins, M. Lovell, R. Kennedy, J. Helly, and C. Frenk, *Dark matter halo merger histories beyond cold dark matter–I. Methods and application to warm dark matter*, Monthly Notices of the Royal Astronomical Society **428**, 1774 (2013), arXiv:`1209.3018`.

[290] A. Schneider, R. E. Smith, and D. Reed, *Halo mass function and the free streaming scale*, Monthly Notices of the Royal Astronomical Society **433**, 1573 (2013), arXiv:`1303.0839`.

[291] C. Lacey and S. Cole, *Merger rates in hierarchical models of galaxy formation*, Monthly Notices of the Royal Astronomical Society **262**, 627 (1993).

[292] P. L. Nolan, A. A. Abdo, M. Ackermann, M. Ajello, A. Allafort, E. Antolini, W. B. Atwood, M. Axelsson, L. Baldini, J. Ballet, et al., *Fermi large area telescope second source catalog*, Astrophysical Journal Supplement Series **199**, 31 (2012), arXiv:`1108.1435`.

[293] S. Shandera, A. L. Erickcek, P. Scott, and J. Y. Galarza, *Number counts and non-gaussianity*, Physical Review D **88**, 103506 (2013), arXiv:`1211.7361`.

[294] D. H. Zhao, Y. P. Jing, H. J. Mo, and G. Börner, *Accurate universal models for the mass accretion histories and concentrations of dark matter halos*, Astrophysical Journal **707**, 354 (2009), arXiv:`0811.0828`.

[295] Y. P. Jing, *The density profile of equilibrium and nonequilibrium dark matter halos*, Astrophysical Journal **535**, 30 (2000), arXiv:`astro-ph/9901340`.

[296] V. R. Eke, J. F. Navarro, and M. Steinmetz, *The power spectrum dependence of dark matter halo concentrations*, Astrophysical Journal **554**, 114 (2001), arXiv:`astro-ph/0012337`.

[297] J. S. Bullock, T. S. Kolatt, Y. Sigad, R. S. Somerville, A. V. Kravtsov, A. A. Klypin, J. R. Primack, and A. Dekel, *Profiles of dark haloes: evolution, scatter and environment*, Monthly Notices of the Royal Astronomical Society **321**, 559 (2001), arXiv:`astro-ph/9908159`.

[298] D.-H. Zhao, Y. P. Jing, H. J. Mo, and G. Börner, *Mass and redshift dependence of dark halo structure*, Astrophysical Journal Letters **597**, L9 (2003), arXiv:`astro-ph/0309375`.

[299] V. Avila-Reese, P. Colín, S. Gottlöber, C. Firmani, and C. Maulbetsch, *The dependence on environment of cold dark matter halo properties*, Astrophysical Journal **634**, 51 (2005), arXiv:`astro-ph/0508053`.

[300] A. F. Neto, L. Gao, P. Bett, S. Cole, J. F. Navarro, C. S. Frenk, S. D. M. White, V. Springel, and A. Jenkins, *The statistics of* Λ *CDM halo concentrations*, Monthly Notices of the Royal Astronomical Society **381**, 1450 (2007), arXiv:`0706.2919`.

[301] L. Gao, J. F. Navarro, S. Cole, C. S. Frenk, S. D. M. White, V. Springel, A. Jenkins, and A. F. Neto, *The redshift dependence of the structure of massive* Λ *cold dark matter haloes*, Monthly Notices of the Royal Astronomical Society **387**, 536 (2008), arXiv:`0711.0746`.

[302] A. R. Duffy, J. Schaye, S. T. Kay, and C. Dalla Vecchia, *Dark matter halo concentrations in the Wilkinson Microwave Anisotropy Probe year 5 cosmology*, Monthly Notices of the Royal Astronomical Society Letters **390**, L64 (2008), erratum: 415, L85 (2011), arXiv:`0804.2486`.

[303] A. V. Macciò, A. A. Dutton, and F. C. van den Bosch, *Concentration, spin and shape of dark matter haloes as a function of the cosmological model: WMAP 1, WMAP 3 and WMAP 5 results*, Monthly Notices of the Royal Astronomical Society **391**, 1940 (2008), arXiv:`0805.1926`.

[304] J. C. Muñoz-Cuartas, A. V. Macciò, S. Gottlöber, and A. A. Dutton, *The redshift evolution of* Λ *cold dark matter halo parameters: concentration, spin and shape*, Monthly Notices of the Royal Astronomical Society **411**, 584 (2011), arXiv:`1007.0438`.

[305] A. A. Klypin, S. Trujillo-Gomez, and J. Primack, *Dark matter halos in the standard cosmological model: Results from the bolshoi simulation*, Astrophysical Journal **740**, 102 (2011), arXiv:`1002.3660`.

[306] C. Giocoli, G. Tormen, and R. K. Sheth, *Formation times, mass growth histories and concentrations of dark matter haloes*, Monthly Notices of the Royal Astronomical Society **422**, 185 (2012), arXiv:`1111.6977`.

[307] F. Prada, A. A. Klypin, A. J. Cuesta, J. E. Betancort-Rijo, and J. Primack, *Halo concentrations in the standard* Λ *cold dark matter cosmology*, Monthly Notices of the Royal Astronomical Society **423**, 3018 (2012), arXiv:`1104.5130`.

[308] A. D. Ludlow, J. F. Navarro, M. Li, R. E. Angulo, M. Boylan-Kolchin, and P. E. Bett, *The dynamical state and mass–concentration relation of galaxy clusters*, Monthly Notices of the Royal Astronomical Society **427**, 1322 (2012), arXiv:`1206.1049`.

[309] A. D. Ludlow, J. F. Navarro, M. Boylan-Kolchin, P. E. Bett, R. E. Angulo, M. Li, S. D. M. White, C. Frenk, and V. Springel, *The mass profile and accretion history of cold dark matter haloes*, Monthly Notices of the Royal Astronomical Society **432**, 1103 (2013), arXiv:`1302.0288`.

[310] S. Bhattacharya, S. Habib, K. Heitmann, and A. Vikhlinin, *Dark matter halo profiles of massive clusters: Theory versus observations*, Astrophysical Journal **766**, 32 (2013), arXiv:`1112.5479`.

[311] M. Meneghetti and E. Rasia, *Reconciling extremely different concentration-mass relations* (2013), arXiv:`1303.6158`.

[312] A. A. Dutton and A. V. Macciò, *Cold dark matter haloes in the Planck era: evolution of structural parameters for Einasto and NFW profiles*, Monthly Notices of the Royal Astronomical Society **441**, 3359 (2014), arXiv:`1402.7073`.

[313] A. D. Ludlow, J. F. Navarro, R. E. Angulo, M. Boylan-Kolchin, V. Springel, C. Frenk, and S. D. M. White, *The mass–concentration–redshift relation of cold dark matter haloes*, Monthly Notices of the Royal Astronomical Society **441**, 378 (2014), arXiv:`1312.0945`.

[314] B. Diemer and A. V. Kravtsov, *A universal model for halo concentrations*, Astrophysical Journal **799**, 108 (2015), arXiv:`1407.4730`.

[315] C. A. Correa, J. S. B. Wyithe, J. Schaye, and A. R. Duffy, *The accretion history of dark matter haloes–III. A physical model for the concentration–mass relation*, Monthly Notices of the Royal Astronomical Society **452**, 1217 (2015), arXiv:`1502.00391`.

[316] C. Okoli and N. Afshordi, *Concentration, ellipsoidal collapse, and the densest dark matter haloes*, Monthly Notices of the Royal Astronomical Society **456**, 3068 (2016), arXiv:`1510.03868`.

[317] A. Klypin, G. Yepes, S. Gottlöber, F. Prada, and S. Hess, *MultiDark simulations: the story of dark matter halo concentrations and density profiles*, Monthly Notices of the Royal Astronomical Society **457**, 4340 (2016), arXiv:`1411.4001`.

[318] P. W. Angel, G. B. Poole, A. D. Ludlow, A. R. Duffy, P. M. Geil, S. J. Mutch, A. Mesinger, and J. S. B. Wyithe, *Dark-ages reionization and galaxy formation simulation–II. Spin and concentration parameters for dark matter haloes during the epoch of reionization*, Monthly Notices of the Royal Astronomical Society **459**, 2106 (2016), arXiv:`1512.00560`.

[319] A. J. Benson, M. Kamionkowski, and S. H. Hassani, *Self-consistent theory of halo mergers*, Monthly Notices of the Royal Astronomical Society **357**, 847 (2005), arXiv:`astro-ph/0407136`.

[320] E. Neistein and A. Dekel, *Merger rates of dark matter haloes*, Monthly Notices of the Royal Astronomical Society **388**, 1792 (2008), arXiv:`0802.0198`.

[321] J. Diemand, B. Moore, and J. Stadel, *Earth-mass dark-matter haloes as the first structures in the early universe*, Nature **433**, 389 (2005), arXiv:`astro-ph/0501589`.

[322] G. W. Angus and H. Zhao, *Cold dark matter microhalo survival in the Milky Way*, Monthly Notices of the Royal Astronomical Society **375**, 1146 (2007), arXiv:`astro-ph/0608580`.

[323] V. Berezinsky, V. Dokuchaev, and Y. Eroshenko, *Destruction of small-scale dark matter clumps in the hierarchical structures and galaxies*, Physical Review D **73**, 063504 (2006), arXiv:`astro-ph/0511494`.

[324] A. M. Green and S. P. Goodwin, *On mini-halo encounters with stars*, Monthly Notices of the Royal Astronomical Society **375**, 1111 (2007), arXiv:`astro-ph/0604142`.

[325] T. Goerdt, O. Y. Gnedin, B. Moore, J. Diemand, and J. Stadel, *The survival and disruption of cold dark matter microhaloes: implications for direct and indirect detection experiments*, Monthly Notices of the Royal Astronomical Society **375**, 191 (2007), arXiv:`astro-ph/0608495`.

[326] H. Zhao, D. Hooper, G. W. Angus, J. E. Taylor, and J. Silk, *Tidal disruption of the first dark microhalos*, Astrophysical Journal **654**, 697 (2007), arXiv:`astro-ph/0508215`.

[327] A. Schneider, L. Krauss, and B. Moore, *Impact of dark matter microhalos on signatures for direct and indirect detection*, Physical Review D **82**, 063525 (2010), arXiv:`1004.5432`.

[328] F. C. van den Bosch, G. Ogiya, O. Hahn, and A. Burkert, *Disruption of dark matter substructure: fact or fiction?*, Monthly Notices of the Royal Astronomical Society **474**, 3043 (2018), arXiv:`1711.05276`.

[329] E. Aprile, J. Aalbers, F. Agostini, M. Alfonsi, L. Althueser, F. D. Amaro, M. Anthony, F. Arneodo, L. Baudis, B. Bauermeister, et al. (XENON Collaboration), *Dark matter search results from a one ton-year exposure of XENON1T*, Physical Review Letters **121**, 111302 (2018), arXiv:`1805.12562`.

[330] D. S. Akerib, S. Alsum, H. M. Araújo, X. Bai, A. J. Bailey, J. Balajthy, P. Beltrame, E. P. Bernard, A. Bernstein, T. P. Biesiadzinski, et al. (LUX Collaboration), *Results from a search for dark matter in the complete LUX exposure*, Physical Review Letters **118**, 021303 (2017), arXiv:`1608.07648`.

[331] X. Cui, A. Abdukerim, W. Chen, X. Chen, Y. Chen, B. Dong, D. Fang, C. Fu, K. Giboni, F. Giuliani, et al. (PandaX-II Collaboration), *Dark matter results from 54-ton-day exposure of PandaX-II experiment*, Physical Review Letters **119**, 181302 (2017), arXiv:`1708.06917`.

[332] Y. B. Zel'Dovich, *Gravitational instability: An approximate theory for large density perturbations*, Astronomy and Astrophysics **5**, 84 (1970).

[333] Y. Suto, *Correlation Function in Decaying Particle Cosmology*, Astrophysical Journal **321**, 36 (1987).

[334] K. Enqvist, S. Nadathur, T. Sekiguchi, and T. Takahashi, *Decaying dark matter and the tension in σ_8*, Journal of Cosmology and Astroparticle Physics **09**, 067 (2015), arXiv:`1505.05511`.

[335] J. Dakin, S. Hannestad, and T. Tram, *Fully relativistic treatment of decaying cold dark matter in n-body simulations*, Journal of Cosmology and Astroparticle Physics **06**, 032 (2019), arXiv:`1904.11773`.

[336] M. S. Delos, M. Bruff, and A. L. Erickcek, *Predicting the density profiles of the first halos*, Physical Review D **100**, 023523 (2019), arXiv:`1905.05766`.

[337] J. F. Navarro, A. Ludlow, V. Springel, J. Wang, M. Vogelsberger, S. D. M. White, A. Jenkins, C. S. Frenk, and A. Helmi, *The diversity and similarity of simulated cold dark matter haloes*, Monthly Notices of the Royal Astronomical Society **402**, 21 (2010).

[338] D. Lynden-Bell, *Statistical mechanics of violent relaxation in stellar systems*, Monthly Notices of the Royal Astronomical Society **136**, 101 (1967).

[339] N. E. Drakos, J. E. Taylor, A. Berrouet, A. S. G. Robotham, and C. Power, *Major mergers between dark matter haloes–II. Profile and concentration changes*, Monthly Notices of the Royal Astronomical Society **487**, 1008 (2019), arXiv:`1811.12844`.

[340] E. Hayashi, J. F. Navarro, J. E. Taylor, J. Stadel, and T. Quinn, *The structural evolution of substructure*, Astrophysical Journal **584**, 541 (2003), arXiv:`astro-ph/0203004`.

[341] J. Penarrubia, A. J. Benson, M. G. Walker, G. Gilmore, A. W. McConnachie, and L. Mayer, *The impact of dark matter cusps and cores on the satellite galaxy population around spiral galaxies*, Monthly Notices of the Royal Astronomical Society **406**, 1290 (2010), arXiv:`1002.3376`.

[342] G. Ogiya, F. C. Van den Bosch, O. Hahn, S. B. Green, T. B. Miller, and A. Burkert, *DASH: a library of dynamical subhalo evolution*, Monthly Notices of the Royal Astronomical Society **485**, 189 (2019), arXiv:`1901.08601`.

[343] J. Diemand, M. Kuhlen, and P. Madau, *Dark matter substructure and gamma-ray annihilation in the Milky Way halo*, Astrophysical Journal **657**, 262 (2007), arXiv:`1507.08656`.

[344] L. E. Strigari, S. M. Koushiappas, J. S. Bullock, and M. Kaplinghat, *Precise constraints on the dark matter content of Milky Way dwarf galaxies for gamma-ray experiments*, Physical Review D **75**, 083526 (2007), arXiv:`astro-ph/0611925`.

[345] L. Pieri, G. Bertone, and E. Branchini, *Dark matter annihilation in substructures revised*, Monthly Notices of the Royal Astronomical Society **384**, 1627 (2008), arXiv:`0706.2101`.

[346] T. E. Jeltema and S. Profumo, *Searching for dark matter with X-ray observations of local dwarf galaxies*, Astrophysical Journal **686**, 1045 (2008), arXiv:`0805.1054`.

[347] R. Bartels and S. Ando, *Boosting the annihilation boost: Tidal effects on dark matter subhalos and consistent luminosity modeling*, Physical Review D **92**, 123508 (2015), arXiv:`1507.08656`.

[348] S. Ando, T. Ishiyama, and N. Hiroshima, *Halo substructure boosts to the signatures of dark matter annihilation*, Galaxies **7**, 68 (2019), arXiv:`1903.11427`.

[349] A. F. Boden, M. Shao, and D. Van Buren, *Astrometric observation of macho gravitational microlensing*, Astrophysical Journal **502**, 538 (1998), arXiv:`astro-ph/9802179`.

[350] M. Dominik and K. C. Sahu, *Astrometric microlensing of stars*, Astrophysical Journal **534**, 213 (2000), arXiv:`astro-ph/9805360`.

[351] A. L. Erickcek and N. M. Law, *Astrometric microlensing by local dark matter subhalos*, Astrophysical Journal **729**, 49 (2011), arXiv:`1007.4228`.

[352] K. Van Tilburg, A.-M. Taki, and N. Weiner, *Halometry from astrometry*, Journal of Cosmology and Astroparticle Physics **07**, 041 (2018), arXiv:`1804.01991`.

[353] E. R. Siegel, M. P. Hertzberg, and J. N. Fry, *Probing dark matter substructure with pulsar timing*, Monthly Notices of the Royal Astronomical Society **382**, 879 (2007), arXiv:`astro-ph/0702546`.

[354] M. Buschmann, J. Kopp, B. R. Safdi, and C.-L. Wu, *Stellar wakes from dark matter subhalos*, Physical Review Letters **120**, 211101 (2018), arXiv:`1711.03554`.

[355] J. E. Gunn and J. R. Gott III, *On the infall of matter into clusters of galaxies and some effects on their evolution*, Astrophysical Journal **176**, 1 (1972).

[356] J. R. Gott, *On the formation of elliptical galaxies*, Astrophysical Journal **201**, 296 (1975).

[357] J. E. Gunn, *Massive galactic halos. I-Formation and evolution*, Astrophysical Journal **218**, 592 (1977).

[358] Y. Hoffman and J. Shaham, *Local density maxima-progenitors of structure*, Astrophysical Journal **297**, 16 (1985).

[359] B. S. Ryden and J. E. Gunn, *Galaxy formation by gravitational collapse*, Astrophysical Journal **318**, 15 (1987).

[360] S. Zaroubi and Y. Hoffman, *Gravitational collapse in an expanding universe: asymptotic self-similar solutions*, Astrophysical Journal **416**, 410 (1993).

[361] E. L. Ł.okas and Y. Hoffman, *Formation of cuspy density profiles: a generic feature of collisionless gravitational collapse*, Astrophysical Journal Letters **542**, L139 (2000), arXiv:`astro-ph/0005566`.

[362] N. Dalal, Y. Lithwick, and M. Kuhlen, *The origin of dark matter halo profiles* (2010), arXiv:`1010.2539`.

[363] B. S. Ryden, *Self-similar collapse of axisymmetric systems*, Astrophysical Journal **418**, 4 (1993).

[364] Y. Lithwick and N. Dalal, *Self-similar solutions of triaxial dark matter halos*, Astrophysical Journal **734**, 100 (2011), arXiv:`1010.3723`.

[365] S. D. M. White and D. Zaritsky, *Models for galaxy halos in an open universe*, Astrophysical Journal **394**, 1 (1992).

[366] A. Nusser, *Self-similar spherical collapse with non-radial motions*, Monthly Notices of the Royal Astronomical Society **325**, 1397 (2001).

[367] Y. Ascasibar, G. Yepes, S. Gottlöber, and V. Müller, *On the physical origin of dark matter density profiles*, Monthly Notices of the Royal Astronomical Society **352**, 1109 (2004), arXiv:`astro-ph/0312221`.

[368] Y. Ascasibar, Y. Hoffman, and S. Gottlöber, *Secondary infall and dark matter haloes*, Monthly Notices of the Royal Astronomical Society **376**, 393 (2007), arXiv:`astro-ph/0609713`.

[369] P. Zukin and E. Bertschinger, *Self-similar spherical collapse with tidal torque*, Physical Review D **82**, 104044 (2010), arXiv:`1008.0639`.

[370] P. Zukin and E. Bertschinger, *Velocity structure of self-similar spherically collapsed halos*, Physical Review D **82**, 104045 (2010), arXiv:`1008.1980`.

[371] E. Salvador-Solé, J. Viñas, A. Manrique, and S. Serra, *Theoretical dark matter halo density profile*, Monthly Notices of the Royal Astronomical Society **423**, 2190 (2012), arXiv:`1104.2334`.

[372] E. Juan, E. Salvador-Solé, G. Domènech, and A. Manrique, *Fixing a rigorous formalism for the accurate analytic derivation of halo properties*, Monthly Notices of the Royal Astronomical Society **439**, 719 (2014), arXiv:`1401.7335`.

[373] R. K. Sheth, H. J. Mo, and G. Tormen, *Ellipsoidal collapse and an improved model for the number and spatial distribution of dark matter haloes*, Monthly Notices of the Royal Astronomical Society **323**, 1 (2001), arXiv:`astro-ph/9907024`.

[374] R. K. Sheth and G. Tormen, *An excursion set model of hierarchical clustering: ellipsoidal collapse and the moving barrier*, Monthly Notices of the Royal Astronomical Society **329**, 61 (2002), arXiv:`astro-ph/0105113`.

[375] V. Avila-Reese, C. Firmani, A. Klypin, and A. V. Kravtsov, *Density profiles of dark matter haloes: diversity and dependence on environment*, Monthly Notices of the Royal Astronomical Society **310**, 527 (1999), arXiv:`astro-ph/9906260`.

[376] P. Colin, A. Klypin, O. Valenzuela, and S. Gottlöber, *Dwarf dark matter halos*, Astrophysical Journal **612**, 50 (2004), arXiv:`astro-ph/0308348`.

[377] K. Dolag, M. Bartelmann, F. Perrotta, C. Baccigalupi, L. Moscardini, M. Meneghetti, and G. Tormen, *Numerical study of halo concentrations in dark-energy cosmologies*, Astronomy and Astrophysics **416**, 853 (2004), arXiv:`astro-ph/0309771`.

[378] K. Heitmann, N. Frontiere, C. Sewell, S. Habib, A. Pope, H. Finkel, S. Rizzi, J. Insley, and S. Bhattacharya, *The Q continuum simulation: Harnessing the power of GPU accelerated supercomputers*, Astrophysical Journal Supplement Series **219**, 34 (2015), arXiv:`1411.3396`.

[379] W. A. Hellwing, C. S. Frenk, M. Cautun, S. Bose, J. Helly, A. Jenkins, T. Sawala, and M. Cytowski, *The Copernicus Complexio: a high-resolution view of the small-scale universe*, Monthly Notices of the Royal Astronomical Society **457**, 3492 (2016), arXiv:`1505.06436`.

[380] H. L. Child, S. Habib, K. Heitmann, N. Frontiere, H. Finkel, A. Pope, and V. Morozov, *Halo profiles and the concentration–mass relation for a ΛCDM universe*, Astrophysical Journal **859**, 55 (2018), arXiv:`1804.10199`.

[381] F. C. v. d. Bosch, F. Jiang, A. Hearin, D. Campbell, D. Watson, and N. Padmanabhan, *Coming of age in the dark sector: how dark matter haloes grow their gravitational potential wells*, Monthly Notices of the Royal Astronomical Society **445**, 1713 (2014), arXiv:`1409.2750`.

[382] A. D. Ludlow, S. Bose, R. E. Angulo, L. Wang, W. A. Hellwing, J. F. Navarro, S. Cole, and C. S. Frenk, *The mass–concentration–redshift relation of cold and warm dark matter haloes*, Monthly Notices of the Royal Astronomical Society **460**, 1214 (2016), arXiv:`1601.02624`.

[383] B. Diemer and M. Joyce, *An accurate physical model for halo concentrations*, Astrophysical Journal **871**, 168 (2019), arXiv:`1809.07326`.

[384] J. R. Bond and S. T. Myers, *The peak-patch picture of cosmic catalogs. I. Algorithms*, Astrophysical Journal Supplement Series **103**, 1 (1996).

[385] Y. Ascasibar and S. Gottlöber, *The dynamical structure of dark matter haloes*, Monthly Notices of the Royal Astronomical Society **386**, 2022 (2008), arXiv:`0802.4348`.

[386] P. Bode, J. P. Ostriker, and N. Turok, *Halo formation in warm dark matter models*, Astrophysical Journal **556**, 93 (2001), arXiv:`astro-ph/0010389`.

[387] M. Viel, G. D. Becker, J. S. Bolton, and M. G. Haehnelt, *Warm dark matter as a solution to the small scale crisis: New constraints from high redshift Lyman-α forest data*, Physical Review D **88**, 043502 (2013), arXiv:`1306.2314`.

[388] A. M. Green, S. Hofmann, and D. J. Schwarz, *The power spectrum of SUSY-CDM on subgalactic scales*, Monthly Notices of the Royal Astronomical Society **353**, L23 (2004), arXiv:`astro-ph/0309621`.

[389] R. E. Angulo, O. Hahn, and T. Abel, *The warm dark matter halo mass function below the cut-off scale*, Monthly Notices of the Royal Astronomical Society **434**, 3337 (2013), arXiv:`1304.2406`.

[390] M. R. Lovell, C. S. Frenk, V. R. Eke, A. Jenkins, L. Gao, and T. Theuns, *The properties of warm dark matter haloes*, Monthly Notices of the Royal Astronomical Society **439**, 300 (2014), arXiv:`1308.1399`.

[391] P. S. Behroozi, R. H. Wechsler, H.-Y. Wu, M. T. Busha, A. A. Klypin, and J. R. Primack, *Gravitationally consistent halo catalogs and merger trees for precision cosmology*, Astrophysical Journal **763**, 18 (2012), arXiv:1110.4370.

[392] J. Binney and S. Tremaine, *Galactic Dynamics* (Princeton University Press, Princeton, NJ, 1987).

[393] J. R. Bond and S. T. Myers, *The peak-patch picture of cosmic catalogs. II. Validation*, Astrophysical Journal Supplement Series **103**, 41 (1996).

[394] G. Stein, M. A. Alvarez, and J. R. Bond, *The mass-Peak Patch algorithm for fast generation of deep all-sky dark matter halo catalogues and its N-body validation*, Monthly Notices of the Royal Astronomical Society **483**, 2236 (2018), arXiv:1810.07727.

[395] M. S. Delos, *Tidal evolution of dark matter annihilation rates in subhalos*, Physical Review D **100**, 063505 (2019), arXiv:1906.10690.

[396] A. Brooks, *Re-examining astrophysical constraints on the dark matter model*, Annalen der Physik **526**, 294 (2014), arXiv:1407.7544.

[397] H. Mo, F. Van den Bosch, and S. White, *Galaxy Formation and Evolution* (Cambridge University Press, Cambridge, England, 2010).

[398] S. Chandrasekhar, *Dynamical friction. I. General considerations: the coefficient of dynamical friction*, Astrophysical Journal **97**, 255 (1943).

[399] R. Errani and J. Peñarrubia, *Can tides disrupt cold dark matter subhaloes?*, Monthly Notices of the Royal Astronomical Society **491**, 4591 (2020), arXiv:1906.01642.

[400] V. Berezinsky, V. Dokuchaev, and Y. Eroshenko, *Small-scale clumps in the galactic halo and dark matter annihilation*, Physical Review D **68**, 103003 (2003), arXiv:astro-ph/0301551.

[401] M. A. Sánchez-Conde and F. Prada, *The flattening of the concentration–mass relation towards low halo masses and its implications for the annihilation signal boost*, Monthly Notices of the Royal Astronomical Society **442**, 2271 (2014), arXiv:1312.1729.

[402] B. Anderson, S. Zimmer, J. Conrad, M. Gustafsson, M. Sánchez-Conde, and R. Caputo, *Search for gamma-ray lines towards galaxy clusters with the Fermi-LAT*, Journal of Cosmology and Astroparticle Physics **02**, 026 (2016), arXiv:1511.00014.

[403] L. Gao, C. S. Frenk, A. Jenkins, V. Springel, and S. D. M. White, *Where will supersymmetric dark matter first be seen?*, Monthly Notices of the Royal Astronomical Society **419**, 1721 (2012), arXiv:1107.1916.

[404] V. Springel, S. D. M. White, C. S. Frenk, J. F. Navarro, A. Jenkins, M. Vogelsberger, J. Wang, A. Ludlow, and A. Helmi, *Prospects for detecting supersymmetric dark matter in the Galactic halo*, Nature **456**, 73 (2008), arXiv:0809.0894.

[405] M. Stref and J. Lavalle, *Modeling dark matter subhalos in a constrained galaxy: Global mass and boosted annihilation profiles*, Physical Review D **95**, 063003 (2017), arXiv:1610.02233.

[406] M. Stref, T. Lacroix, and J. Lavalle, *Remnants of galactic subhalos and their impact on indirect dark-matter searches*, Galaxies **7**, 65 (2019), arXiv:1905.02008.

[407] N. Hiroshima, S. Ando, and T. Ishiyama, *Modeling evolution of dark matter substructure and annihilation boost*, Physical Review D **97**, 123002 (2018), arXiv:1803.07691.

[408] F. C. van den Bosch, *Dissecting the evolution of dark matter subhaloes in the bolshoi simulation*, Monthly Notices of the Royal Astronomical Society **468**, 885 (2017), arXiv:1611.02657.

[409] F. C. van den Bosch and G. Ogiya, *Dark matter substructure in numerical simulations: a tale of discreteness noise, runaway instabilities, and artificial disruption*, Monthly Notices of the Royal Astronomical Society **475**, 4066 (2018), arXiv:1801.05427.

[410] J. E. Taylor and A. Babul, *The dynamics of sinking satellites around disk galaxies: a poor man's alternative to high-resolution numerical simulations*, Astrophysical Journal **559**, 716 (2001), arXiv:astro-ph/0012305.

[411] J. Peñarrubia and A. J. Benson, *Effects of dynamical evolution on the distribution of substructures*, Monthly Notices of the Royal Astronomical Society **364**, 977 (2005), arXiv:astro-ph/0412370.

[412] F. C. van den Bosch, G. Tormen, and C. Giocoli, *The mass function and average mass-loss rate of dark matter subhaloes*, Monthly Notices of the Royal Astronomical Society **359**, 1029 (2005), arXiv:astro-ph/0409201.

[413] A. R. Zentner, A. A. Berlind, J. S. Bullock, A. V. Kravtsov, and R. H. Wechsler, *The physics of galaxy clustering. I. A model for subhalo populations*, Astrophysical Journal **624**, 505 (2005), arXiv:astro-ph/0411586.

[414] M. Kampakoglou and A. J. Benson, *Tidal mass loss from collisionless systems*, Monthly Notices of the Royal Astronomical Society **374**, 775 (2007), arXiv:astro-ph/0607024.

[415] J. Gan, X. Kang, F. C. van den Bosch, and J. Hou, *An improved model for the dynamical evolution of dark matter subhaloes*, Monthly Notices of the Royal Astronomical Society **408**, 2201 (2010), arXiv:1007.0023.

[416] A. R. Pullen, A. J. Benson, and L. A. Moustakas, *Nonlinear evolution of dark matter subhalos and applications to warm dark matter*, Astrophysical Journal **792**, 24 (2014), arXiv:1407.8189.

[417] F. Jiang and F. C. van den Bosch, *Statistics of dark matter substructure–I. Model and universal fitting functions*, Monthly Notices of the Royal Astronomical Society **458**, 2848 (2016), arXiv:1403.6827.

[418] S. Kazantzidis, L. Mayer, C. Mastropietro, J. Diemand, J. Stadel, and B. Moore, *Density profiles of cold dark matter substructure: implications for the missing-satellites problem*, Astrophysical Journal **608**, 663 (2004), arXiv:astro-ph/0312194.

[419] J. I. Read, M. I. Wilkinson, N. W. Evans, G. Gilmore, and J. T. Kleyna, *The tidal stripping of satellites*, Monthly Notices of the Royal Astronomical Society **366**, 429 (2006), arXiv:astro-ph/0506687.

[420] B. Moore, *Evidence against dissipation-less dark matter from observations of galaxy haloes*, Nature **370**, 629 (1994).

[421] J. I. Read, M. G. Walker, and P. Steger, *The case for a cold dark matter cusp in Draco*, Monthly Notices of the Royal Astronomical Society **481**, 860 (2018), arXiv:1805.06934.

[422] L. M. Widrow, *Distribution functions for cuspy dark matter density profiles*, Astrophysical Journal Supplement Series **131**, 39 (2000).

[423] M. Fujii, Y. Funato, and J. Makino, *Dynamical friction on satellite galaxies*, Publications of the Astronomical Society of Japan **58**, 743 (2006), arXiv:`astro-ph/0511651`.

[424] M. Fellhauer and D. N. C. Lin, *The influence of mass-loss from a star cluster on its dynamical friction–I. Clusters without internal evolution*, Monthly Notices of the Royal Astronomical Society **375**, 604 (2007), arXiv:`astro-ph/0611557`.

[425] O. Y. Gnedin, L. Hernquist, and J. P. Ostriker, *Tidal shocking by extended mass distributions*, Astrophysical Journal **514**, 109 (1999), arXiv:`astro-ph/9709161`.

[426] L. S. Spitzer, Jr, *Dynamical Evolution of Globular Clusters* (Princeton University Press, Princeton, NJ, 1987).

[427] M. D. Weinberg, *Adiabatic invariants in stellar dynamics: I. Basic concepts*, Astronomical Journal **108**, 1398 (1994), arXiv:`astro-ph/9404015`.

[428] M. D. Weinberg, *Adiabatic invariants in stellar dynamics: II. Gravitational shocking*, Astronomical Journal **108**, 1403 (1994), arXiv:`astro-ph/9404016`.

[429] O. Y. Gnedin and J. P. Ostriker, *On the self-consistent response of stellar systems to gravitational shocks*, Astrophysical Journal **513**, 626 (1999), arXiv:`astro-ph/9902326`.

[430] A. Klypin, S. Gottlöber, A. V. Kravtsov, and A. M. Khokhlov, *Galaxies in N-body simulations: overcoming the overmerging problem*, Astrophysical Journal **516**, 530 (1999), arXiv:`astro-ph/9708191`.

[431] A. Klypin, F. Prada, G. Yepes, S. Heß, and S. Gottlöber, *Halo abundance matching: accuracy and conditions for numerical convergence*, Monthly Notices of the Royal Astronomical Society **447**, 3693 (2015), arXiv:`1310.3740`.

[432] M. S. Delos, *Evolution of dark matter microhalos through stellar encounters*, Physical Review D **100**, 083529 (2019), arXiv:`1907.13133`.

[433] G. Tormen, *The rise and fall of satellites in galaxy clusters*, Monthly Notices of the Royal Astronomical Society **290**, 411 (1997), arXiv:`astro-ph/9611078`.

[434] S. Khochfar and A. Burkert, *Orbital parameters of merging dark matter halos*, Astronomy and Astrophysics **445**, 403 (2006), arXiv:`astro-ph/0309611`.

[435] A. R. Wetzel, *On the orbits of infalling satellite haloes*, Monthly Notices of the Royal Astronomical Society **412**, 49 (2011), arXiv:`1001.4792`.

[436] L. Jiang, S. Cole, T. Sawala, and C. S. Frenk, *Orbital parameters of infalling satellite haloes in the hierarchical ΛCDM model*, Monthly Notices of the Royal Astronomical Society **448**, 1674 (2015), arXiv:`1409.1179`.

[437] M. S. Delos, T. Linden, and A. L. Erickcek, *Breaking a dark degeneracy: The gamma-ray signature of early matter domination*, Physical Review D **100**, 123546 (2019), arXiv:`1910.08553`.

[438] J. S. Bullock and M. Boylan-Kolchin, *Small-scale challenges to the ΛCDM paradigm*, Annual Review of Astronomy and Astrophysics **55**, 343 (2017), arXiv:`1707.04256`.

[439] V. S. Berezinsky, V. I. Dokuchaev, and Y. N. Eroshenko, *Small-scale clumps of dark matter*, Physics-Uspekhi **57**, 1 (2014), arXiv:`1405.2204`.

[440] E. D'Onghia, V. Springel, L. Hernquist, and D. Keres, *Substructure depletion in the Milky Way halo by the disk*, Astrophysical Journal **709**, 1138 (2010), arXiv:`0907.3482`.

[441] Q. Zhu, F. Marinacci, M. Maji, Y. Li, V. Springel, and L. Hernquist, *Baryonic impact on the dark matter distribution in Milky Way-sized galaxies and their satellites*, Monthly Notices of the Royal Astronomical Society **458**, 1559 (2016), arXiv:`1506.05537`.

[442] R. Errani, J. Peñarrubia, C. F. P. Laporte, and F. A. Gómez, *The effect of a disc on the population of cuspy and cored dark matter substructures in Milky Way-like galaxies*, Monthly Notices of the Royal Astronomical Society Letters p. slw211 (2016), arXiv:`1608.01849`.

[443] S. Garrison-Kimmel, A. Wetzel, J. S. Bullock, P. F. Hopkins, M. Boylan-Kolchin, C.-A. Faucher-Giguère, D. Kereš, E. Quataert, R. E. Sanderson, A. S. Graus, et al., *Not so lumpy after all: modelling the depletion of dark matter subhaloes by Milky Way-like galaxies*, Monthly Notices of the Royal Astronomical Society **471**, 1709 (2017), arXiv:`1701.03792`.

[444] T. Kelley, J. S. Bullock, S. Garrison-Kimmel, M. Boylan-Kolchin, M. S. Pawlowski, and A. S. Graus, *Phat ELVIS: The inevitable effect of the Milky Way's disc on its dark matter subhaloes*, Monthly Notices of the Royal Astronomical Society **487**, 4409 (2019), arXiv:`1811.12413`.

[445] M. Hütten, M. Stref, C. Combet, D. Maurin, and J. Lavalle, *γ-ray and ν searches for dark-matter subhalos in the Milky Way with a baryonic potential*, Galaxies **7**, 60 (2019), arXiv:`1904.10935`.

[446] A. W. McConnachie, *The observed properties of dwarf galaxies in and around the local group*, Astronomical Journal **144**, 4 (2012), arXiv:`1204.1562`.

[447] S. Ghigna, B. Moore, F. Governato, G. Lake, T. Quinn, and J. Stadel, *Dark matter haloes within clusters*, Monthly Notices of the Royal Astronomical Society **300**, 146 (1998), arXiv:`astro-ph/9801192`.

[448] G. Tormen, A. Diaferio, and D. Syer, *Survival of substructure within dark matter haloes*, Monthly Notices of the Royal Astronomical Society **299**, 728 (1998), arXiv:`astro-ph/9712222`.

[449] L. Gao, S. D. M. White, A. Jenkins, F. Stoehr, and V. Springel, *The subhalo populations of ΛCDM dark haloes*, Monthly Notices of the Royal Astronomical Society **355**, 819 (2004), arXiv:`astro-ph/0404589`.

[450] A. V. Kravtsov, A. A. Berlind, R. H. Wechsler, A. A. Klypin, S. Gottlöber, B. Allgood, and J. R. Primack, *The dark side of the halo occupation distribution*, Astrophysical Journal **609**, 35 (2004), arXiv:`astro-ph/0308519`.

[451] C. Giocoli, G. Tormen, and F. C. Van Den Bosch, *The population of dark matter subhaloes: mass functions and average mass-loss rates*, Monthly Notices of the Royal Astronomical Society **386**, 2135 (2008), arXiv:`0712.1563`.

[452] C. Giocoli, G. Tormen, R. K. Sheth, and F. C. van den Bosch, *The substructure hierarchy in dark matter haloes*, Monthly Notices of the Royal Astronomical Society **404**, 502 (2010), arXiv:`0911.0436`.

[453] S. Hofmann, D. J. Schwarz, and H. Stöcker, *Damping scales of neutralino cold dark matter*, Physical Review D **64**, 083507 (2001), arXiv:`astro-ph/0104173`.

[454] T. Ishiyama and S. Ando, *The abundance and structure of subhaloes near the free streaming scale and their impact on indirect dark matter searches*, Monthly Notices of the Royal Astronomical Society **492**, 3662 (2020), arXiv:`1907.03642`.

[455] K. Belotsky, A. Kirillov, and M. Khlopov, *Gamma-ray evidence for dark matter clumps*, Gravitation and Cosmology **20**, 47 (2014), arXiv:`1212.6087`.

[456] J. Chen and S. M. Koushiappas, *Gravitational nanolensing from subsolar mass dark matter halos*, Astrophysical Journal **724**, 400 (2010), arXiv:`1008.2385`.

[457] S. Baghram, N. Afshordi, and K. M. Zurek, *Prospects for detecting dark matter halo substructure with pulsar timing*, Physical Review D **84**, 043511 (2011), arXiv:`1101.5487`.

[458] K. Kashiyama and M. Oguri, *Detectability of small-scale dark matter clumps with pulsar timing arrays* (2018), arXiv:`1801.07847`.

[459] A. X. Gonzalez-Morales, O. Valenzuela, and L. A. Aguilar, *Constraining dark matter substructure with the dynamics of astrophysical systems*, Journal of Cosmology and Astroparticle Physics **03**, 001 (2013), arXiv:`1211.6745`.

[460] J. Peñarrubia, *Fluctuations of the gravitational field generated by a random population of extended substructures*, Monthly Notices of the Royal Astronomical Society **474**, 1482 (2017), arXiv:`1710.06443`.

[461] J. Binney and A. Knebe, *Two-body relaxation in cosmological simulations*, Monthly Notices of the Royal Astronomical Society **333**, 378 (2002), arXiv:`astro-ph/0105183`.

[462] S. B. Green and F. C. van den Bosch, *The tidal evolution of dark matter substructure – I. Subhalo density profiles*, Monthly Notices of the Royal Astronomical Society **490**, 2091 (2019), arXiv:`1908.08537`.

[463] J. Einasto, *On the construction of a composite model for the galaxy and on the determination of the system of galactic parameters*, Trudy Astrofizicheskogo Instituta Alma-Ata **5**, 87 (1965).

[464] B. Moore, *An upper limit to the mass of black holes in the halo of the galaxy*, Astrophysical Journal **413**, L93 (1993).

[465] I. R. King, *The structure of star clusters. III. Some simple dynamical models*, Astronomical Journal **71**, 64 (1966).

[466] W. Liu, X.-J. Bi, S.-J. Lin, and P.-F. Yin, *Constraints on dark matter annihilation and decay from the isotropic gamma-ray background*, Chinese Physics C **41**, 045104 (2017), arXiv:`1602.01012`.

[467] C. Blanco and D. Hooper, *Constraints on decaying dark matter from the isotropic gamma-ray background*, Journal of Cosmology and Astroparticle Physics **03**, 019 (2019), arXiv:`1811.05988`.

[468] K. Griest and M. Kamionkowski, *Unitarity limits on the mass and radius of dark-matter particles*, Physical Review Letters **64**, 615 (1990).

[469] A. Loeb and M. Zaldarriaga, *The small-scale power spectrum of cold dark matter*, Physical Review D **71**, 103520 (2005), arXiv:`astro-ph/0504112`.

[470] S. Profumo, K. Sigurdson, and M. Kamionkowski, *What mass are the smallest protohalos?*, Physical Review Letters **97**, 031301 (2006), arXiv:`astro-ph/0603373`.

[471] E. Bertschinger, *Effects of cold dark matter decoupling and pair annihilation on cosmological perturbations*, Physical Review D **74**, 063509 (2006), arXiv:`astro-ph/0607319`.

[472] T. Bringmann and S. Hofmann, *Thermal decoupling of WIMPs from first principles*, Journal of Cosmology and Astroparticle Physics **04**, 016 (2007), erratum: 03, E02 (2016), arXiv:`hep-ph/0612238`.

[473] I. R. Waldstein, A. L. Erickcek, and C. Ilie, *Quasidecoupled state for dark matter in nonstandard thermal histories*, Physical Review D **95**, 123531 (2017), arXiv:`1609.05927`.

[474] G. B. Gelmini and P. Gondolo, *Ultra-cold WIMPs: relics of non-standard pre-BBN cosmologies*, Journal of Cosmology and Astroparticle Physics **10**, 002 (2008), arXiv:`0803.2349`.

[475] D. J. Eisenstein and W. Hu, *Baryonic features in the matter transfer function*, Astrophysical Journal **496**, 605 (1998), arXiv:`astro-ph/9709112`.

[476] N. Aghanim et al. (Planck Collaboration), *Planck 2018 results. VI. Cosmological parameters* (2018), arXiv:`1807.06209`.

[477] M. Ackermann et al. (Fermi-LAT Collaboration), *The spectrum of isotropic diffuse gamma-ray emission between 100 MeV and 820 GeV*, Astrophysical Journal **799**, 86 (2015), arXiv:`1410.3696`.

[478] M. Cirelli, P. Panci, and P. D. Serpico, *Diffuse gamma ray constraints on annihilating or decaying dark matter after Fermi*, Nuclear Physics B **840**, 284 (2010), arXiv:`0912.0663`.

[479] M. G. Baring, T. Ghosh, F. S. Queiroz, and K. Sinha, *New limits on the dark matter lifetime from dwarf spheroidal galaxies using Fermi-LAT*, Physical Review D **93**, 103009 (2016), arXiv:`1510.00389`.

[480] G. D. Martinez, *A robust determination of Milky Way satellite properties using hierarchical mass modelling*, Monthly Notices of the Royal Astronomical Society **451**, 2524 (2015), arXiv:`1309.2641`.

[481] N. F. Martin, J. T. A. de Jong, and H.-W. Rix, *A comprehensive maximum likelihood analysis of the structural properties of faint Milky Way satellites*, Astrophysical Journal **684**, 1075 (2008), arXiv:`0805.2945`.

[482] J. Woo, S. Courteau, and A. Dekel, *Scaling relations and the fundamental line of the local group dwarf galaxies*, Monthly Notices of the Royal Astronomical Society **390**, 1453 (2008), arXiv:`0807.1331`.

[483] H. C. Plummer, *On the problem of distribution in globular star clusters*, Monthly Notices of the Royal Astronomical Society **71**, 460 (1911).

[484] P. Kroupa, *The initial mass function of stars: evidence for uniformity in variable systems*, Science **295**, 82 (2002), arXiv:`astro-ph/0201098`.

[485] A. Aparicio, R. Carrera, and D. Martínez-Delgado, *The star formation history and morphological evolution of the Draco dwarf spheroidal galaxy*, Astronomical Journal **122**, 2524 (2001), arXiv:`astro-ph/0108159`.

[486] D. Foreman-Mackey, D. W. Hogg, D. Lang, and J. Goodman, *emcee: The MCMC Hammer*, Publications of the Astronomical Society of the Pacific **125**, 306 (2013), arXiv:`1202.3665`.

[487] A. Geringer-Sameth, S. M. Koushiappas, and M. Walker, *Dwarf galaxy annihilation and decay emission profiles for dark matter experiments*, Astrophysical Journal **801**, 74 (2015), arXiv:1408.0002.

[488] A. Z. Bonanos, K. Z. Stanek, A. H. Szentgyorgyi, D. D. Sasselov, and G. A. Bakos, *The RR Lyrae distance to the Draco dwarf spheroidal galaxy*, Astronomical Journal **127**, 861 (2004), errata: 133, 756 (2007); 136, 896 (2008), arXiv:astro-ph/0310477.

[489] M. Ackermann et al. (Fermi-LAT Collaboration), *Dark matter constraints from observations of 25 Milky Way satellite galaxies with the Fermi Large Area Telescope*, Physical Review D **89**, 042001 (2014), arXiv:1310.0828.

[490] D. Hooper and T. Linden, *On the gamma-ray emission from Reticulum II and other dwarf galaxies*, Journal of Cosmology and Astroparticle Physics **09**, 016 (2015), arXiv:1503.06209.

[491] Fermi-L. A. T. Collaboration, *Fermi Large Area Telescope fourth source catalog* (2019), arXiv:1902.10045.

[492] F. Calore, P. D. Serpico, and B. Zaldivar, *Dark matter constraints from dwarf galaxies: a data-driven analysis*, Journal of Cosmology and Astroparticle Physics **10**, 029 (2018), arXiv:1803.05508.

[493] S. Hoof, A. Geringer-Sameth, and R. Trotta, *A global analysis of dark matter signals from 27 dwarf spheroidal galaxies using ten years of Fermi-LAT observations* (2018), arXiv:1812.06986.

[494] T. Linden, *A robust method for treating astrophysical mismodeling in dark matter annihilation searches of dwarf spheroidal galaxies* (2019), arXiv:1905.11992.

[495] T. Daylan, D. P. Finkbeiner, D. Hooper, T. Linden, S. K. N. Portillo, N. L. Rodd, and T. R. Slatyer, *The characterization of the gamma-ray signal from the central Milky Way: A case for annihilating dark matter*, Physics of the Dark Universe **12**, 1 (2016), arXiv:1402.6703.

[496] R. J. Jennings, J. M. Cordes, and S. Chatterjee, *Detecting gravitational scattering of interstellar objects using pulsar timing* (2019), arXiv:1910.08608.

[497] W. Dehnen, *Towards optimal softening in three-dimensional N-body codes—I. Minimizing the force error*, Monthly Notices of the Royal Astronomical Society **324**, 273 (2001), arXiv:astro-ph/0011568.

[498] E. Athanassoula, E. Fady, J. C. Lambert, and A. Bosma, *Optimal softening for force calculations in collisionless N-body simulations*, Monthly Notices of the Royal Astronomical Society **314**, 475 (2000), arXiv:astro-ph/9912467.

[499] C. Power, J. F. Navarro, A. Jenkins, C. S. Frenk, S. D. M. White, V. Springel, J. Stadel, and T. Quinn, *The inner structure of ΛCDM haloes—I. A numerical convergence study*, Monthly Notices of the Royal Astronomical Society **338**, 14 (2003), arXiv:astro-ph/0201544.

[500] R. J. Splinter, A. L. Melott, S. F. Shandarin, and Y. Suto, *Fundamental discreteness limitations of cosmological N-body clustering simulations*, Astrophysical Journal **497**, 38 (1998), arXiv:astro-ph/9706099.

[501] A. L. Melott, S. F. Shandarin, R. J. Splinter, and Y. Suto, *Demonstrating discreteness and collision error in cosmological N-body simulations of dark matter gravitational clustering*, Astrophysical Journal Letters **479**, L79 (1997), arXiv:astro-ph/9609152.

[502] S. Weinberg, *Cosmology* (Oxford University Press, Oxford, 2008).

[503] J. Barnes and P. Hut, *A hierarchical O (N log N) force-calculation algorithm*, Nature **324**, 446 (1986).

[504] N. E. Drakos, J. E. Taylor, and A. J. Benson, *The phase-space structure of tidally stripped haloes*, Monthly Notices of the Royal Astronomical Society **468**, 2345 (2017), arXiv:`1703.07836`.

[505] J. I. Read, G. Lake, O. Agertz, and V. P. Debattista, *Thin, thick and dark discs in ΛCDM*, Monthly Notices of the Royal Astronomical Society **389**, 1041 (2008), arXiv:`0803.2714`.

[506] P. J. McMillan, *Mass models of the Milky Way*, Monthly Notices of the Royal Astronomical Society **414**, 2446 (2011), arXiv:`1102.4340`.

[507] S. T. Sohn, G. Besla, R. P. Van Der Marel, M. Boylan-Kolchin, S. R. Majewski, and J. S. Bullock, *The space motion of Leo I: Hubble space telescope proper motion and implied orbit*, Astrophysical Journal **768**, 139 (2013), arXiv:`1210.6039`.

[508] F. Nesti and P. Salucci, *The dark matter halo of the Milky Way, AD 2013*, Journal of Cosmology and Astroparticle Physics **07**, 016 (2013), arXiv:`1304.5127`.

[509] A. Helmi, F. Van Leeuwen, P. J. McMillan, D. Massari, T. Antoja, A. C. Robin, L. Lindegren, U. Bastian, F. Arenou, C. Babusiaux, et al. (Gaia Collaboration), *Gaia Data Release 2-Kinematics of globular clusters and dwarf galaxies around the Milky Way*, Astronomy and Astrophysics **616**, A12 (2018), arXiv:`1804.09381`.

[510] T. K. Fritz, G. Battaglia, M. S. Pawlowski, N. Kallivayalil, R. Van Der Marel, S. T. Sohn, C. Brook, and G. Besla, *Gaia DR2 proper motions of dwarf galaxies within 420 kpc-orbits, Milky Way mass, tidal influences, planar alignments, and group infall*, Astronomy and Astrophysics **619**, A103 (2018), arXiv:`1805.00908`.